USE OF NON-DESTRUCTIVE X-RAY MICROSCOPIC TECHNIQUES TO STUDY FLUID TRANSPORT IN CEMENT-BASED MATERIALS

By

MEHDI KHANZADEH MORADLLO

Master of Science in Civil Engineering
University of Tehran
Tehran, Iran
2010

Submitted to the Faculty of the
Graduate College of the
Oklahoma State University
in partial fulfillment of
the requirements for
the Degree of
DOCTOR OF PHILOSOPHY
December, 2016

USE OF NON-DESTRUCTIVE X-RAY

MICROSCOPIC TECHNIQUES TO STUDY FLUID

TRANSPORT IN CEMENT-BASED MATERIALS

Dissertation Approved:

Dr. Matthew Tyler Ley

Dissertation Adviser

Dr. Bruce W. Russell

Dr. Julie Ann Hartell

Dr. Jay C. Hanan

ACKNOWLEDGEMENTS

First, I would like to express my sincere appreciation to my advisor, Dr. Tyler Ley, for his insights, guidance, encouragement, and especially his continuous support throughout this study. Dr. Ley has consistently and enthusiastically provided me valuable advice and suggestions which made the completion of this research an enjoyable experience. I would like to thank Dr. Bruce Russell, Dr. Julie Hartell, and Dr. Jay Hanan for agreeing to serve on my committee and their support and enlightenment in this research.

I would like to acknowledge the financial support from the Oklahoma Department of Transportation (ODOT 2229), Federal Highway Association (FHWA) Exploratory Advanced Research (EAR) Program (Project No. CMMI 1030972), and the United State National Science Foundation CMMI 1635878 and CMMI 1150404 CAREER Award. The experimental works presented in this dissertation were performed in Bert Cooper Engineering, Advanced Technology and Research Center, and Venture I Microscopy Laboratories at Oklahoma State University. I would like to thank the support from technical staff of these Laboratories that has made their operation possible. I would like to especially thank Professor Kerry Havner for his support through “Kerry and Roberta Havner Fellowship in Structures and Mechanics”.

I would like to extend my thanks to all my colleagues and friends at Oklahoma State University, especially Bryan Sudbrink, Dr. Qinang Hu, Dr. Mohammed Aboustait, Amir Hajibabaee, Morteza Khatibmasjedi, Chad Stevenson, Jeffery Terronez, and Katelyn Oquin, for their assistance and contributions to the content of this dissertation.

I want to thank my beloved and supportive family, especially my parents for unconditionally loving and supporting me. A special thank you goes to my beloved and wonderful wife, Mina, for her love and support over the years. I couldn't have done this journey without her love, inspiration and endurance.

Name: MEHDI KHANZADEH MORADLLO

Date of Degree: DECEMBER, 2016

Title of Study: USE OF NON-DESTRUCTIVE X-RAY MICROSCOPIC TECHNIQUES TO STUDY FLUID TRANSPORT IN CEMENT-BASED MATERIALS

Major Field: CIVIL ENGINEERING

Abstract: Most of the urban infrastructure is made of concrete with a design service life of over 50 years. Unfortunately, many concrete structures suffer from premature deterioration due to durability issues, most commonly caused by corrosion. The external penetration of ions into cementitious materials is the primary factor influencing the long-term durability of concrete structures. Current test methods to study ion transport in cement-based materials are typically destructive, time consuming, labor intensive, and have a poor spatial resolution to study complex transport phenomenon and capture the effect of complex geometries on fluid transport. In addition, there is little knowledge of the dynamic process of fluid penetration into cement-based materials because few experimental techniques are able to give quantitative spatial measurements of the fluid movement without damaging the sample. This study aims to develop a systematic approach to use micro X-ray fluorescence (μXRF) and Transmission X-ray microscopy (TXM) to study ion transport in different cementitious systems. Examples were shown where these powerful, non-destructive techniques can identify the influence of local abnormalities on ion transport with high spatial resolution and can image the early age combined ion transport mechanisms in real time. The current study uses these techniques to evaluate and compare the time-dependent resistance of different alternative cementitious materials (ACMs) to ion penetration. In addition, the effect of degree of saturation, which is a crucial factor in durability of cement-based materials, on ion penetration into partially-saturated samples were investigated by using the developed X-ray imaging techniques. Furthermore, the performance of silane treatments, which is a commonly used surface treatment to reduce fluid entry into concrete was evaluated by μXRF. Also, the effective lifespan of this treatment in concrete bridge decks was determined. The use of developed techniques and observed results from this study helps to expand our understanding of ion transport in cement-based materials and to greatly improve the current models of mass transport and service life predictions of the concrete. This can help a large amount of money to be saved in repair, maintenance, and management of concrete structures.

TABLE OF CONTENTS

Chapter Page

Chapter Page

Chapter Page

LIST OF TABLES

Table Page

LIST OF FIGURES

Figure Page

Figure Page

Figure Page

Figure Page

Figure Page

CHAPTER I

INTRODUCTION

1.1 Overview

Concrete is the most commonly used construction materials in the world. Unfortunately, concrete structures face a multitude of problems that threaten the serviceability of the structure such as corrosion, alkali silica reaction, sulfate attack, bulk freezing and thawing damage, and scaling [1-2]. For instance, it was estimated that corrosion damages to highway bridges cost $8.3 billion per year in the United States [3]. A number of concrete durability problems are caused by potentially harmful external fluids penetrating into concrete materials. Therefore, the transport properties of concrete materials play an important role in the durability performance of concrete structures [4-5]. Unfortunately, most widely used test methods to investigate fluid transport into cementitious materials are based on average section measurements and have a poor spatial resolution to obtain the influence of complex transport phenomenon such as combined transport mechanisms in partially-saturated samples and cannot provide fundamental observation of the effect of complex geometries such as cracks on mass transport and subsequently provide important insights about concrete deterioration mechanisms. In addition, the shortage in determining transport properties of cement-based materials with high spatial resolution can cause significant discrepancies between the predicted service life of structures based on simulation models and their performance in real field condition.

Therefore, a technique is needed that is rapid, non-destructive, and able to provide useful and direct observations of fluid movement in concrete materials at a useful length scale and with high spatial resolution.

One solution to this problem would be to use non-destructive micro-analysis X-ray imaging techniques such as micro X-ray fluorescence (μXRF) and Transmission X-ray microscopy (TXM) to learn more about fluid movement in cement-based materials. μXRF is capable of mapping chemistry and discern between the aggregate and the paste with minimal human intervention. This technique could also identify local abnormalities that will alter the penetration results like cracks, Cl rich aggregates, or presence of surface treatments. TXM works based on the principle of X-ray radiation attenuation upon passing through matter where X-rays interact with the electron shell of the atom. In TXM the materials will appear to have different gray values depending on their X-ray absorption. While this technique does not provide direct compositional information about the irradiated materials, it does provide clues about compositional consistency. This method provides data with high spatial resolution in 2D or 3D to obtain greater insight about the mechanisms of fluid transport into cement-based materials. Also, because this method is non-destructive it can be used to conduct in-situ imaging. The use of fluid transport properties based on these methods will greatly improve the current models of mass transport and service life predictions of the concrete.

1.2 Research Objectives

The main objectives of this research are to:

- Develop a systematic approach to use a powerful, non-destructive μXRF method to determine different ion concentration profiles in cementitious materials.
- Develop a novel approach to use TXM to investigate in-situ ion transport in cement-based materials in 2D or 3D.

- Develop in-situ TXM method to study the effect of degree of saturation on ion penetration and provide important insights on early age combined ion transport mechanisms in partially-saturated cementitious materials.
- Study the time-dependent performance of various Alternative Cementitious Materials (ACMs) against ion intrusion by using the developed μXRF and TXM techniques.
- Detection of silane treatments by using the μXRF technique.
- Determining the effective lifespan of silane treatments in bridge decks.

1.3 Overview of Dissertation

This dissertation is organized in eight chapters in paper-based format. The first chapter of this dissertation presents the introduction of this study.

- The second chapter demonstrates the use of μXRF, a non-destructive chemical imaging technique, to obtain equivalent or better information than profile grinding methods (e.g. ASTM C 1556) with less human involvement. Examples are presented where the spatial measurements made by μXRF provide insights that are not possible with the conventional profile grinding method. This chapter in the present format was published in the journal of Cement and Concrete Research.
- The third chapter presents a systematic approach to use TXM to image in-situ and time resolved ion diffusion into cement-based materials in 2D and 3D. In addition, a 3D tomography data set is included to show how the technique can be used to measure complex phenomena such as filling of larger air voids at different fluid concentrations. Results from TXM were compared to μXRF and good agreement was found. This chapter in the present format was accepted for publication in the journal of Construction and Building Materials.
- In the fourth chapter, the influence of degree of saturation on ion penetration in cement paste was imaged and quantitatively measured by using X-ray imaging. In addition, important insights about combined ion transport mechanisms have been observed. Furthermore, an experimental model was

developed to determine the ion transport rate in partially-saturated samples based on fully saturated sample result. A comparison was made between results from TXM and conventional gravimetric method. This chapter in the present format was submitted for publication in the journal of Construction and Building Materials.

- In the fifth chapter, TXM and μXRF methods were used to investigate in-situ ion diffusion in paste and mortar samples modeled after successful structural concrete mixtures with five commercially available ACMs and an ordinary portland cement. The use of TXM offers advantages over conventional methods to investigate the resistance of cement-based materials with different chemistry against ion intrusion. This chapter in the present format was submitted for publication in the journal of Cement and Concrete Composites.

- The sixth chapter uses μXRF to compare the time-dependent Cl penetration resistance of the new two-part silane-epoxy system with a widely used type of silane in Oklahoma. It shows the utility of using μXRF to efficiently and rapidly evaluate the effectiveness of different surface treatment systems in deleterious environment. This chapter was prepared and presented as a conference paper for the NACE Concrete Service Life Extension Conference.

- In the seventh chapter, optical staining techniques and statistical analysis were used to investigate the 360 cores taken from 60 bridge decks treated with silane that have been in-service between 6 y and 20 y in order to determine the effective lifespan of silane treatments in concrete bridge decks. This chapter in the present format was published in the journal of Construction and Building Materials.

- Finally, chapter eight summarizes all the findings of this study and discusses the main conclusions of a current dissertation. Suggestions for future work are also provided.

The research presented in this dissertation is based on the work performed by the author at Oklahoma State University. The papers discussed above were published with the author as the primary author.

Coauthors are: Bryan Sudbrink, Qinang Hu, Mohammed Aboustait, Braden Tabb, Jeffrey Davis and Tyler Ley. Their contributions are acknowledged and are greatly appreciated.

References

[1] P.K. Mehta, Durability of Concrete- Fifty Years of Progress?, ACI SP 126-1, (1991) 1-31.

[2] F. Ghassemzadeh, M. Shekarchi, S. Sajedi, M.J. Mohebbi, M. Khanzadeh Moradllo, (2011). Performance of repair concretes in marine environments. In Proceedings of the annual conference Canadian society for civil Engineering, Ottawa, Canada, pp. 1654–1664.

[3] G.H. Koch, M.P. Brongers, N.G. Thompson, Y.P. Virmani, J.H. Payer, Corrosion costs and preventive strategies in the United States, Report by CC Technologies Laboratories, Inc. to Federal Highway Administration (FHWA)-RD-01-151, September 2001.

[4] F. Ghassemzadeh, M. Shekarchi, S. Sajedi, M. Khanzadeh Moradllo, S. Sadati, (2010). Effect of silica fume and GGBS on shrinkage in the high performance concrete. In Proceedings of the sixth international conference on concrete under severe conditions: environment and loading, Yucatan, Mexico, pp. 1007–1012.

[5] S. Sadati, M. Khanzadeh Moradllo, M. Shekarchi, Long-term durability of onshore coated concrete — chloride ion and carbonation effects, Frontiers of Struct. & Civil Eng., 10 (2016) 150–161. doi:10.1007/s11709-016-0341-2.

CHAPTER II

USING MICRO X-RAY FLUORESCENCE TO IMAGE CHLORIDE PROFILES IN CONCRETE

Abstract

Corrosion of steel reinforcement in concrete is not easy to detect until cracking has initiated. When there is a question about Cl intrusion into concrete, cores are taken, the sample is ground in controlled thicknesses, and then the powder is analyzed by titration. This paper uses micro X-ray fluorescence (μXRF), a non-destructive chemical imaging technique, to obtain equivalent or better information than profile grinding methods with less human involvement. Fifteen different comparisons are made between profile grinding and μXRF from the same concrete and the results are comparable. Examples are also presented where the spatial measurements made by μXRF provide insights that are not possible with the conventional profile grinding method. This means the Cl profile can be obtained with μXRF with less human effort while providing additional insights not possible with the typical profile grinding analysis.

Keywords: μXRF; Service life; Durability; Chloride; Corrosion.

2.1 Introduction

The most prevalent and costly durability problem with structural concrete is the corrosion of internal reinforcing steel from Cl ions [1-4]. According to the Federal Highway Administration (FHWA), corrosion causes $8.3 billion in damage annually to the transportation infrastructure [1]. The Cl ions are typically contributed by deicing salts, ocean water, or from clays rich in ionic salts [5]. While these materials are sometimes found within materials used to make concrete, typically they penetrate the concrete from an external surface.

The most widely used method to investigate Cl ingress into concrete is to destructively take cores, powder the concrete at controlled depths, and then analyze the powder with titration for Cl concentration. A version of this technique is used in many standards, including ASTM C1152, AASHTO T 260-97 and NT Build 208. These measurements provide insight into the rate of Cl ingress and can be used to evaluate the quality of concrete, the amount of Cl present, and to project the long term service life of the structure.

These techniques require that at least 10 g be collected from a number of different depths of the concrete. This can be time consuming. The collected powder is a combination of both aggregate and cement paste. Since the Cl is primarily contained in the paste, the aggregate dilute the sample. It would be possible to reduce the amount of material and time needed to complete the test if it was possible to focus the examination of chlorides within the paste.

One solution to this problem would be to use imaging techniques capable of mapping chemistry and discern between the aggregate and the paste with minimal human intervention. This technique could also identify local abnormalities that will alter the results like cracks, Cl rich aggregates, or other forms of chemical attack like alkali silica reaction, sulfate attack, or carbonation. The current profile grinding technique only investigates the average Cl concentration and so cannot provide insight into any of these phenomenon.

Several chemical imaging techniques have been used to investigate Cl penetration in concrete and paste. Jensen et al. [6] and Mori et al. [7] used electron probe microanalysis (EPMA) to measure Cl concentration profiles in cement paste and concrete samples. In addition, Dempere et al. [8] used both a scanning electron microscopy with electron dispersive spectrometer (SEM-EDS) and EPMA techniques to map Cl content in concrete. These studies all used electrons to interrogate the surface of the sample. The results also showed that the Cl concentration was consistently overestimated when compared with results from profile grinding. Another important conclusion was that the results from SEM-EDS and EPMA are dependent on the sample preparation [6-8]. For all of these reasons, electron based imaging methods are not widely used to evaluate Cl concentration in concrete or paste.

This work uses a non-destructive micro-analysis technique called micro X-ray fluorescence (μXRF) to image a cross section of concrete and determine the Cl concentrations. This technique is similar to bulk X-ray fluorescence (XRF), but uses a polycapillary optic to focus X-rays to a size of approximately 50 μm in diameter, whereas bulk XRF investigates the sample with a 1 cm diameter spot.

μXRF has many advantages over electron based imaging techniques such as SEM – EDS or EPMA with their typical configurations [9-12]. X-rays interact more weakly with matter than electrons and so they penetrate deeper into the sample (up to 1 mm for X-rays compared to a few microns for electrons) [13-14]. This deeper penetration will make a more representative measurement of the sample and makes the results less sensitive to the surface roughness. Furthermore, μXRF does not require conductive coatings to reduce electron build up or charging [6-9, 15]. This higher energy level and beam size also decreases the acquisition time required for large area maps [15].

A previous publication has used μXRF to investigate the Cl profiles within mortar [16]. This work used individual points at different depths to determine Cl content but they did not compare their measurements to profile grinding at comparable times. This work makes fifteen different comparisons between μXRF and profile grinding, and examples are given where spatial measurements made by μXRF provide insights that are not possible with profile grinding.

2.2 Experimental Methods

2.2.1 Materials and Mixtures

Six different concrete mixtures were investigated in this work. The mixtures have a water-to-cementitious ratio (w/cm) of 0.45. Four ASTM C618 Class C and one Class F fly ashes are used as 20% of the mass of the binder. One mixture used only portland cement as the binder. The cement is an ASTM C150; Type I. The chemical composition of cementitious materials is in **Table 2.1** and was obtained by bulk XRF. The coarse aggregate is a dolomitic limestone and the fine aggregate is a locally available natural sand.

2.2.2 Mixture Proportion and Sample Preparation

The concrete mixtures were prepared according to ASTM C192. All of the aggregate, both coarse and fine, were brought into the temperature controlled mixing facility at least a day before and their batch weights were corrected based on their moisture content. The aggregates were charged into the mixer along with approximately two-thirds of the mixing water. The combination was mixed for 3 min. Next, the walls of the mixer were scraped to remove material that stuck to the walls. Then the cement and fly ash was loaded into the mixer, followed by the remaining mixing water. The mixer was turned on for 3 min. Once this mixing period was complete, the mixture was left to ‘‘rest’’ for 2 min while buildup of material along the walls was removed. Next the mixer was run for 3 min. The slump, unit weight, and the air content were measured according to

ASTM C143, ASTM C138, and ASTM C231, respectively. The concrete mixture proportions and fresh properties are given in **Table 2.2**.

Table 2.1 Chemical composition with bulk XRF (% weight)

Oxide	Cement (PC)	FA-C1	FA-C2	FA-C3	FA-C4	FA-F
SiO_2	20.40	39.13	36.21	38.34	38.13	56.72
Al_2O_3	5.03	20.37	19.94	19.87	20.99	20.29
Fe_2O_3	2.95	6.15	6.67	6.12	5.46	5.62
CaO	62.89	21.18	23.96	23.07	15.54	9.95
MgO	2.08	5.33	5.17	5.16	3.71	2.97
Na_2O	0.35	1.60	1.67	1.53	7.88	0.54
K_2O	0.35	0.65	0.52	0.62	0.77	1.38
TiO_2	0.28	1.33	1.44	1.43	1.31	1.12
MnO_2	0.10	0.02	0.03	0.02	0.04	0.09
P_2O_5	0.16	1.60	1.44	1.09	0.67	0.13
SrO	0.16	0.34	0.38	0.35	0.72	0.27
BaO	0.12	0.72	0.69	0.64	1.47	0.26
SO_3	3.05	1.37	1.44	1.14	2.90	0.51
L.O.I	2.09	0.24	0.15	0.62	0.41	0.16
Moisture	0.16	0.11	0.04	0.01	0.03	0.02

Table 2.2 Concrete mixture proportions

Mixture	Cement (kg/m^3)	Fly Ash (kg/m^3)	Coarse Agg. (kg/m^3)	Fine Agg. (kg/m^3)	Water (kg/m^3)	Slump (cm)	Unit weight (kg/m^3)	NaCl Exposure ages (days)
C1	289.6	72.4	1097	714	163	16.5	2370.7	45, 90, 135
C2	289.6	72.4	1097	714	163	15.0	2379.7	45, 90, 135
C3	289.6	72.4	1097	714	163	16.5	2383.5	90, 135
C4	289.6	72.4	1097	714	163	17.5	2368.2	45, 90, 135
F	289.6	72.4	1097	714	163	14.0	2366.8	90, 135
OPC	362	-	1103	721	163	7.5	2346.5	45, 90

The concrete was placed in 12 x 12 x 8 cm plastic molds. The samples were cured for seven days at 23°C with a lid. Next the sample was stored in a saturated lime solution for seven days to minimize mass transport other than concentration driven diffusion. Next, the area between the

concrete and the container was sealed with silicone and the specimen was then placed in 165 g/L aqueous sodium chloride solution according to ASTM C1556 for either 45, 90, or 135 days at 23°C. Next, the Cl solution was removed and the samples were stored for 24 hours in laboratory conditions. Then, the sample was powdered at 1-5, 5-10, 10-15, and 15-20 mm depths parallel to the exposed surface using a drill press with 25 mm core bit. These depths were different than those recommended by ASTM C1556. The profile had a length of approximately 7.5 cm across the surface of the sample to obtain 15 g powder for each investigated layer. Finally, the powder was analyzed for acid-soluble Cl content with silver nitrate according with ASTM C1152.

After the powder was collected, the remaining sample was split and the exposed cross section was polished on a sanding belt for 15 minutes with 120 grit sandpaper to create a flat surface. Ethanol was then used to remove dirt and residue from the polished surface. This flat surface allowed for easier interpretation of the μXRF and optical microscopy results.

In addition, two concrete cores were taken from local in-service bridges that were 10 cm diameter and 15 cm height. These samples were polished with the same procedure and then analyzed with μXRF. There were no historical records available providing specific information on concrete mix design of the field samples.

2.2.3 μXRF Test Procedure

The μXRF analysis was conducted using the Orbis by EDAX. The instrument uses an 80 mm^2 Silicon Drift Detector Energy Dispersive Spectrometer (SDD-EDS) and a capillary optic that produces a 50 μm diameter beam. Images are created by moving the sample under the stationary X-ray beam. The X-ray beam causes characteristic fluorescence X-rays to be emitted at each spot, the intensity of these characteristic X-rays are measured by the SDD-EDS and stored in a database for later processing and analysis. This analysis is able to detect elements at 0.1% by weight [17]. A laser control system with a fixed focal length was used as a secondary focusing

tool to ensure a consistent geometry between the X-ray source, sample, and detector. This system is used to adjust the height of the sample such that the sample is in optimal focus.

Table 2.3 summarizes the settings used by the μXRF in this work. More details can be found in other publications [12]. An overall count rate of 20,000 counts per second was obtained with a 400 ms dwell time per pixel by using an accelerating voltage of 40 keV, a probe current of 1 mA, and a detector dead time near 20% as suggested by Janssens [17]. Each scan was ≈ 20 h per sample but did not require human intervention. This time can be reduced with future refinements to the method.

Table 2.3 Summary of μXRF settings used

counts per second	minimum of 20,000
current	1 mA
dead time	maximum of 20%
dwell time	400 ms/pixel
filter	25 μm Al
vacuum	1.35 Torr
voltage	40 keV

The μXRF uses a rhodium X-ray tube to produce polychromatic X-rays. The rhodium Lα line overlaps with the chlorine Kα line, complicating compositional analysis. Because of this a 25 μm thick Al filter was used to remove the low energy rhodium radiation. All scans were conducted under a 1.35 Torr vacuum to reduce the absorption of X-ray emission by N_2, O_2 and Ar gas [17-18].

The raw data from μXRF is the number of fluoresced X-rays in a certain energy window which includes background radiation as well. To determine concentration information, a set of reference standards were used to develop a calibration curve to change the count data to Cl concentration. This was done by making concrete samples with w/cm of 0.45 with known amounts of NaCl. A similar concrete mix design as the mixture with no fly ash was used to make the reference samples. The samples were then cured for seven days, polished, and then cleaned

as described previously. The initial chloride content of the standard concrete samples was assumed to be equal to zero. A summary of the calibration curve is shown in **Fig. 2.1**.

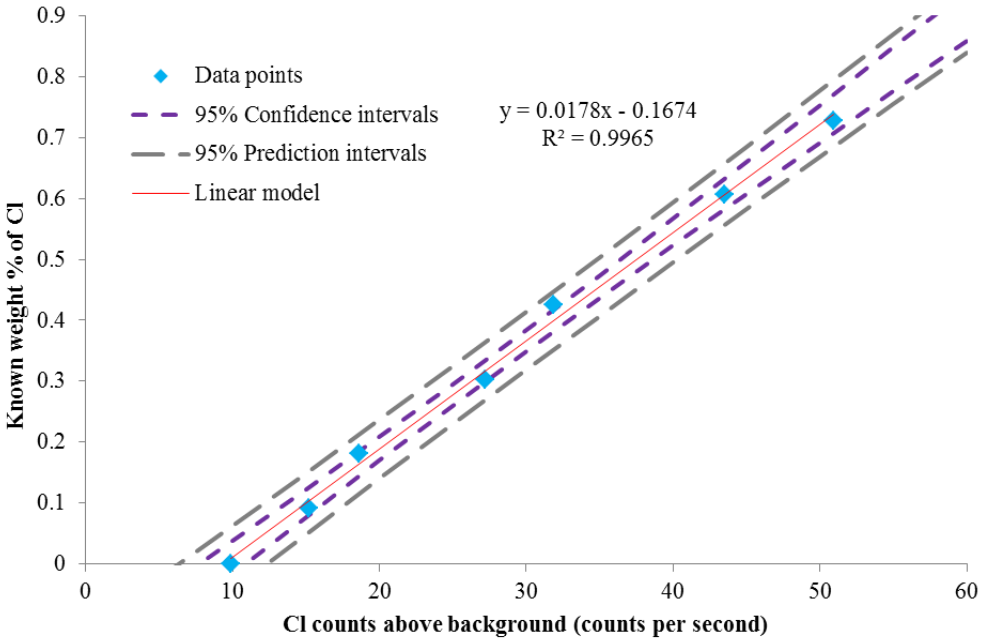

Fig. 2.1 Cl calibration curve used to change from counts to weight percentage in the µXRF analysis.

2.3 µXRF Data Analysis

2.3.1 µXRF Raw Data

As mentioned, the raw data from µXRF is the number of fluoresced X-rays in a certain energy window which includes background radiation as well. This data provides the user with detailed elemental information and is typically called a spectrum. In addition, spectral data can be used to produce maps of individual elements that a sample contains as shown in **Fig. 2.2**. As the concentration of an element increases then so does the brightness of the pixel in the image. These maps can give the illusion that the concentration is almost zero in low concentration regions. This can be resolved by the data segmentation analysis presented in the next section.

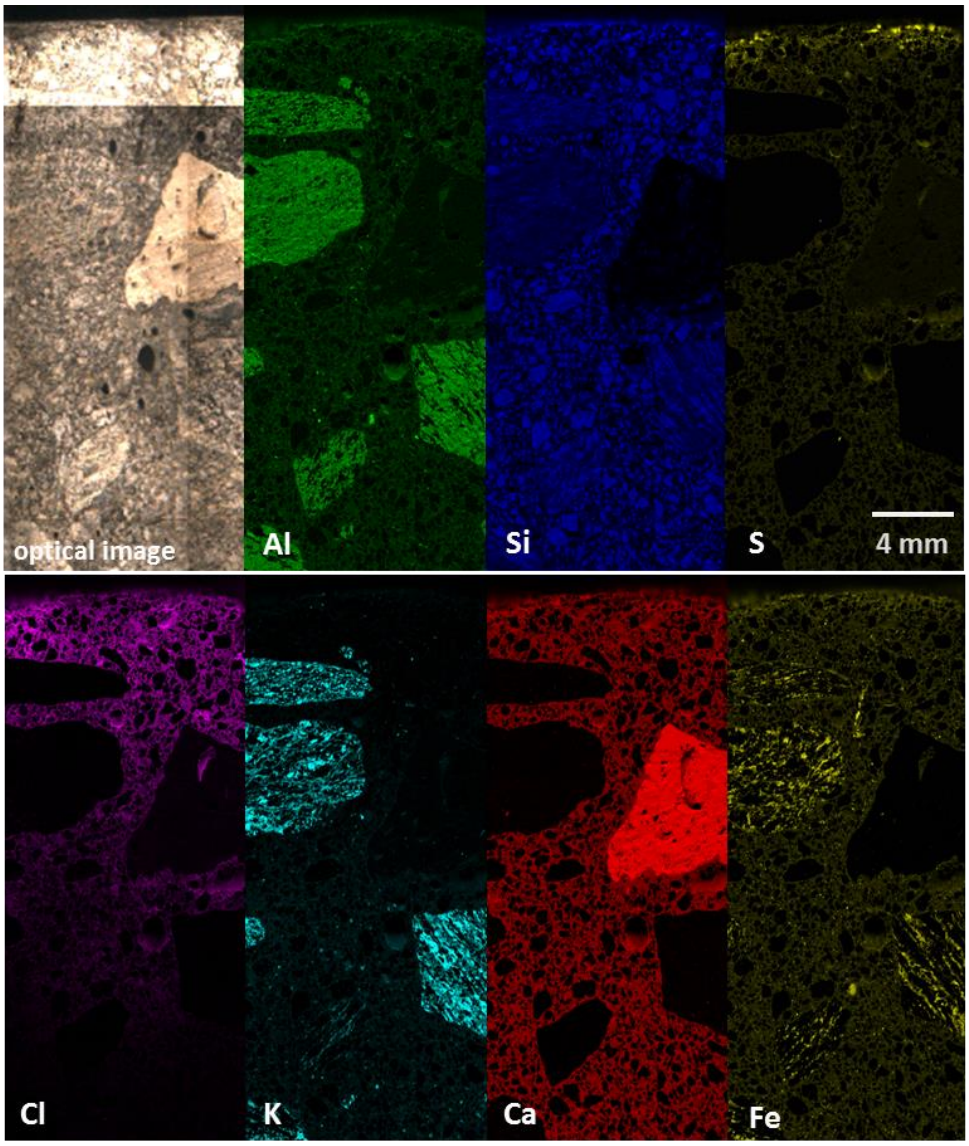

Fig. 2.2 Example of elemental images provided by μXRF.

2.3.2 Data Segmentation

After each sample is scanned with μXRF, the compositional maps were analyzed with an image processing software package called Lispix [19]. Lispix contains extensive image processing tools to extract spectral and image information from large datacubes [20]. This analysis is helpful as one can combine individual compositional maps into a single map that simultaneously provides unique compositions and location. This separation or unique regions is useful in data display and

analysis. More details about the software principles and applications can be found in other publications [19-22].

First, general aggregate locations were identified by the user by combining optical images and regions of high elemental concentration such as silicon (for silicate aggregates) and calcium (for limestone aggregates) as shown in **Fig. 2.3**. After identifying a few typical regions then other similar regions could be identified by Lispix. Next, the remaining pixels consisted of cement paste. These regions were separated by using different elemental concentration levels (i.e., low, medium and high counts of a given element) as shown in **Fig. 2.4**. These ranges were chosen by the user to show that there are distinct differences in concentration within the sample. Next the paste and aggregate phases were encoded as binary masks, assigned colors, and plotted as shown in **Fig. 2.5**. These final images provide a separation of the different types of aggregates, and Cl levels in the paste and is useful for qualitative observations. Additional details can be found in previous publication [12].

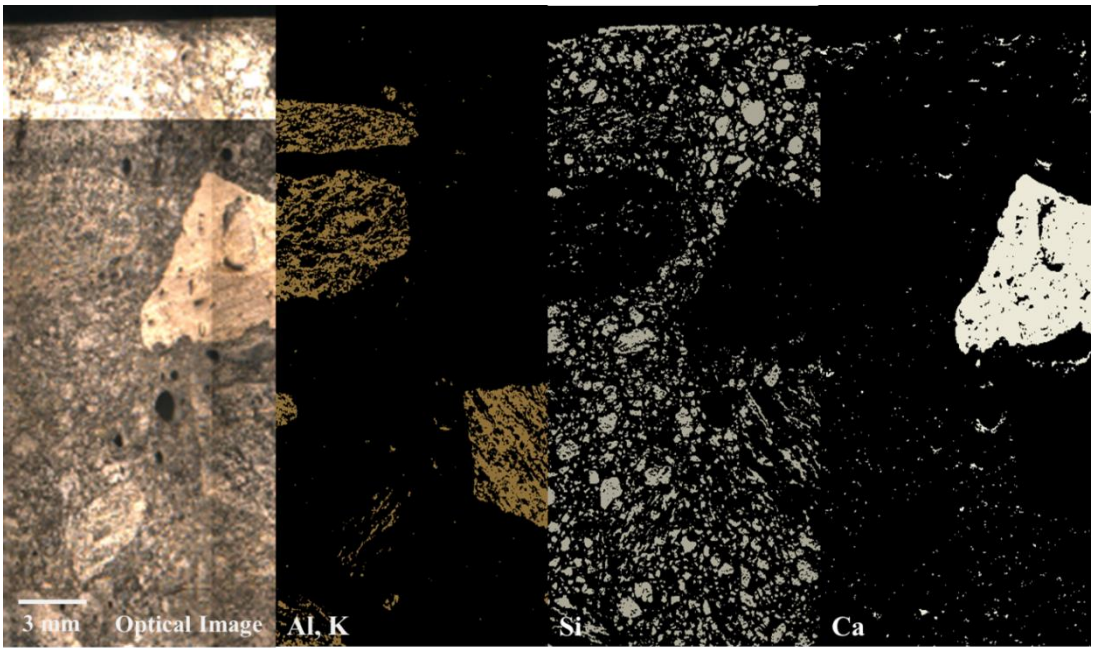

Fig. 2.3 Example of various types of aggregates categorized into individual clusters. Optical image (Left), cluster of aggregates rich in Al and K (middle left), cluster of siliceous aggregate (middle right), cluster of Ca rich aggregate (right). The different light levels in the optical image is caused by different normalization while stitching the images together.

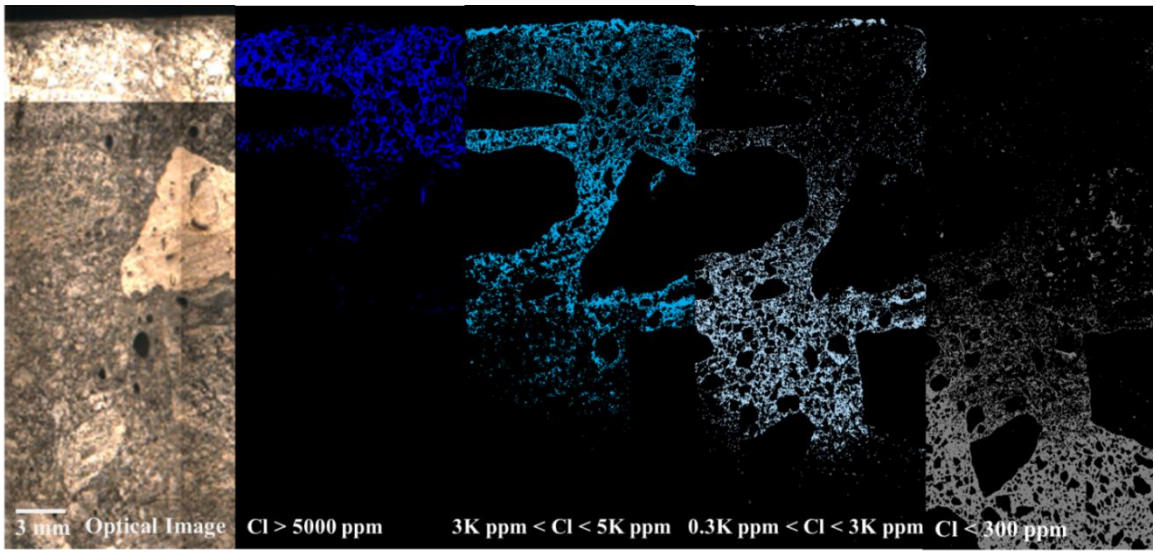

Fig. 2.4 Example of clustering cement paste based on varying levels of Cl concentrations. Optical image (left), Cl concentration higher than 5000 ppm (middle left), Cl concentration between 3000 and 5000 ppm (middle), Cl concentration between 300 and 3000 ppm (middle right), and Cl concentration less than 300 ppm (right). The different light levels in the optical image is caused by different normalization while stitching the images together.

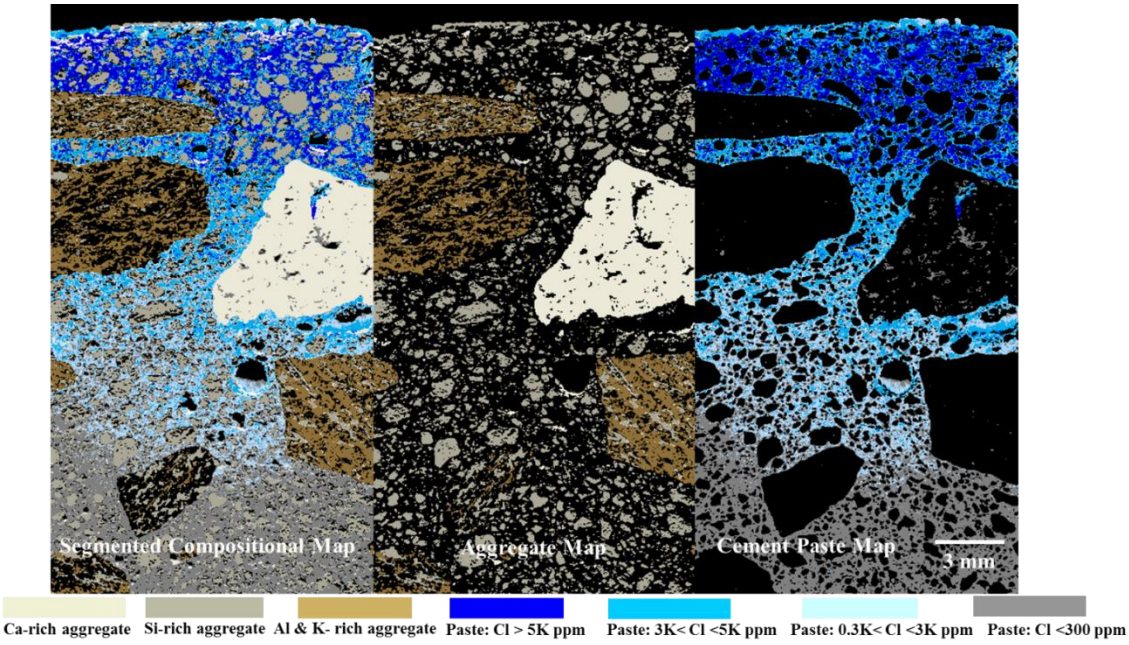

Fig. 2.5 An example of a compositional map showing the aggregate and paste (left), aggregate (middle), and cement paste (right).

2.3.3 Quantitative Analysis of μXRF Data

Finally, an image analysis code in Matlab was developed to analyze the spatial and compositional data. An overview of the program is shown in **Fig. 2.6**. First, the paste and the aggregate regions are isolated. This is helpful so that the Cl concentration contributed by the aggregate and paste can be compared. Next, the top surface of the sample is found by locating the surface pixel that can be classified as either paste or aggregate. This approach is especially helpful for samples with irregular surfaces.

The sample is then separated into 0.50 mm layers of equal thickness from the surface of the sample through the entire depth as shown in **Fig. 2.6d**. Several different thicknesses were tried but 0.50 mm was chosen because it provided the details necessary without oversampling the data. The average Cl concentration in each layer can then be plotted for different depths by using the developed calibration curve. To compare with the results from profile grinding analysis the total chlorine counts from both the aggregates and paste were combined at each depth.

2.3.4 Cl Diffusion Coefficient Calculation

A nonlinear regression is then conducted on the Cl profile with Fick's second law as shown in **Eq. (2.1)** [23], the value of apparent diffusion coefficient was determined.

$$C_{(x,t)} = C_s\left(1 - \mathrm{erf}\left(\frac{x}{2\sqrt{D_c t}}\right)\right) \qquad (2.1)$$

$$C_{(x,0)} = 0 \quad x > 0, \quad C_{(0,t)} = C_s \quad t \geq 0$$

where x is distance from concrete surface; t denotes time; D_c is diffusion coefficient; C_s is surface Cl concentration; $C_{(x,t)}$ represents Cl concentration at the depth of x from the surface after time t; and erf is the error function.

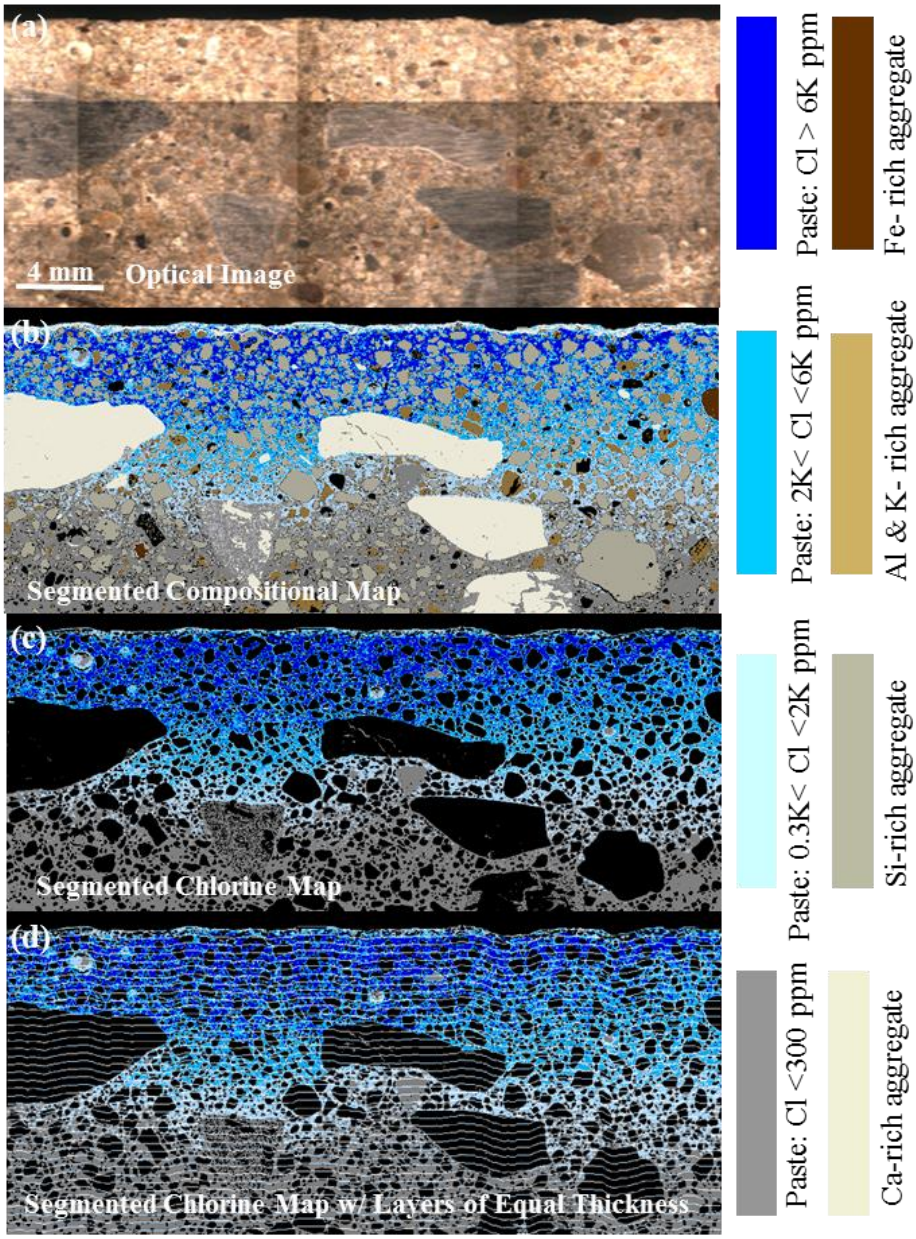

Fig. 2.6 An example of using the self-authored program to remove the aggregates and divide the sample into layers of equal thickness from the surface: (a) optical image (b) segmented compositional map (c) segmented Cl profile map (d) segmented Cl profile map with layers of equal thickness.

2.4 Results and Discussion

2.4.1 Cl Concentration Profiles

Figs 2.7 to **2.9** show a comparison of the Cl profiles between the µXRF and profile grinding results for three samples. The average Cl concentration for each 0.5 mm slice is shown with triangles. Each data point is an average of ≈ 9000 measurements from the sample. The results from the profile grinding are shown as a star. The calculated apparent diffusion coefficient is shown for both techniques along with the percent difference. In order to better compare the two methods, the µXRF data was averaged over the same distances used to complete the profile grinding and plotted at the midpoint of each depth to compare the results between the two techniques. Additional comparisons are included in the supplementary section. **Figure 2.10** compares the individual measurements from the profile grinding to the average µXRF values over the same depths. The slope of the linear trend line is 0.948 which is close to the ideal value of 1, with the µXRF data being slightly lower on average than the data from the profile grinding. Overall, the two techniques show a good correlation. The differences in the measurements could be caused by differences in the amount of aggregate in the analysis. The impact of aggregate content on the µXRF results is discussed later in the paper.

2.4.2 Diffusion Coefficient Comparison

The calculated apparent diffusion coefficient values from µXRF measurements and profile grinding are summarized in **Table 2.4**. While the concentration profile shows general agreement between the two methods, the diffusion coefficients from µXRF was on average 30% higher. A t-test with the assumption of unequal variances was conducted to compare the mean diffusion coefficient of the two methods. Based on this analysis, the t-test results in insignificant p-value ($0.257 >> 0.05$). Since the difference between means was not significant then this suggests that these two methods provide comparable results.

Furthermore, based on ASTM C1556, the apparent diffusion coefficient results of two properly conducted tests should not differ by more than 39.8 % of the mean value. Therefore, the obtained average 30% difference is less than the specified sample to sample variation by ASTM C1556. It is also important to note that the apparent diffusion coefficient from Fickian diffusion is sensitive to the slope of Cl profiles. Because there are a greater number of data points captured by the µXRF then this technique is expected to have a more accurate slope and therefore a more accurate diffusion coefficient than profile grinding. Obtaining a more accurate apparent diffusion coefficient would more accurately predict the effective life of in place structures, improve service life model predictions, and guide material selection for long life predictions.

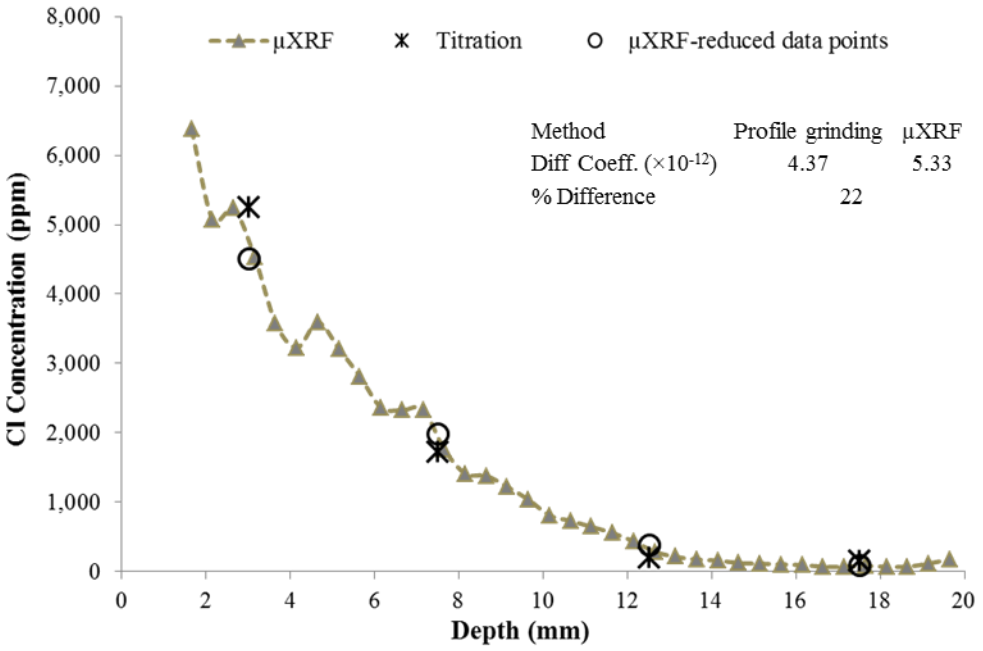

Fig. 2.7 An example of the Cl profile of samples ponded 45 days in NaCl (C2-45).

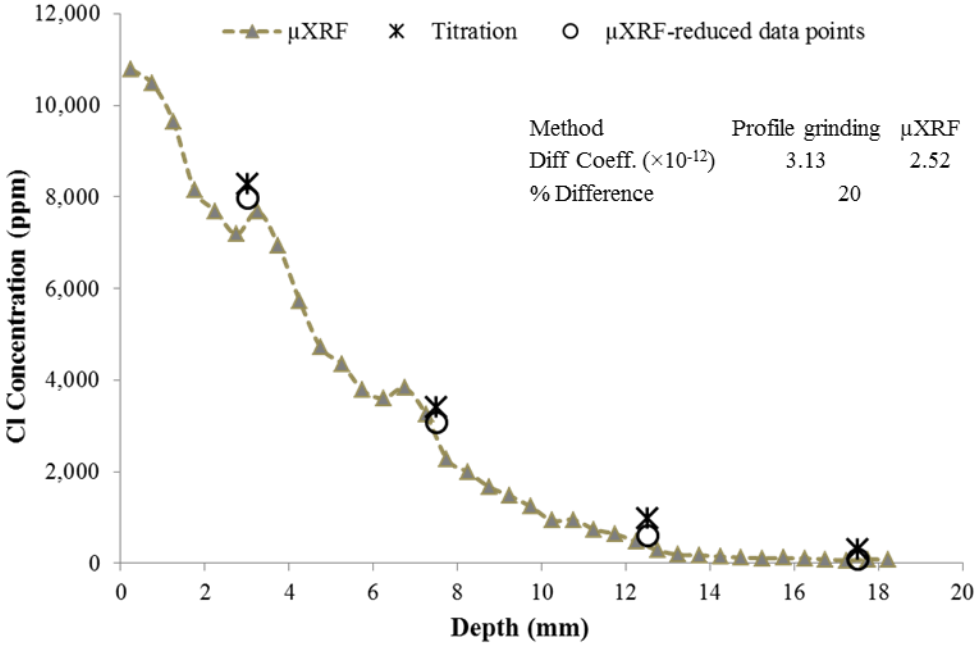

Fig. 2.8 An example of Cl profile of samples ponded 90 days in NaCl (C1-90).

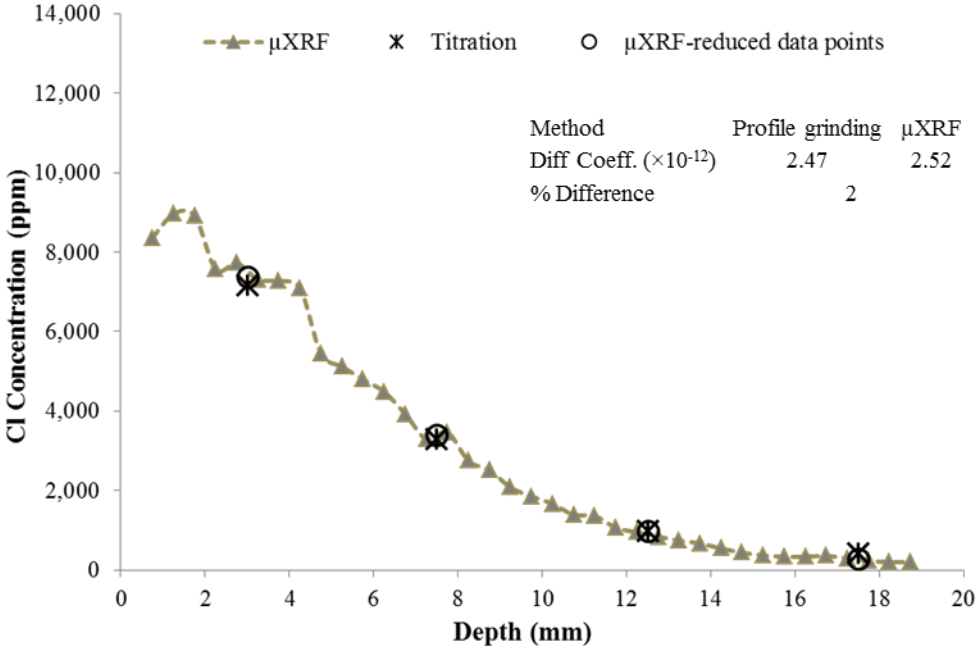

Fig. 2.9 An example of Cl profile of samples ponded 135 days in NaCl (F-135).

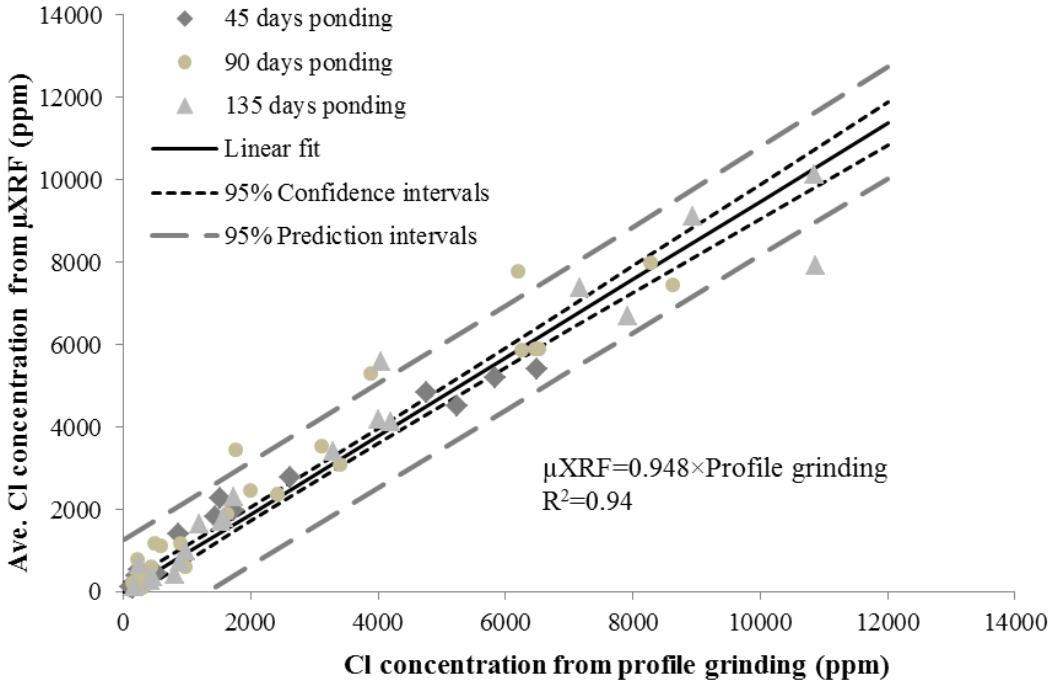

Fig. 2.10 Correlation between results from μXRF and profile grinding.

Table 2.4 Comparison between diffusion coefficients from profile grinding and μXRF

Sample	Profile grinding Diff Coef×10^{-12} (m^2/sec)	R^2	μXRF Diff Coef×10^{-12} (m^2/sec)	R^2	% Difference $\frac{(\mu XRF - grinding)}{grinding \times 0.01}$	Depth of Cl Penetration (mm)*
C1-45	3.50	0.99	6.00	0.97	71	14.00
C2-45	4.37	0.99	5.33	0.99	22	13.50
C4-45	2.59	0.99	2.73	0.95	5	12.00
PC-45	8.13	0.98	11.4	0.95	40	18.50
C1-90	3.13	0.99	2.52	0.99	-20	14.50
C2-90	2.65	0.99	2.94	0.99	11	16.00
C3-90	3.80	0.99	4.66	0.95	23	17.50
C4-90	1.75	0.99	2.23	0.97	27	15.00
F-90	2.28	0.99	2.65	0.96	16	18.50
PC-90	4.27	0.99	9.25	0.96	116	24.00
C1-135	1.88	0.99	2.45	0.99	30	19.50
C2-135	2.07	0.99	2.38	0.99	15	17.00
C3-135	2.77	0.99	2.94	0.98	6	21.50
C4-135	0.99	0.99	1.50	0.99	52	15.50
F-135	2.47	0.99	2.52	0.99	2	19.00
Average difference between μXRF and profile grinding ± Std					30.4 ± 30.06	

* Depth of Cl penetration is calculated based on μXRF measurement for Cl > 200 ppm.

2.4.3 Quantitative Estimation of Cl Penetration Depth using µXRF

It is sometimes important to compare the depth of penetration of Cl to the depth of the reinforcing steel. This can be determined from the µXRF data sets by finding the location where the Cl concentration increases above the background level. A threshold value of Cl > 200 ppm was used to determine the depth of penetration in this paper. Two examples are shown in **Fig. 2.11**. The depth of penetration for each sample is given in **Table 2.4**. The threshold value can be adjusted for other materials and situations.

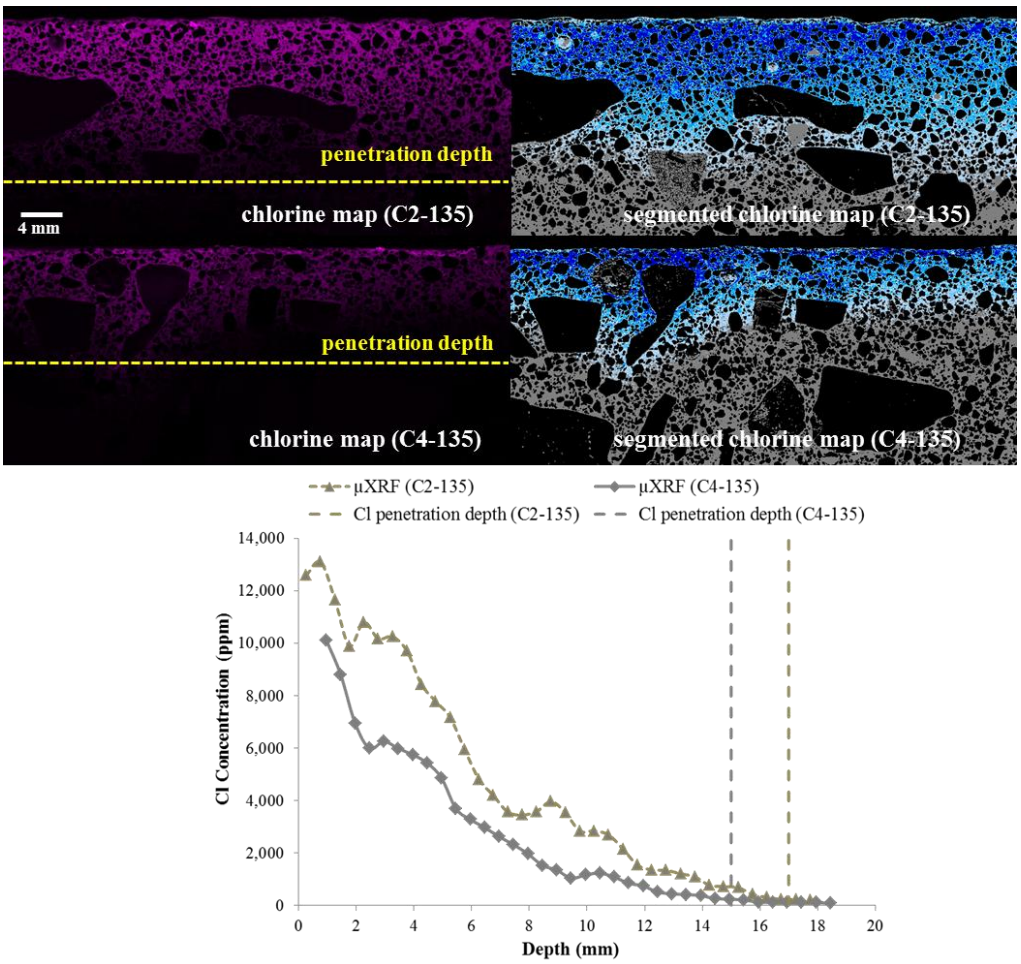

Fig. 2.11 Cl penetration depth comparison between two samples with a 200 ppm Cl threshold value.

2.4.4 The Impact of Cracks on Cl Transport

In practice, it is common to have cracks in concrete structures. Cracks are assumed to be a direct path for ingress of deleterious species such as Cl ions into the concrete and decrease the lifespan of concrete structures [24-28]. However, not all cracks are expected to perform the same. Unfortunately, the profile grinding technique is not able to provide information on the location, size, or the impact that cracks have on Cl penetration because the technique has poor spatial resolution. However, μXRF can provide important insights to this issue. **Figure 2.12** shows the μXRF analysis of a core from a bridge. The sample is oriented so that the finished surface is at the top of the image. Two horizontal cracks are highlighted in **Fig. 2.12b**. One crack has a width of ≈ 100 μm and the area around the crack has a similar Cl concentration as the surrounding paste. However, the second crack is much wider (≈ 400 μm) and the Cl concentration surrounding the crack is similar to the surface of the concrete despite the crack being over 30 mm away from the surface. This highlights how the spatial distribution measured by μXRF is useful to study the impacts of cracking on Cl penetration into concrete.

2.4.5 The Impact of Cl Rich Aggregate on the Cl Profile

Another advantage of μXRF over conventional profile grinding is that it is possible to identify the cause of unexpected changes in the Cl profiles. An example is shown in **Fig. 2.13** where a Cl rich aggregate was found in a sample. This aggregate caused an unexpected peak in Cl concentration at the level of the aggregate. This can be handled by manually removing the aggregate from the analysis and developing a new Cl profile. Profiles with and without the Cl rich aggregate are shown in **Fig. 2.13**.

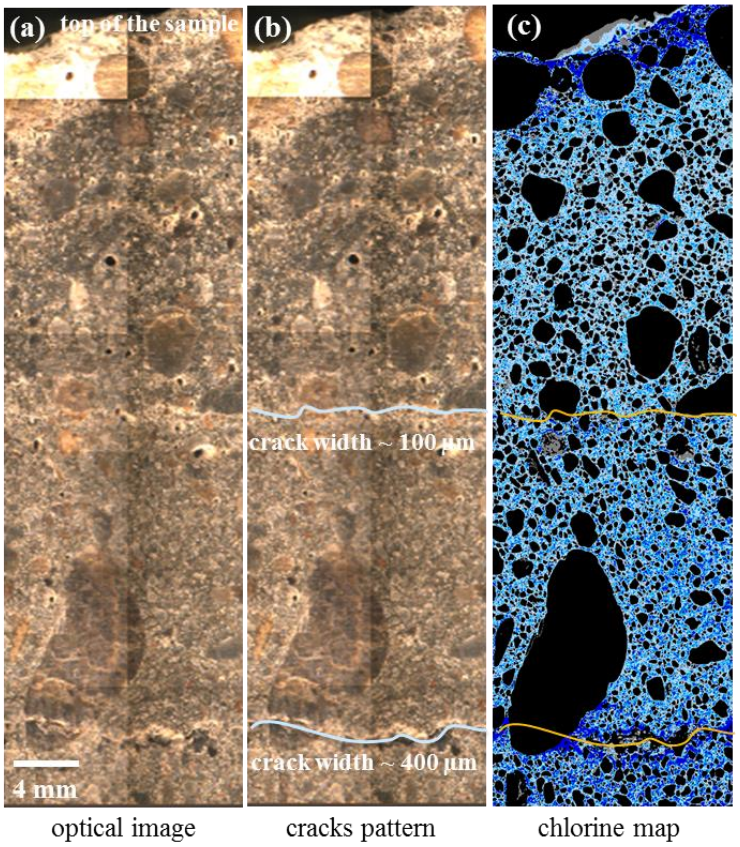

Fig. 2.12 A concrete sample from a bridge deck with horizontal cracks: (a) optical image (b) optical image with cracks highlighted (c) segmented Cl profile map with cracks highlighted.

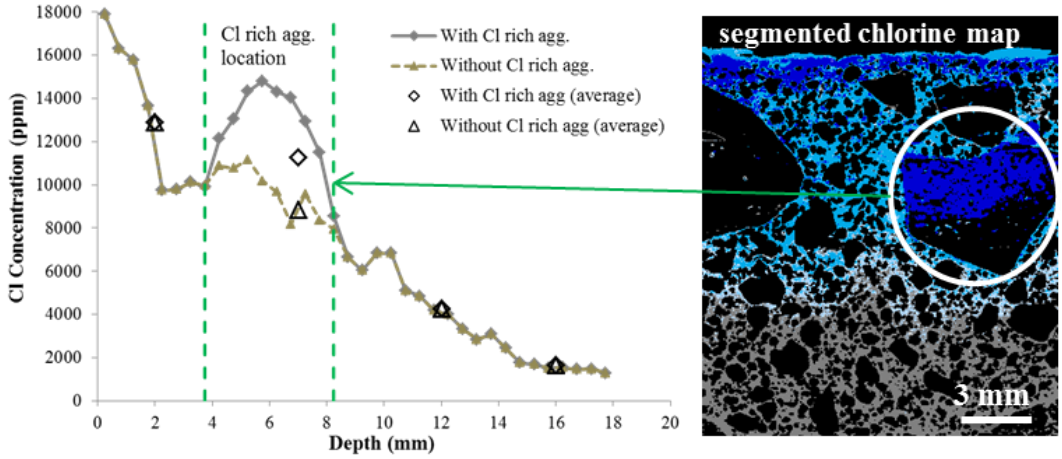

Fig. 2.13 A concrete sample with Cl rich aggregate: (left) Cl concentration profiles with and without including Cl rich aggregate (right) segmented chlorine map.

2.4.6 Impact of Aggregate on µXRF Results

As mentioned earlier, aggregates dilute the measurements made by profile grinding. Because of the poor spatial resolution of profile grinding, it is not possible to determine the impact of the local aggregate distribution on the Cl profile measurements. With the spatial resolution of µXRF these challenges can be overcome. **Figure 2.14** shows the µXRF analysis of sample C1-135. The sample is divided into four regions with different amounts of aggregate in each region. Subsequently, Cl profiles were determined for each region. The results are shown in **Fig. 2.14**. Region 2 had a higher aggregate content than the others (69% compared to 49%, 46% and 43%). Because of the aggregates do not contain significant Cl, Region 2 will have a lower average Cl profile. This can be seen in **Fig. 2.14d** as the profile of Region 2 has 3000 ppm of Cl less between 5 mm and 10 mm than the profiles from the other regions. This is reinforced by comparing the apparent Cl diffusion coefficient in **Table 2.5** for the different regions. The diffusion coefficient in Region 2 is 67% lower than the analysis that uses the entire sample and 78% lower than the adjacent areas. To investigate this further, the aggregate was removed from the analysis and instead the Cl profiles were calculated based solely on the paste. Results in **Fig. 2.14e** and **Table 2.5** show that there is little variability between the Cl profiles and apparent diffusion coefficients in the different regions when only paste was used in the analysis.

This suggests that the local amount of aggregate could have a significant impact on results from profile grinding and µXRF. However, Cl profiles based solely on the paste will be less variable than profiles based on the total mass of the concrete. Since the spatial location of the aggregates can be easily observed with µXRF then this allows the user to determine if the sample has a representative aggregate distribution or allow them to just measure the paste. Because of this ability to detect aggregates, it may be possible to investigate samples that are much smaller than is typically needed for profile grinding. This would make it easier and less destructive to sample from field structures.

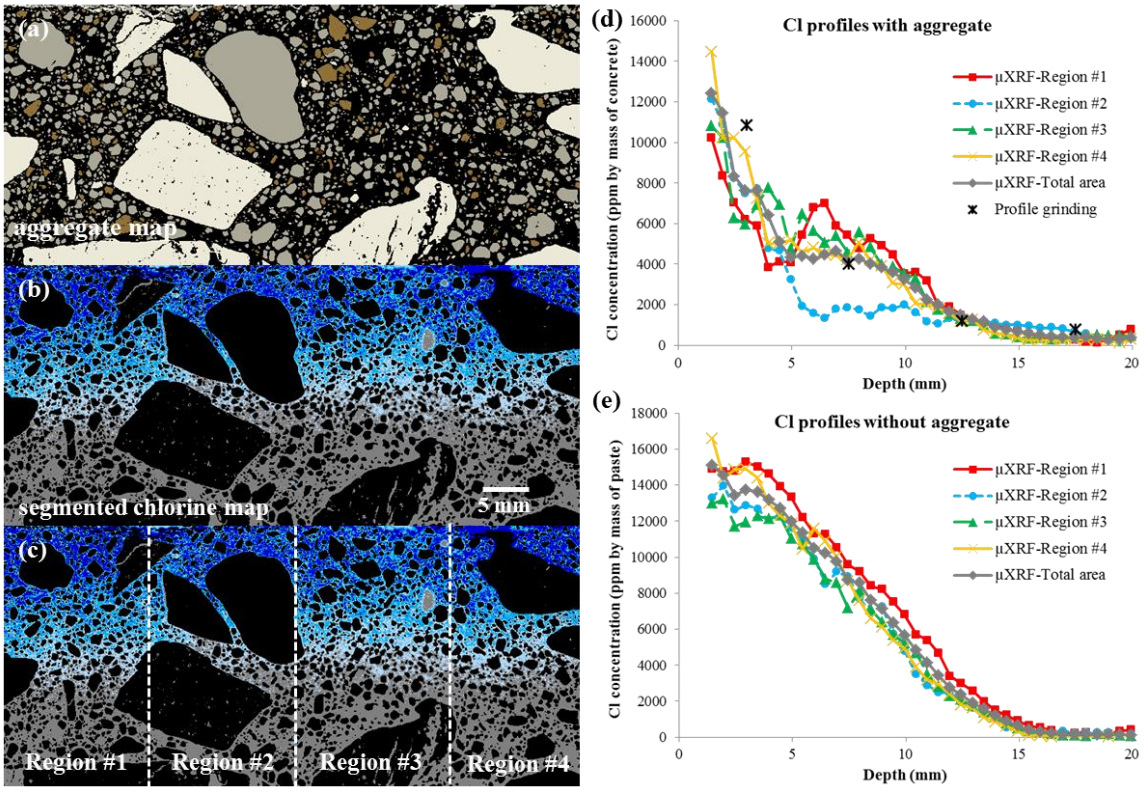

Fig. 2.14 Example of a Cl profile with and without including aggregate in analysis: (a) segmented aggregate map (b) segmented chlorine map (c) selected regions for Cl profiling (d) Cl profiles with aggregates (e) Cl profiles without aggregate.

Table 2.5 Comparison between diffusion coefficients from different regions of C1-135

Area	Region #1	Region #2	Region #3	Region #4	Total area
Diff Coeff × 10^{-12} (with aggregate)	3.60	0.80	3.10	2.24	2.45
Diff Coeff × 10^{-12} (without aggregate)	3.22	3.28	3.46	2.98	3.01
Aggregate content (%)	48.8	68.9	43.2	45.6	51.7

2.5 Conclusions

µXRF is a powerful, non-destructive, X-ray based imaging technique that simultaneously provides chemical composition and position within concrete with minimal sample preparation.

This technique was used to determine Cl profiles in concrete. Fifteen different comparisons are made between profile grinding and μXRF and good agreement was found. The following conclusions can be drawn from this work:

- The trendline for the average Cl concentrations at comparable depths from μXRF and profile grinding has a slope of 0.948 which is close to the ideal value of 1.
- The apparent Cl diffusion coefficient was found to be on average 30% higher for μXRF than profile grinding.
- The statistical t-test showed that the difference between mean diffusion coefficients from μXRF and profile grinding methods is not significant.
- The depth of Cl penetration can be quantitatively determined with μXRF.
- μXRF was able to image the presence of cracks > 100 μm in concrete and their impact on local Cl penetration.
- μXRF identified Cl rich aggregate in a sample and allowed it to be removed in order to find the Cl concentrations.
- A high local concentration of aggregates caused an underestimation of the apparent diffusion coefficient. μXRF can be used to resolve this issue by solely investigating Cl profiles based on the paste.

This work shows the utility of using μXRF to efficiently and rapidly evaluate Cl profiles in laboratory and field concrete. Furthermore, μXRF can determine the average Cl profile at a higher resolution than profile grinding. This higher resolution data, and the ability to recognize anomalies like cracks and Cl rich aggregates, leads to more reliable analysis of the sample and determination of the apparent diffusion coefficient.

Acknowledgments

The authors acknowledge the financial support from the Oklahoma Department of Transportation (ODOT), Federal Highway Association (FHWA) Exploratory Advanced Research (EAR) Program, and the United State National Science Foundation CMMI 1150404 CAREER Award. We would also like to thank Jim Hardy for his discussion and assistance in this research. He will be missed dearly.

References

[1] G.H. Koch, M.P. Brongers, N.G. Thompson, Y.P. Virmani, J.H. Payer, Corrosion costs and preventive strategies in the United States, Report by CC Technologies Laboratories, Inc. to Federal Highway Administration (FHWA)-RD-01-151, September 2001.

[2] P.K. Mehta, Durability of Concrete- Fifty Years of Progress?, ACI SP 126-1, (1991) 1-31.

[3] A.M. Vaysburd, P.H. Emmons, Corrosion inhibitors and other protective systems in concrete repair: Concepts or misconcepts, Cem. Concr. Compos. 26 (2004) 255–263. doi:10.1016/S0958-9465(03)00044-1.

[4] M. Khanzadeh Moradllo, M. Shekarchi, M. Hoseini, Time-dependent performance of concrete surface coatings in tidal zone of marine environment, Constr. Build. Mater. 30 (2012) 198–205. doi:10.1016/j.conbuildmat.2011.11.044.

[5] K. Basham, J. Meredith, Measuring water penetration: A simple, inexpensive tube test can yield valuable, quantitative information, Mag. Mason. Constr. 8 (1995) 539-543.

[6] O.M. Jensen, a. M. Coats, F.P. Glasser, Chloride ingress profiles measured by electron probe micro analysis, Cem. Concr. Res. 26 (1996) 1695–1705. doi:10.1016/S0008-8846(96)00158-5.

[7] D. Mori, K. Yamada, Y. Hosokawa, M. Yamamoto, Applications of Electron Probe Microanalyzer for Measurement of Cl Concentration Profile in Concrete, J. Adv. Concr. Technol. 4 (2006) 369–383. doi:10.3151/jact.4.369.

[8] L.M. Dempere, B. Willenberg, R. Deist, Use of Scanning Electron Microscopy and Microanalysis to Determine Chloride Content of Concrete and Raw Materials. Florida Department of Transportation 2013; BDK75 977-15.

[9] J.M. Davis, D.E. Newbury, A. Fahey, N.W.M. Ritchie, E. Vicenzi, D. Bentz, Bridging the micro-to-macro gap: a new application for micro X-ray fluorescence., Microsc. Microanal. 17 (2011) 410–417. doi:10.1017/S1431927611000183.

[10] J.M. Davis, D.E. Newbury, P.R. Rangaraju, S. Soundrapanian, C. Giebson, Milli X-ray fluorescence X-ray spectrum imaging for measuring potassium ion intrusion into concrete samples, Cem. Concr. Compos. 31 (2009) 171–175. doi:10.1016/j.cemconcomp.2008.12.005.

[11] D. Bentz, M. Peltz, K. Snyder, J. Davis, VERDiCT: viscosity enhancers reducing diffusion in concrete technology, Concr. Int. 31 (2009) 31–36.

[12] B. Sudbrink, M. Khanzadeh Moradllo, Q. Hu, M.T. Ley, J.M. Davis, N. Materer, A. Apblett, Imaging the presence of silane coatings in concrete with micro X-ray fluorescence. Cem. Concr. Res. (2016); accepted for publication. doi:10.1016/j.cemconres.2016.11.019.

[13] H. Yakowitz, W.D. Forgeng, Fifty years of progress in metallographic techniques, ASTM STP 430. (1968) 78.

[14] K.A. Snyder, D.P. Bentz, J.M. Davis, Using Viscosity Modifiers to Reduce Effective Diffusivity in Mortars, J. Mater. Civ. Eng. 24 (2012) 1017–1024. doi:10.1061/(ASCE)MT.1943-5533.0000524.

[15] J. Goldstein, D.E. Newbury, P. Echlin, D.C. Joy, A.D. Romig Jr., C.E. Lyman, E. Lifshin, Scanning electron microscopy and X-ray microanalysis: a text for biologists, materials scientists, and geologists, second ed., Springer Science & Business Media, New York, 2012.

[16] K. Peterson, G. Julio-Betancourt, L. Sutter, R.D. Hooton, D. Johnston, Observations of chloride ingress and calcium oxychloride formation in laboratory concrete and mortar at 5 C, Cem. Concr. Res. 45 (2013) 79–90. doi:10.1016/j.cemconres.2013.01.001.

[17] K.H.A. Janssens, F. Adams, A. Rindby, Microscopic x-ray fluorescence analysis, John Wiley & Sons Inc, New York, 2000.

[18] K. Janssens, B. Vekemans, L. Vincze, F. Adams, a. Rindby, A micro-XRF spectrometer based on a rotating anode generator and capillary optics, Spectrochim. Acta - Part B At. Spectrosc. 51 (1996) 1661–1678. doi:10.1016/S0584-8547(96)01551-0.

[19] D. Bright, Lispix: An image processing and analysis tool for the PC, 2011. http://www.nist.gov/lispix/doc/contents.htm, (last accessed on July 2015).

[20] D. Newbury, N. Ritchie, D.S. Bright, Characterizing heterogeneous particles with SEM/SDD-EDS mapping and NIST Lispix, In: Proceeding of SPIE 7378, Scanning Microscopy, 2009, 11 pages. doi: 10.1117/12.820874.

[21] D.S. Bright, Principal component analysis, scatter diagrams and color overlays for analysis of compositional maps, In: Proceeding of Microbeam Analysis, VCH, NY, 1995, pp. 403-404.

[22] D.S. Bright, A Lisp-based image analysis system with applications to microscopy, J. Microscopy 148 (1987) 51–87.

[23] J. Crank, The mathematics of diffusion, second ed., Oxford Science Publication, London, 1975.

[24] D.P. Bentz, E.J. Garboczi, Y. Lu, N. Martys, A.R. Sakulich, W.J. Weiss, Modeling of the influence of transverse cracking on chloride penetration into concrete, Cem. Concr. Compos. 38 (2013) 65–74. doi:10.1016/j.cemconcomp.2013.03.003.

[25] P.P. Win, M. Watanabe, A. Machida, Penetration profile of chloride ion in cracked reinforced concrete, Cem. Concr. Res. 34 (2004) 1073–1079. doi:10.1016/j.cemconres.2003.11.020.

[26] F. Ghasemzadeh, R. Rashetnia, D. Smyl, M. Pour-ghaz, A comparison of methods to evaluate mass transport in damaged mortar, Cem. Concr. Compos. 70 (2016) 119–129. doi:10.1016/j.cemconcomp.2016.03.007.

[27] F. Ghasemzadeh, M. Pour-ghaz, Effect of Damage on Moisture Transport in Concrete, 27 (2015) 1–12. doi:10.1061/(ASCE)MT.1943-5533.0001211.

[28] D. Smyl, F. Ghasemzadeh, M. Pour-ghaz, Modeling water absorption in concrete and mortar with distributed damage, Constr. Build. Mater. 125 (2016) 438–449. doi:10.1016/j.conbuildmat.2016.08.044.

Supplementary Section

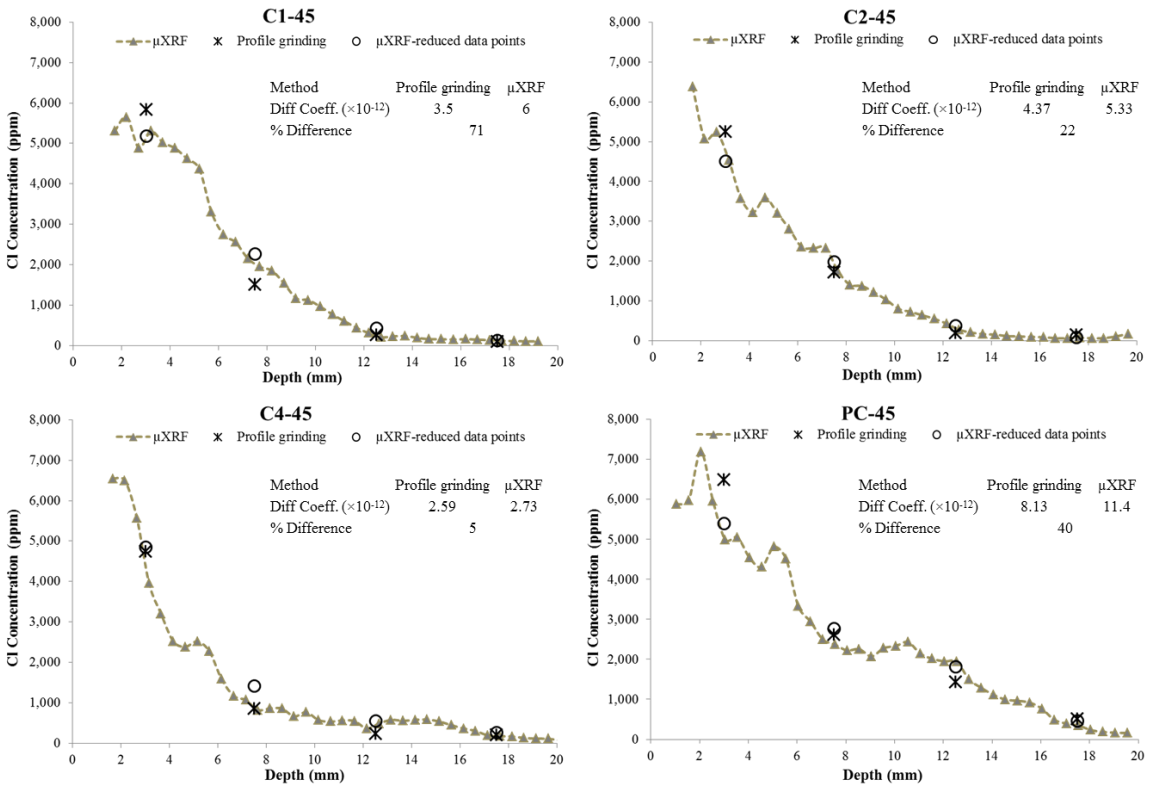

Fig. 2.S1 Comparison between Cl profiles from profile grinding and µXRF methods for 45 days ponded samples in NaCl. (Top left) C1-45 (top right) C2-45 (bottom left) C4-45 (bottom right) PC-45.

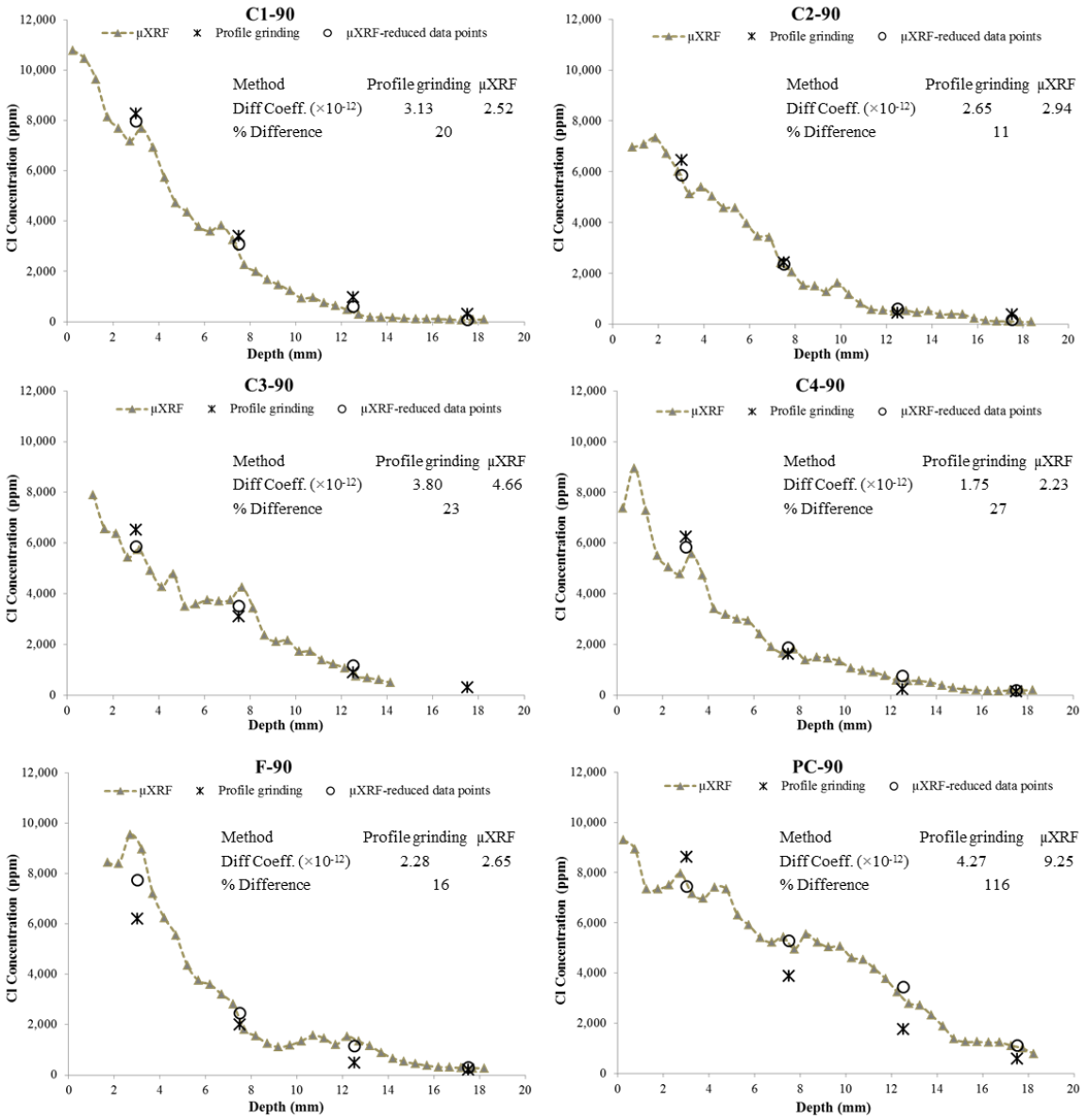

Fig. 2.S2 Comparison between Cl profiles from profile grinding and µXRF methods for 90 days ponded samples in NaCl. (Top left) C1-90 (top right) C2-90 (middle left) C3-90 (middle right) C4-90 (bottom left) F-90 (bottom right) PC-90.

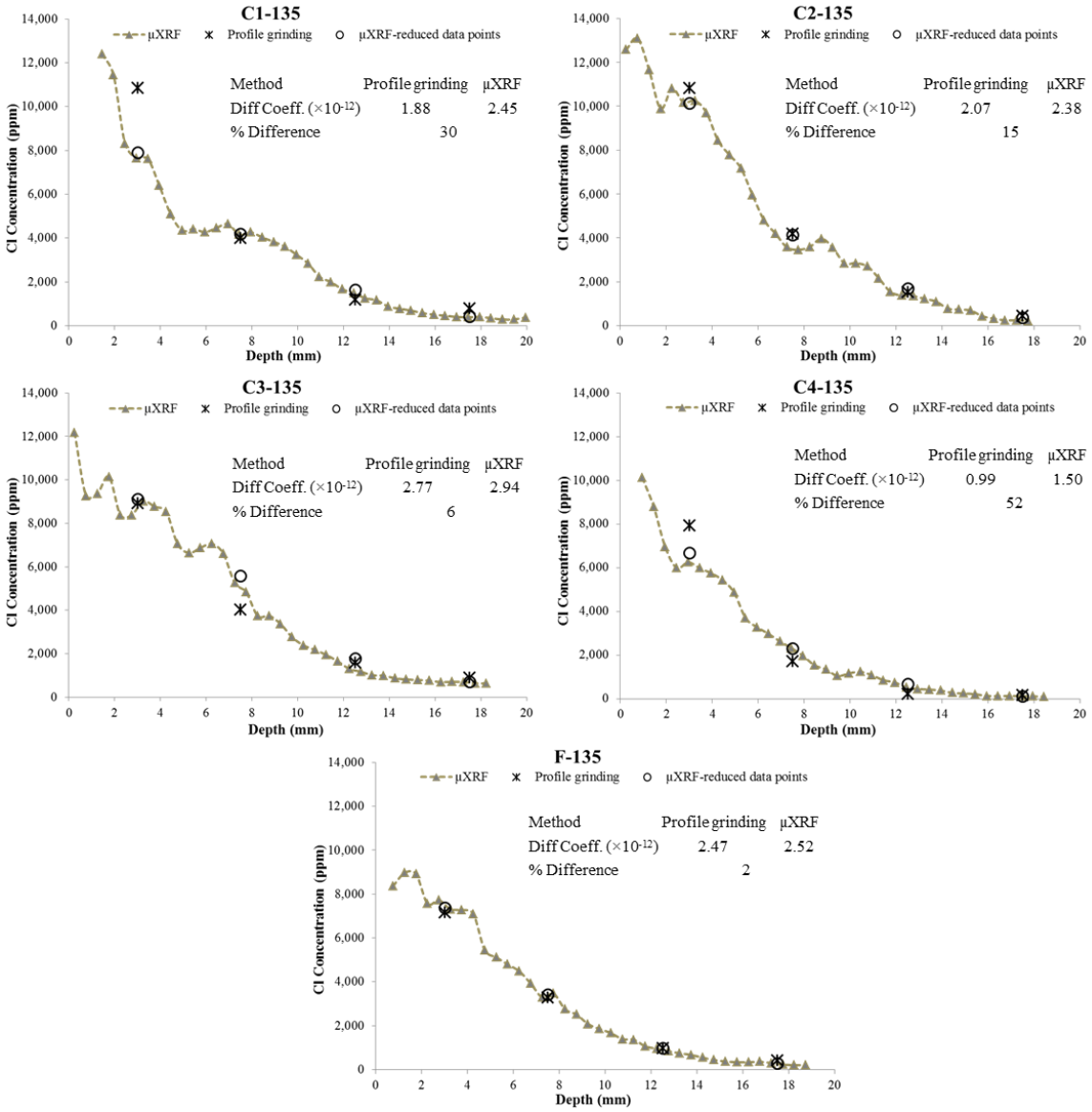

Fig. 2.S3. Comparison between Cl profiles from profile grinding and µXRF methods for 135 days ponded samples in NaCl. (Top left) C1-135 (top right) C2-135 (middle left) C3-135 (middle right) C4-135 (bottom) F-135.

CHAPTER III

USING X-RAY IMAGING TO INVESTIGATE IN-SITU ION DIFFUSION IN CEMENTITIOUS MATERIALS

Abstract

The external penetration of ions into cementitious materials plays an important role in long-term durability of concrete structures. Current test methods to study bulk diffusion of ions in cement-based materials are typically destructive, time consuming and labor intensive. This paper uses laboratory transmission X-ray microscopy (TXM) and X-ray computed microtomography (μCT) to image iodide diffusion in cement paste. These techniques can non-destructively image the distribution of the dissolved ions at 9 μm resolution in minutes with a 2D analysis and a few hours for 3D. This method does not aim to measure the size of the pores, instead it aims to image the movement of the fluid through the pores. The tests were completed on cement paste mixtures with water-to-solid ratios (w/s) of 0.35, 0.40, and 0.45. The findings were validated with micro X-ray fluorescence (μXRF) imaging. Iodide and chloride diffusivity is also compared for paste samples with w/s of 0.40 and shown to provide comparable results. Results are also presented of void filling at high degrees of saturation.

Keywords: X-ray microscopy; Iodide; Chloride; Service life; Durability; Corrosion.

3.1 Introduction

Concrete structures face many threats to their service life. A number of durability problems are caused by external fluids penetrating into cement-based materials [1-3]. This fluid, which contains potentially harmful ionic species, can lead to damage from corrosion, sulfate attack, alkali silica reaction, bulk freeze thaw, and salt scaling [4]. Therefore, the ion transport properties of cement-based materials play an important role in the durability performance of concrete structures [5-6].

The most widely used method to investigate ion ingress into cement-based materials is to place the desired solution on one surface of the concrete sample for a specified time period, then destructively powder the sample at controlled depths, and then analyze the powder by titration for the desired ion. Often chloride ions are used in this test as this resembles field performance of the concrete. A version of this technique is used in many standards, including ASTM C 1152, AASHTO T260-97 and NT Build 208. These measurements provide insight into the rate of ion ingress and can be used to evaluate the transport properties of cement-based materials, the amount of ions present, and to project the long-term service life of the structure.

However, this technique is destructive and requires that a significant mass of powder be collected from a number of different depths of the concrete. The measurement is an average of all of the material collected. The test is also time consuming and labor intensive. In addition, this method is slow because of the extended ponding period (at least 35 d) in order to obtain spatial distribution in the measurements [5]. The diffusion cell test is another common ion penetration test that monitors the electrical current passed through a water-saturated concrete specimen subjected to 60 V of direct current for 6 h according to ASTM C1202. The total charge passed is determined and is useful to compare different concrete mixtures. However, the current passed is related to all ions in the pore solution, not just chloride ions. Also, the measurements are made

before steady-state migration is achieved and the test is reported to have a low inherent repeatability [5, 7-8]. While both of these tests are useful, they could be improved if they were non-destructive, required less human intervention, and provided higher spatial information to give greater insights into the ion movement.

Recently, neutron and X-ray imaging techniques have been used to visualize fluid flow in cement-based materials [5-6, 9-13]. Both of these methods are based on the same principle of radiation attenuation upon passing through matter. But, X-rays interact with the electron shell of the atom while neutrons interact with the nucleus. Therefore, there is a higher probability for X-ray interaction because of the higher number of electrons in an atom [10-11]. One drawback of the neutron imaging is that it requires a high energy source that is typically only available at synchrotron beamlines. This reduces the availability of the method. In addition, neutron imaging currently has a spatial resolution limited to ≈ 50 microns per pixel [14]. Neutron imaging is also sensitive to hydrogen atoms and is not able to measure specific ions. This may or may not be important depending on the information needed.

Transmission X-ray microscopy (TXM) and X-ray computed microtomography (μCT) have been used to learn more about moisture movement in cement-based materials [5-6, 12-16]. These studies have been completed with both synchrotron and lab scale instruments. In both TXM and μCT the materials will appear to have different gray values depending on their X-ray absorption. While this technique does not provide direct compositional information about the irradiated materials, it does provide clues about compositional consistency [17-18]. Previous studies using these methods have tried to simulate the diffusivity of cement-based materials by extracting the microstructure from μCT data without conducting a diffusion experiment [5, 19-20]. Unfortunately, there is porosity at a length scale smaller than can be measured by the technique and so this pore structure is not included in the analysis. In addition, selecting a threshold value to distinguish the pore space from the solid phase has an impact on calculated porosity and

tortuosity and consequently on the estimated diffusion coefficient from this method. Also, previous works have tried to use TXM to image water penetration into the paste samples [6, 12-13]. Unfortunately, X-rays react weakly with light atoms such as hydrogen. This limits the detection sensitivity of water in the method [14]. One method to address the low sensitivity of water is to use low X-ray energies to identify small changes in material density due to water movement [6]. However, this limits the density of the material and the sample size that can be investigated with this method. In addition, these publications have not been validated by other experimental techniques. Therefore, a technique is needed that is rapid, non-destructive, and able to provide useful and direct observations of ion movement in cement-based materials at a useful length scale.

In this work, the moisture penetration is imaged with the aid of adding a salt with an electron dense cation. This is also known as a contrast agent or tracer. In this study potassium iodide (KI) is used as it is easy to obtain and does not require special handling requirements. Iodine is strongly X-ray attenuating because of its high atomic number. Furthermore, iodide and chloride ions are similar in size (iodide radius is 206 pm versus a chloride radius of 167 pm). This property makes iodide an excellent tracer for fluid transport study in concrete [21-24].

As the tracer penetrates into the cement paste it is possible to see the corresponding changes in X-ray absorption or gray value of the material in the radiograph or tomograph. By taking time resolved images, a rate of penetration or an effective transport constant can be calculated. Since this technique is non-destructive, the same sample can be monitored over time and under different conditions. The method requires minimal sample preparation and the technique can image at a spatial resolution of 200 nm to 20 μm with laboratory equipment.

This work aims to use a systematic approach to use TXM to follow in-situ iodide diffusion for paste with water-to-solids ratios (w/s) of 0.35, 0.40, and 0.45. In addition, a 3D tomography data

set from μCT is included to show how the technique can be used to measure complex phenomena such as filling of larger pores at different fluid concentration levels and 3D time-dependent ion movement.

In addition, the samples investigated with TXM were also examined with micro X-ray fluorescence (μXRF) in order to compare their results. μXRF is similar to bulk X-ray fluorescence (XRF) but this method uses a polycapillary optic to focus X-rays to a size of approximately 50 μm in diameter, whereas bulk XRF investigates the sample with a 1 cm diameter spot. In addition, μXRF provides individual compositional maps which can be combined into a single map that simultaneously provides unique compositions and location [25-26]. Furthermore, μXRF imaging was used to compare iodide and chloride concentration profiles and diffusion coefficients in paste samples with w/s of 0.40.

3.2 Experimental Methods

3.2.1 Mixture Proportion and Sample Preparation

Three different cement paste mixtures with w/s ratios of 0.35, 0.40, and 0.45 were investigated. The cement is an ASTM C 150; Type I. The chemical composition of cement with bulk XRF is provided in **Table 3.1**.

The paste mixtures were prepared according to ASTM C 305 and the mixture proportions are given in **Table 3.2**. Cylindrical micro vials with inside dimensions of 7×40 mm and 9.5×46 mm were used to cast the samples. A lid was used to seal each vial. Four samples of each size were made from each mixture. The vials were only partially filled so that there was room to provide solution above them. These samples were cured for 28 days in a sealed condition at 23°C. The samples with dimensions of 9.5×46 mm were used to conduct the majority of TXM measurements and analysis and samples with smaller dimensions were used to study the variability in TXM method. A paste sample with w/s of 0.40 was also made and a single fine

aggregate was embedded. This sample was cured for 14 days in a sealed condition at 23℃ for conducting an experiment with μCT.

In addition, a paste sample with w/s of 0.40 was made and was cured for 14 days in a sealed condition at 23°C to compare the iodide and chloride ion diffusivity. The cement is an ASTM C 150, Type I/II. Mixing was performed in accordance with ASTM C 305. The mixture proportions are given in **Table 3.2**. Polycarboxlate based high-range water-reducing admixture with addition rate of 112 mL/100kg of cement was used so that the results could be compared to other materials not included in this paper. Cylindrical micro vials with inside dimensions of 9.5×46 mm were used to cast the samples.

Table 3.1 Chemical composition of cements with bulk XRF

Oxide content (%)	SiO_2	Al_2O_3	Fe_2O_3	CaO	MgO	Na_2O	K_2O	TiO_2	SO_3	L.O.I
Type I	20.40	5.03	2.95	62.89	2.08	0.35	0.35	0.28	3.05	2.09
Type I/ II	17.39	4.87	4.71	65.15	1.4	0.46	0.48	0.39	2.51	2.12

Table 3.2 Cement paste mixture proportions

Mixture	water (g)	cement (g)	w/c
P-45	372.41	827.59	0.45
P-40	342.86	857.14	0.40
P-35	311.11	888.89	0.35
P-40-II	356	891	0.40

3.2.2 In-Situ Diffusion Test Using TXM and μCT

An aluminum wire of 0.6 mm thickness was attached to the side of the sample to help align the images and to act as a standard material between scans. This helped detect variations in X-ray transmissions between images. The schematic diagram of the experimental setup is shown in **Fig. 3.1**.

After curing, samples were ponded with 0.6 mol/L KI solution for 28 days. This KI concentration was selected based on preliminary experiments to attain suitable contrast between the KI solution and the paste. A laboratory Skyscan 1172 μCT scanner was used to conduct the experiments. A radiograph was taken from the paste samples before and immediately after the ponding with the KI solution. These were used as reference radiographs. Radiographs were also taken over time to determine the changes in the sample as the fluid penetrated into the sample. In addition, a radiograph was taken from the air after each scan to subtract the background attenuation. The radiograph used a pixel size of 8.8 μm (2096×2096 pixels) and tube voltage and current of 100 KeV and 100 μA. A 0.5 mm Al and 0.5 mm Cu filter was used to absorb lower energy X-rays and allow high energy X-rays to interact with the sample. Acquisition time of 8 s per frame was used to collect radiographs. Table 3 summarizes the TXM settings. The KI solution was refreshed every 5 days to maintain a constant KI concentration. This time interval was selected as it kept the X-ray absorption of the KI solution constant. The amount of KI solution on the surface of samples was kept constant for all paste samples (0.4±0.01 mL and 0.6±0.01 mL for micro vials with diameter of 7 and 9.5 mm, respectively). Samples were stored inside a sealed container at 23°C during the diffusion testing.

After investigating with TXM, the sample was polished on a sanding belt for 2 min with 120 grit sandpaper to create a flat surface for further analysis with μXRF. Ethanol was used to remove dirt and residue from the polished surface.

The same experimental setup was used to study the paste sample with μCT, but instead of radiographs, a tomograph was used to better understand the 3D distribution of the fluid and learn more about when the air voids filled in the sample. A 3D tomography scan was conducted on a sample before the ponding as reference and while the sample was ponded. A Zeiss Xradia 410 Versa scanner was used for this experiment. The experiment was conducted for 60 days to follow

the changes. A summary of the scan setting can be found in **Table 3.3**. The sample was polished and then analyzed with µXRF after the ponding period.

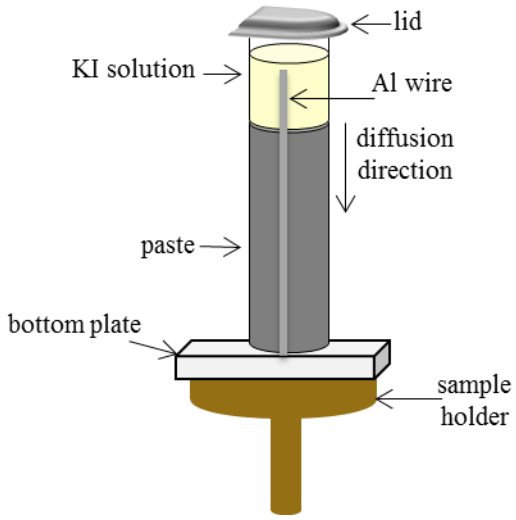

Fig. 3.1 Schematic diagram of the diffusion test setup.

3.2.3 Cl and I Diffusion Test Using µXRF

The paste samples were ponded with 0.6 mol/L KI and 0.6 mol/L NaCl solutions for 28 days to compare I and Cl ions diffusivity. After the ponding period, the sample was polished for analysis with µXRF. Two samples were tested per solution. As explained earlier, the investigated samples from TXM and µCT were also analyzed with µXRF to compare the results.

The µXRF analysis was conducted using the Orbis by EDAX. The instrument uses an 80 mm² Silicon Drift Detector Energy Dispersive Spectrometer (SDD-EDS) and a capillary optic that produces a 50 µm diameter beam. Images are created by moving the sample under the stationary X-ray beam. The X-ray beam causes characteristic fluorescence X-rays to be emitted at each spot, the intensity of these characteristic X-rays are measured by the SDD-EDS and stored in a database for later processing and analysis. This analysis is able to detect elements at 0.1% by weight [27]. Table 3 summarizes the settings used by the µXRF in this work. More details can be found in other publications [25-26].

Table 3.3 Summary of TXM, μCT, and μXRF settings used

parameter	TXM	μCT	μXRF
voltage (keV)	100	90	40
current (μA)	100	111	1000
filter	0.5 mm Al + 0.5 mm Cu	low energy glass filter	25 μm Al
pixel size (μm)	8.8	20	50
acquisition time	8 s	2 s	400 ms/pixel (dwell time)
chamber condition	air	air	vacuum
dead time	-	-	maximum of 20%

3.2.4 TXM Data Analysis

Figure 3.2 presents an example of time series radiographs taken from a paste sample with w/s of 0.35 and the subtracted images are presented by using the reference radiograph before ponding was started. The gray value changes of the paste allow the time dependent I diffusion front to be determined in both the time series radiographs and the subtracted images. Next, steps were taken to make quantitative measurements from the data.

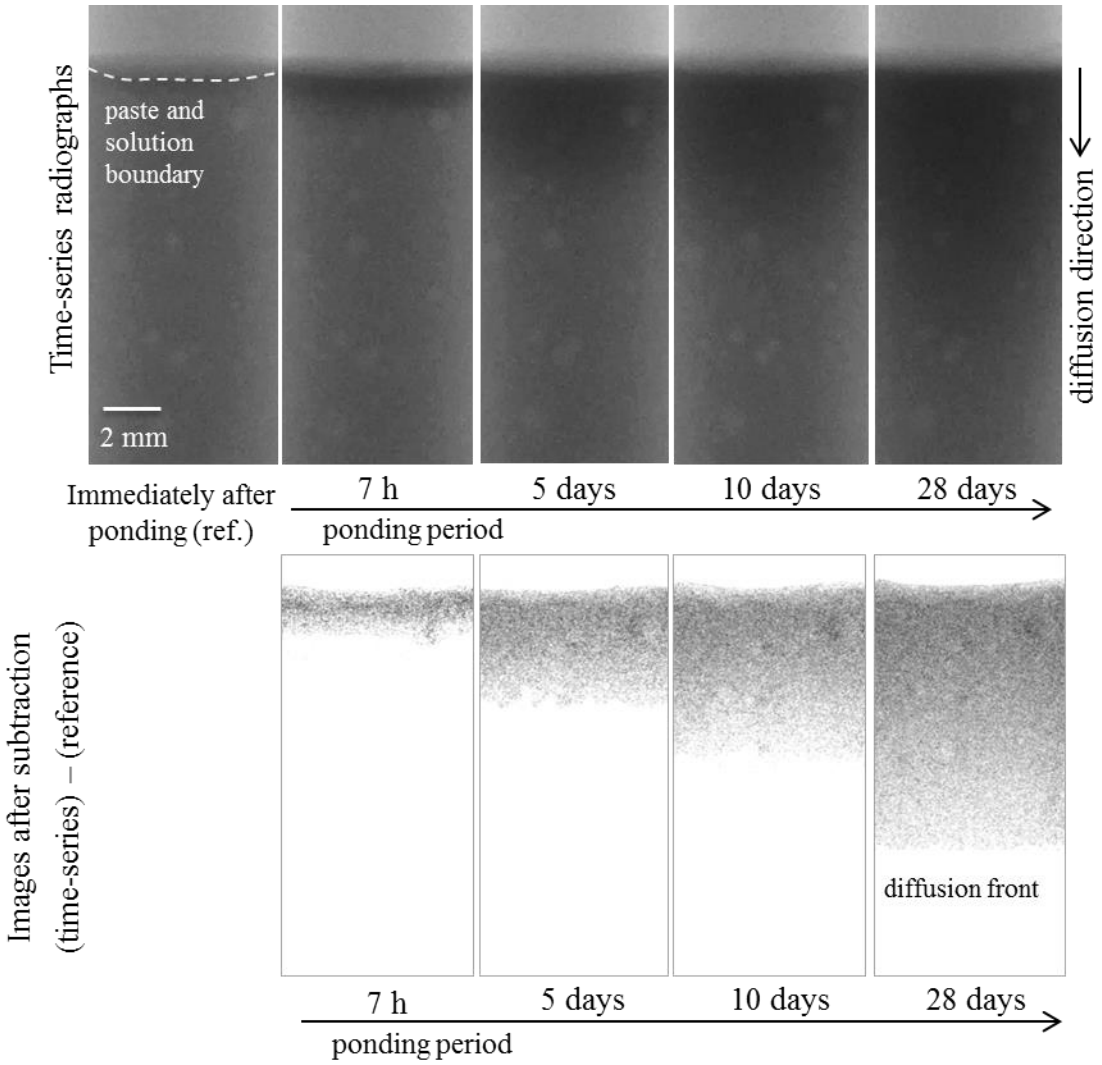

Fig. 3.2 Example of time-series radiographs (top) and images after subtraction (bottom) – w/s = 0.35.

An overview of the data analysis procedure is shown in **Fig. 3.3**. First, the radiographs of the air were subtracted from sample scans to remove the background attenuation effects. Next, an average gray value profile was calculated through the sample depth. Ten scan lines were randomly used to measure the average gray value with depth as shown in **Fig. 3.3a**. These lines were located at the middle 40% (4 mm) of the sample to avoid beam hardening and to keep the analyzed region at an almost constant depth. Next, each time-series radiograph gray value profile was subtracted from the gray value profile of the radiograph before solution was added to the

sample (a reference radiograph). This allowed the change in the gray value to be easily observed and the spatial changes due to absorption from the I to be mapped. The Beer-Lambert Law (**Eq. 3.1**) [21-22] was used to calculate a change in attenuation due to I ($\Delta\mu$) at different depths of sample.

$$(\Delta\mu)_x = \ln(I_{ref})_x - \ln(I_t)_x \qquad (3.1)$$

where $(I_{ref})_x$ is the transmitted X-ray intensity (gray value) at depth x on the reference profile and $(I_t)_x$ is the transmitted X-ray intensity at the same location at a future time. The diffusion accessible porosity and the sample thickness are not included in **Eq. (3.1)** since these parameters are constant for each sample.

Next, to determine I concentration profiles a set of reference paste standards with different KI concentrations was added to the cement paste while mixing in order to develop a calibration curve. The same sample sizes, mixtures, curing procedure, and scan setup were used in both the experiments and to develop the calibration curves. Next, the same calibration samples were polished and then analyzed with μXRF to develop a calibration curve for that technique. This allowed counts from μXRF to be converted to concentrations. This also allowed an independent method to be used to validate the TXM results. The calibration curves are included in the supplementary section (**Figs 3.S1-3.S4**).

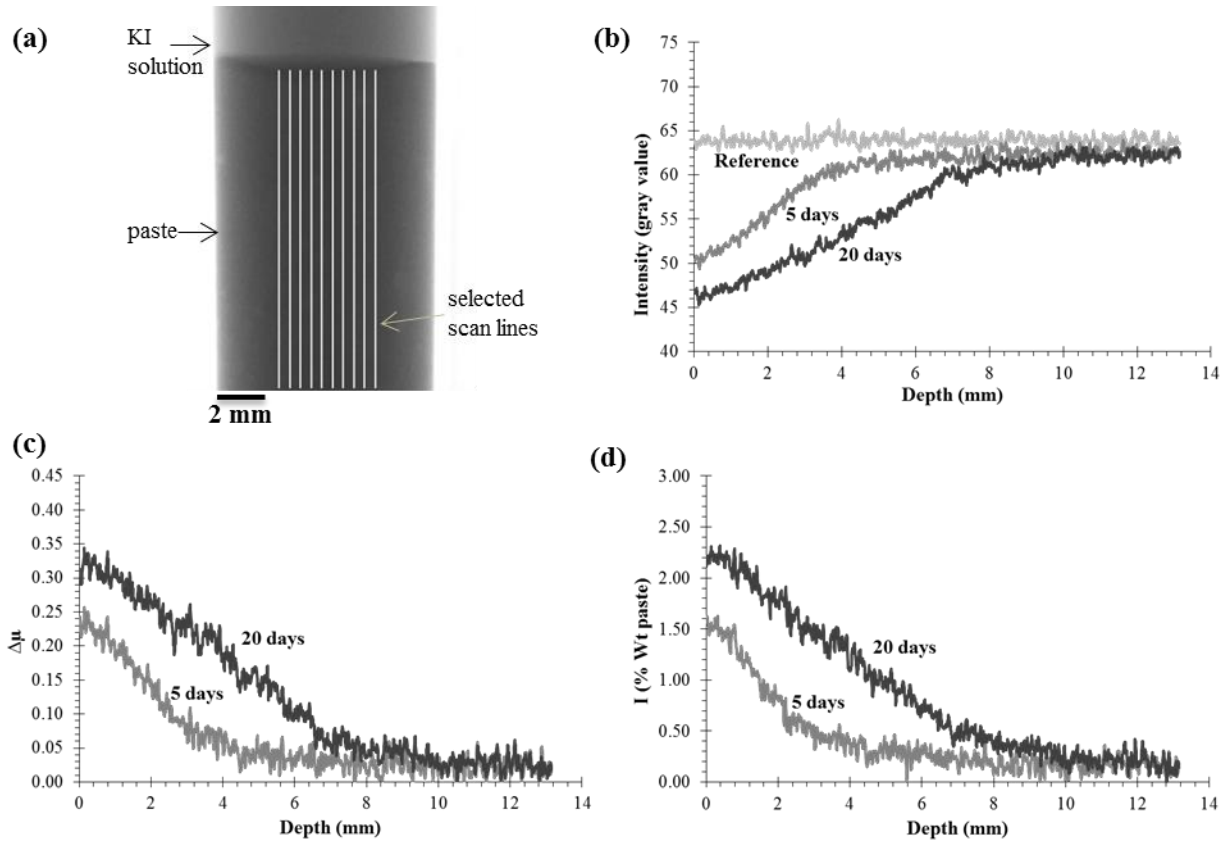

Fig. 3.3 X-ray radiography data analysis procedure: (a) calculating average gray value from radiographs (b) average gray value profiles over time (c) attenuation due to I (Δμ) profiles (d) I concentration profiles.

3.2.5 μCT Data Analysis

The reconstruction of μCT data was completed with the Xradia software XMReconstructor. To compare the μCT data for different time stages the intensity ranges of different scans were first adjusted to make their gray values comparable by using the Al wires. Next, to allow the same locations on the sample to be compared, the coordinate systems of all μCT data were aligned using a 3D image registration algorithm developed in Matlab that used the features of the void system. The regions of the sample were segmented by choosing a threshold value to minimize the noise in the solid paste regions and background. The voids were determined as the empty spaces within the boundary of the sample. A constant threshold value was applied on different

scans in order to show the changes of the voids over time. Next, to observe and quantify the filled air voids, the voids systems of initial stage and final stage (60 days after ponding) were directly compared. The voids detected before KI solution being added to the sample that could not be found within the scan at 60 days were identified as filled voids. Any voids less than ≈ 60 μm diameter (7 continuous voxels) were excluded in this analysis since they could not be distinguished from noise due to the limitation of the scan resolution. Investigation of smaller voids will be covered in future research efforts. Furthermore, a threshold value was used to segment the regions of iodide penetration in order to create the 3D diffusion fronts for different time stages. This threshold value was determined by matching the average depth of penetration at 60 days μCT data with the corresponding μXRF measurement. The Amira software package was used for 3D visualizations [28].

3.2.6 μXRF Data Analysis

After each sample was scanned with μXRF, the compositional maps were analyzed with an image processing software package called Lispix [29]. This program groups areas of similar composition, which are referred to as clusters. This analysis is helpful as one can combine individual compositional maps into a single map that simultaneously provides unique compositions and location. This separation of unique regions is useful in data display and analysis. For example, the cement paste was defined and separated by different elemental concentration levels (i.e., different levels of I), as shown in **Fig. 3.4**. These regions were separated by the user selecting threshold values for different elemental concentration levels (i.e., what the user identified as low, medium and high counts of a given element). These ranges were chosen by the user to show that there are distinct differences in concentration within the sample. This single map of paste provides a complete separation of the different I levels in the paste and is useful for displaying the data.

Finally, an image analysis code in Matlab was developed to analyze the spatial and compositional data. A border detection algorithm is used to find the top surface of the sample. The sample is then separated into 0.50 mm layers of equal thickness from the surface of the sample through the entire depth. The average I and Cl counts in each layer can then be plotted for different depths. Next, a developed calibration curve is used to convert I and Cl counts to concentrations. Additional details can be found in previous publications [25-26].

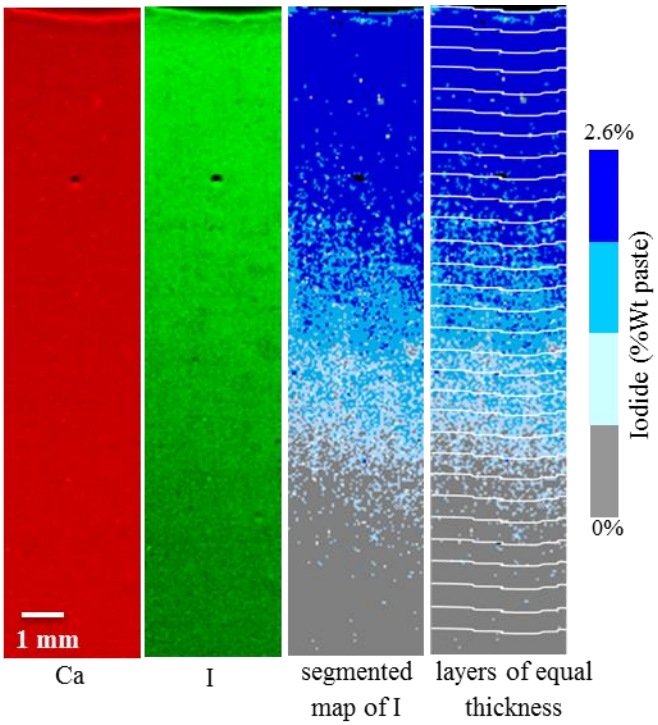

Fig. 3.4 An example of µXRF compositional maps: (left to right) calcium elemental map, I elemental map, segmented map of I, and layers of equal thickness for the analysis.

3.2.7 I and Cl Diffusion Coefficient and Surface Concentration Calculation

A nonlinear regression was then conducted on I and Cl profiles with Fick's second law as shown in **Eq. (3.2)** [30], the values of apparent diffusion coefficient and surface concentration were determined.

$$C_{(x,t)} = C_s\left(1 - \mathrm{erf}\left(\frac{x}{2\sqrt{D_c t}}\right)\right) \qquad (3.2)$$

$$C_{(x,0)} = 0 \quad x > 0, \quad C_{(0,t)} = C_s \quad t \geq 0$$

where x is distance from sample surface; t denotes time; D_c is diffusion coefficient; C_s is surface I or Cl concentration; $C_{(x,t)}$ represents I or Cl concentration at the depth of x from the surface after time t; and erf is the error function.

3.3 Results and Discussion

3.3.1 Comparison of the I and Cl Diffusivity

Figure 3.5 shows a comparison between I and Cl concentration profiles and diffusion coefficients of the paste sample with w/s of 0.4 after 28 days ponding with 0.6 M KI and 0.6 M NaCl solutions. Based on **Fig. 3.5**, the curves are very close except for a higher I concentration from the surface to 4 mm in depth; this is approximately the first 30% of the penetration depth. This suggests that about 70% of the profiles match and I shows an increase in diffusion coefficient over Cl of about 24% for these samples. Because of the differences in size and ionic mobility we would not expect the diffusion to be the same for these two different ions. Overall, I shows a similar diffusion performance to Cl and serves as a satisfactory substitute for the methods presented in this paper.

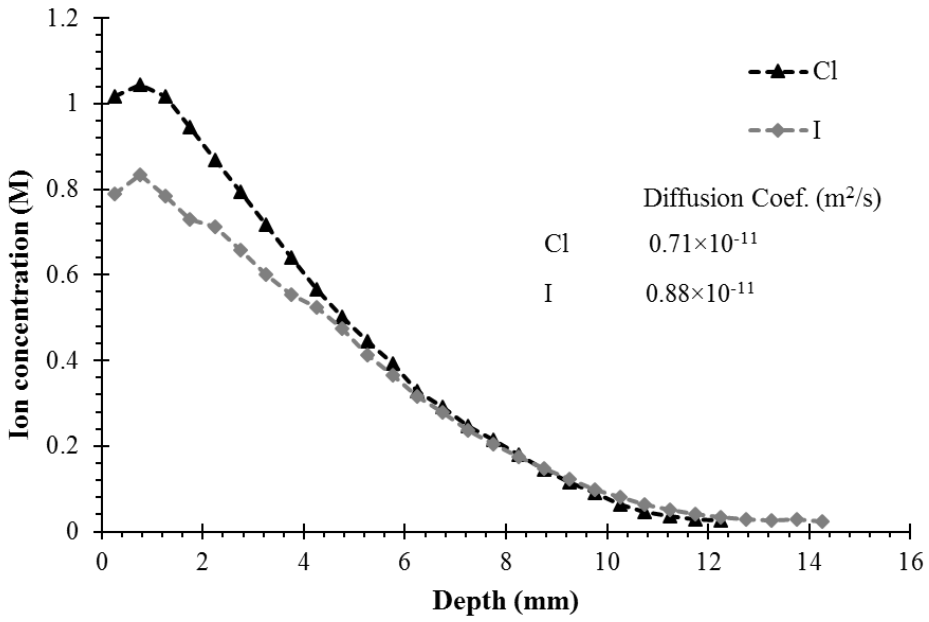

Fig. 3.5 Comparison of I and Cl concentration profiles and diffusion coefficients in paste samples with w/s of 0.40.

3.3.2 Comparison with μXRF

This section aims to compare findings between μXRF and TXM. **Figure 3.6** presents a comparison between μXRF and TXM for different w/s ratios. The calculated I diffusion coefficients from both methods are summarized in **Table 3.4**. The percent difference in diffusion coefficients between the two methods is also included. The I diffusion coefficients from TXM was on average 8% higher (5%, 5.4%, 13.5%). This shows that there is good agreement between μXRF and TXM for these samples and conditions. In addition, a two tail t-test with the assumption of unequal variances was conducted to compare the mean I diffusion coefficient of the two methods. Based on this analysis, the difference between means was not significant (p-value= 0.774 >> 0.05). This shows that these two methods provide statistically comparable results.

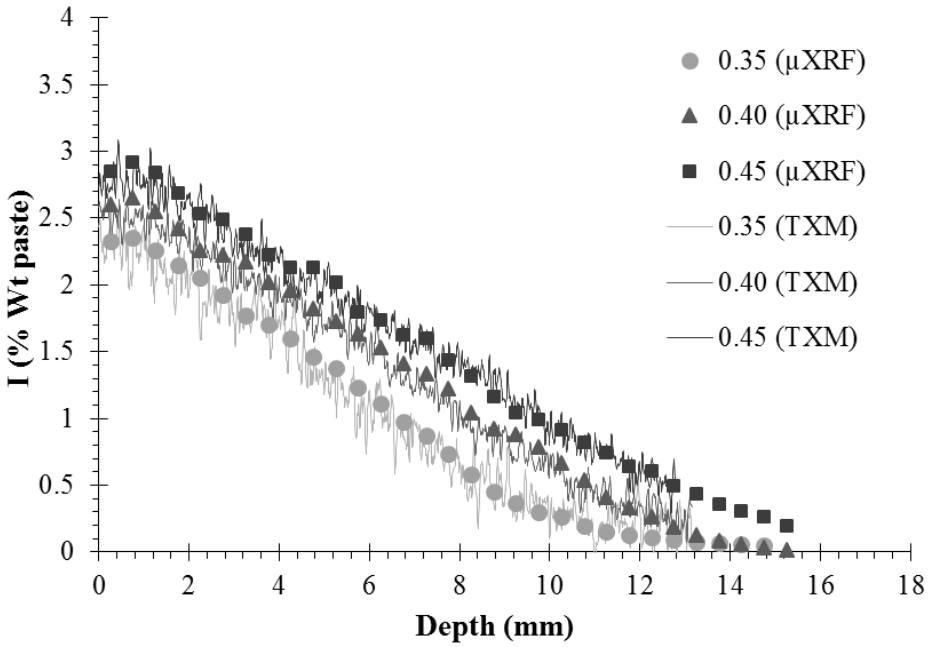

Fig. 3.6 Comparison of TXM results with results from µXRF.

Table 3.4 Comparison between I diffusion coefficients from TXM and µXRF

Sample	TXM Diff Coef×10^{-11} (m^2/sec)	R^2	µXRF Diff Coef×10^{-11} (m^2/sec)	R^2	% Difference $\frac{(TXM - \mu XRF)}{\mu XRF \times 0.01}$
P-35	1.05	0.96	1.00	0.98	5.0
P-40	1.55	0.97	1.47	0.97	5.4
P-45	2.18	0.97	1.92	0.99	13.5

3.3.3 I Concentration Profiles Over Time

Figs 3.7 to **3.9** show the change in time of the I concentration profiles determined from their corresponding radiographs during ponding for a paste sample with w/s of 0.35, 0.4, and 0.45 based on developed calibration curves. In addition, the calculated time-dependent surface I concentration based on **Eq. (3.2)** for paste samples with different w/s ratios is plotted in **Fig. 3.10**. This data shows that TXM is capable of providing time-series concentration profiles with high spatial resolution. Because of the high resolution of the data, the I profile can be measured within

hours of adding the material to the surface. This data can then be used to trace the time-dependent change in concentration profile shape and slope.

Based on **Fig. 3.10**, the I surface concentration increases from ponding until it reaches a maximum between 1.3% to 2% weight of the paste after 30 h. This could be explained by both capillary absorption and diffusion at the initial penetration of the solution. Also, the I surface concentration became almost constant after 15 days ponding in samples with w/s of 0.40 and 0.45 (2.6% and 2.9% weight of the paste for samples with w/s of 0.40 and 0.45, respectively). This suggests that the concentrations in the solid paste and the solution come into equilibrium with a w/s of 0.40 and 0.45 after almost 15 days of ponding. For the w/s of 0.35 it appears to take longer than 28 d.

In addition, TXM provides a good comparison of the resistance of paste samples with different w/s against I penetration at early ages. As an example, the diffusion front and measured concentration profiles of different paste mixtures after 20 days of ponding are compared in **Fig. 3.11**. According to **Fig. 3.11**, the I concentration increases through the entire depth of paste sample with an increase of w/s. This can be quantitatively measured as the I diffusion coefficient decreases by about 23% and 48% by decreasing the paste w/s from 0.45 to 0.40 and 0.35, respectively.

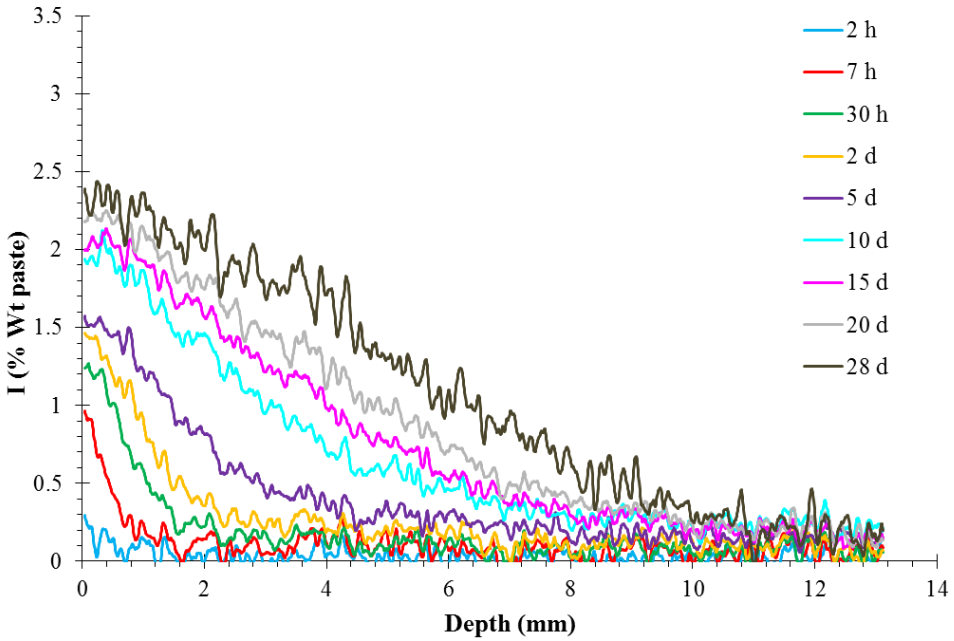

Fig. 3.7 Time-series I concentration profiles – w/s = 0.35.

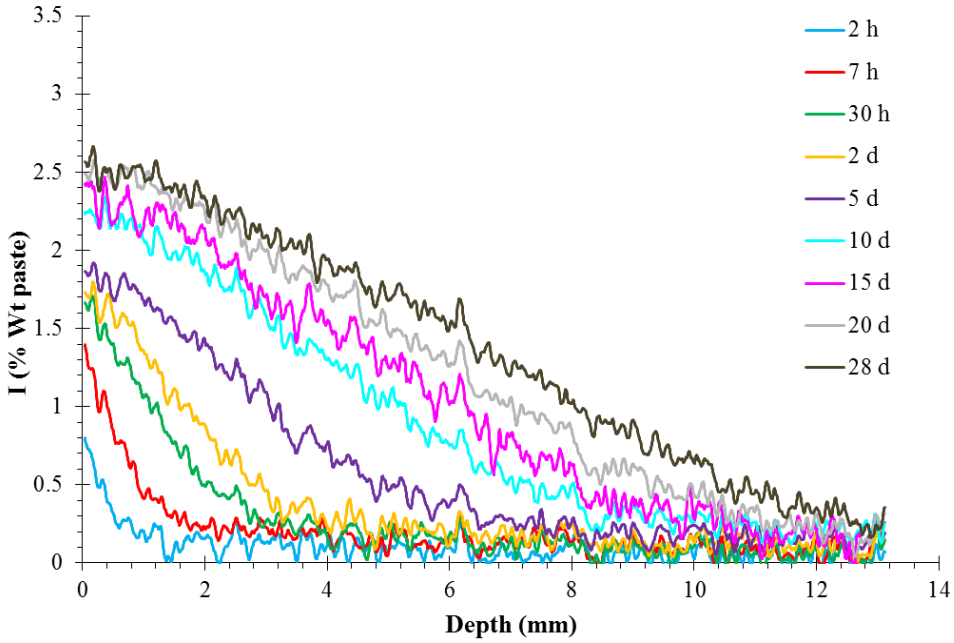

Fig. 3.8 Time-series I concentration profiles – w/s = 0.40.

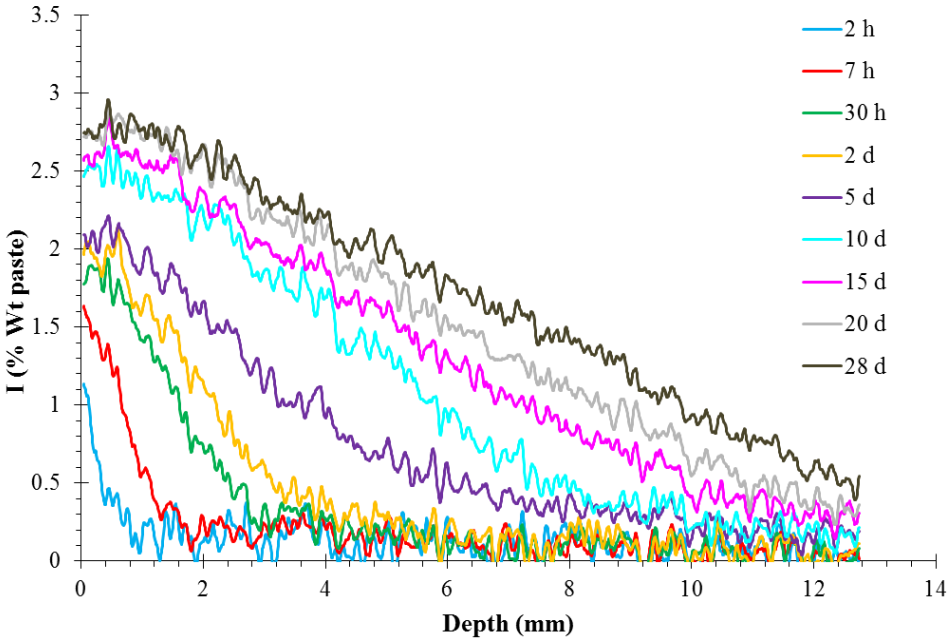

Fig. 3.9 Time-series I concentration profiles – w/s = 0.45.

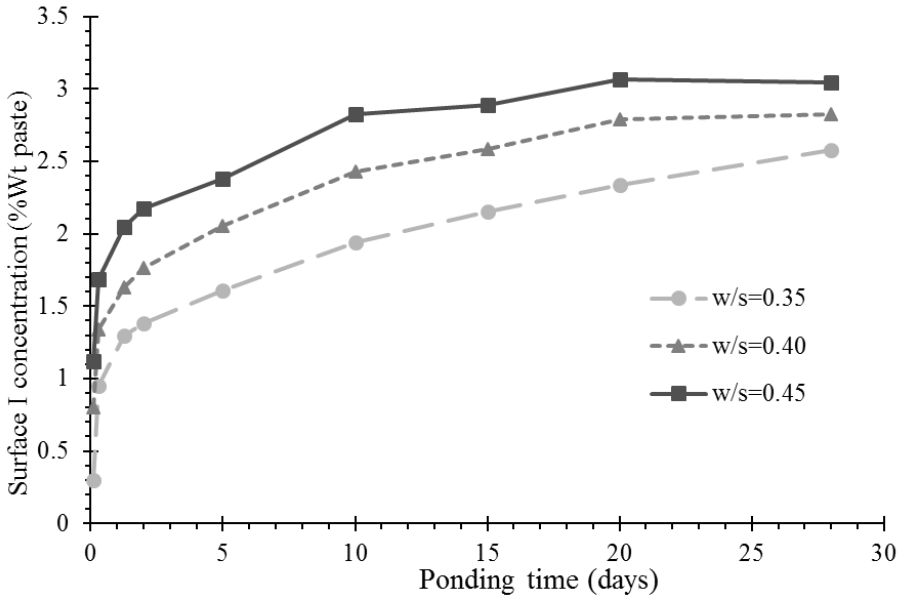

Fig. 3.10 Time-dependent surface I concentration by TXM.

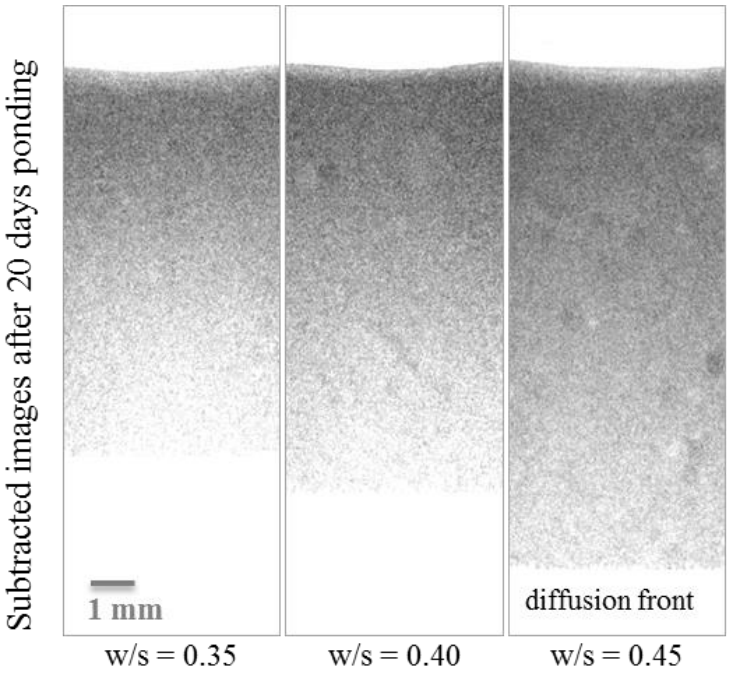

	w/s = 0.35	w/s = 0.40	w/s = 0.45
Diffusion coefficient (m^2/s)	1.09×10^{-11}	1.62×10^{-11}	2.11×10^{-11}
Penetration depth (mm)	10	11.8	13.9

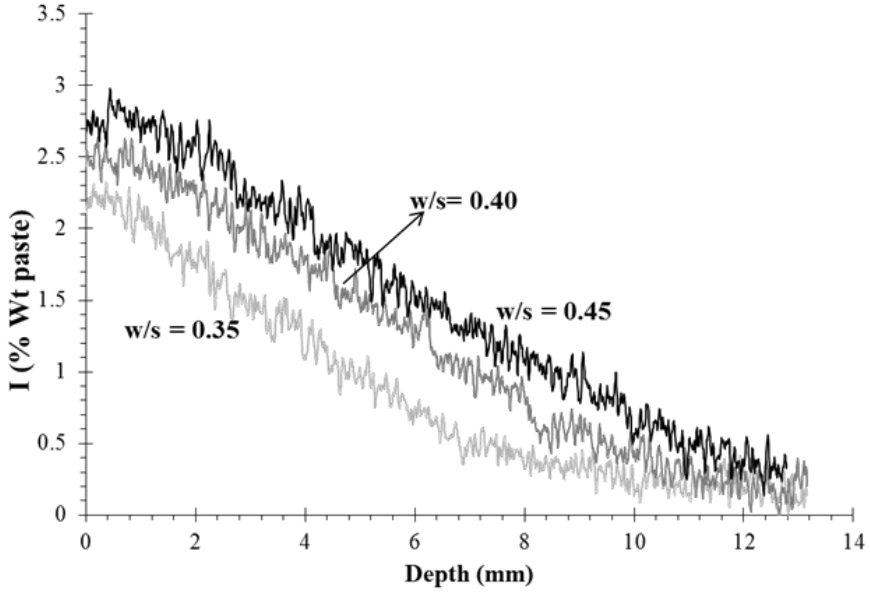

Fig. 3.11 Comparison of different paste mixtures performance against I diffusion after 20 days ponding.

Atkinson and Nickerson [31-32] have studied diffusion of I (1 M KI solution) in water saturated cement pastes with different w/s by conducting diffusion cell tests. They reported the intrinsic I diffusion coefficients of 0.75×10^{-11} m^2/s and $3.5\times10^{-11} m^2/s$ for 28 days wet-cured cement pastes with w/s of 0.40 and 0.50, respectively. The I diffusion coefficients after 28 days ponding from TXM are 1.05×10^{-11}, 1.55×10^{-11}, and 2.18×10^{-11} m^2/s for samples with w/s of 0.35, 0.40, and 0.45, respectively. Therefore, the results of the TXM experiments are in agreement with previous diffusion cell studies on cement paste samples. The difference in results may be due to the different KI concentration usage (0.6M vs 1M). In addition, Atkinson and Nickerson [31] measured the interdiffusion of Cl and I ions by introducing potassium chloride solution (KCl) to the other side of the diffusion cell which can also affect the calculated diffusion coefficient.

According to the previous studies [31, 33-35], the reported Cl diffusion coefficient for a cement paste with w/s of 0.40 has a range of 1.1×10^{-11} to 2.6×10^{-11} m^2/s based on different test methods. Therefore, the I diffusion coefficient based on this study ($1.55\times10^{-11} m^2/s$) is within this measured range. This validation of the methods results is promising. This also reinforces that Cl and I have similar diffusion coefficients in cement paste. As mentioned earlier, the paste samples with w/s of 0.40 also showed a similar diffusion coefficient for I and Cl after 28 days ponding with 0.6 M KI and 0.6 M NaCl solutions for the materials and dimensions used in this study.

3.3.4 Time-dependent I Diffusion Coefficient

Figure 3.12 displays time-dependent I diffusion coefficient for cement paste mixtures with different w/s from TXM. Based on **Fig. 3.12**, the apparent diffusion coefficient slightly increases over the first 5 days of ponding with I, and then the value is almost constant after 15 days. This trend is very similar for the three different mixtures investigated. As discussed earlier, this initial increase in diffusion coefficient can be due to the combined penetration mechanism from the capillary absorption and diffusion near the surface of the sample. This has been called transient

behavior in the literature [31]. Atkinson and Nickerson [31] reported this transient behavior based on results of diffusion cell test on saturated cement paste. In addition, the time-dependent diffusion coefficients highlight that the mixed mode of mass transport changes to a steady state after 15 days of ponding.

This phenomenon does not seem to be dependent on the w/s as Fig. 12 shows that the change in diffusion coefficient over time is constant between the samples after 5 days of ponding. This difference is about 22% on average between the paste samples with w/s of 0.40 and 0.45 and 46% on average between samples with w/s of 0.45 and 0.35.

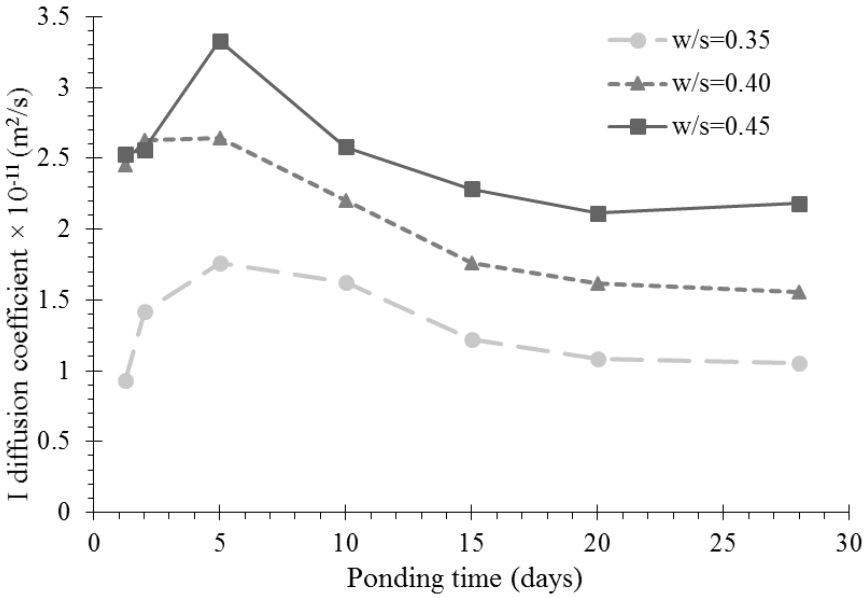

Fig. 3.12 Time-dependent I diffusion coefficients by TXM.

3.3.5 Variability in the TXM Method

One concern in conducting X-ray imaging is the impact of the sample thickness on X-ray attenuation behavior and correspondingly the effect on derived results from this technique [6]. As mentioned earlier, the paste samples with two different diameters (7 and 9.5 mm) were used to conduct TXM experiment in order to determine the impact of sample thickness on I diffusion

results. **Figure 3.13** compares the I concentration profiles and calculated diffusion coefficients of paste samples with w/s of 0.35 with different diameters. Similar information for other paste mixtures is provided in the supplementary section (**Figs 3.S5** and **3.S6**). Based on **Fig. 3.13**, there is good agreement between results from two different sample sizes. According to results, the standard deviations between diffusion coefficients of different sample sizes are $\pm 0.14\times10^{-11}$, $\pm 0.16\times10^{-11}$, and $\pm 0.19\times10^{-11}$ for paste mixtures with w/s of 0.35, 0.40, and 0.45, respectively. These standard deviations are similar to the sample to sample variation of diffusion coefficient within the same sample size. This means that the sample thickness impact on results from TXM is not significant. In addition, two-way analysis of variance (ANOVA) was used to determine the significance of sample thickness impact on I diffusion coefficient. In two-way ANOVA, the dependent variable was the I diffusion coefficient, and the independent variables were the sample thickness and w/s. Based on this analysis, the two-way ANOVA results in insignificant p-value ($0.095 > 0.05$) for the sample thickness effect on diffusion coefficient. This suggests that the sample thickness between the sizes investigated does not have a statistically significant impact on the results.

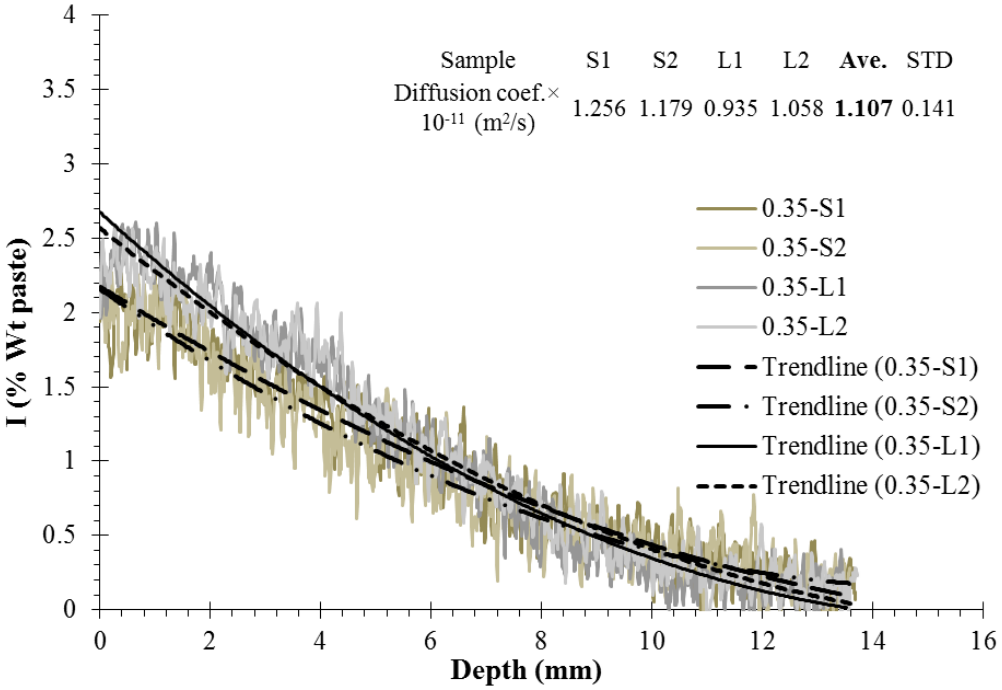

Fig. 3.13 I concentration profiles and diffusion coefficients of samples with various diameters – w/s = 0.35. Note: The "S" and "L" letters represent small and large samples with inside diameters of 7 mm and 9.5 mm, respectively.

3.3.6 Time-Dependent Ion Movement and Distribution of Filled Air Voids from 3D Tomography

Fig. 3.14 shows the 3D time-dependent iodide movement front inside a paste sample with w/s of 0.40 with a single embedded aggregate inside the sample. Based on **Fig. 3.14**, iodide shows non-uniform penetration when the solution reaches larger features like aggregates and large air voids. In addition, the iodide rate of penetration is higher at 3 days from the ponding when compared to the further ponding times. This is consistent with TXM results.

Furthermore, it has been known that the air void system of cement-based materials plays an important role in saturation level and subsequently in freeze-thaw durability of these materials [36-37]. Previous research [38] discussed the potential of µCT to quantify the air voids distribution in cement-based materials. However, this work uses µCT to image the voids before

and after being filled with solution. This shows the versatility of the methods presented to measure very complex phenomena.

Fig. 3.15 shows the 3D configuration of air voids inside a paste sample with w/s of 0.40 and the distribution of total, filled, and empty air voids with different diameters after 60 days ponding with 0.6 M KI solution. Based on results, it is observed that only the air voids with diameter of less than 200 µm within a top 6 mm height of the sample filled with KI solution after 60 days ponding. Based on **Fig. 3.15b**, more than 90% of air voids with diameter of less than 80 µm filled with KI solution within a top 6 mm height of the sample. As the void size increased the percentage of full voids decreased. The I concentration for the sample at 60 days is shown in **Fig. 3.16**. This data shows that the I concentration was almost constant and likely at a very high degree of saturation in the air void filling region of the sample. More quantitative work on this topic is underway and will be published in future papers.

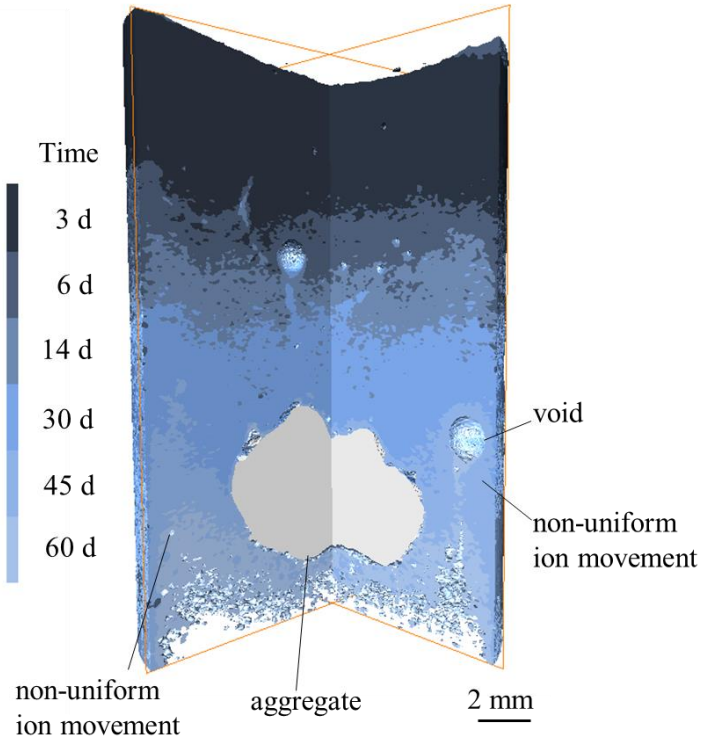

Fig. 3.14 Results from 3D tomography; time-dependent iodide movement front inside a paste sample with w/s of 0.40 with a single embedded aggregate inside the sample.

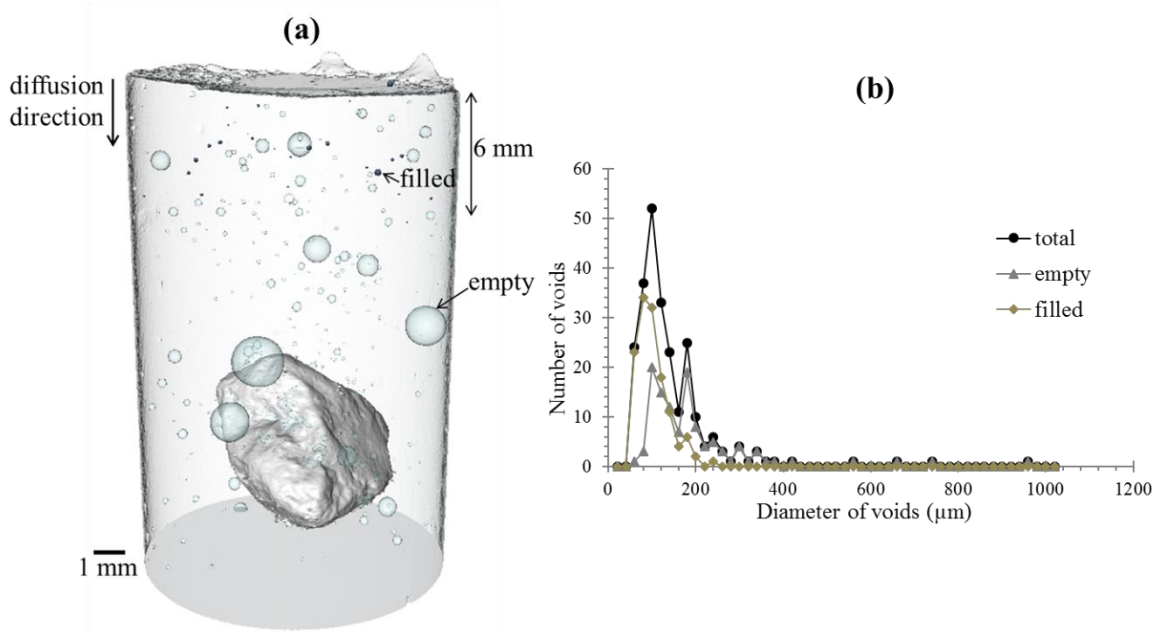

Fig. 3.15 Results from 3D tomography: (a) 3D visualization of filled and empty air voids inside a paste sample with w/s of 0.40 after 60 days ponding with 0.6 M KI solution (empty and filled voids are shown with bright and dark colors, respectively) (b) distribution of total, filled, and empty air voids with different diameters within a top 6 mm height of the sample after 60 days ponding with 0.6 M KI solution.

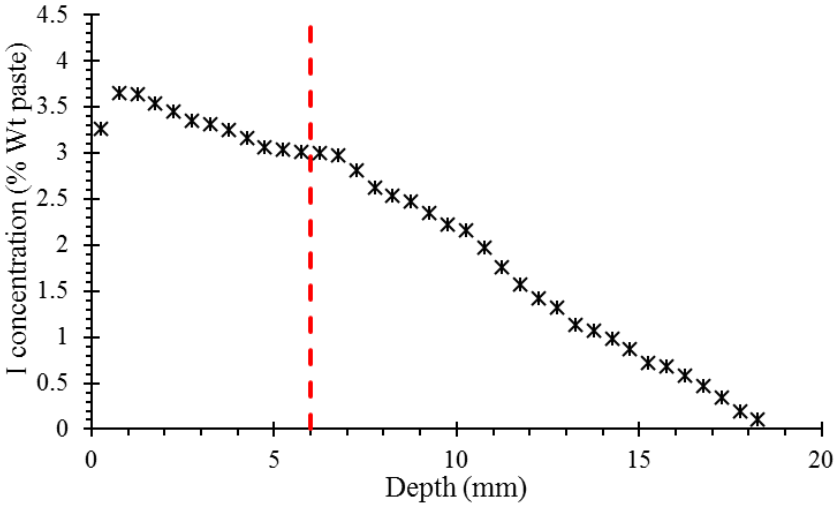

Fig. 3.16 An I concentration profile of paste sample with w/s of 0.40 after 60 days ponding with KI solution by μXRF.

3.3.7 Future Applications of the Method

This study helps to establish an important and useful non-destructive technique to evaluate the performance of different cement-based materials in a short period of time with very little human effort. This method also provides data that is comparable to other methods. Furthermore, high spatial resolution of these techniques in 2D or 3D can be used to provide greater insight into the mechanisms of fluid transport into cement-based materials. This method can detect preferential pathways for fluid transport and also provide important insights into fluid concentrations when certain size pores fill. Also, because this method is non-destructive it can be used to conduct in-situ imaging. This makes the method well suited to image combined fluid transport mechanisms. Furthermore, this technique can be quite useful to study ion transport in complex geometries (e.g. cracks) as well as different durability mechanisms such as freeze thaw attack, alkali silica reaction, physical salt attack, salt scaling, sulfate attack, and impact of temperature changes. Finally, the produced data sets can be used in computational modeling efforts.

While the techniques presented in this paper used a μCT scanner to collect the data, this does not have to be the case. The 2D data and quantification of the effective diffusion coefficient could be obtained by using the same methodologies outlined but using a X-ray machine used in the medical field to investigate the skeletal structure of humans or animals. By using standards and carefully controlled settings then the same quantitative data about the effective diffusion coefficient could be obtained. Since X-ray machines are so widely available they could be used to economically gather the data. Furthermore, this technique could be used to more rapidly determine the effective diffusion coefficient as one would only have to wait about 15 days to determine this value as it was shown to not drastically change after this point. This may be able

to provide an alternate test method to directly measure the penetration of ions into porous media. Additional work is underway to further investigate this.

3.4 Conclusions

Both TXM and μCT are powerful, non-destructive, and fast imaging techniques that are capable of providing valuable spatial and quantitative information about the penetration of ions into cement-based materials. The presented work provides a systematic approach to use 2D X-ray radiography to image in-situ and time resolved iodide diffusion into cement paste samples with w/s of 0.35, 0.40, and 0.45. Time resolved concentration profiles were developed and the results at 28 days were compared to μXRF and good agreement was found. Also, μXRF was used to compare I and Cl concentration profiles and diffusion coefficients in paste samples with w/s of 0.4 at 28 days. In addition, a 3D tomography data set from μCT is included to show how the technique can be used to measure complex phenomena such as filling of air voids at different fluid concentrations.

The following conclusions can be drawn from this work:

- When comparing I and Cl diffusion, μXRF showed I to have a 24% higher diffusion coefficient but a similar concentration profile to Cl.
- The TXM method was on average 8% higher than the μXRF measurement at comparable time periods.
- The apparent I diffusion coefficients after 28 days ponding from TXM are 1.05×10^{-11}, 1.55×10^{-11}, and 2.18×10^{-11} m^2/s for samples with w/s of 0.35, 0.40, and 0.45, respectively. These values are in agreement with previous studies that use other experimental methods.
- The apparent I diffusion coefficient increased over the first 5 days of ponding, and then decreased to a constant value after 15 days. This happened for w/s of 0.35, 0.40 and 0.45.

- The sample thicknesses investigated did not have an impact on the results of TXM for the materials and dimensions used in this study.

- Features such as large air voids and aggregates are shown to influence the fluid flow within cement paste.

- Based on 3D μCT, only the air voids with diameter of less than 200 μm within a top 6 mm height of the sample filled with KI solution after 60 days ponding. This happens where the I concentration became almost constant and the I concentration profile reaches a plateau.

The use of TXM offers advantages over conventional methods to measure diffusion coefficients and over other neutron, electron, or X-ray imaging techniques that measure chemical concentrations. Since TXM allows non-destructive and time-dependent diffusion profiles to be measured with no sample preparation the method can be used to measure performance at early ages, image complex transport phenomenon, and can be quite useful to study ion transport in complex geometries (e.g. cracks) as well as different durability mechanisms.

Acknowledgments

The authors acknowledge the financial support from the Oklahoma Department of Transportation (ODOT 2229), Federal Highway Association (FHWA) Exploratory Advanced Research (EAR) Program (Project No. CMMI 1030972), and the United State National Science Foundation CMMI 1150404 CAREER Award. The authors would like to thank Mr. Chad Stevenson for his assistance with casting the samples.

References

[1] G.H. Koch, M.P. Brongers, N.G. Thompson, Y.P. Virmani, J.H. Payer, Corrosion costs and preventive strategies in the United States, Report by CC Technologies Laboratories, Inc. to Federal Highway Administration (FHWA)-RD-01-151, September 2001.

[2] P.K. Mehta, Durability of Concrete- Fifty Years of Progress?, ACI SP 126-1, (1991) 1-31.

[3] M. Khanzadeh Moradllo, M.H. Meshkini, E. Eslamdoost, S. Sadati, M. Shekarchi, Effect of Wet Curing Duration on Long-Term Performance of Concrete in Tidal Zone of Marine Environment, Int. J. Concr. Struct. Mater. (2015). doi:10.1007/s40069-015-0118-3.

[4] K. Basham, J. Meredith, Measuring water penetration: A simple, inexpensive tube test can yield valuable, quantitative information, Mag. Mason. Constr. 8 (1995) 539-543.

[5] S. Lu, E.N. Landis, D.T. Keane, X-ray microtomographic studies of pore structure and permeability in Portland cement concrete, Mater. Struct. 39 (2007) 611–620. doi:10.1617/s11527-006-9099-7.

[6] G. Sant, W.J. Weiss, Using X-Ray Absorption to Assess Moisture Movement in Cement-Based Materials, J. ASTM Int. 6 (2009) 15. doi:10.1520/JAI102234.

[7] K.D. Stanish, R.D. Hooton, M.D. Thomas, Testing the Chloride Penetration Resistance of Concrete: A Literature Review, FHWA Contract DTFH61-97-R-00022, 1997.

[8] P. Joshi, C. Chan, Rapid Chloride Permeability Testing, Concr. Constr. - World Concr. (2002).

[9] H. Derluyn, M. Griffa, D. Mannes, I. Jerjen, J. Dewanckele, P. Vontobel, et al., Characterizing saline uptake and salt distributions in porous limestone with neutron radiography and X-ray micro-tomography, J. Build. Phys. 36 (2013) 353–374. doi:10.1177/1744259112473947.

[10] C.L. Lucero, D.P. Bentz, D.S. Hussey, D.L. Jacobson, W.J. Weiss, Using Neutron Radiography to Quantify Water Transport and the Degree of Saturation in Entrained Air Cement Based Mortar (In Press), Phys. Procedia (10 World Conf. Neutron Radiogr. 69 (2014) 1–8. doi:10.1016/j.phpro.2015.07.077.

[11] C. Lucero, Quantifying Moisture Transport in Cementitious Materials Using Neutron Radiography, In: MSc thesis, Purdue University, West Lafayette, Indiana, USA, 2015.

[12] D.P. Bentz, K.K. Hansen, Preliminary observations of water movement in cement pastes during curing using X-ray absorption, Cem. Concr. Res. 30 (2000) 1157–1168. doi:10.1016/s0008-8846(00)00273-8.

[13] S. Roels, J. Carmeliet, Analysis of moisture flow in porous materials using microfocus X-ray radiography, Int. J. Heat Mass Transf. 49 (2006) 4762–4772. doi:10.1016/j.ijheatmasstransfer.2006.06.035.

[14] M. A. Hickner, N.P. Siegel, K.S. Chen, D.S. Hussey, D.L. Jacobson, M. Arif, In Situ High-Resolution Neutron Radiography of Cross-Sectional Liquid Water Profiles in Proton Exchange Membrane Fuel Cells, J. Electrochem. Soc. 155 (2008) B427. doi:10.1149/1.2826287.

[15] I.S. Darma, T. Sugiyama, M.A.B. Promentilla, Application of X-Ray CT to Study Diffusivity in Cracked Concrete Through the Observation of Tracer Transport, J. Adv. Concr. Technol. 11 (2013) 266–281. doi:10.3151/jact.11.266.

[16] R. Henkensiefken, T. Nantung, J. Weiss, Saturated lightweight aggregate for internal curing in low w/c mixtures: Monitoring water movement using x-ray absorption, Strain. 47 (2011) 432–441. doi:10.1111/j.1475-1305.2009.00626.x.

[17] E.N. Landis, D.T. Keane, X-ray microtomography, Mater. Charact. 61 (2010) 1305–1316. doi:10.1016/j.matchar.2010.09.012.

[18] Q. Hu, M.T. Ley, J. Davis, J.C. Hanan, R. Frazier, Y. Zhang, 3D chemical segmentation of fly ash particles with X-ray computed tomography and electron probe microanalysis, Fuel. 116 (2014) 229–236. doi:10.1016/j.fuel.2013.07.037.

[19] M. Zhang, Y. He, G. Ye, D. a. Lange, K. Van Breugel, Computational investigation on mass diffusivity in Portland cement paste based on X-ray computed microtomography (uCT) image, Constr. Build. Mater. 27 (2012) 472–481. doi:10.1016/j.conbuildmat.2011.07.017.

[20] D.P. Bentz, D. a. Quenard, H.M. Kunzel, J. Baruchel, F. Peyrin, N.S. Martys, et al., Microstructure and transport properties of porous building materials. II: Three-dimensional X-ray tomographic studies, Mater. Struct. 33 (2000) 147–153. doi:10.1007/BF02479408.

[21] V.C. Tidwell, L.C. Meigs, T. Christian-Frear, C.M. Boney, Effects of spatially heterogeneous porosity on matrix diffusion as investigated by X-ray absorption imaging, J. Contam. Hydrol. 42 (2000) 285–302. doi:10.1016/S0169-7722(99)00087-X.

[22] L. Cavé, T. Al, Y. Xiang, P. Vilks, A technique for estimating one-dimensional diffusion coefficients in low-permeability sedimentary rock using X-ray radiography: Comparison with through-diffusion measurements, J. Contam. Hydrol. 103 (2009) 1–12. doi:10.1016/j.jconhyd.2008.08.001.

[23] S.J. Altman, M. Uchida, V.C. Tidwell, C.M. Boney, B.P. Chambers, Use of X-ray absorption imaging to examine heterogeneous diffusion in fractured crystalline rocks, J. Contam. Hydrol. 69 (2004) 1–26. doi:10.1016/S0169-7722(03)00153-0.

[24] A. Sato, D. Fukahori, K. Sugawara, A. Sawada, A. Takebe, Visualization of 2D Diffusion Phenomena in Rock by Means of X-ray CT, Adv. X-Ray Tomogr. Geomaterials. (2010) 315–321. doi:10.1002/9780470612187.ch32.

[25] B. Sudbrink, M. Khanzadeh Moradllo, Q. Hu, M.T. Ley, J.M. Davis, N. Materer, A. Apblett, Imaging the presence of silane coatings in concrete with micro X-ray fluorescence. Cem.Concr. Res. (2016); accepted for publication. doi:10.1016/j.cemconres.2016.11.019.

[26] M. Khanzadeh Moradllo, B. Sudbrink, Q. Hu, M. Aboustait, B. Tabb, M.T. Ley, J.M. Davis, Using micro X-ray fluorescence to image chloride profiles in concrete. Cem.Concr. Res. (2016), in press. doi:10.1016/j.cemconres.2016.11.014.

[27] K.H.A. Janssens, F. Adams, A. Rindby, Microscopic x-ray fluorescence analysis, John Wiley & Sons Inc, New York, 2000.

[28] AMIRA (Version 4.1) [Software]. Burlington, MA: VSG.

[29] D. Bright, Lispix: An image processing and analysis tool for the PC, 2011. http://www.nist.gov/lispix/doc/contents.htm, (last accessed on July 2015).

[30] J. Crank, The mathematics of diffusion, second ed., Oxford Science Publication, London, 1975.

[31] A. Atkinson, A. K. Nickerson, The diffusion of ions through water-saturated cement, J. Mater. Sci. 19 (1984) 3068–3078. doi:10.1007/BF01026986.

[32] A. Atkinson, A.K. Nickerson, Diffusion and Sorption of Cesium, Strontium, and Iodine in Water-Saturated Cement, Nucl. Technol. 81 (1988) 100–113.

[33] K. Byfors, Influence of Silica Fume and Flyash on Chloride Diffusion and pH Values in Cement Paste, Cem. Concr. Res. 17 (1987) 115–130. doi:10.1016/0008-8846(87)90066-4.

[34] O.M. Jensen, P.F. Hansen, A.M. Coats, F.P. Glasser, Chloride ingress in cement paste and mortar, Cem. Concr. Res. 29 (1999) 1497–1504. doi:10.1016/s0008-8846(99)00131-3.

[35] C.L. Page, N.R. Short, A. El Tarras, Diffusion of chloride ions in hardened cement pastes, Cem. Concr. Res. 11 (1981) 395–406. doi:10.1016/0008-8846(81)90111-3.

[36] T.C. Powers, T.F. Willis, The air requirement of frost resistant concrete. In Highway Research Board Proceedings, Chicago,1949;29, pp:184-211.

[37] W.A. Cordon, D. Merrill, Requirements for freezing and thawing durability for concrete, Proceedings, ASTM, 1963;63, pp:1026–1036.

[38] T.S. Yun, K.Y. Kim, J. Choo, D.H. Kang, Quantifying the distribution of paste-void spacing of hardened cement paste using X-ray computed tomography, Mater. Charact. 73 (2012) 137–143. doi:10.1016/j.matchar.2012.08.008.

Supplementary Section

I and Cl Calibration Curves

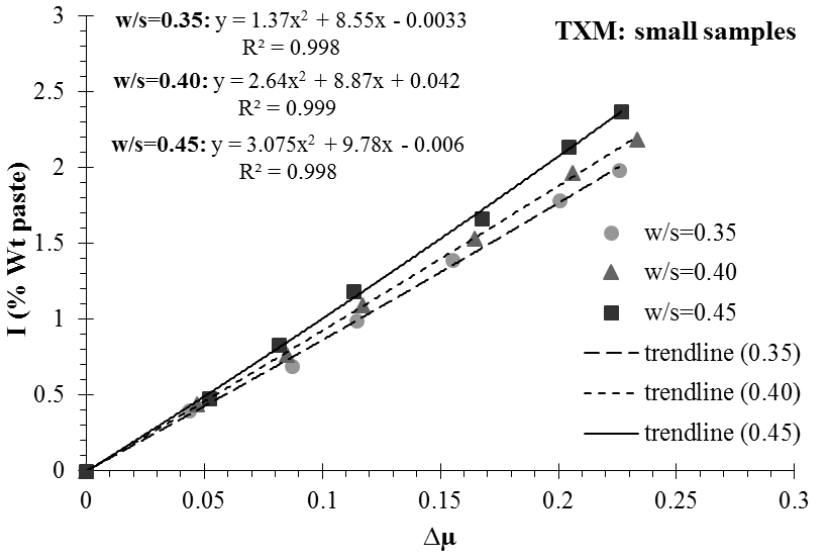

Fig. 3.S1 I calibration curve used to change from attenuation to weight percentage in the TXM analysis – small samples.

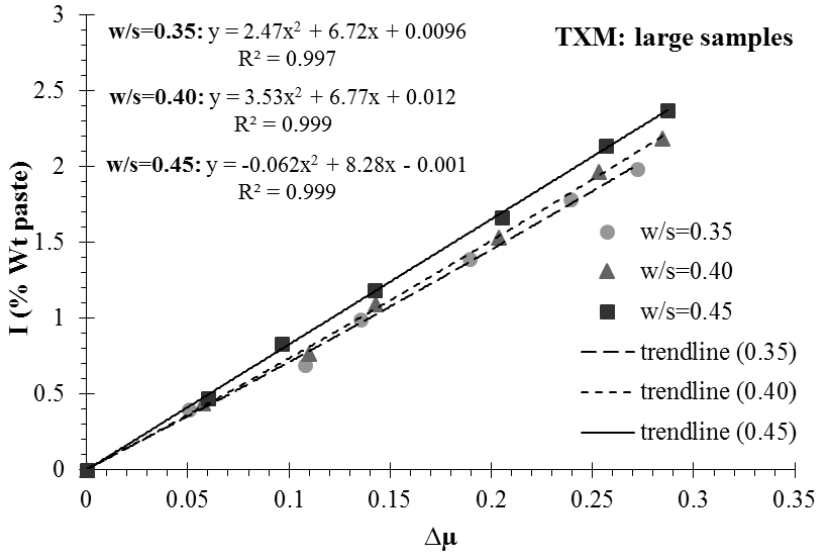

Fig. 3.S2 I calibration curve used to change from attenuation to weight percentage in the TXM analysis – large samples.

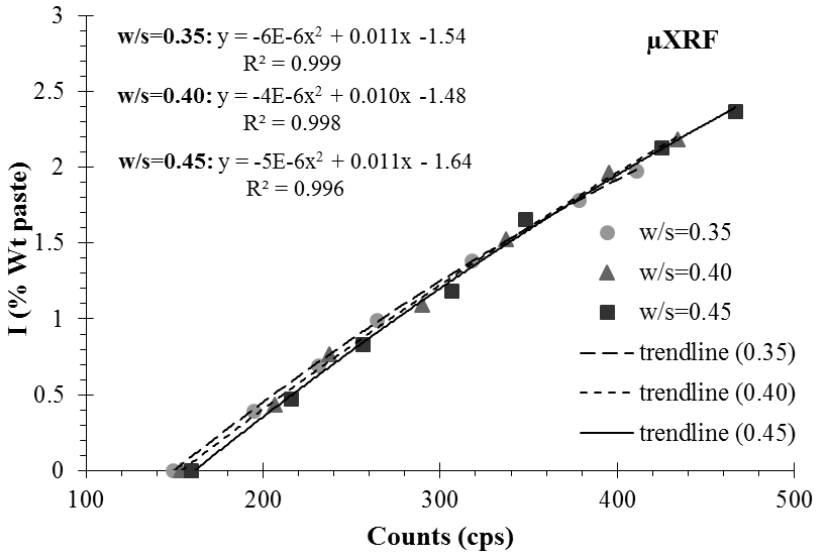

Fig. 3.S3 I calibration curve used to change from counts to weight percentage in the µXRF analysis.

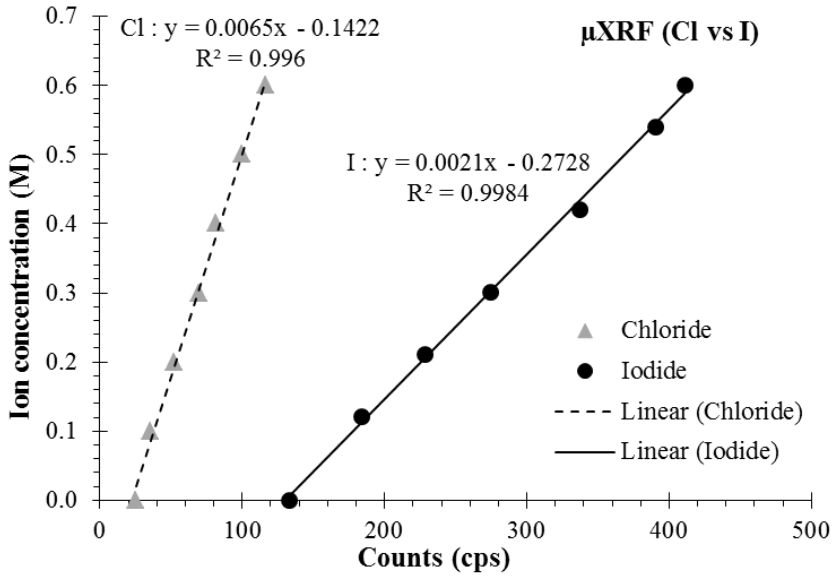

Fig. 3.S4 Cl and I calibration curves used to change from counts to concentration (M) in the µXRF analysis of the paste samples – w/s=0.40.

Variability in the TXM Method

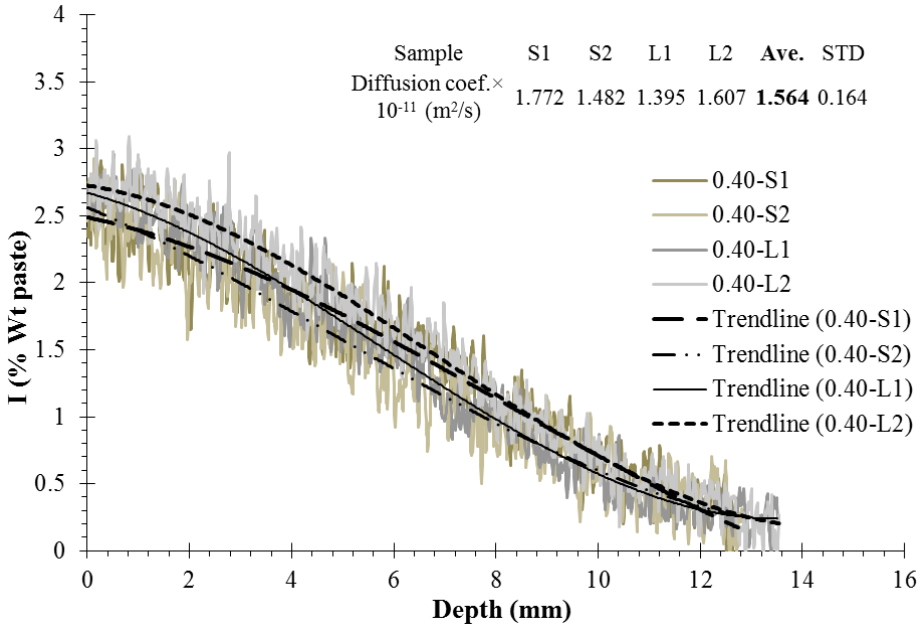

Fig. 3.S5 I concentration profiles and diffusion coefficients of samples with various diameters – w/s = 0.40. Note: The "S" and "L" letters represent small and large samples with inside diameters of 7 mm and 9.5 mm, respectively.

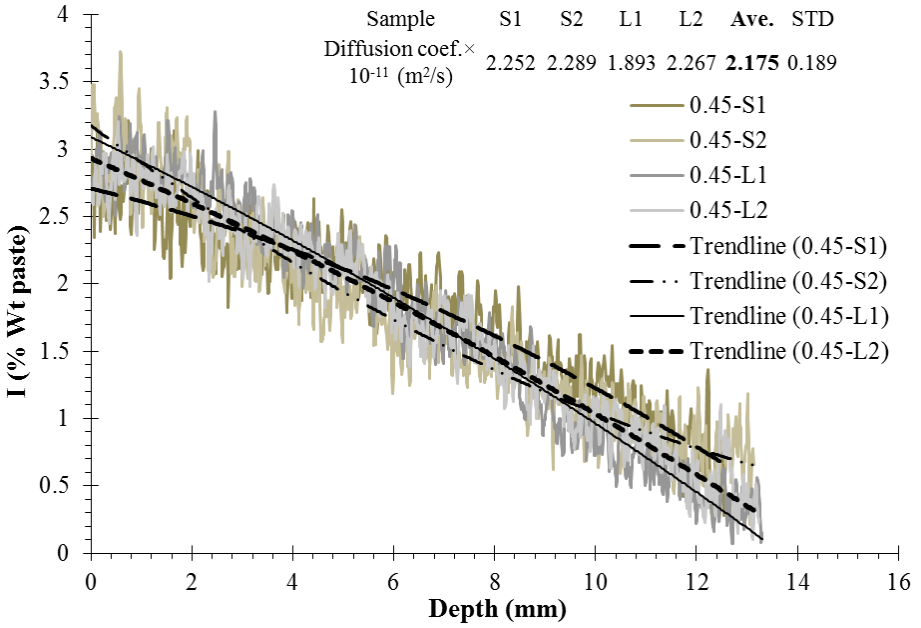

Fig. 3.S6 I concentration profiles and diffusion coefficients of samples with various diameters – w/s = 0.45. Note: The "S" and "L" letters represent small and large samples with inside diameters of 7 mm and 9.5 mm, respectively.

CHAPTER IV

QUANTITATIVE MEASUREMENT OF THE INFLUENCE OF DEGREE OF SATURATION ON ION PENETRATION IN CEMENT PASTE BY USING X-RAY IMAGING

Abstract

The external penetration of ions into cement paste plays an important role in long-term durability of concrete structures. In addition, the degree of saturation (DoS) of the paste has a large impact on rate and mechanisms of fluid penetration into the concrete. There is little knowledge of the dynamic process of fluid penetration into these materials because few experimental techniques are able to give quantitative spatial measurements of the fluid movement without damaging the sample. This paper uses laboratory transmission X-ray microscopy (TXM) to investigate the in-situ penetration of an iodide based tracer into cement paste with water-to-cement ratio of 0.40 conditioned at four different relative humidities (RH). This technique can non-destructively image the distribution of the dissolved ions at 8.8 μm resolution in minutes. In addition, micro X-ray fluorescence (μXRF) imaging and conventional gravimetric measurements were used to compare I and Cl penetration rate and validate the results from TXM. Modifications to classic diffusion models have been made to account for ion penetration in partially-saturated samples. The results show that samples conditioned in 35% and 70% RHs (DoS of 40.8% (± 0.1%) and 68.8% (± 0.5%) respectively) show a 40x and 10x increase respectively in the penetration coefficient at 2 d over the saturated sample. Furthermore, important insights about combined ion transport mechanisms have been observed from concentration profiles by TXM.

Keywords: X-ray microscopy; Iodide; Chloride; Service life; Durability; Corrosion.

4.1 Introduction

Concrete structures face many threats to their service life. A number of durability problems are caused by external fluids penetrating into cement-based materials [1-3]. These fluids can contain potentially harmful ionic species, can lead to damage from corrosion, sulfate attack, alkali silica reaction, bulk freeze thaw, and salt scaling [4]. Therefore, the ion transport properties of cement-based materials play an important role in the durability performance of concrete structures [5-6].

In addition, the degree of saturation (DoS) of concrete pores has a large impact on rate of fluid penetration into the concrete [7-11]. In partially saturated concrete, which resembles a majority of concrete in service, the ion transport is more complicated [9-11]. For concrete with very low relative humidity (RH) or low DoS, many capillary pores are empty and will draw in outside fluid from capillary action when wetted. However, more work is needed to understand how materials at different ranges of DoS or conditioned at different RHs impact this process.

The most widely used method to investigate fluid ingress into partially-saturated samples is through gravimetric measurements according to ASTM C 1585 and CEN EN 1925. This test method determines the one-dimensional rate of fluid penetration in cement-based materials by measuring the increase in the weight of a specimen as a function of time. However, this method only measures the total cumulative fluid uptake into the media and does not provide the spatial distribution of fluid in the specimen [10,12-13]. This test makes assumptions about the geometry of the concrete pore network to estimate a depth of penetration [7-8,12]. Furthermore, this method does not account for the porosity, initial DoS of the sample, and the effect of the fluid viscosity and surface tension on the penetration rate [9].

Recently, neutron and X-ray imaging techniques have been used to visualize fluid penetration in cement-based materials [6,10,12-15]. Both of these methods are based on the same principle of

radiation attenuation when passing through matter. However, X-rays interact with the electron shell of the atom while neutrons interact with the nucleus. One drawback of neutron imaging is that it requires a high energy source that is typically only available at synchrotron beamlines. This reduces the availability of the method. Neutron imaging is also sensitive to hydrogen atoms and is not able to measure specific ions. This may or may not be important depending on the information needed.

Transmission X-ray microscopy (TXM) has been used to learn more about moisture movement in cement-based materials [5-6, 10,14,16-17]. Previous studies using this method have tried to image water penetration into the paste and mortar samples [6,10,17]. Unfortunately, X-rays have a weak interaction with light atoms such as hydrogen. This limits the detection sensitivity of water in the method [6,18]. Furthermore, experiments that use TXM to investigate water ingress cannot provide spatial information about the ions and these publications have not been validated by other experimental techniques.

In this work, the moisture penetration is imaged with the aid of using potassium iodide (KI) as a tracer. Iodine is strongly X-ray attenuating because of its high atomic number. Furthermore, iodide and chloride ions are similar in size (iodide radius is 206 pm versus a chloride radius of 167 pm). This property makes iodide an excellent tracer for fluid transport study in concrete [19-22]. As the tracer penetrates into the cement paste it is possible to see the corresponding changes in X-ray absorption or gray value of the material in the radiograph. These images can be captured in less than a minute. This allows time resolved images to be taken and a rate of ion penetration can be calculated. Since this technique is non-destructive, the same sample can be monitored over time or in different conditions. The method requires minimal sample preparation and the technique can image at a spatial resolution of 200 nm to 20 μm with laboratory equipment.

This work aims to use TXM to investigate in-situ iodide penetration in paste samples with water-to-cement ratio (w/c) of 0.40. These samples were conditioned in four different RHs to examine the effect of DoS on the ion penetration progress. The penetration rate of Cl and I in paste samples was also determined gravimetrically and with micro X-ray fluorescence (μXRF) at these same conditions and compared with the TXM results. μXRF provides individual compositional maps which can be combined into a single map that simultaneously provides unique compositions and location [23-27]. Furthermore, μXRF imaging was used to compare I and Cl penetration concentration profiles in paste samples.

4.2 Experimental Methods

4.2.1 Mixture Proportion and Sample Preparation

The cement is an ASTM C 150; Type I. The chemical composition of cement with bulk XRF is provided in **Table 4.1**. The paste mixture had a w/c of 0.40 and the mixture proportion is given in **Table 4.2**. Cylindrical micro vials with inside dimension of 9.5×46 mm were used to cast the samples. A lid was used to seal each vial. Twelve samples were made for each RH condition (three samples for TXM – KI penetration, six samples for gravimetric method – KI and NaCl penetration, and three samples for measuring porosity and DoS). These samples were cured for 35 d in a sealed condition at 23°C to remove the impacts of early hydration on the measurements.

After curing, the samples were demolded and conditioned at four different RHs (0%, 35%, 70%, and 100%). The 35% and 70% RH samples were stored in sealed containers above saturated $MgCl_2$ and KI salt solutions at 23 °C according to ASTM E 104 to reach mass equilibrium, respectively. A RH sensor was used for each container to monitor and verify the RH. The samples were placed in the container and their mass was measured daily until there was less than 0.03% change in mass loss over a 24 h period, at which time it was presumed that the state of moisture

in the pore networks had sufficiently equilibrated with their environment. The 35% and 70% RH samples reached mass equilibrium after 50 d and 30 d, respectively.

The 100% RH samples were submerged in tap water inside a sealed container. The tap water was first boiled and allowed to cool to ambient temperature according to ASTM C 1202. These samples were then measured every 24 h until there was less than 0.03% mass change. This was reached after 5 d. The 0% RH samples were stored in a sealed container above saturated $MgCl_2$ solution (35% RH) at 23 °C for 40 d and then dried in an oven at 50 °C for 7 d until there was no measurable change in mass.

The samples for porosity and DoS were left in their respective environments and the 100% RH sample was kept in a sealed container within an environmental chamber at 97±1 % RH at 23 °C until testing. The other samples were sealed with wax on all sides but the finished surface. Because the samples placed at 35% RH required 50 d to reach mass equilibrium, the other samples were kept inside a sealed container at 23 °C until all samples reached 50 d. The mass of the samples was monitored during the storage before testing and the mass change was found to be negligible.

The porosity and DoS of samples was measured according to ASTM C 642, three samples from each RH condition were submerged in water and weighed after achieving the mass equilibrium, and then the weight of the saturated samples immersed in water was measured. Next, the samples were dried in an oven at 50 °C and weighed again. In all measurements, it was assumed that the sample had reached mass equilibrium when the mass change was less than 0.03% during a 24 h period. The porosity and DoS for each sample at different RH is summarized in **Table 4.3**.

Table 4.1 Chemical composition of cement with bulk XRF

Oxide content (%)	SiO_2	Al_2O_3	Fe_2O_3	CaO	MgO	Na_2O	K_2O	TiO_2	SO_3	L.O.I
Type I	20.40	5.03	2.95	62.89	2.08	0.35	0.35	0.28	3.05	2.09

Table 4.2 Cement paste mixture proportion

Mixture	water (g)	cement (g)	w/c
P-40	340	850	0.40

Table 4.3 Porosity and DoS of paste samples at different RH

RH	Porosity (%)	DoS (%)	D_i (%)*
0%	39.8 ± 0.6	0	0
35%	42.8 ± 0.6	40.8 ± 0.1	17.5 ± 0.3
70%	40.2 ± 0.1	68.8 ± 0.5	27.7 ± 0.4
100%	38.5 ± 0.2	100	38.5 ± 0.2

* D_i is the initial DoS of the sample in volume fraction.

4.2.2 In-Situ Ion Penetration Test Using TXM

After sealing, samples were placed inside a cylindrical plastic vial with dimension of 62×25 mm. A hole with diameter of 10 mm was drilled in the lid of vial to hold the sample, as shown in **Fig. 4.1**. Next, water resistant epoxy was used to properly align the sample vertically and to seal the area between the sample and hole. A small piece of aluminum wire of 0.6 mm thickness was attached to the side of the vial to help align the images. The schematic diagram of the experimental setup is shown in **Fig. 4.1**.

Next, the surface of the sample was ponded with 0.6 mol/L KI up to a level of 33±1 mm for 14 d. This KI concentration was selected based on preliminary experiments to attain suitable contrast between the KI solution and the paste. As shown in **Fig. 4.1a**, the samples were stored where the fluid penetration and gravity effects are in the same direction. This simulates fluid penetration in

flat surfaces such as bridge decks, an important application for the findings of this work. The KI solution level above the surface of samples was kept constant for all paste samples (3±1 mm). The KI solution was refreshed every 5 d to maintain a constant KI concentration. Samples were stored inside a sealed container at 23°C during the penetration testing.

A laboratory Skyscan 1172 μCT scanner was used to conduct the experiments. A radiograph was taken from the paste samples before ponding with the KI solution. This was used as a reference radiograph. Radiographs were also taken over time to track the fluid penetration into the sample. The time intervals for taking radiographs were selected according to ASTM C 1585 recommendations for gravimetric measurements. This allowed a comparison to be made between the moisture penetration into the sample and the mass change. The vial was inverted to stop the fluid penetration during the imaging as shown in **Fig. 4.1b**. Each radiograph took less than 1 min and so this should not disturb the test. Radiographs were also taken with no samples on the stage to be used to subtract the background attenuation. This also helped correct for variations in X-ray transmissions between images. The radiograph used a pixel size of 8.8 μm (2096×2096 pixels) and tube voltage and current of 100 KeV and 100 μA. A 0.5 mm Al and 0.5 mm Cu filter was used to absorb lower energy X-rays and allow high energy X-rays to interact with the sample. Acquisition time of 8 s per frame was used to collect radiographs. **Table 4.4** summarizes the TXM settings.

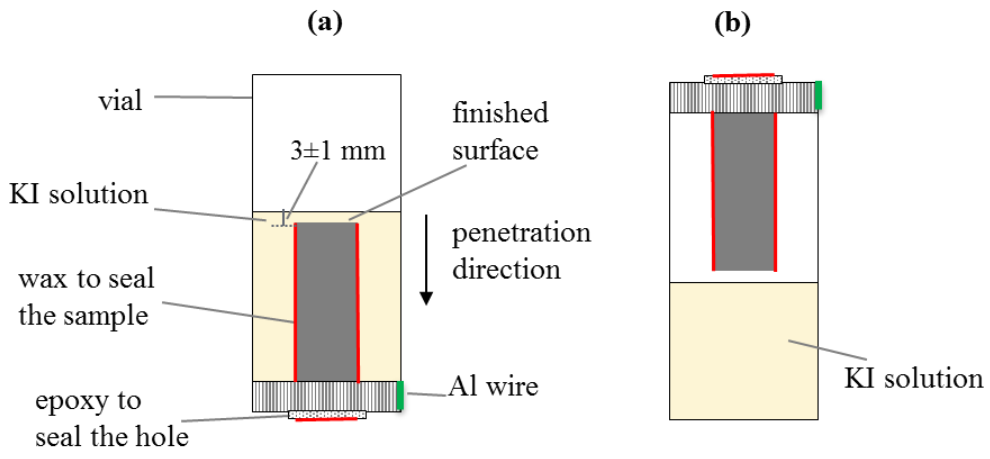

Fig. 4.1 Schematic diagram of the penetration test setup: (a) state of penetration (b) state of scan.

4.2.3 Cl and I Penetration Test Using Gravimetric Method

The same experimental setup as TXM was used to gravimetrically measure ion penetration in paste samples, but instead of radiographs, the mass of the sample was measured. The paste samples were ponded with either 0.6 mol/L KI or 0.6 mol/L NaCl solutions for 14 d to compare I and Cl ion penetration. Three samples were tested per solution. The sample was taken out of vial for the weight measurement and excess solution at the surface and sides of the sample was removed with a damp paper towel before weighing. An empty vial was used on the scale to place the sample and avoid the contact between wet surface of the sample and scale pan. The sample was immediately returned back to solution after measurement. A scale with 0.002% accuracy was used for the gravimetric measurements. The sample was polished and then analyzed with µXRF after the ponding period.

4.2.4 Cl and I Penetration Test Using µXRF

As explained earlier, the paste samples were ponded with either 0.6 mol/L KI or 0.6 mol/L NaCl solutions for 14 d to compare I and Cl ions penetration rate. After the ponding period, the investigated samples from TXM and mass change were polished for analysis with µXRF to

compare the results. Each sample was polished on a sanding belt for 2 min with 120 grit sandpaper to create a flat surface for further analysis with μXRF. Ethanol was used to remove dirt and residue from the polished surface.

The μXRF analysis was conducted using the Orbis by EDAX. The instrument uses an 80 mm^2 Silicon Drift Detector Energy Dispersive Spectrometer (SDD-EDS) and a capillary optic that produces a 50 μm diameter beam. Images are created by moving the sample under the stationary X-ray beam. The X-ray beam causes characteristic fluorescence X-rays to be emitted at each spot. **Table 4.4** summarizes the settings used by the μXRF in this work. More details can be found in other publications [23-24].

Table 4.4 Summary of TXM and μXRF settings used

parameter	TXM	μXRF
voltage (keV)	100	40
current (μA)	100	1000
filter	0.5 mm Al + 0.5 mm Cu	25 μm Al
pixel size (μm)	8.8	50
acquisition time	8 s	400 ms/pixel (dwell time)
chamber condition	air	Vacuum
dead time	-	maximum of 20%

4.2.5 TXM Data Analysis

First, the radiographs of the air were subtracted from sample scans to remove the background attenuation effects. Next, an average gray value profile was calculated through the sample depth. Ten scan lines were randomly used that were perpendicular to the surface of the sample. Each line was located at the middle 40% (4 mm) of the sample to avoid beam hardening and to keep the analyzed region at an almost constant depth. Next, each time series radiograph is subtracted from the radiograph before solution was added to the sample. This allowed the change in the gray value to be easily observed and the spatial changes due to absorption from the I to be

mapped. The Beer-Lambert Law (**Eq. (4.1)**) [20-21] was used to calculate a change in attenuation due to I ($\Delta\mu$) at different depths of sample.

$$(\Delta\mu)_x = \ln(I_{ref})_x - \ln(I_t)_x \quad (4.1)$$

Where $(I_{ref})_x$ is the transmitted X-ray intensity (gray value) at depth x on the reference profile and $(I_t)_x$ is the transmitted X-ray intensity at the same location at a future time. The fluid accessible porosity and the sample thickness are not included in **Eq. (4.1)** since these parameters are constant for each sample. More details can be found in other publications [28-29].

Next, to determine I concentration profiles a set of reference standards with different KI concentrations added to the cement paste while mixing were used to develop a calibration curve. The same sample size, mixtures, curing procedure, and scan setup were used to prepare and investigate the calibration samples for TXM. Next, the same paste calibration samples were polished and then analyzed with µXRF to develop a calibration curve for that technique. This also allowed an independent method to be used to validate the TXM results. In addition, a set of paste standards were made with different NaCl concentrations in order to convert Cl counts from µXRF to concentrations. The calibration curves are included in the supplementary section (**Figs 4.S1** and **4.S2**).

4.2.6 µXRF Data Analysis

A Matlab code was used to analyze the spatial and compositional data. A border detection algorithm was then used to find the top surface of the sample. The sample is then separated into 0.50 mm layers of equal thickness from the surface of the sample through the entire depth. The average I and Cl counts in each layer can then be plotted for different depths. Next, the calibration curves are used to convert I and Cl counts to concentrations. Additional details can be found in previous publications [23-24].

4.2.7 Gravimetric Data Analysis

According to ASTM C 1585, the penetration rate is the change in mass divided by the product of the exposed area of the sample and density of water, as formulated in **Eq. (4.2)**.

$$I = \frac{\Delta m}{A \times \rho_w} \qquad (4.2)$$

where I is the penetration rate; Δm is the change in sample mass; A is the exposed area of the sample; and ρ_w is the density of water.

However, this equation does not account for the porosity and initial DoS of the sample. In addition, it does not consider the effect of fluid viscosity and surface tension on the penetration rate. Therefore, this equation is not directly applicable to salt solutions [9,30]. Farnam et al. [30] proposed a modified equation (**Eq. (4.3))** to estimate the intrinsic penetration rate of the sample exposed to salt solution.

$$I_i = \frac{\Delta m}{A \times \rho_s \times \Phi(1 - D_i)} \times \sqrt{\frac{\gamma_w \times \eta_s}{\gamma_s \times \eta_w}} \qquad (4.3)$$

where I_i is the intrinsic penetration rate (this value is frequently interpreted as the depth of fluid penetration in the sample); ρ_s is the density of solution; Φ denotes the porosity of the sample in volume fraction; D_i is the initial degree of saturation of the sample in volume (See **Table 4.3**); γ_w and γ_s are the surface tensions of water and solution, respectively; and η_w and η_s represent the viscosity of water and solution, respectively. In the current study, **Eq. (4.3)** was used to find the depth of fluid penetration based on the gravimetric measurements and compare to the TXM measurements. The density, viscosity, and surface tension for water and NaCl was obtained from [31-32], and KI from [33]. These values are summarized in **Table 4.5**.

In addition, a linear regression analysis was used to find the intrinsic penetration rate versus square root of time with **Eq. (4.4)** to determine the sorptivity of the samples [7,34]. For the regression analysis, all data points from 1 min to 6 h were used.

$$I_i = S \times \sqrt{t} + B \qquad (4.4)$$

where S is the sorptivity coefficient; t denotes the time; and B is a correction term added to account for surface effects when the sample comes in contact with the solution.

Table 4.5 Density, viscosity, and surface tension of solutions [31-33]

Solution	density (g/cm^3)	viscosity (μPa.s)	surface tension $\times 10^{-6}$ (N/mm)
KI	1.070	949.48	73.5
NaCl	1.023	945.74	72.8
Water	0.997	890.30	71.8

4.2.8 I and Cl Penetration Coefficient

Fick's second law for diffusion, as shown in **Eq. (4.5)** [35].

$$\frac{\partial C}{\partial t} = D_c\left(\frac{\partial^2 C}{\partial x^2}\right) \qquad (4.5)$$

where x is distance from sample surface; t denotes time; D_c is diffusion coefficient; C_s is surface ion concentration; and $C_{(x,t)}$ represents ion concentration at the depth of x from the surface after time t.

A general solution to the equation is given in **Eq. (4.6)**.

$$C_{(x,t)} = C_s\left(1 - \mathrm{erf}\left(\frac{x}{2\sqrt{D_c \times t}}\right)\right) \qquad (4.6)$$

$$C_{(x,0)} = 0 \quad x > 0, \quad C_{(0,t)} = C_s \quad t \geq 0$$

where x is distance from sample surface; t denotes time; C_s is surface ion concentration; $C_{(x,t)}$ represents ion concentration at the depth of x from the surface after time t; and erf is the error function and D_c is the diffusion coefficient in a fully saturated sample.

Both **Eq. (4.5)** and **(4.6)** assume that the porous material is fully saturated; the ion concentration at the exposure surface is constant; and there is no impact of co-existing ions. In addition, this equation does not take into account the effect of other ion penetration mechanisms such as capillary absorption. Although all these assumptions were made in the derivation of these models they may still be useful where diffusion plays a significant role in the penetration of outside ions.

In the case of 0%, 35%, 70%, 100% RH samples, a nonlinear regression was conducted on I and Cl profiles from TXM and μXRF with a modified version of **Eq. (4.6)** that is shown in **Eq. (4.7)**. First, the diffusion coefficient (D_c) was replaced with a term called the penetration coefficient (P_c). These terms primarily controls the slope of the line describing the concentration versus depth into the sample. This term has been renamed because the penetration of the outside ions is controlled by a combination of mechanisms and not just diffusion. Next, a constant value, known as the absorption coefficient (A_c), was added that can account for the initial uptake or absorption of the fluid into the samples. The absorption coefficient was zero for all samples except for the 0% RH sample. Because the 0% RH samples required a combination of both the absorption coefficient (a constant value) and the penetration coefficient (value that controls the slope), the P_c for the 0% RH sample is not able to be compared with the P_c of the other samples. This is likely caused by the vastly different mode of ion transport in this sample. This will be an area of future research.

$$C_{(x,t)} = C_s\left(1 - \mathrm{erf}\left(\frac{x}{2\sqrt{P_c t}}\right)\right) + A_c \qquad (4.7)$$

4.3 Results and Discussion

4.3.1 Comparison of TXM Results with µXRF

This section aims to verify findings from TXM with µXRF. **Figure 4.2** shows a comparison between concentration profiles from µXRF and TXM for paste samples with different DoS after 14 d of ponding with 0.6 M KI solution. In addition, the calculated P_c for I and percent difference from both methods based on **Eq**. **(4.7)** are summarized in **Table 4.6**. Based on **Fig. 4.2**, the two techniques show a good correlation. The difference between the P_c for I from TXM and µXRF was on average 4% for paste samples conditioned in different RHs. This shows that there is good agreement between µXRF and TXM for investigated samples and conditions. In addition, a two tail t-test with the assumption of unequal variances was conducted to compare the mean P_c of the two methods. Based on this analysis, the difference between means was not significant (p-value= 0.93 >> 0.05). This suggests that these two methods provide statistically comparable results.

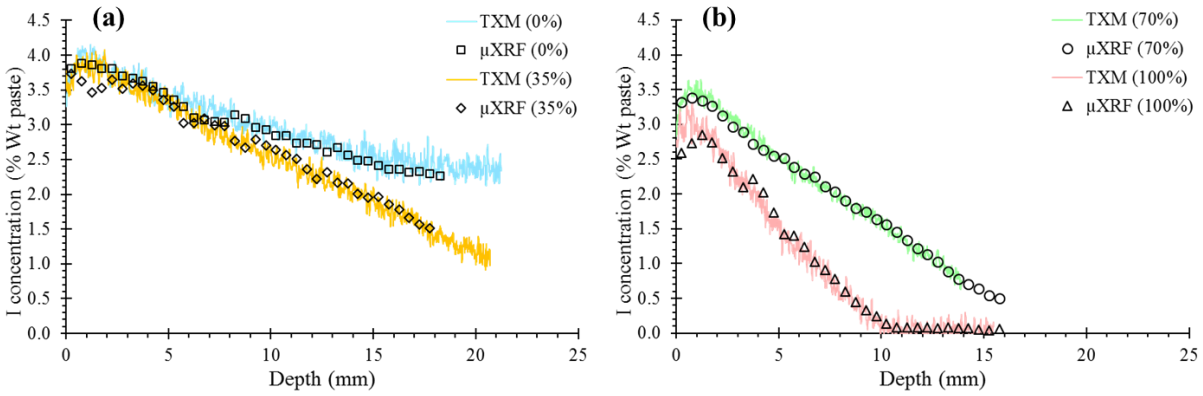

Fig. 4.2 Comparison of TXM results with results from µXRF for paste samples with w/c of 0.40 conditioned in: (a) 0% and 35% RHs (b) 70% and 100% RHs.

Table 4.6 Comparison between I penetration coefficients from TXM and μXRF

Sample	TXM Pen Coef×10^{-11} (m^2/sec)	R^2	μXRF Pen Coef×10^{-11} (m^2/sec)	R^2	% Difference $\frac{(TXM - \mu XRF)}{\mu XRF \times 0.01}$
0%	6.62	0.95	6.56	0.99	0.9
35%	16.13	0.98	17.92	0.99	-10
70%	5.86	0.99	5.89	0.99	-0.5
100%	1.41	0.98	1.47	0.98	-4

4.3.2 Comparison of the I and Cl Penetration Rate

Figure 4.3 shows a comparison between KI and NaCl intrinsic penetration rate by gravimetric measurements of the paste samples with w/c of 0.40 conditioned at different RH and ponded with 0.6 M KI and 0.6 M NaCl solutions for 14 d. In addition, the calculated sorptivity coefficients from the initial penetration versus square root of time by using **Eq. (4.4)** are summarized in **Table 4.7**. Based on **Fig. 4.3**, there is a similar penetration rate for both the KI and NaCl samples with matching DoS. The average difference between the calculated KI and NaCl sorptivity coefficients of different samples is about 15%. KI showed higher sorptivity in samples with lower DoS compared to NaCl. However, the initial penetration rate of KI is lower than NaCl in the case of paste samples with higher DoS (e.g. 70% and 100% RH samples). This can be attributed to the differences in fluid properties such as surface tension.

In addition, the I and Cl concentration profiles of samples from μXRF after 14 d ponding with 0.6 M KI and 0.6 M NaCl solutions are shown in **Fig. 4.4**. The calculated I and Cl penetration coefficients from concentration profiles by using **Eq. (4.7)** are summarized in **Table 4.8**. The average difference between the calculated I and Cl penetration coefficients of different samples is about 6%. Because of the differences in fluid properties, size and ionic mobility we would not expect the penetration rate to be the same for these two different ions. Overall, I shows a similar

penetration performance to Cl in paste samples with different DoS and serves as a satisfactory substitute to understand ion penetration.

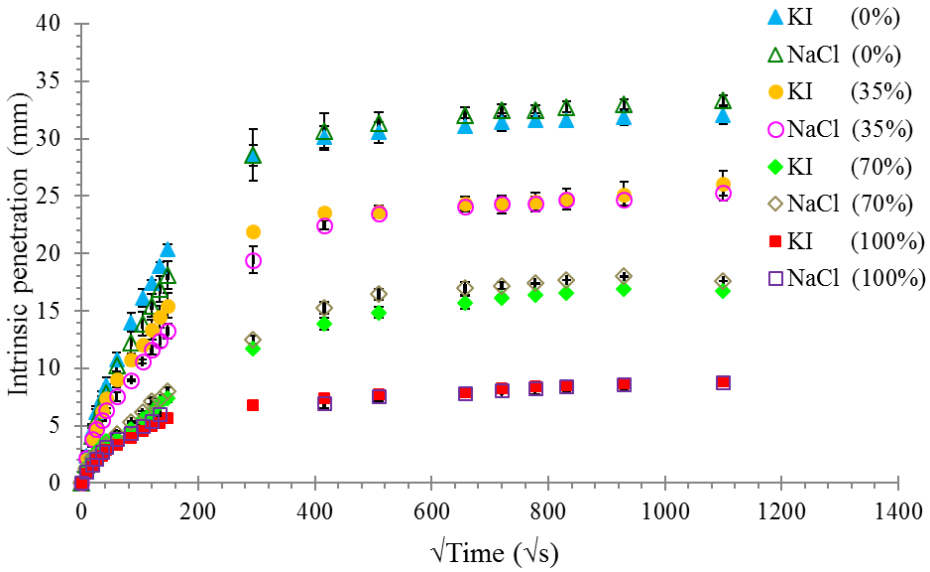

Fig. 4.3 Time-dependent KI and NaCl intrinsic penetration rate in paste samples with w/c of 0.40 conditioned in different RHs by gravimetric method.

Table 4.7 Comparison between KI and NaCl sorptivity coefficients from gravimetric method

RH	parameter	KI	NaCl	% difference (KI-NaCl) /NaCl×0.01
0%	S (mm/√s)	0.123	0.1096	**12.23**
	B (mm)	2.835	2.501	**13.35**
	R^2	0.99	0.98	
35%	S (mm/√s)	0.0902	0.0742	**21.56**
	B (mm)	2.686	2.66	**0.98**
	R^2	0.98	0.99	
70%	S (mm/√s)	0.0392	0.0469	**-16.42**
	B (mm)	1.593	1.256	**26.83**
	R^2	0.99	0.99	
100%	S (mm/√s)	0.0325	0.0369	**-11.92**
	B (mm)	1.129	1.227	**-7.99**
	R^2	0.97	0.97	

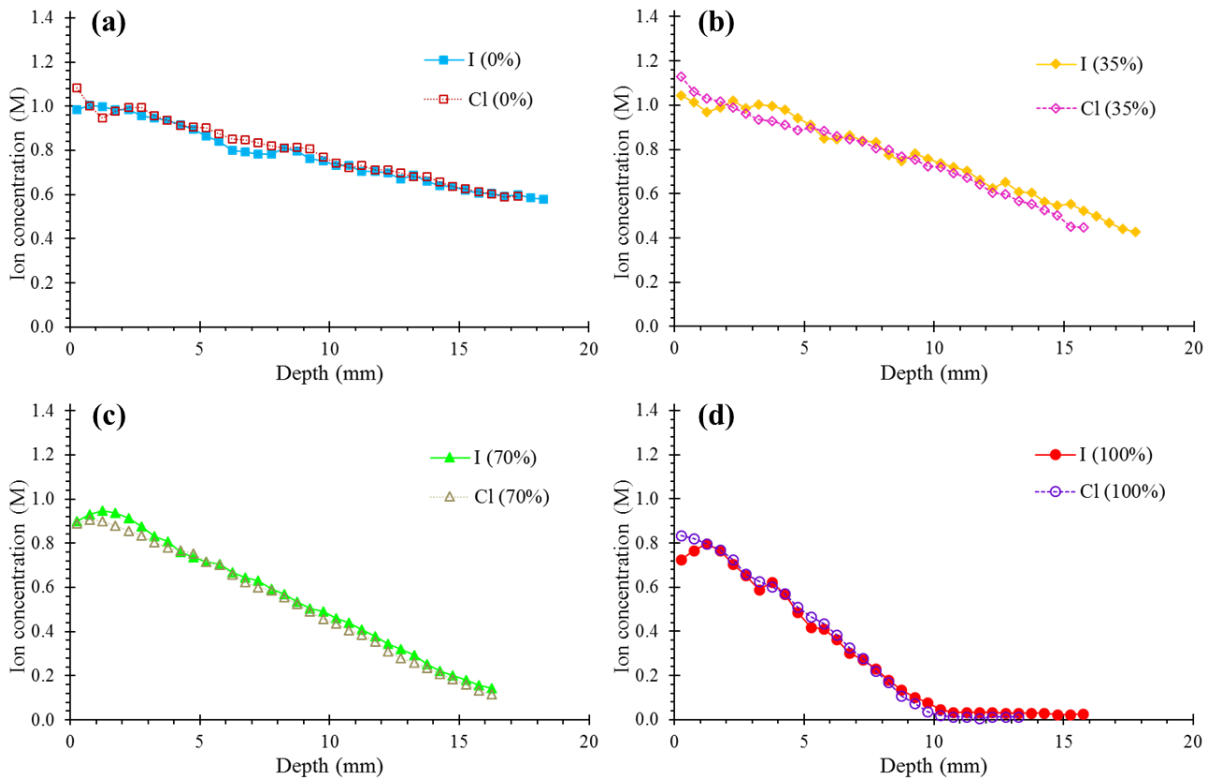

Fig. 4.4 Comparison of I and Cl concentration profiles in paste samples with w/c of 0.40 conditioned in: (a) 0% RH (b) 35% RH (c) 70% RH (d) 100% RH from µXRF after 14 d of ponding with 0.6 M solution.

Table 4.8 Comparison between I and Cl penetration coefficients from µXRF after 14 d of ponding with 0.6 M solution

Sample	I Pen Coef×10^{-11} (m^2/sec)	R^2	Cl Pen Coef×10^{-11} (m^2/sec)	R^2	% Difference $\frac{(I - Cl)}{Cl \times 0.01}$
0%	6.56	0.99	7.72	0.99	-15
35%	17.92	0.99	17.76	0.98	0.9
70%	5.89	0.99	6.13	0.98	-3.9
100%	1.47	0.98	1.55	0.97	-5

4.3.3 Comparison of I Penetration Depth and Concentration Profiles Over Time by TXM

Figs 4.5 to **4.13** compare the I penetration and concentration profiles of the paste samples after 5 min, 30 min, 1 h, 2 h, 6 h, 1 d, 5 d, 8 d and 14 d of ponding with the KI solution. The depth of

penetration was estimated by reporting where the I concentration was greater than 0.10 % weight of the paste (≈ 0.14 % weight of the cement). This value was chosen so that it was statistically greater than background I concentration found at inner depths of the samples where the solution has not penetrated. This data shows that TXM is capable of providing time-series penetration depths and concentration profiles with high spatial resolution. Because of the high resolution of the data, the I profile can be measured within minutes of adding the material to the surface.

Based on **Figs 4.5** to **4.13**, all paste samples showed initial absorption within 2 mm to 4 mm of the surface after 5 min of ponding. However, the rate of I penetration in samples with lower DoS (0% and 35% RH) is much higher than samples with higher DoS with time. The 0% and 35% RH samples showed 3.5x more penetration than the 100% RH samples after 1 h of ponding. The I penetrated for the 0% and 35% RH samples was observed over the entire scan depth (≈ 20 mm) after only 6 h of ponding. After 14 d of ponding the I penetration of the 100% RH sample reached ≈ 11.5 mm. This highlights the change in ion transport with different saturation levels. The low DoS samples will have a higher number of empty pores. These empty pores will create greater capillary forces that draw the fluid into the sample. Modeling efforts are underway and will be presented in future publications.

In addition, the non-destructive nature of TXM enables us to visualize and quantify the combined transport mechanisms at early ages. Based on **Figs 4.5** to **4.13**, the concentration profiles can be categorized into three different types of transport: diffusion-based profiles (e.g. profiles of 100% RH sample); absorption-based profiles (e.g. profiles of 0% RH samples at early ages; **Fig. 4.5**); and profiles from combined transport mechanisms (e.g. profiles of 35% RH and 75% RH samples).

Figure 4.14 provides an overview of the ion penetration for the 0% RH sample. There is a constant I concentration following the ion penetration front. The initial ion penetration is likely

caused by capillary absorption. This occurs at the onset of ion penetration into the sample and is described by a front progressing through the sample. Following this region, the concentration profile seems to change so that there are two modes of ion penetration. It is interesting that the 0% RH and the 35% RH samples have almost the same ion concentration from the sample surface until 4 mm from the surface for all of the time periods investigated. This can be due to higher capillary forces at surface of these samples resulting from the lower DoS.

The 35% RH and 70% RH samples show an almost linear slope over the depth of penetration. This shape is different from pure ionic diffusion and could be caused by a mixed mode of ion transport from diffusion and capillary absorption. The 100% RH sample shows a more typical diffusion shaped curve. A comparison between the calculated P_c of samples with different degree of saturations will be discussed later in the paper.

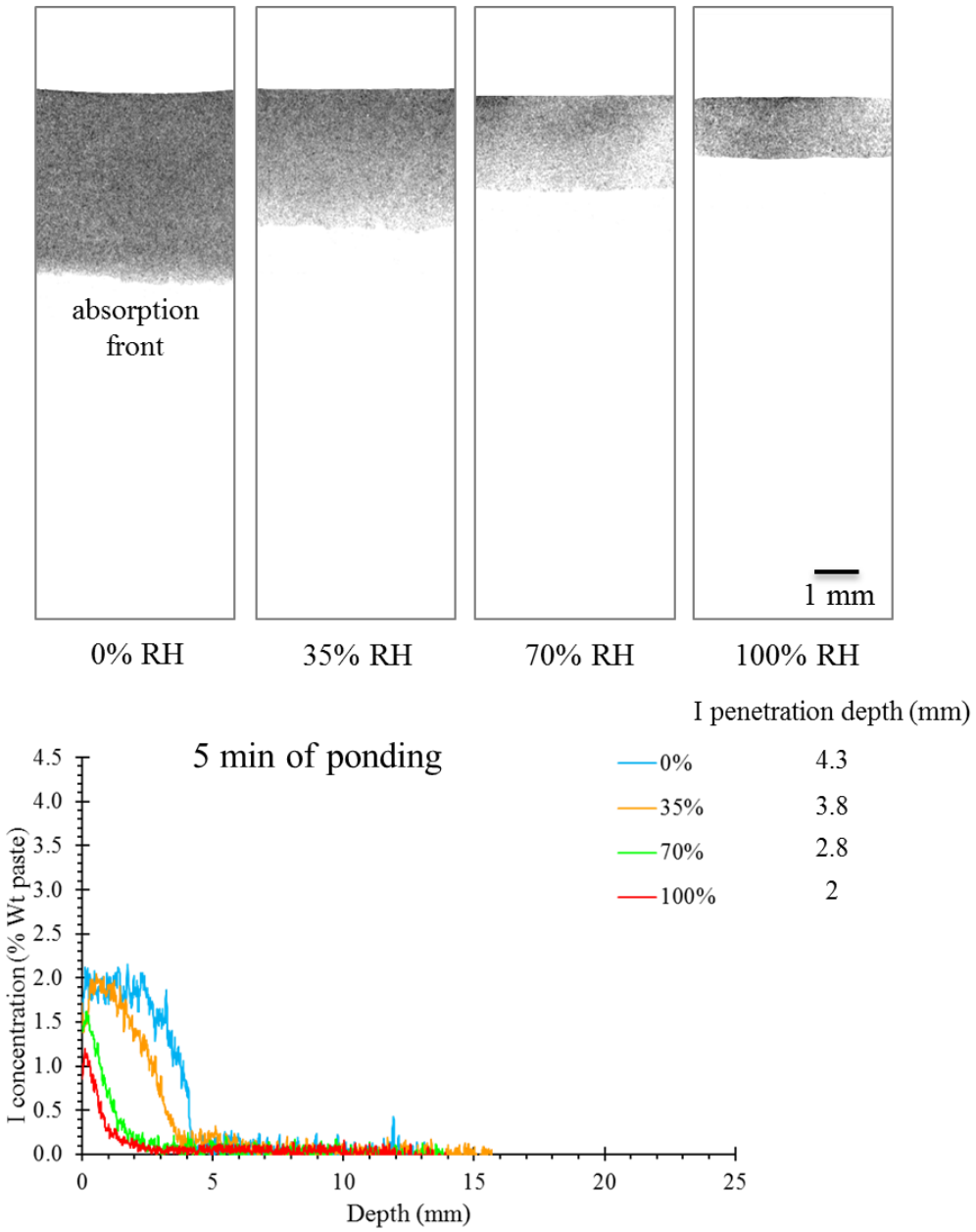

Fig. 4.5 TXM comparison of I penetration in different RH after 5 min ponding.

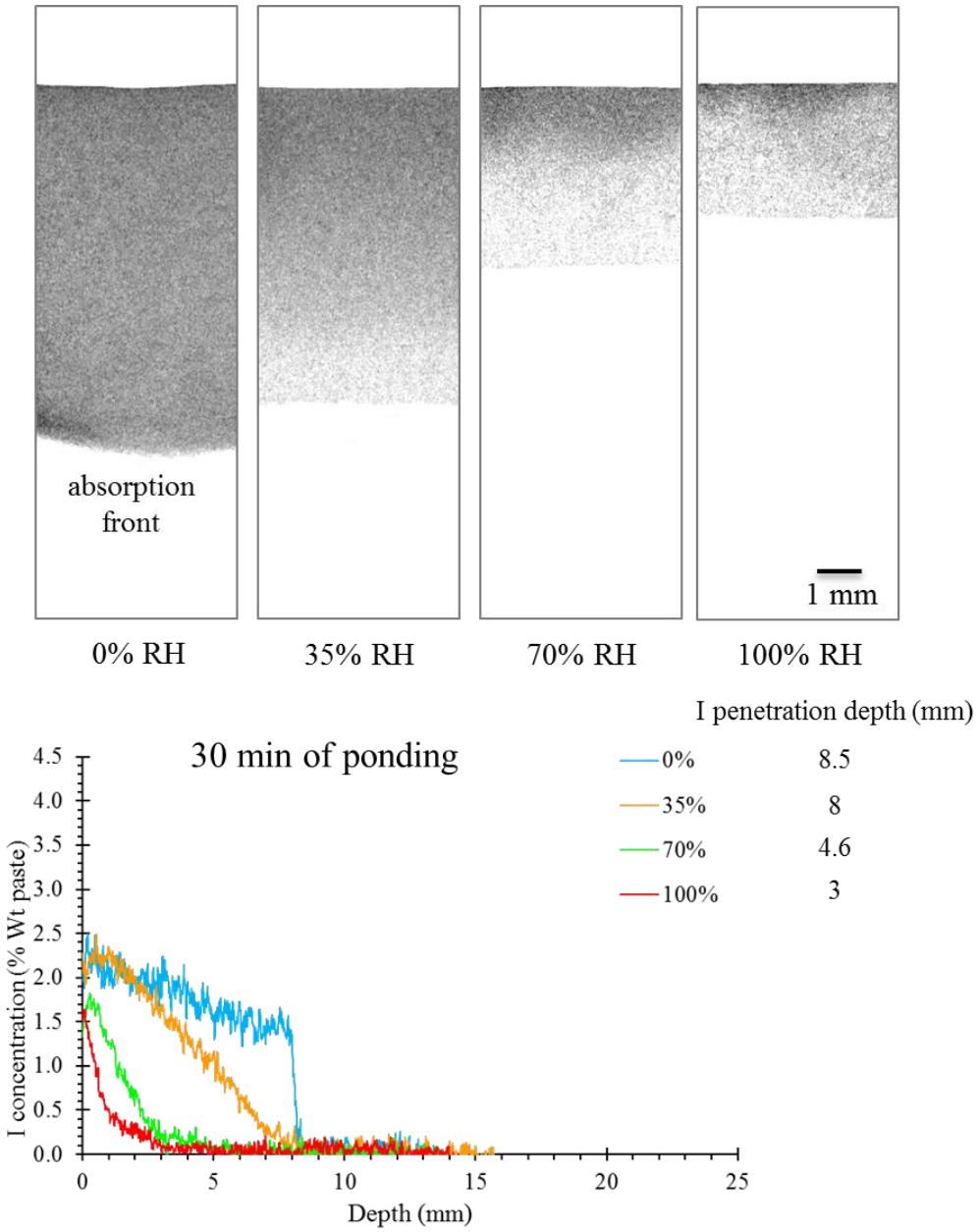

Fig. 4.6 TXM comparison of I penetration in different RH after 30 min ponding.

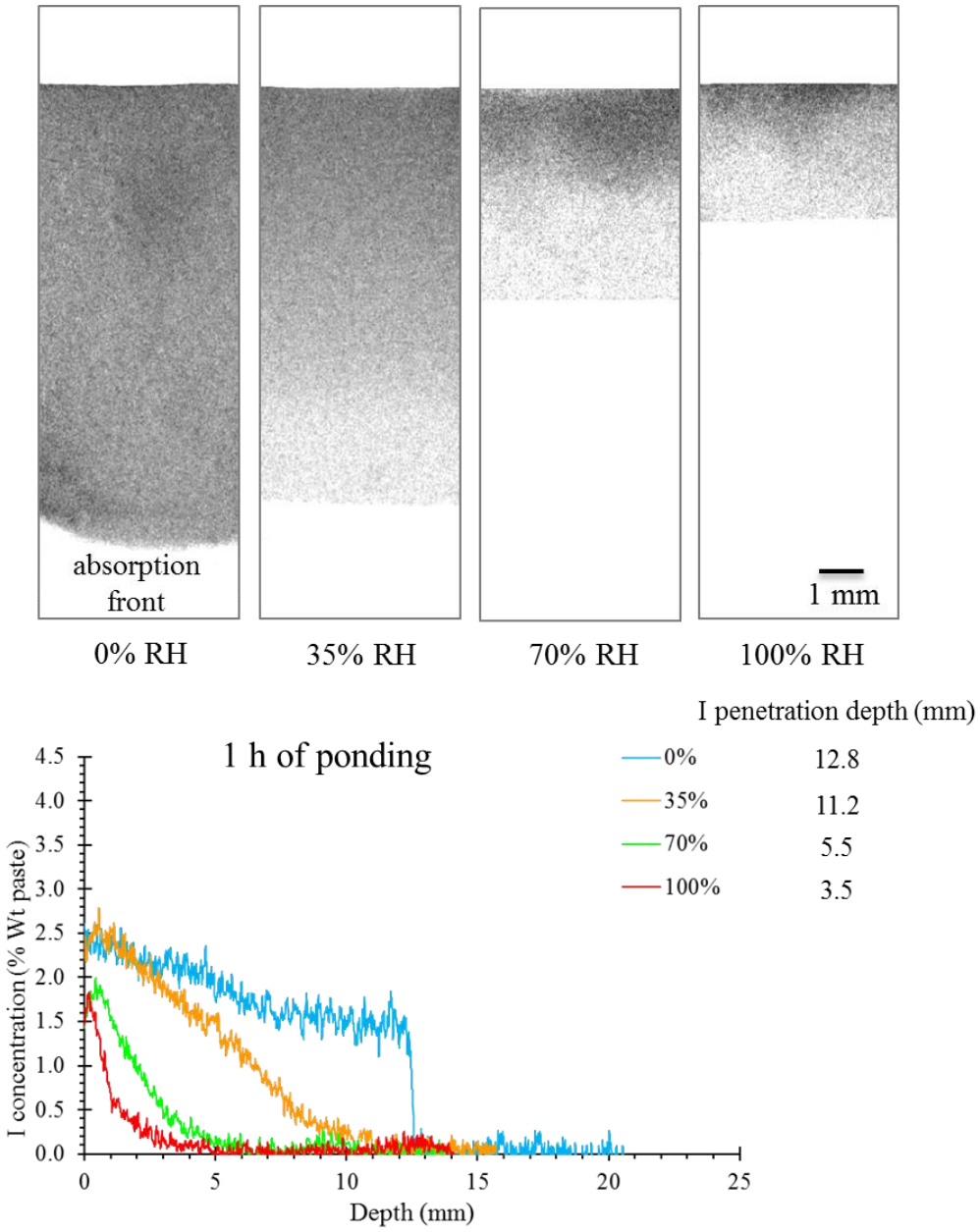

Fig. 4.7 TXM comparison of I penetration in different RH after 1 h ponding.

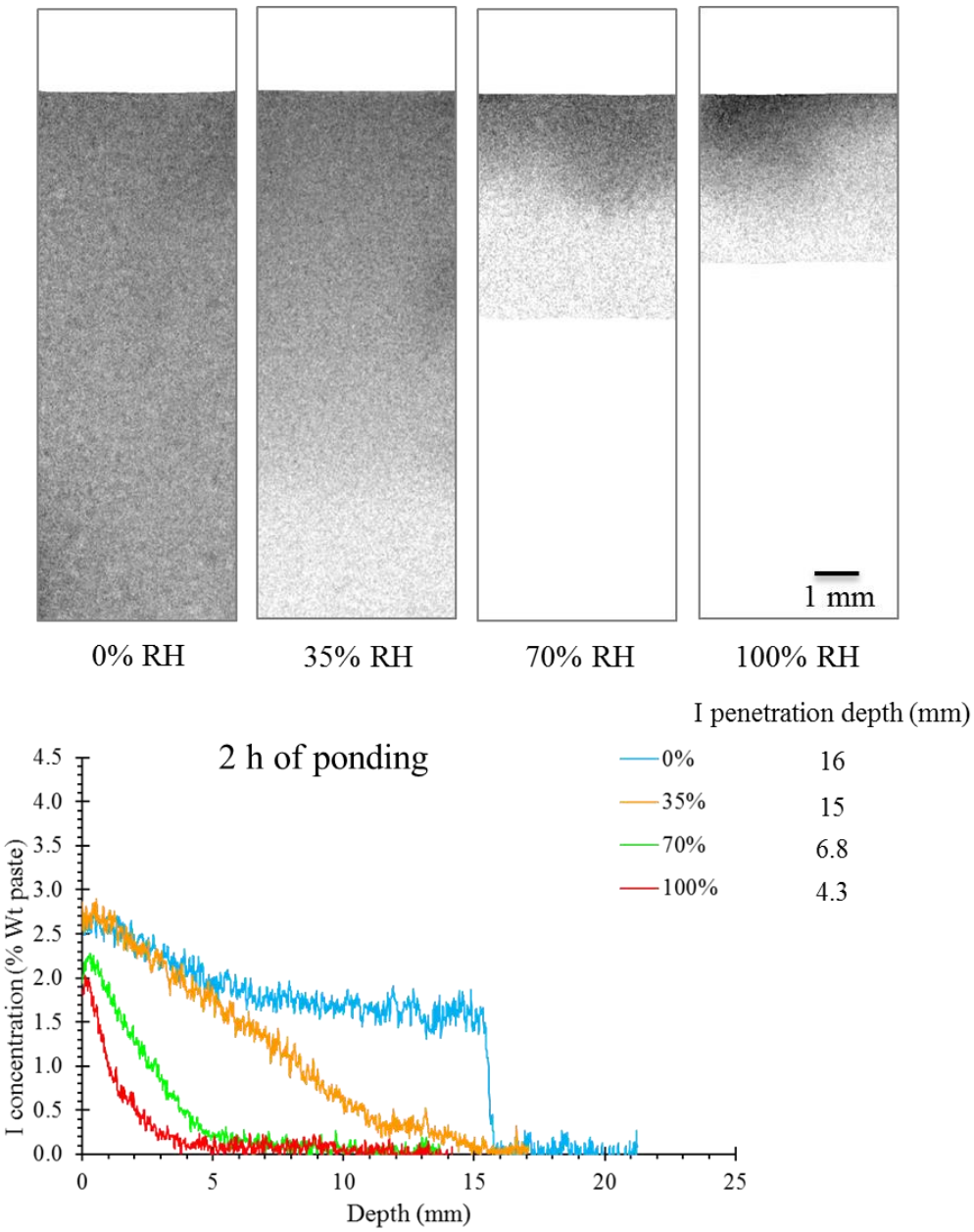

Fig. 4.8 TXM comparison of I penetration in different RH after 2 h ponding.

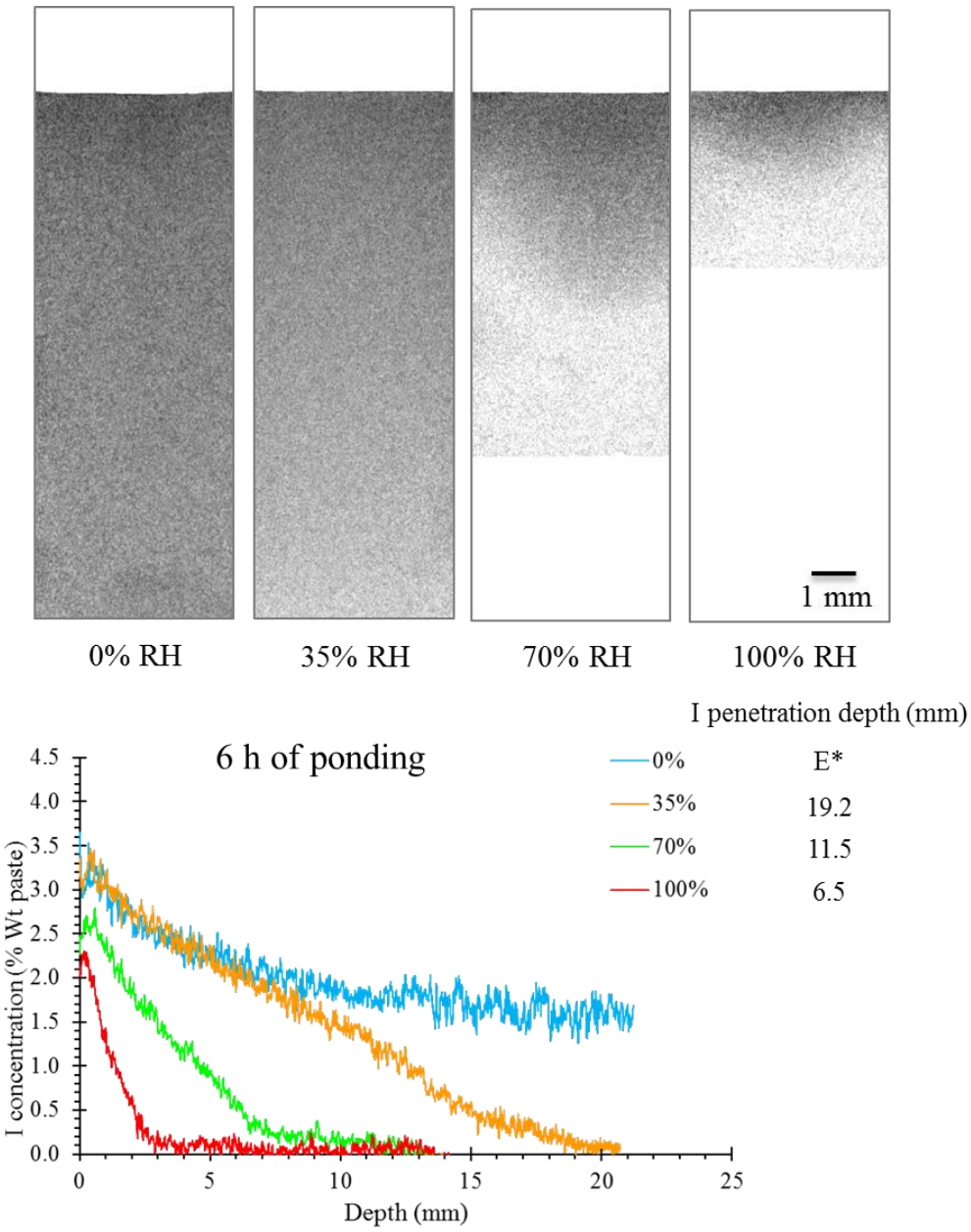

Fig. 4.9 TXM comparison of I penetration in different RH after 6 h ponding. *The ion penetrated through the entire scan depth.

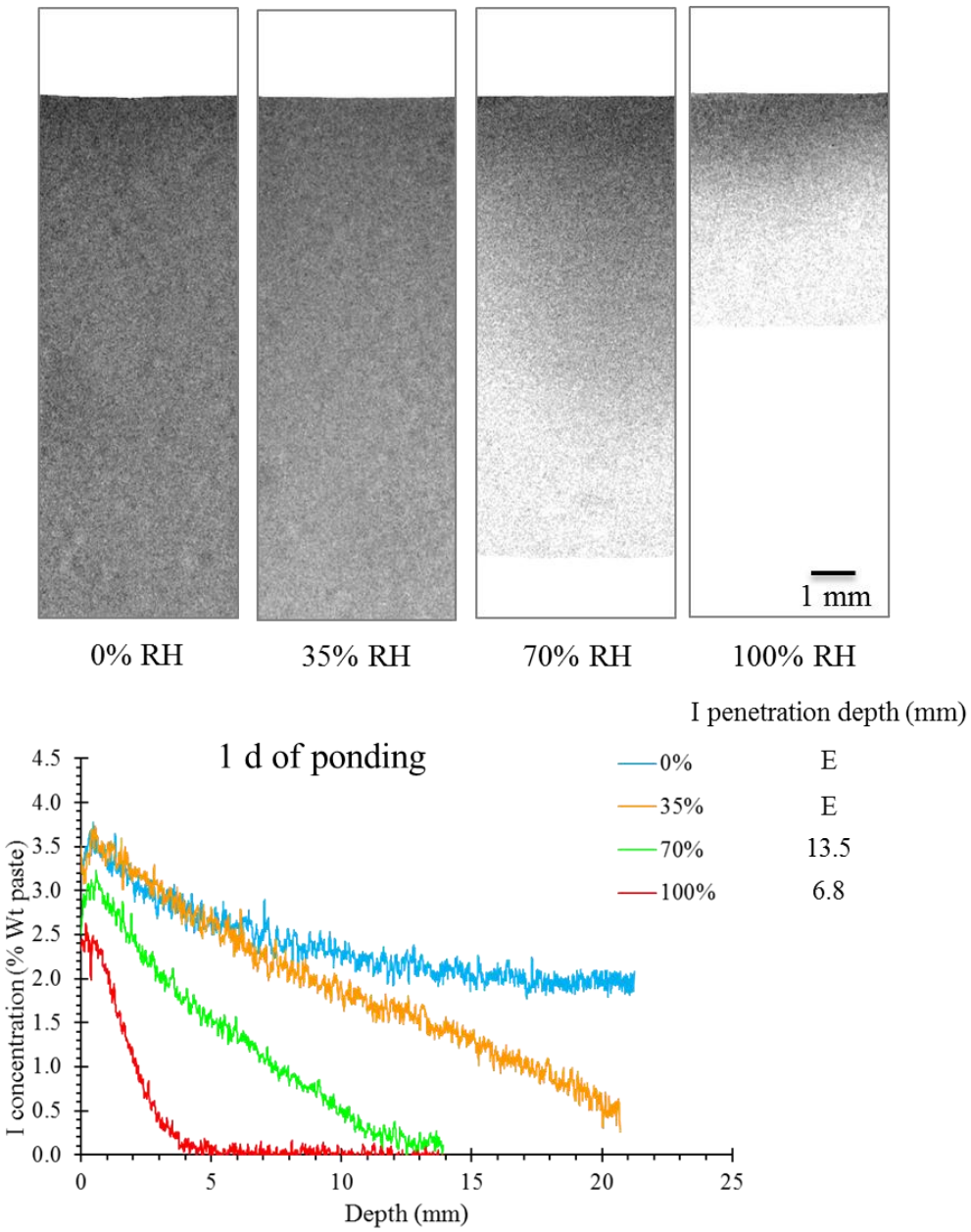

Fig. 4.10 TXM comparison of I penetration in different RH after 1 d ponding.

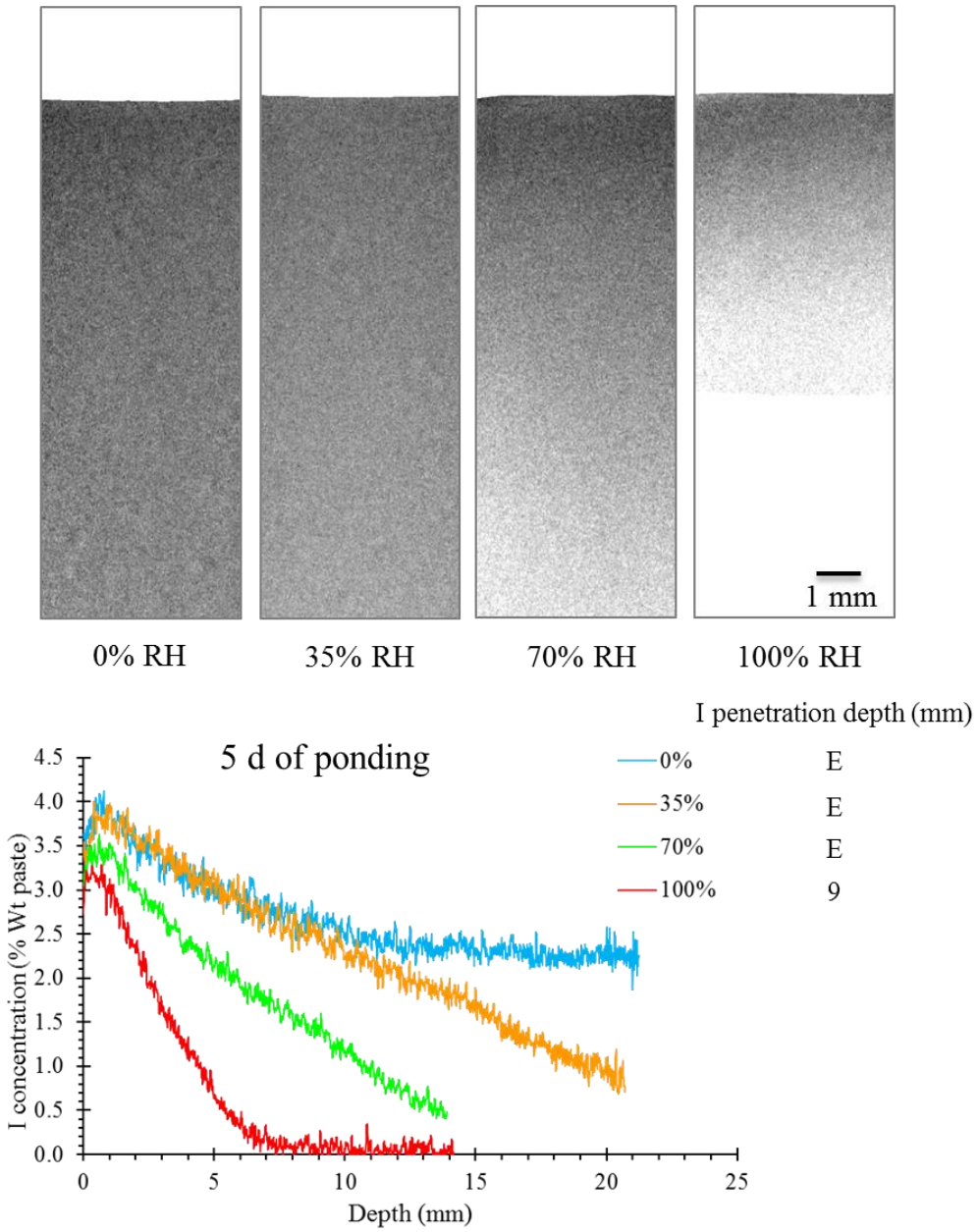

Fig. 4.11 TXM comparison of I penetration in different RH after 5 d ponding.

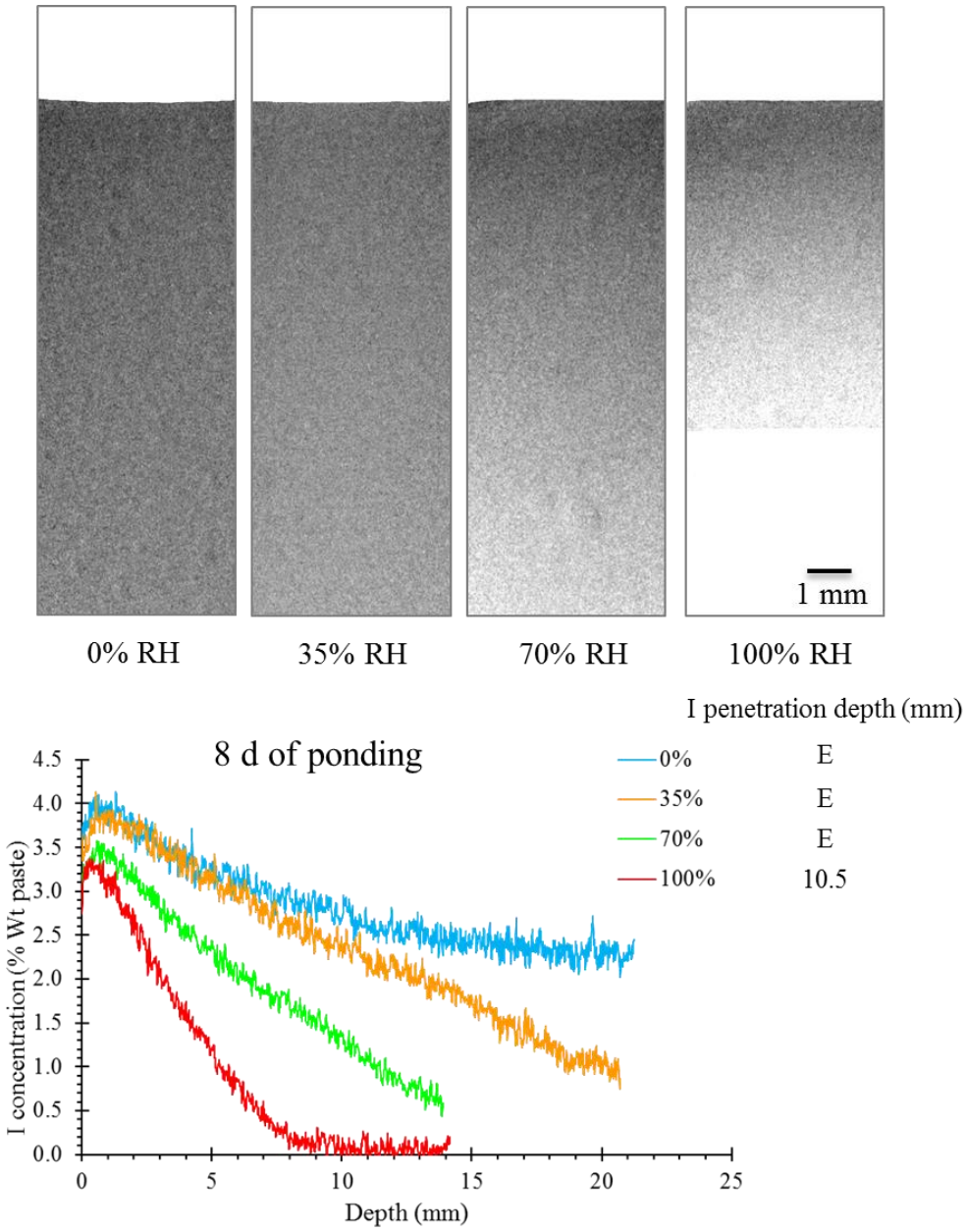

Fig. 4.12 TXM comparison of I penetration in different RH after 8 d ponding.

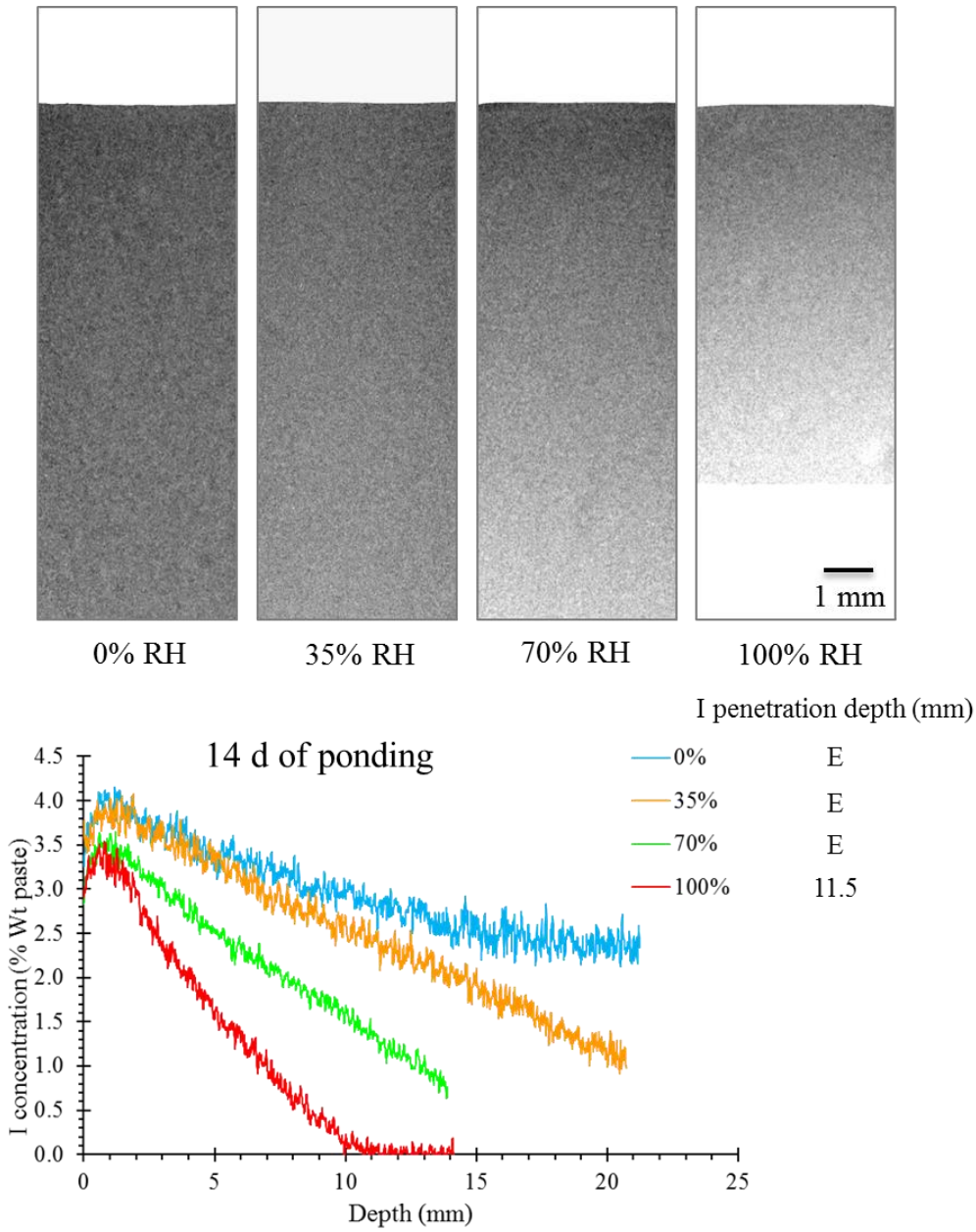

Fig. 4.13 TXM comparison of I penetration in different RH after 14 d ponding.

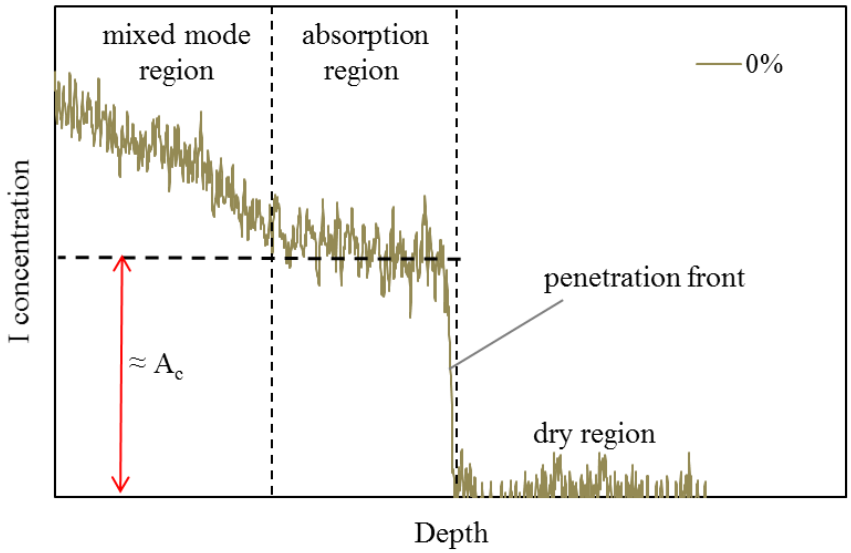

Fig. 4.14 An example of two modes I penetration in dry sample.

4.3.4 Comparison of TXM Results with Gravimetric Method

Figure 4.15 compares the I penetration depths from TXM with calculated penetration depths from gravimetric measurements based on **Eq. (4.3)** over the first 6 h of ponding. In addition, the calculated sorptivity coefficients from both techniques based on **Eq. (4.4)** are summarized in **Table 4.9**. Based on **Fig. 4.15**, **Eq. (4.3)** underestimates the estimated penetration depth when compared to the measured penetration depths from TXM. These differences show an even wider variation over time. This difference is about 23% on average for samples with different degree of saturations after 6 h of ponding. In addition, the average difference between the calculated sorptivity coefficients and the correction constants (B) of different samples from TXM and gravimetric method is about 25%. Again, the gravimetric method underestimates the sorptivity coefficient in all of samples conditioned in different RHs compared to TXM results. Consequently, the use of these equations would overestimate the service life of concrete structures. This difference can be attributed to the generalized assumptions made in **Eq. (4.3)** such as simplified capillary pore structure.

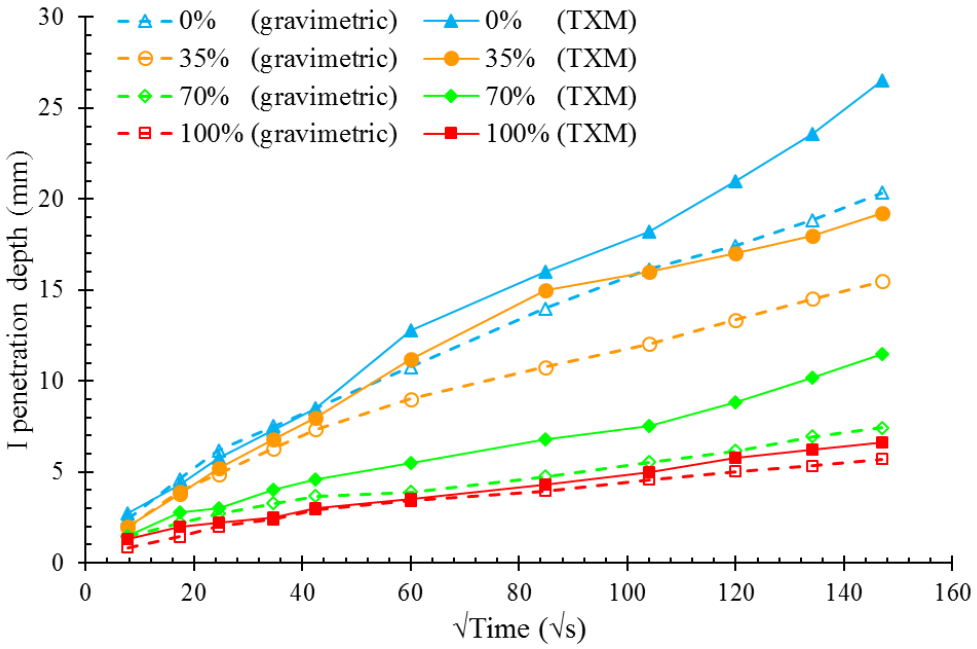

Fig. 4.15 Comparison between I penetration depths from TXM and gravimetric method.

Table 4.9 Comparison between I sorptivity values from TXM and gravimetric method

RH	parameter	gravimetric	TXM	% difference (GV-TXM) /(TXM×0.01)
0%	S (mm/√s)	0.123	0.1653	**-25.59**
	B (mm)	2.835	1.672	**69.56**
	R^2	0.99	0.99	
35%	S (mm/√s)	0.0902	0.1229	**-26.61**
	B (mm)	2.686	2.431	**10.49**
	R^2	0.98	0.97	
70%	S (mm/√s)	0.0392	0.0645	**-39.22**
	B (mm)	1.593	1.467	**8.59**
	R^2	0.99	0.99	
100%	S (mm/√s)	0.0325	0.0369	**-11.92**
	B (mm)	1.129	1.253	**-9.89**
	R^2	0.97	0.99	

4.3.5 Time-dependent I Penetration Coefficient

Figure 4.16 displays time-dependent I P_c based on **Eq. (4.7)** for cement paste samples conditioned at 35%, 70%, and 100% RH from TXM. As explained earlier, the calculated P_c considers the combined effect from capillary absorption and diffusion in partially-saturated samples. The calculated P_c and A_c of the 0% RH sample based on **Eq. (4.7)** is shown in **Fig. 4.17** over time. Based on **Fig. 4.16**, the P_c of 35% RH sample is about 40x the sample conditioned in 100% RH at 2 d of ponding. This ratio decreases over time and reaches 11x after 14 d of ponding. The 70% RH sample also has a higher P_c when compared to 100% RH sample ($P_{c,(70\%)}$ / $P_{c,(100\%)}$ = 10 at 2 d of ponding). This can be caused by the early age combined transport mechanisms in partially-saturated samples. This highlights the importance of DoS in ion transport into cement-based materials.

As shown in **Fig. 4.17**, the ratio of P_c of 0% RH to P_c of 100% RH is about 12 at 2 d of ponding. This ratio decreases to 4 after 14 d of ponding. As mentioned earlier, the calculated P_c of 0% RH sample based on **Eq. (4.7)** does not take into account the effect of capillary absorption. Therefore, the calculated P_c for 0% RH sample is not directly comparable with P_c of other partially-saturated samples. Furthermore, the calculated P_c of 0% RH sample shows a decreasing rate until 7 d of ponding, then it starts to slightly increase from 7 d to 14 d of ponding. The A_c constant, which accounts for the effect of capillary absorption, also decreases from 7 d to 14 d of ponding. This could be caused by a change from capillary absorption to diffusion in the 0% RH samples after 7 d of ponding. It has been reported that capillary forces decreases after 24 h from ponding resulting from the increasing DoS and further penetration of ions occurs as a result of diffusion process [34].

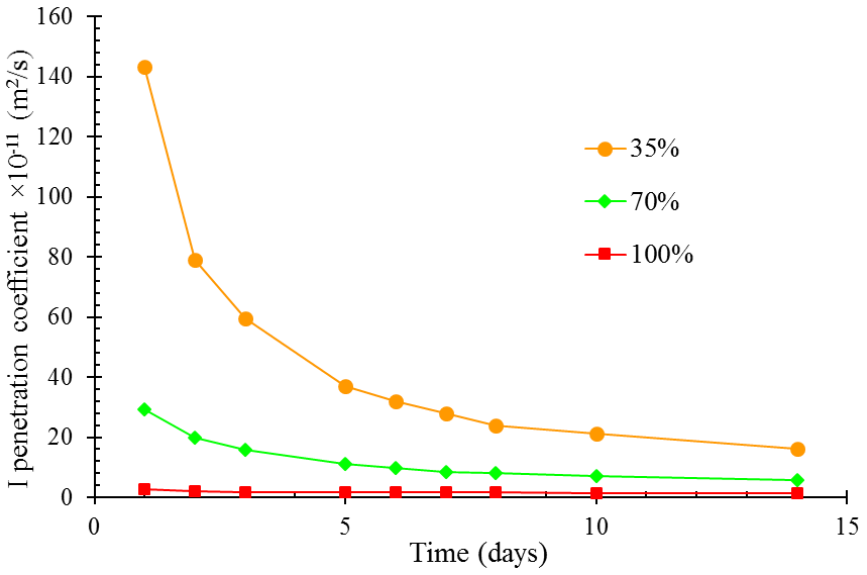

Fig. 4.16 Time-dependent I penetration coefficients of 35%, 70%, and 100% RH samples by TXM.

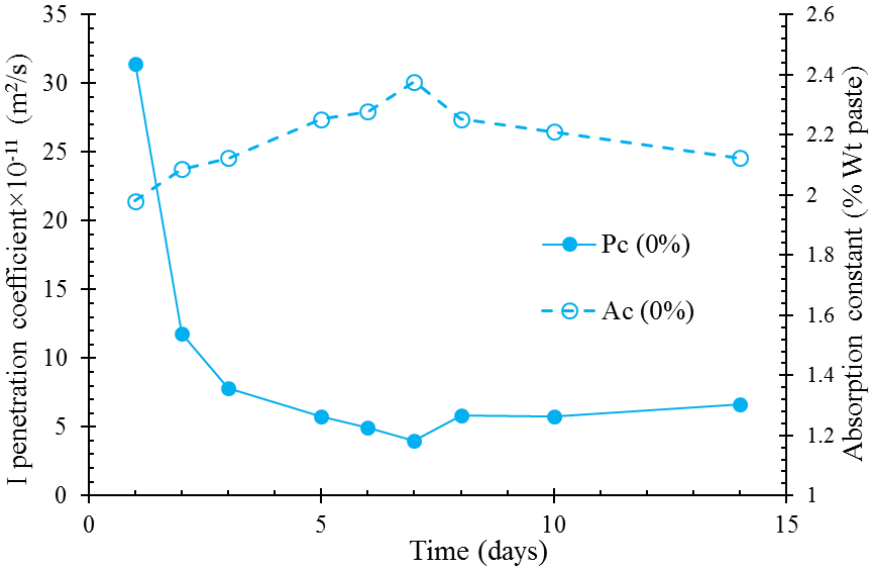

Fig. 4.17 Time-dependent Pc and Ac for 0% RH samples by TXM; estimated by using Eq. (7). Pc is penetration coefficient and Ac is the capillary absorption constant.

In addition, a power model based on the experimental results is shown in **Eq. (4.8)** to estimate the P_c of partially-saturated paste samples with w/c of 0.40 from a fully saturated sample, as formulated in **Eq. (4.8)**.

$$\frac{P_h}{P_{100\%}} = a \times t^{-\left(1-\frac{h}{100}\right)} \qquad (4.8)$$

where P_h is penetration coefficient of the sample conditioned at relative humidity of h, which accounts for the combined transport mechanisms from capillary absorption and diffusion; $P_{100\%}$ is penetration coefficient of the sample conditioned at 100% RH; t denotes the time; and a is the regression constant. The regression results for 35% and 70% RH samples is summarized in **Fig. 4.18**. Based on **Fig. 4.18**, there is good correlation between the developed model and experimental results. The regression constant, "a", decreases with the increase of DoS in the sample. Additional work is needed to extend **Eq. (4.8)** to other RH and mixture proportions. The produced experimental model can be used in computational modeling efforts to predict the service life of concrete structures in harsh environments.

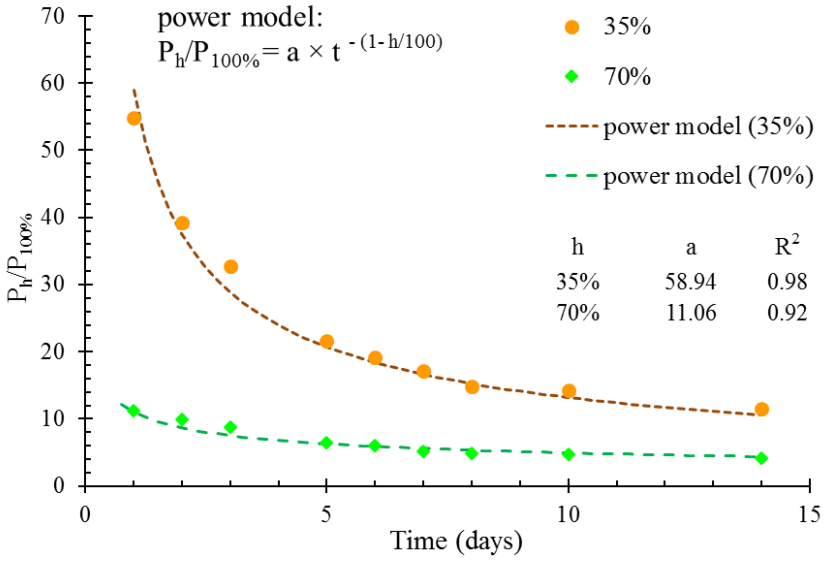

Fig. 4.18 A power model to estimate time-dependent penetration coefficients of 35% and 70% RH samples from 100% RH results.

4.3.6 Practical Implications

This work provides quantitative insights into the penetration of ions into cement paste at different moisture conditions. Typically, laboratory testing is carried out at 100% RH and the

results from the testing are used to predict the long term resistance to Cl penetration. This work provides important data that makes quantitative measurements of how partially-saturated samples perform in these tests and shows that rate of penetration is higher in these situations. Furthermore, a power model has been presented that would allow testing results from saturated samples to be used to predict performance in partially-saturated materials. This is a useful contribution to the literature. Although more work is needed to extend these findings to different materials and conditions, this work is an important step to improve our predictive powers of the durability of concrete infrastructure. Furthermore, the findings from this work show that the previously suggested equation to estimate the depth of ion transport based on ASTM C 1585 is unconservative by ≈ 23% for the materials and conditions investigated.

4.4 Conclusions

The presented work uses non-destructive and rapid imaging method to investigate in-situ and time resolved I penetration into cement paste samples with different degree of saturations. The sorptivity of Cl and I ions in paste samples was also determined gravimetrically and compared with the TXM results. In addition, the same samples from TXM and gravimetric methods were also examined with μXRF in order to verify their results and compare the I and Cl penetration. Furthermore, time-series I concentration profiles and penetration depths with 8.8 μm resolution from TXM were used to obtain sorptivity and penetration coefficients at different conditions and observe important insights about combined ion transport mechanisms in partially-saturated samples. This work also suggests a modified version of simplified solution to Fick's second law to take into account the capillary absorption and complex penetration of outside chemicals into cement paste.

The following conclusions can be drawn from this work:

- The saturated samples showed about 75% reduction in I penetration depth compared to samples conditioned at 0% and 35% RHs even at 1 h of ponding.

- The I penetrated for the 0% and 35% RH samples over the entire scan depth (≈ 20 mm) after only 6 h of ponding.

- The 0% RH sample showed a constant I concentration in entire penetration depth due to capillary absorption at early ages. Then, the concentration profile changes so that there are two modes of ion penetration in 0% RH sample.

- The P_c of the 35% and 70% RH samples is about 40x and 10x higher than the saturated sample at 2 d of ponding, respectively. This ratio decreases over time. However, this calculated P_c combines the effect of capillary absorption and diffusion in partially-saturated samples.

- Previously suggested equations to estimate the depth of ion transport based on gravimetric analysis is unconservative by ≈ 23% for the materials and conditions investigated and can cause an overestimation of the predicted service life.

- The oven dried samples showed an almost constant P_c after 5 d of ponding.

- A power model was successfully used to estimate the P_c of partially-saturated paste samples based on the P_c of fully saturated samples.

- Iodide shows a similar absorption (≈ 15% difference in sorptivity coefficient) and penetration (≈ 6% difference in penetration coefficient) performance to Cl in samples with different DoS.

- µXRF and TXM techniques showed a good correlation and statistically comparable results (4% difference between the calculated P_c from µXRF and TXM techniques).

The use of TXM offers advantages over conventional methods to investigate the effect of degree of saturation for ion penetration into cement-based materials with a number of different conditions. Since TXM allows non-destructive and time-dependent concentration profiles to be measured with little sample preparation, TXM can be used to measure the evolution of the penetration over time. These findings show promise to help refine service life modeling techniques for concrete materials and to ultimately improve the predictive capabilities of the lifetime of concrete structures. This data quantifies the impacts of partial saturation on ion transport and shows that even partial drying of concrete will increase the penetration of outside ions through mixed modes of mass transport. This can help owners in dry environments better predict and maintain their concrete structures. Additional modeling efforts are underway to provide even more insights.

Acknowledgments

The authors acknowledge the financial support from the Oklahoma Department of Transportation (ODOT 2229), Federal Highway Association (FHWA) Exploratory Advanced Research (EAR) Program (Project No. CMMI 1030972), and the United State National Science Foundation CMMI 1635878 and CMMI 1150404 CAREER Award. The authors would also like to recognize their collaborators Dr. Kimberly Kurtis, Dr. Lisa Burris, and Prasanth Alapati of Georgia Tech, Dr. Neal Berke of Tourney Consulting and Dr. Robert Moser of the US Army Corps of Engineers for their assistance and discussion on this work.

References

[1] G.H. Koch, M.P. Brongers, N.G. Thompson, Y.P. Virmani, J.H. Payer, Corrosion costs and preventive strategies in the United States, Report by CC Technologies Laboratories, Inc. to Federal Highway Administration (FHWA)-RD-01-151, September 2001.

[2] F. Ghasemzadehsomarin, The Effect of Damage on Mass-Transportation in Cement-based Materials, Ph.D. Thesis, North Carolina State University, 2015.

[3] M. Khanzadeh-moradllo, M.H. Meshkini, E. Eslamdoost, S. Sadati, M. Shekarchi, Effect of Wet Curing Duration on Long-Term Performance of Concrete in Tidal Zone of Marine Environment, Int. J. Concr. Struct. Mater. (2015). doi:10.1007/s40069-015-0118-3.

[4] K. Basham, J. Meredith, Measuring water penetration: A simple, inexpensive tube test can yield valuable, quantitative information, Mag. Mason. Constr. 8 (1995) 539-543.

[5] S. Lu, E.N. Landis, D.T. Keane, X-ray microtomographic studies of pore structure and permeability in Portland cement concrete, Mater. Struct. 39 (2007) 611–620. doi:10.1617/s11527-006-9099-7.

[6] G. Sant, W.J. Weiss, Using X-Ray Absorption to Assess Moisture Movement in Cement-Based Materials, J. ASTM Int. 6 (2009) 15. doi:10.1520/JAI102234.

[7] C. Hall, Water sorptivity of mortars and concretes: a review, Mag. Concr. Res. 41 (1989) 51-61.

[8] N.S. Martys, C.E. Ferraris, Capillary transport in mortars and concrete, Cem. Concr. Res. 27 (1997) 747–760.

[9] J. Castro, D. Bentz, J. Weiss, Effect of sample conditioning on the water absorption of concrete, Cem. Concr. Comp. 33 (2011) 805–813. doi:10.1016/j.cemconcomp.2011.05.007.

[10] B. Van Belleghem, R. Montoya, J. Dewanckele, N. Van Den Steen, I. De Graeve, J. Deconinck, Capillary water absorption in cracked and uncracked mortar – A comparison between experimental study and finite element analysis, Constr. Build. Mater. 110 (2016) 154–162. doi:10.1016/j.conbuildmat.2016.02.027.

[11] M. Janz, Methods of Measuring the Moisture Diffusivity at High Moisture Levels, Licentiate Thesis, University of Lund, 1997.

[12] V. Cnudde, M. Dierick, J. Vlassenbroeck, B. Masschaele, High-speed neutron radiography for monitoring the water absorption by capillarity in porous materials, NIM B 266 (2008) 155–163. doi:10.1016/j.nimb.2007.10.030.

[13] C. Lucero, Quantifying Moisture Transport in Cementitious Materials Using Neutron Radiography, In: MSc thesis, Purdue University, West Lafayette, Indiana, USA, 2015.

[14] H. Derluyn, M. Griffa, D. Mannes, I. Jerjen, J. Dewanckele, P. Vontobel, et al., Characterizing saline uptake and salt distributions in porous limestone with neutron radiography and X-ray micro-tomography, J. Build. Phys. 36 (2013) 353–374. doi:10.1177/1744259112473947.

[15] C.L. Lucero, D.P. Bentz, D.S. Hussey, D.L. Jacobson, W.J. Weiss, Using Neutron Radiography to Quantify Water Transport and the Degree of Saturation in Entrained Air Cement Based Mortar (In Press), Phys. Procedia (10 World Conf. Neutron Radiogr. 69 (2014) 1–8. doi:10.1016/j.phpro.2015.07.077.

[16] D.P. Bentz, K.K. Hansen, Preliminary observations of water movement in cement pastes during curing using X-ray absorption, Cem. Concr. Res. 30 (2000) 1157–1168. doi:10.1016/s0008-8846(00)00273-8.

[17] S. Roels, J. Carmeliet, Analysis of moisture flow in porous materials using microfocus X-ray radiography, Int. J. Heat Mass Transf. 49 (2006) 4762–4772. doi:10.1016/j.ijheatmasstransfer.2006.06.035.

[18] M. A. Hickner, N.P. Siegel, K.S. Chen, D.S. Hussey, D.L. Jacobson, M. Arif, In Situ High-Resolution Neutron Radiography of Cross-Sectional Liquid Water Profiles in Proton Exchange Membrane Fuel Cells, J. Electrochem. Soc. 155 (2008) B427. doi:10.1149/1.2826287.

[19] I.S. Darma, T. Sugiyama, M.A.B. Promentilla, Application of X-Ray CT to Study Diffusivity in Cracked Concrete Through the Observation of Tracer Transport, J. Adv. Concr. Technol. 11 (2013) 266–281. doi:10.3151/jact.11.266.

[20] V.C. Tidwell, L.C. Meigs, T. Christian-Frear, C.M. Boney, Effects of spatially heterogeneous porosity on matrix diffusion as investigated by X-ray absorption imaging, J. Contam. Hydrol. 42 (2000) 285–302. doi:10.1016/S0169-7722(99)00087-X.

[21] L. Cavé, T. Al, Y. Xiang, P. Vilks, A technique for estimating one-dimensional diffusion coefficients in low-permeability sedimentary rock using X-ray radiography: Comparison with through-diffusion measurements, J. Contam. Hydrol. 103 (2009) 1–12. doi:10.1016/j.jconhyd.2008.08.001.

[22] S.J. Altman, M. Uchida, V.C. Tidwell, C.M. Boney, B.P. Chambers, Use of X-ray absorption imaging to examine heterogeneous diffusion in fractured crystalline rocks, J. Contam. Hydrol. 69 (2004) 1–26. doi:10.1016/S0169-7722(03)00153-0.

[23] B. Sudbrink, M. Khanzadeh Moradllo, Q. Hu, M.T. Ley, J.M. Davis, N. Materer, A. Apblett, Imaging the presence of silane coatings in concrete with micro X-ray fluorescence. Cem.Concr. Res. (2016); accepted for publication. doi:10.1016/j.cemconres.2016.11.019.

[24] M. Khanzadeh Moradllo, B. Sudbrink, Q. Hu, M. Aboustait, B. Tabb, M.T. Ley, J.M. Davis, Using micro X-ray fluorescence to image chloride profiles in concrete. Cem.Concr. Res. (2016), in press. doi:10.1016/j.cemconres.2016.11.014.

[25] J.M. Davis, D.E. Newbury, A. Fahey, N.W.M. Ritchie, E. Vicenzi, D. Bentz, Bridging the micro-to-macro gap: a new application for micro X-ray fluorescence., Microsc. Microanal. 17 (2011) 410–417. doi:10.1017/S1431927611000183.

[26] J.M. Davis, D.E. Newbury, P.R. Rangaraju, S. Soundrapanian, C. Giebson, Milli X-ray fluorescence X-ray spectrum imaging for measuring potassium ion intrusion into concrete samples, Cem. Concr. Compos. 31 (2009) 171–175. doi:10.1016/j.cemconcomp.2008.12.005.

[27] D. Bentz, M. Peltz, K. Snyder, J. Davis, VERDiCT: viscosity enhancers reducing diffusion in concrete technology, Concr. Int. 31 (2009) 31–36.

[28] M. Khanzadeh Moradllo, Q. Hu, M.T. Ley, Using X-ray imaging to investigate in-situ ion diffusion in cementitious materials. Constr. Build. Mater. (2016); Submitted for publication.

[29] M. Khanzadeh Moradllo, M.T. Ley, Comparing in-situ ion diffusion in Alternative Cementitious Materials by using X-ray imaging. Cem. Concr. Comp. (2016); Submitted for publication.

[30] Y. Farnam, T. Washington, J. Weiss, The influence of calcium chloride salt solution on the transport properties of cementitious materials, Advances in Civil Engineering 2015 (2015) 1-13.

[31] C. Hall, W.D. Hoff, Water-transport in brick, stone and concrete, second ed., CRC Press, London, 2009.

[32] R.P. Spragg, J. Castro, W. Li, M. Pour-ghaz, P. Huang, J. Weiss, Wetting and drying of concrete using aqueous solutions containing deicing salts, Cem. Concr. Compos. 33 (2011) 535–542. doi:10.1016/j.cemconcomp.2011.02.009.

[33] A.V. Wolf, Aqueous Solutions and Body Fluids, Hoeber Medical Division, New York, 1966.

[34] W.J. McCarter, H. Ezirim, M. Emerson, Absorption of water and chloride into concrete, Mag. Concr. Res. 44 (1992) 31-37.

[35] J. Crank, The mathematics of diffusion, second ed., Oxford Science Publication, London, 1975.

Supplementary Section

I and Cl Calibration Curves

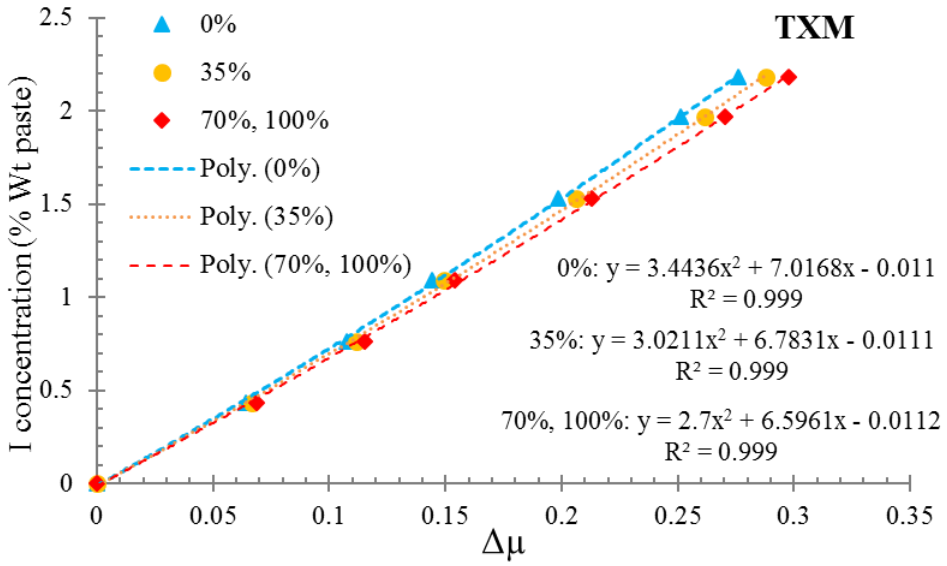

Fig. 4.S1 I calibration curve used to change from attenuation to weight percentage in the TXM analysis – w/c=0.40.

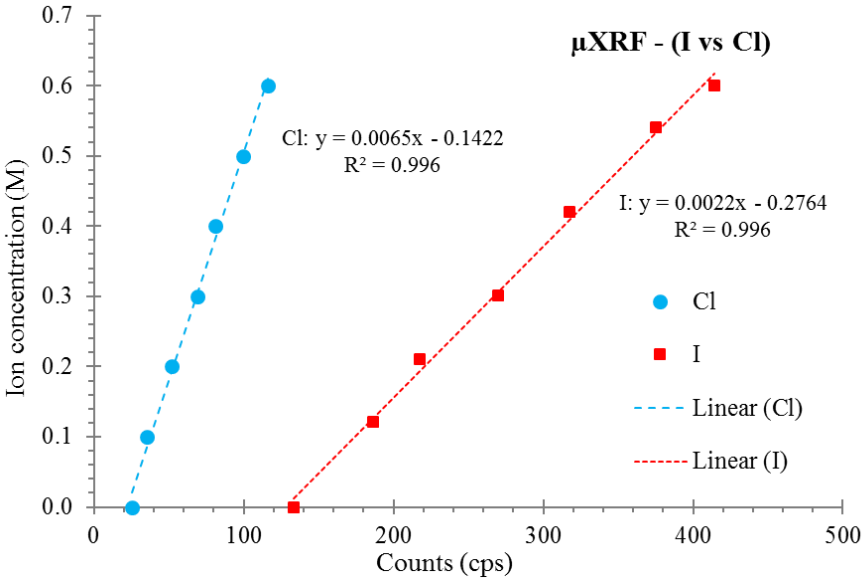

Fig. 4.S2 Cl and I calibration curves used to change from counts to concentration (M) in the µXRF analysis of the paste samples – w/c=0.40.

CHAPTER V

COMPARING IN-SITU ION DIFFUSION IN ALTERNATIVE CEMENTITIOUS MATERIALS BY USING X-RAY IMAGING

Abstract

Alternative cementitious materials (ACMs) are currently receiving increasing attention worldwide while there is a lack of knowledge around the resistance of these materials against harmful ion intrusion. In addition, current accelerated test methods based on ionic diffusion under an electric field are not a reliable indicator of ion diffusion when comparing binders with vastly different pore solution chemistry and so there are distinct advantages in measuring the ion penetration. This paper uses laboratory transmission X-ray microscopy (TXM) and micro X-ray fluorescence (μXRF) imaging to make in-situ measurements of ion diffusion in paste and mortar samples modeled after successful structural concrete mixtures with five commercially available ACMs and an ordinary portland cement.

The results compare the effective ion diffusion rate and depth, quantify the change in the effective ion diffusion rate over time, and give strong insights into ion binding. The results show that after 42 d of ion exposure that the calcium aluminate samples showed high resistance while the alkali activated and calcium sulfoaluminate samples show lower resistance to ion penetration than portland cement samples.

In addition, both the alkali-activated and calcium sulfoaluminate samples showed a decrease in the rate of penetration over time that is important for the long term durability of the material. These measurements are important to quantify the sustainability of ACMs, better justify their uses where durability are a concern and guide future durability testing of ACMs.

Keywords: X-ray microscopy; Calcium aluminate cement; Calcium sulfoaluminate cement; Alkali-activated binders; Durability; Sustainability.

5.1 Introduction

The manufacturing of portland cement accounts for approximately 5% of anthropogenic CO_2 emission [1]. The development and use of novel alternative cementitious materials and binders (ACMs) with intrinsically lower energy requirements on manufacture than portland cement is one way of reducing CO_2 emission associated with concrete production [2-5].

Currently, a wide range of ACMs have been developed and used for various applications. However, calcium aluminate cements (CAC), calcium sulfoaluminate cements (CSA), and alkali-activated binders (AA) show particular potential as portland cement alternatives [3,5]. CACs contain around 40–50% of Al_2O_3 as a principle oxide, mainly in the form of monocalcium aluminate (CA), which reacts with water to give calcium aluminate hydrates (C-A-H) [3,6]. CSA cements are composed of ye'elimite ($C_4A_3S^{\overline{}}$) around 30-70% as main mineral phase, belite (C_2S), and anhydrite or gypsum [7-8]. The primary products of CSA cements are ettringite, monosulfate, and strätlingite [3]. Alkali-activated binders can be produced by mixing an alkaline solution with a reactive solid aluminosilicate powder such as fly ash, blast furnace slag, or metakaolin [3,9-10]. The reaction product of AA binders is variant as a consequence of the chemical differences between various precursors and the influences of different activator concentrations and chemistries [11-12].

ACMs are currently receiving increasing attention worldwide while there is a lack of knowledge around the durability of these materials in harsh environments [3,5,13]. A number of durability problems are caused by external fluids penetrating into cement-based materials [14-16]. Fluids which contain potentially harmful ionic species can lead to damage from corrosion, sulfate attack, alkali silica reaction, bulk freeze thaw, and salt scaling [17]. Therefore, the ion transport properties of cement-based materials play an important role in the durability performance of concrete structures [18-19]. There are a limited number of studies concerning the penetration of ions in ACMs [13,20-24]. In addition, current accelerated test methods based on ionic diffusion under an electric field are not reliable indicator of ion diffusion when comparing different types of ACM concrete with different pore solution chemistry [13,25].

This work uses transmission X-ray microscopy (TXM) to image the movement of ions in ACMs. This technique is rapid, non-destructive, and able to provide useful and direct observations of ion movement in cement-based materials at a useful length scale. This method is based on measuring X-ray attenuation differences of paste or concrete. In TXM different materials will appear to have different gray values depending on their X-ray absorption. While this technique does not provide direct compositional information about the investigated materials, it does provide clues about compositional consistency [26-27].

In this study, the moisture penetration is imaged with the aid of adding potassium iodide (KI) as a contrast agent or tracer. Iodine is strongly X-ray attenuating because of its high atomic number. Furthermore, iodide and chloride ions are similar in size (iodide radius is 206 pm versus a chloride radius of 167 pm). This property makes iodide an excellent tracer for fluid transport study of concrete with X-rays [28-29]. As the tracer penetrates into the material it is possible to see the corresponding changes in X-ray absorption or gray value in the radiograph. By taking images over time then a rate of penetration or an effective transport constant can be calculated. Since this technique is non-destructive, the same sample can be monitored over time and under

different conditions. The method requires minimal sample preparation and the technique can image at a spatial resolution of 200 nm to 20 µm with laboratory equipment.

This work aims to use TXM to investigate in-situ iodide diffusion for paste and mortar samples with three general classes of ACMs (CAC, CSA and AA binders) as well as portland cement. These same samples were investigated with micro X-ray fluorescence (µXRF) in order to compare their results. µXRF is similar to bulk X-ray fluorescence (XRF) but this method uses a polycapillary optic to focus X-rays to a size of approximately 50 µm in diameter, whereas bulk XRF investigates the sample with a 1 cm diameter investigation area. In addition, µXRF provides individual compositional maps which can be combined into a single map that simultaneously provides unique compositions and location [30-31]. Furthermore, µXRF imaging was used to compare iodide and chloride concentration profiles and diffusion coefficients in paste mixtures with different types of binders.

5.2 Experimental Methods

5.2.1 Materials

Six commercially available binders were used in this study: an ordinary portland cement Type I/II according to ASTM C 150 (OPC); a calcium sulfoaluminate cement (CSA2); a calcium sulfoaluminate cement with a polymer additive to reduce the porosity (CSA2B); a calcium aluminate cement (CAC3); a blended cement consisting of primarily calcium aluminate with some calcium sulfate and OPC (CAC2); and an alkali activated binder with a Class C fly ash according to ASTM C 618 as a solid precursor (AA1). These binders are commercial products and so in depth investigation of their formulation was not within the scope of the research. However, the chemical composition of binders, measured using bulk XRF, is provided in **Table 5.1**. More details can be found in other publications [5].

A commercial two component activator was used as the activating solution for the preparation of AA1 paste and mortar mixtures. Polycarboxlate based high-range water-reducing (HRWR) admixture was used to improve the workability of the fresh paste and mortar mixtures of investigated binders except CAC3 and AA1 mixtures. The dosage level was chosen for each mixture to provide consistent slump in concrete mixtures. These details are provided in **Table 5.2**. A food-grade citric acid was used as a retarder to control set time of CSA2, CSA2B, and CAC2 cements. In addition, plasticizer – set retarder (PSR) was used in preparation of CAC3 samples to assure a good workability and a delay of set. The dosages of these set modifying admixtures were chosen based on isothermal calorimetry experiments so that rapid hydration began at 2 h. More details can be found in other publications [5]. The fine aggregate is a natural river sand with a specific gravity of 2.60, and an absorption of 0.86% was used to prepare the mortar mixtures.

Table 5.1 Chemical composition of binders with bulk XRF (% weight)

Binder type	OPC	CSA2, CSA2B	CAC2	CAC3	Fly Ash
SiO_2	17.39	14.24	14.95	5.50	38.24
Al_2O_3	4.87	14.84	12.03	45.16	17.87
Fe_2O_3	4.71	1.12	2.66	6.90	5.88
CaO	65.15	49.23	55.15	37.68	24.75
MgO	1.40	1.55	2.57	0.22	6.24
SO_3	2.51	13.55	7.72	0.07	1.56
K_2O	0.48	0.67	0.83	0.26	0.34
Na_2O	0.46	0.21	0.28	0	1.85
P_2O_5	0.13	0.11	0.14	0.09	-
TiO_2	0.39	0.70	0.51	2.11	-
Mn_2O_3	0.11	0.02	0.16	0.02	-
SrO	0.15	0.20	0.21	0.04	-
ZnO	0.03	0.01	0.11	0	-
Cr_2O_3	0.09	0.05	0.07	0.089	-
LOI	2.12	3.51	2.61	1.86	0.20

5.2.2 Mixture Proportion and Sample Preparation

A cement paste mixture and a mortar mixture with water-to-binder ratio (w/b) of 0.40 were investigated for all binders except AA1. Based on manufacturer recommendation, a w/b of 0.21 was used to make AA1 paste and mortar mixtures. For AA1 the water is used as a plasticizer as per the manufacturer recommendations. This water content was chosen as it provided an equivalent slump in concrete mixtures made with these materials [32]. The paste and mortar mixtures were prepared according to ASTM C 305 and the mixture proportions are given in **Table 5.2**. In the mixing of AA1, the Class C fly ash was used in replacement of the cement and the activator was added to the water. The activator was used at a dose of 4% by weight of the fly ash as per the manufacturer recommendations. The mortar mixture contains 52% aggregate by weight for all binders except AA1 mortar mix which consists 58% aggregate by weight.

Cylindrical micro vials with inside dimension of 9.5×46 mm were used to cast the samples. A lid was used to seal each vial. Six samples were made from each mixture (three samples for each ponding solution; KI and NaCl). The vials were only partially filled so that there was room to provide solution above them. These samples were cured for 14 d in a sealed condition at 23°C.

Table 5.2 Paste and mortar mixtures proportions

Mixture		binder (g)	water (g)	aggregate (g)	HRWR (mL)	PSR (mL)	citric acid (g)	activator (g)
paste	OPC	891	354	-	1	-	-	-
	CSA2	875	350	-	0.45	-	4	-
	CSA2B	875	350	-	0.45	-	4	-
	CAC2	882	351	-	0.4	-	13.2	-
	CAC3	886	353	-	-	0.4	-	-
	AA1	1381	284	-	-	-	-	55.9
mortar	OPC	891	354	1336.5	1	-	-	-
	CSA2	875	350	1312.6	0.7	-	4	-
	CSA2B	875	350	1312.6	0.5	-	4	-
	CAC2	882	351	1323	0.4	-	13.2	-
	CAC3	886	353	1329	-	0.4	-	-
	AA1	1381	284	2283.5	-	-	-	55.9

5.2.3 In-Situ Diffusion Test Using TXM

An aluminum wire of 0.6 mm thickness was attached to the side of the sample to help align the images and to act as a standard material between scans. This helped detect variations in X-ray transmissions between images. The schematic diagram of the experimental setup is shown in **Fig. 5.1**.

After curing, samples were ponded with 0.6 mol/L KI solution for 28 d. This KI concentration was selected based on preliminary experiments to attain suitable contrast between the KI solution and the paste. A laboratory Skyscan 1172 µCT scanner was used to conduct the experiments. A radiograph was taken from the paste and mortar samples before and immediately after the ponding with the KI solution. These were used as reference radiographs. Radiographs were also taken over time to determine the changes in the sample as the fluid penetrated. In addition, a radiograph was taken from the air after each scan to subtract the background attenuation. The radiograph used a pixel size of 8.8 µm (2096×2096 pixels) and tube voltage and current of 100 KeV and 100 µA. An acquisition time of 8 s was used to collect a single radiograph. **Table 5.3** summarizes the TXM settings. More details can be found in other publications [33]. The KI solution was refreshed every 5 d to maintain a constant KI concentration. The amount of KI solution on the surface of samples was kept constant for all samples (0.6±0.01 mL). Samples were stored inside a sealed container at 23°C during the diffusion testing.

After TXM investigation the paste samples were polished on a sanding belt for 2 min with 120 grit sandpaper to create a flat surface for further analysis with µXRF. Ethanol was used to remove dirt and residue from the polished surface.

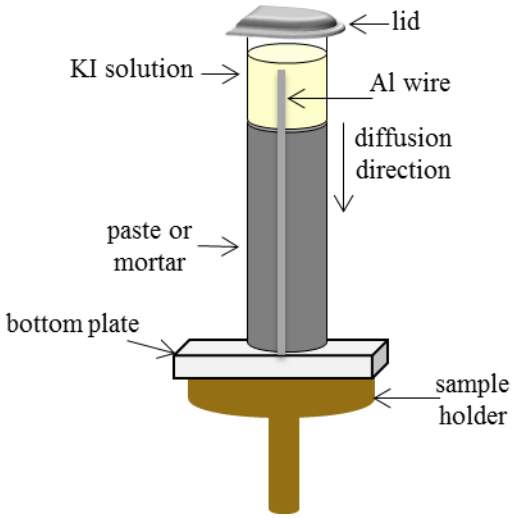

Fig. 5.1 Schematic diagram of the diffusion test setup.

5.2.4 Cl and I Diffusion Test Using µXRF

As explained earlier, the paste samples that were investigated with TXM were also analyzed with µXRF to compare the results after 28 d ponding with 0.6 mol/L KI. In addition, the paste samples with different types of binders were ponded with 0.6 mol/L NaCl solution for 28 d to compare I and Cl ions diffusivity. After the ponding period, the sample was polished for analysis with µXRF. Three samples were tested per solution.

The µXRF analysis was conducted using the Orbis by EDAX. The instrument uses an 80 mm^2 Silicon Drift Detector Energy Dispersive Spectrometer (SDD-EDS) and a capillary optic that produces a 50 µm diameter beam. Images are created by moving the sample under the stationary X-ray beam. The X-ray beam causes characteristic fluorescence X-rays to be emitted at each spot, the intensity of these characteristic X-rays are measured by the SDD-EDS and stored in a database for later processing and analysis. This analysis is able to detect elements at 0.1% by weight [34]. **Table 5.3** summarizes the settings used by the µXRF in this work. More details can be found in other publications [30-31].

Table 5.3 Summary of TXM and μXRF settings used

Parameter	TXM	μXRF
voltage (keV)	100	40
current (μA)	100	1000
Filter	0.5 mm Al + 0.5 mm Cu	25 μm Al
pixel size (μm)	8.8	50
acquisition time	8 s	400 ms/pixel (dwell time)
chamber condition	air	vacuum
dead time	-	maximum of 20%

5.2.5 TXM Data Analysis

An overview of the data analysis procedure is shown in **Fig. 5.2**. First, the radiographs of the air were subtracted from sample scans to remove the background attenuation effects. Next, an average gray value profile was calculated through the sample depth. Ten scan lines were randomly used to measure the average gray value with depth as shown in **Fig. 5.2a**. These lines located at the middle 40% (4 mm) of the sample to avoid beam hardening and to keep the analyzed region at an almost constant depth. Next, each time series radiograph gray value profile is subtracted from the gray value profile of the radiograph before solution was added to the sample (a reference radiograph). This allowed the change in the gray value to be easily observed and the spatial changes due to absorption from the I to be mapped. The Beer-Lambert Law (**Eq. (5.1)**) [28-29] was used to calculate a change in attenuation due to I ($\Delta\mu$) at different depths of sample.

$$(\Delta\mu)_x = \ln(I_{ref})_x - \ln(I_t)_x \qquad (5.1)$$

Where $(I_{ref})_x$ is the transmitted X-ray intensity (gray value) at depth x on the reference profile and $(I_t)_x$ is the transmitted X-ray intensity at the same location at a future time. The diffusion accessible porosity and the sample thickness are not included in **Eq. (5.1)** since these parameters are constant for each sample.

Next, to determine I concentration profiles a set of reference paste and mortar standards with different KI concentrations added to the cement paste and mortar mixtures while mixing were used to develop a calibration curve for each of investigated binders. The same sample size, mixtures, curing procedure, and scan setup were used to prepare and investigate the calibration samples for TXM. Next, the same paste calibration samples were polished and then analyzed with µXRF to develop a calibration curve for that technique. This allowed counts from µXRF to be converted to concentrations. This also allowed an independent method to be used to validate the TXM results. In addition, a set of paste standards with each binder type were made with different NaCl concentration in order to convert Cl counts from µXRF to concentrations. The calibration curves are included in the supplementary section (**Figs 5.S1-5.S4**).

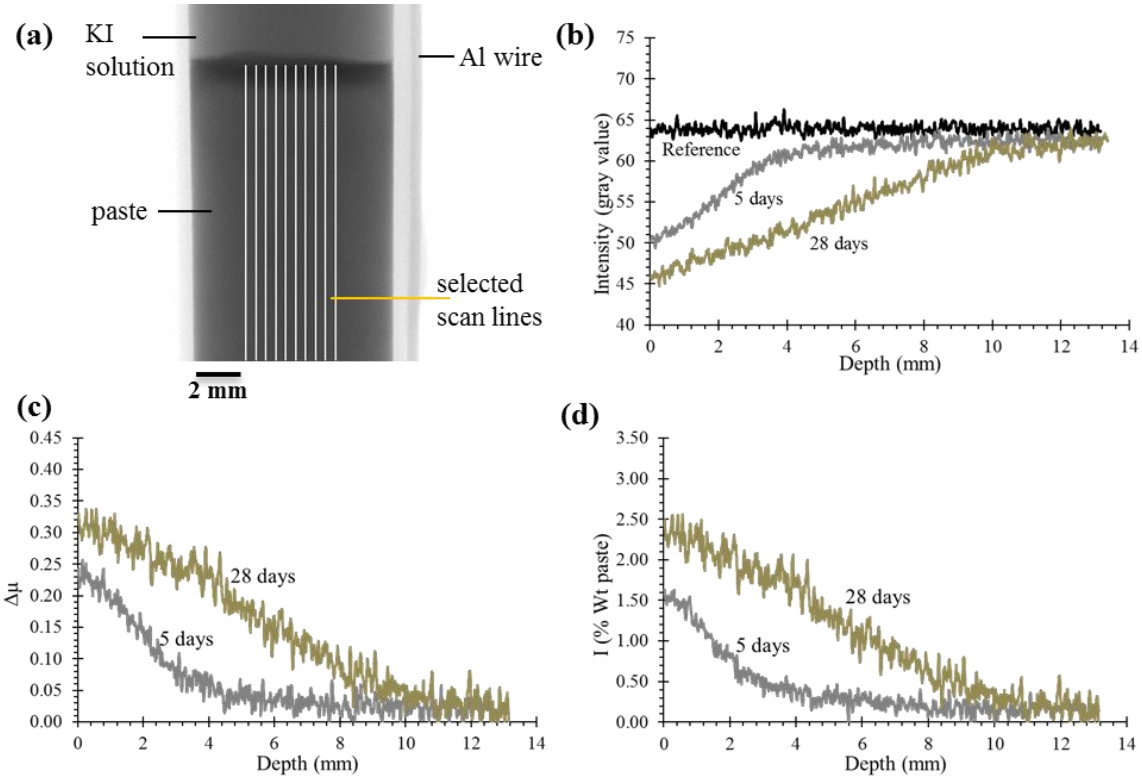

Fig. 5.2 X-ray radiography data analysis procedure: (a) calculating average gray value from radiographs (b) average gray value profiles over time (c) attenuation due to I (Δµ) profiles (d) I concentration profiles.

5.2.6 µXRF Data Analysis

After each sample is scanned with µXRF, the compositional maps were analyzed with an image processing software package called Lispix [35]. This program groups areas of similar composition, which are referred to as clusters. This analysis is helpful as one can combine individual compositional maps into a single map that simultaneously provides unique compositions and location. This separation of unique regions is useful in data display and analysis. For example, the cement paste was defined and separated by different elemental concentration levels (i.e., different levels of I). These regions were separated by selecting threshold values for different elemental concentration levels (i.e., observed low, medium and high counts of a given element). These ranges were chosen by the user to show that there are distinct differences in concentration within the sample. This single map of paste provides a complete separation of the different I levels in the paste and is useful for displaying the data.

Finally, an image analysis code in Matlab was developed to analyze the spatial and compositional data. A border detection algorithm is used to find the top surface of the sample. The sample is then separated into 0.50 mm layers of equal thickness from the surface of the sample through the entire depth. The average I and Cl counts in each layer can then be plotted for different depths. Next, a developed calibration curve is used to convert I and Cl counts to concentrations. Additional details can be found in previous publications [30,31,33].

5.2.7 I and Cl Diffusion Coefficient and Surface Concentration Calculation

A nonlinear regression is then conducted on I and Cl profiles with Fick's second law as shown in **Eq. (5.2)** [36], the values of apparent diffusion coefficient and surface concentration were determined. The highest Cl or I concentration within the sample is assumed as the surface concentration for samples that showed a reduction in Cl or I content at the surface.

$$C_{(x,t)} = C_s\left(1 - \mathrm{erf}\left(\frac{x}{2\sqrt{D_c t}}\right)\right) \qquad (5.2)$$

$$C_{(x,0)} = 0 \quad x > 0, \quad C_{(0,t)} = C_s \quad t \geq 0$$

Where x is the distance from sample surface; t denotes time; D_c is diffusion coefficient; C_s is surface I or Cl concentration; $C_{(x,t)}$ represents I or Cl concentration at the depth of x from the surface after time t; and erf is the error function.

5.3 Results and Discussion

5.3.1 Comparison of the I and Cl Diffusivity

Figure 5.3 shows a comparison between I and Cl concentration profiles of the paste samples with different types of binders after 28 d of ponding with 0.6 M KI and 0.6 M NaCl solutions. **Figure 5.4** compares the Cl concentration to the I concentration at individual depths for different types of ACMs and OPC. In addition, the calculated I and Cl diffusion coefficients from concentration profiles by using **Eq. (5.2)** are summarized in **Table 5.4**. Based on **Fig. 5.3**, the I and Cl show a very similar penetration trend over depth of the paste samples with different types of binders. According to **Fig. 5.4**, the slope of the linear trend line between Cl and I concentration values of individual depths is 1.086, which showing that the Cl concentration is about 8.6% higher on average than the I concentration over depth. In addition, the average difference between the calculated I and Cl diffusion coefficients of different samples is about 13.6%. Because of the differences in size and ionic mobility we would not expect the diffusion to be the same for these two different ions. Overall, I shows a similar diffusion performance to Cl in paste samples with different types of binders and serves as a satisfactory substitute to understand ion penetration.

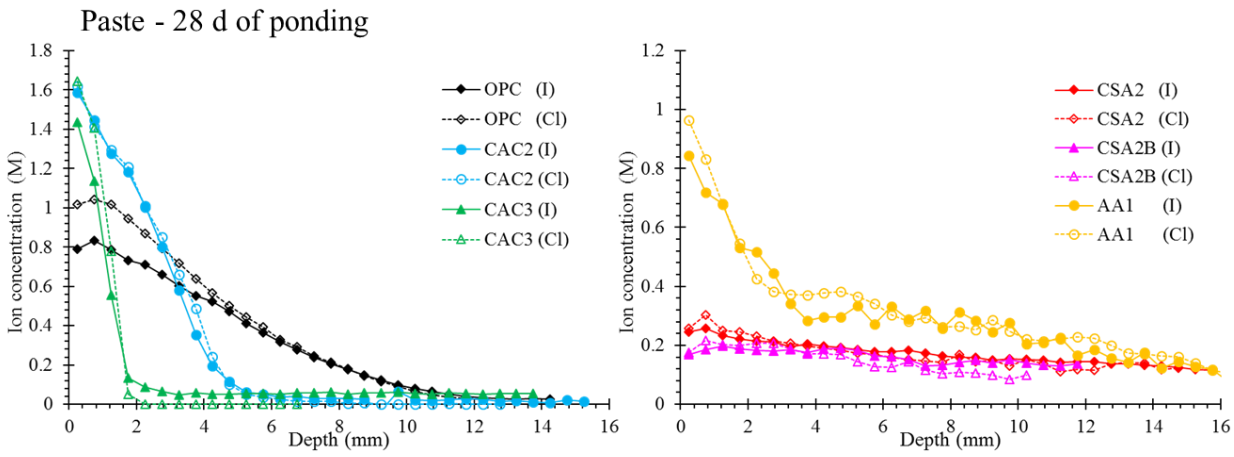

Fig. 5.3 Comparison of I and Cl concentration profiles in paste samples at 28 d: (left) OPC, CAC2, and CAC3 (right) CSA2, CSA2B, and AA1.

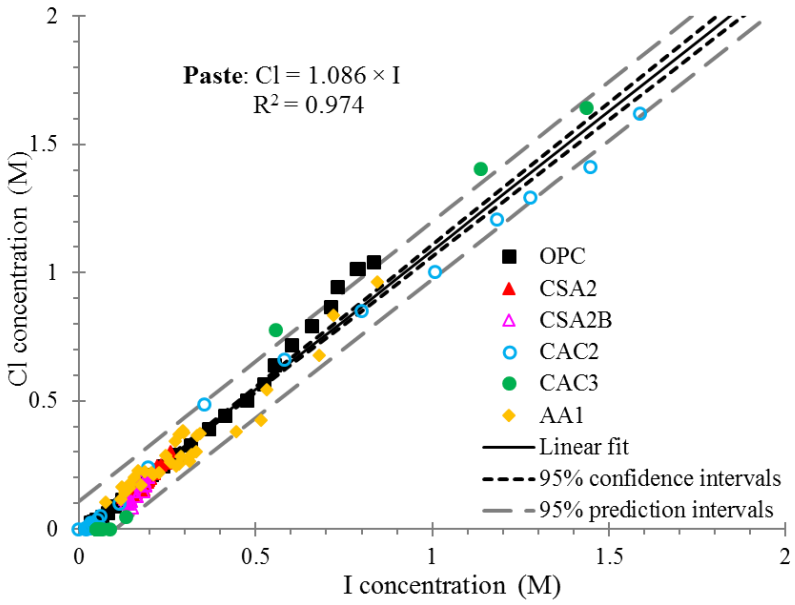

Fig. 5.4 Comparison of I and Cl concentration values at individual depths in paste samples with different types of binders.

Table 5.4 Comparison between I and Cl diffusion coefficients from μXRF

Sample	I Diff Coef×10^{-12} (m^2/sec)	R^2	Cl Diff Coef×10^{-12} (m^2/sec)	R^2	% Difference $\frac{(I - Cl)}{Cl \times 0.01}$
OPC	8.80	0.99	7.08	0.99	24
CSA2	91.13	0.96	75.29	0.86	21
CSA2B	N/A*	-	N/A	-	-
CAC2	1.996	0.98	2.119	0.98	-5.8
CAC3	0.282	0.98	0.297	0.95	-5.0
AA1	36.44	0.86	41.49	0.93	-12

*Regression was not possible.

5.3.2 Comparison with μXRF

This section aims to compare findings between μXRF and TXM. **Figure 5.5** presents a comparison between concentration profiles from μXRF and TXM for different mixtures. In addition, **Fig. 5.6** compares the average I concentration from the μXRF to the average TXM values over the same depths. The TXM data was averaged over the same distances used to average the μXRF results in order to compare the results between the two techniques. The calculated I diffusion coefficients from both methods are summarized in **Table 5.5**. The percent difference in diffusion coefficients between the two methods is also included. Based on **Figs 5.5** and **5.6**, the two techniques show a good correlation. The slope of the linear trend line is 1.054 which is close to the ideal value of 1, with the μXRF data being about 5.4% higher on average than the data from the TXM. The difference between the I diffusion coefficients from TXM and μXRF was on average 11% for μXRF. This shows that there is good agreement between μXRF and TXM for paste samples with different types of binders. In addition, a two tail t-test with the assumption of unequal variances was conducted to compare the mean I diffusion coefficient of the two methods. Based on this analysis, the difference between means was not significant (p-value= 0.901 >> 0.05). This suggests that these two methods provide comparable results.

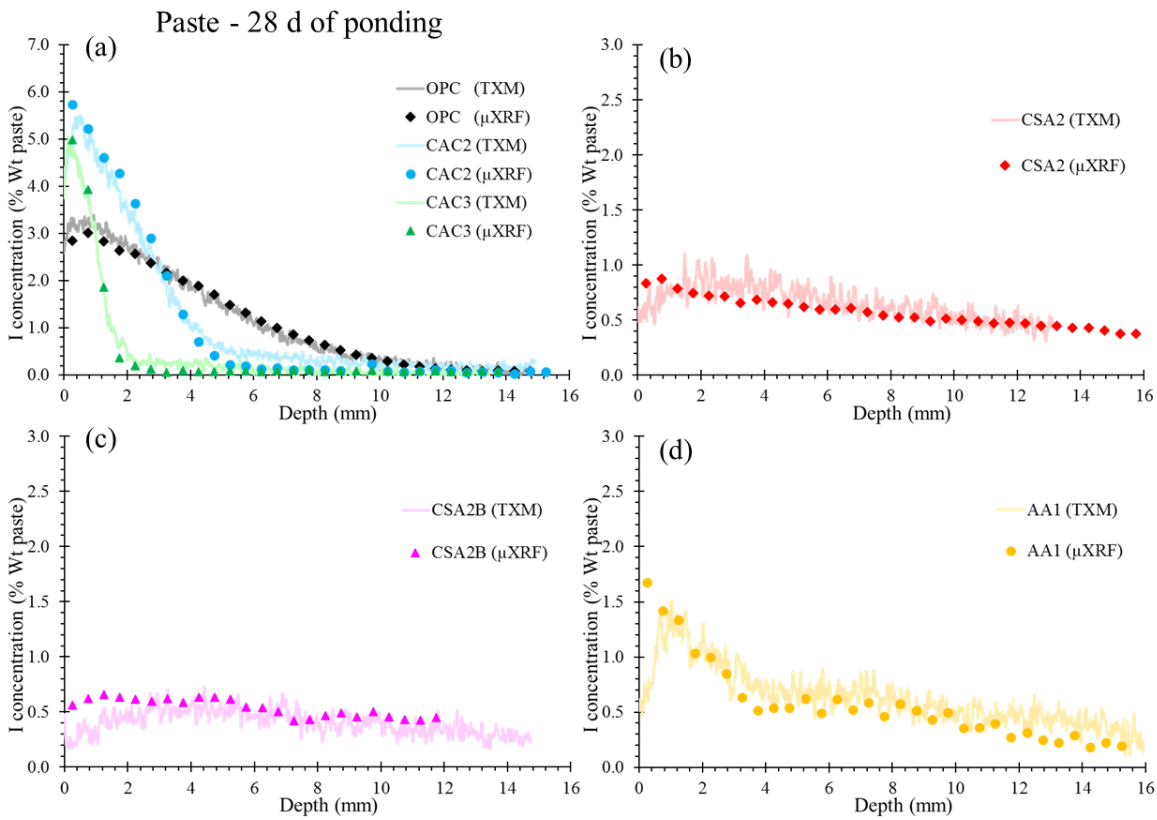

Fig. 5.5 Comparison of TXM results with results from µXRF for paste samples after 28 d of ponding: (a) OPC, CAC2, and CAC3 (b) CSA2 (c) CSA2B (d) AA1.

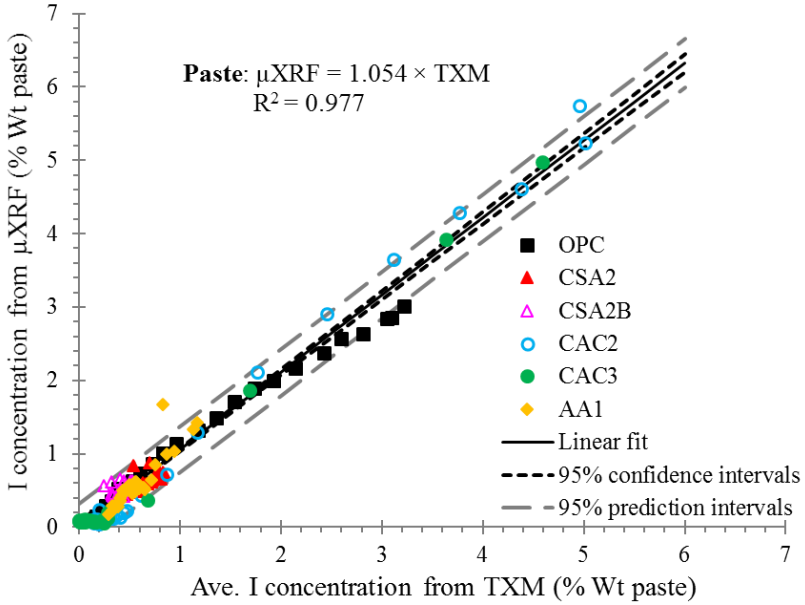

Fig. 5.6 Correlation between results from TXM and μXRF.

Table 5.5 Comparison between I diffusion coefficients from TXM and μXRF

Sample	TXM Diff Coef×10^{-12} (m^2/sec)	R^2	μXRF Diff Coef×10^{-12} (m^2/sec)	R^2	% Difference $\frac{(\mu XRF - TXM)}{TXM \times 0.01}$
OPC	7.68	0.99	8.80	0.99	14.5
CSA2	79.18	0.85	91.13	0.96	15
CSA2B	69.36	0.68	N/A*	-	-
CAC2	2.10	0.98	2.00	0.98	-4.8
CAC3	0.34	0.94	0.28	0.98	-16
AA1	34.82	0.83	36.44	0.86	-4.7

*Regression was not possible.

5.3.3 Comparison of I Concentration Profiles Over Time by TXM

Figs 5.7 to **5.10** show images of the I penetration and concentration of the same samples after 1, 5, 15, and 28 d of ponding with the KI solution. In addition, **Fig. 5.11** shows the same results after 28 d of ponding in mortars made with the same cements. The depth of penetration was estimated by reporting where the I concentration was greater than 0.10 % weight of the paste (≈ 0.14 % weight of the binder). This value was chosen based on concentration values at inner depth of OPC, CAC2, and CAC3 samples after 1 d of ponding where the solution has not penetrated. The I concentration from the mortar samples is shown in terms of the weight % of the paste for comparison between the paste results.

This data shows that TXM is capable of providing time-series concentration profiles with high spatial resolution. Because of the high resolution of the data, the I profile can be measured within hours of adding the material to the surface. Based on **Figs 5.7** and **5.8**, each ACM performs differently when compared to OPC from an early age. The I penetrated through the entire scanned depth of the CSA2 sample (≈ 15 mm) after only 1 d. The CSA2B sample showed limited penetration of the I (≈ 3.5 mm) at 1 d of ponding. This highlights the change in ion transport

from the added polymer. The CAC2 sample presents a similar depth of penetration to the OPC sample (≈ 7 mm at 5 d of ponding). However, the I concentration is higher at surface of the CAC2 sample when compared to the OPC sample (2.8 weight % for CAC2 and 1.9 weight % for OPC at 5 d of ponding). The CAC3 sample also displays high concentration of I at surface (3.8 weight % of the paste at 5 d of ponding) but the I concentration decreases to zero at a depth of 2 mm from the sample surface. The AA1 sample shows non-uniform penetration of I at 1 d and 5 d of ponding and the I reaches the bottom of the sample before 5 d of ponding.

The higher penetration depth of I in CSA2 is likely caused by the interconnected pores created among the ettringite crystals [21,23]. In addition, the expansion of ettringite crystals during curing may cause cracking and alter the porosity [37-38]. The comparison of results of the CSA2 and CSA2B samples also suggests that the addition of the polymer additive improved the performance of CSA paste against ion intrusion, especially at early ages. The higher concentration of I and Cl at surface of CAC2 and CAC3 samples is likely attributed to the higher level of ion binding in these cements. According to previous studies, the high level of Al_2O_3 in CACs would enhance the Cl binding capacity of the cement matrix from the formation of Friedel's salt [22,39]. A similar phenomenon may be occurring with I. The early age non-uniform penetration of I in AA1 sample may be explained by the heterogeneous matrix of the AA1 binder due to the variable chemical and physical nature of the particles present in the fly ash precursor [11,13,40-41]. While these are all probable explanations, more in depth work is needed to better understand these phenomena.

Figure 5.11 shows that the I concentration profiles of the mortar samples are consistent with the results from the paste except the mortar samples show higher I concentration at equivalent depths when compared to the paste samples. This is likely caused by the higher porosity of mortar samples due to the transition zone between the aggregates and the paste matrix.

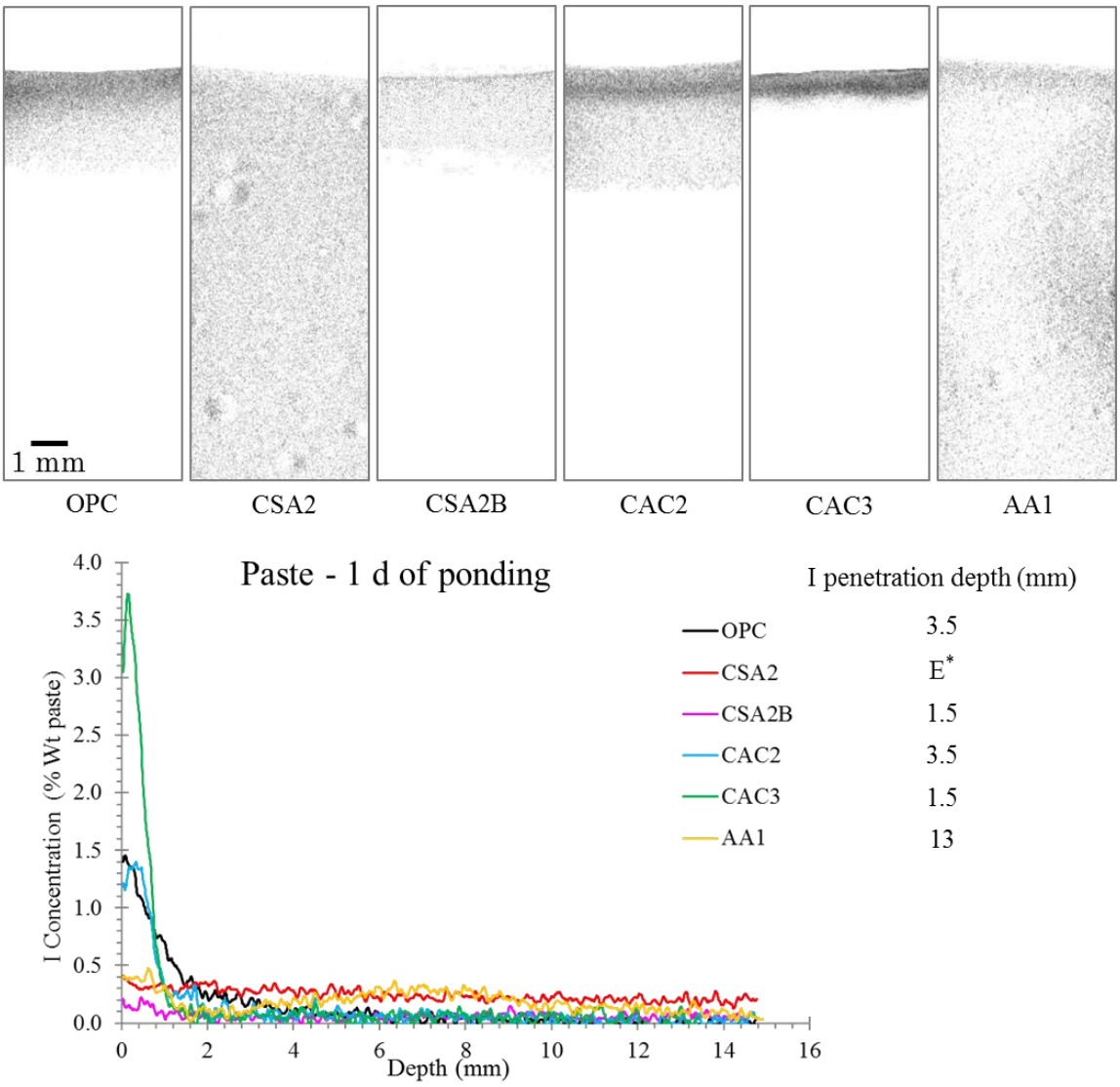

Fig. 5.7 Comparison of different paste mixtures performance against I intrusion after 1 d ponding. Note: *A solution infiltrated through the entire scanned depth of the sample.

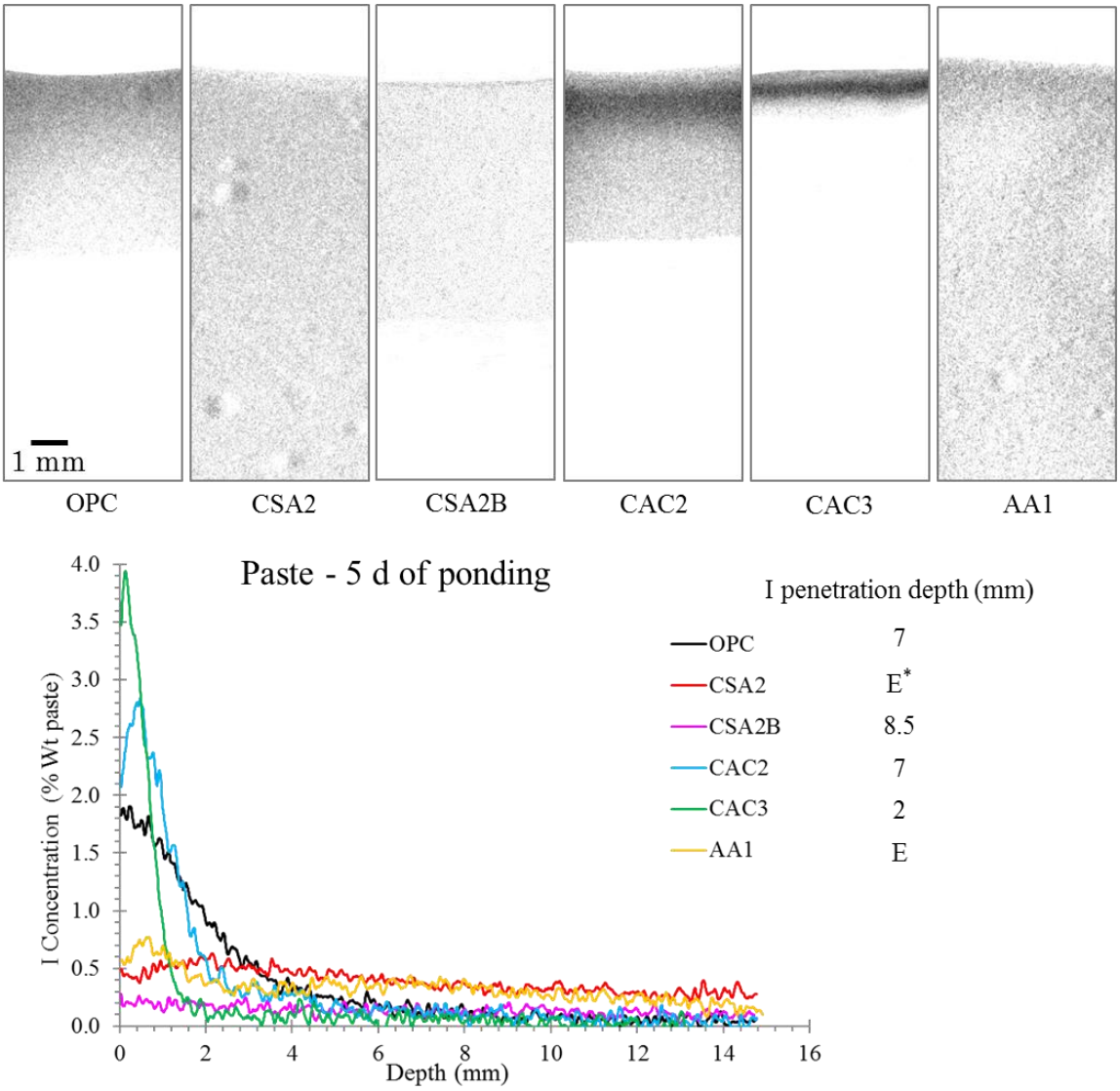

Fig. 5.8 Comparison of different paste mixtures performance against I intrusion after 5 d ponding. Note: *A solution infiltrated through the entire scanned depth of the sample.

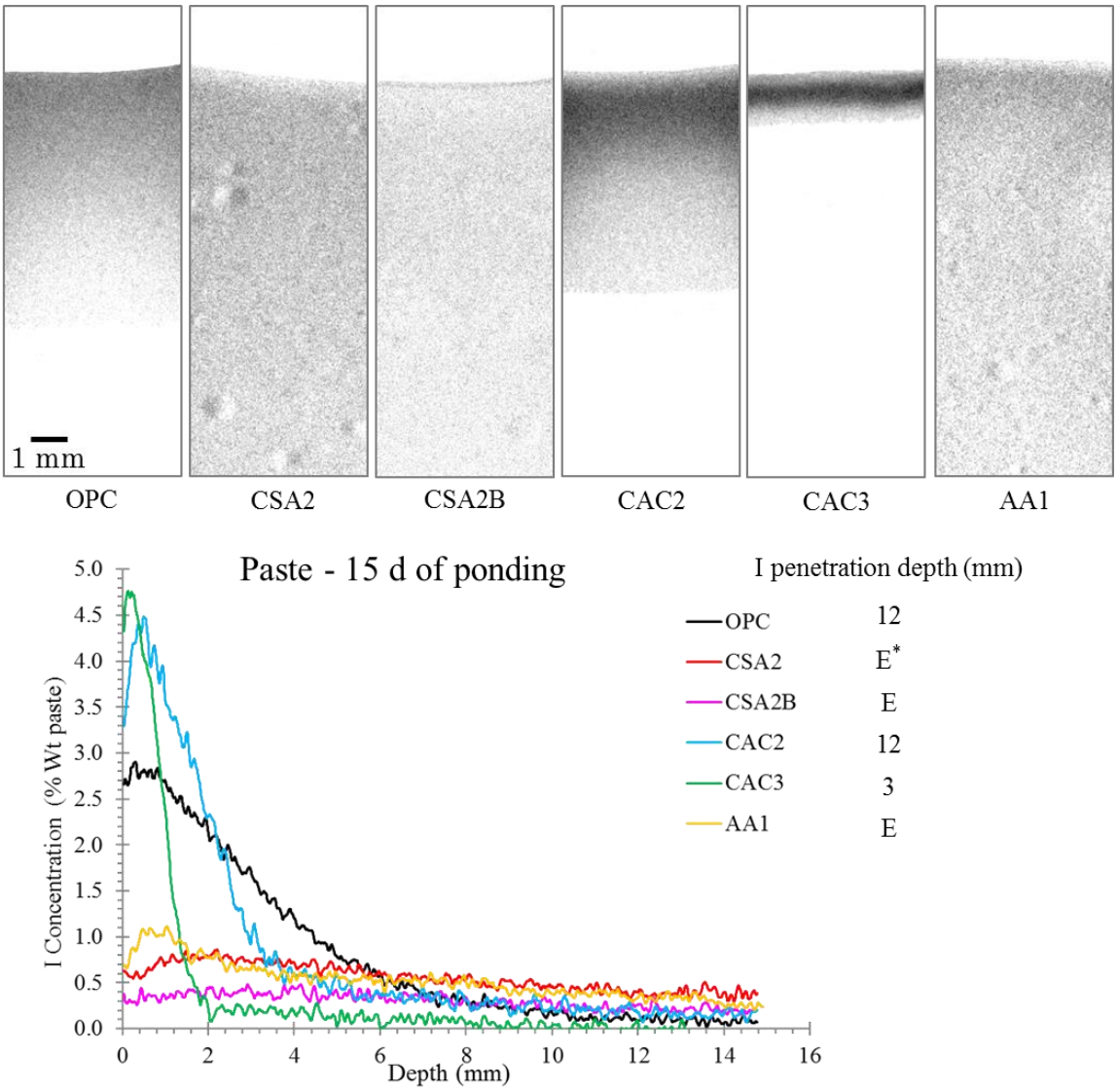

Fig. 5.9 Comparison of different paste mixtures performance against I intrusion after 15 d ponding. Note: *A solution infiltrated through the entire scanned depth of the sample.

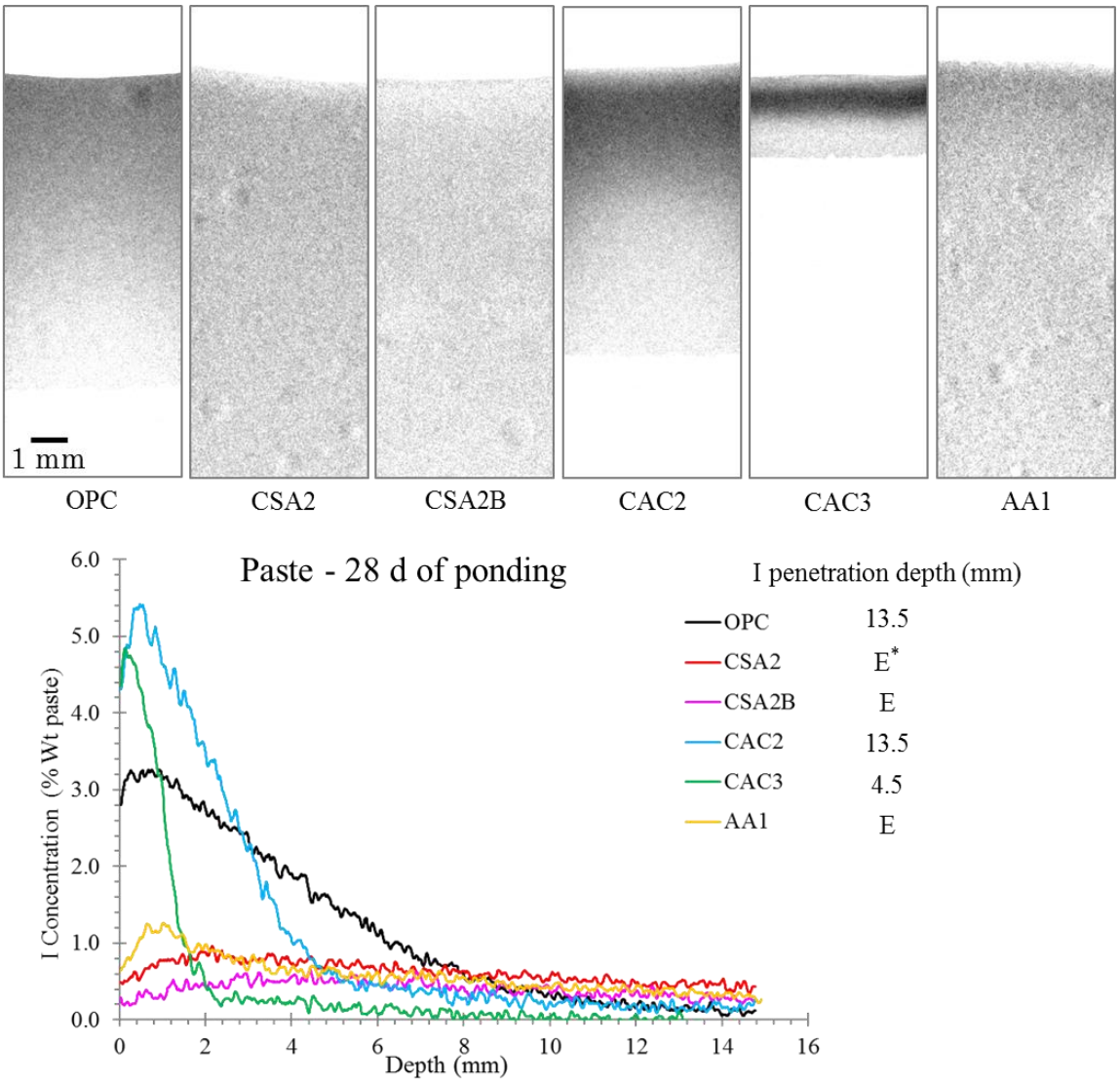

Fig. 5.10 Comparison of different paste mixtures performance against I intrusion after 28 d ponding. Note: *A solution infiltrated through the entire scanned depth of the sample.

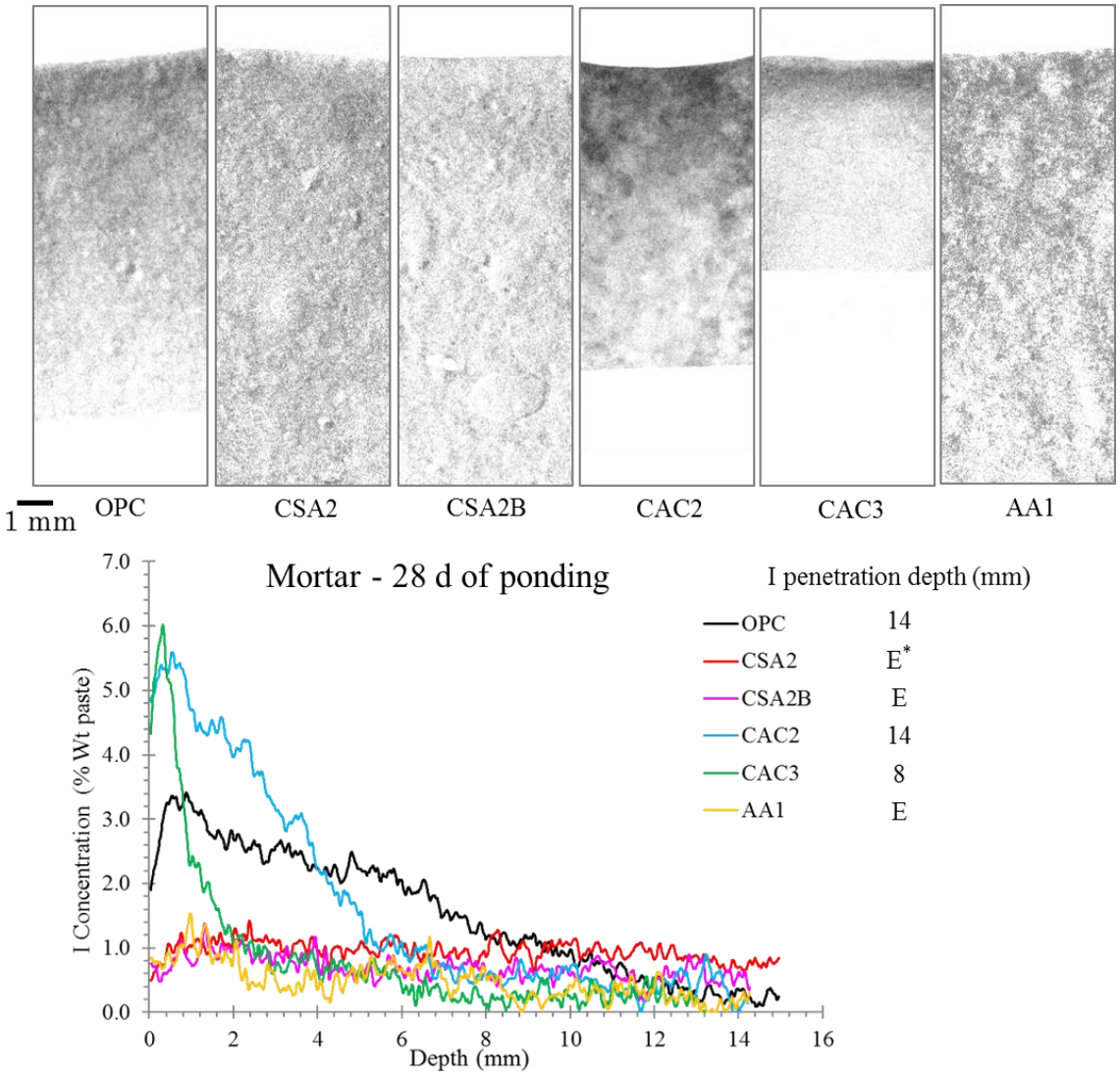

Fig. 5.11 Comparison of different mortar mixtures performance against I diffusion after 28 d ponding. Note: *A solution infiltrated through the entire scanned depth of the sample.

5.3.4 Use of the Results to Estimate Cl Penetration within ACMs

As explained earlier, the Cl and I diffusivity were compared for different mixtures and the Cl concentration is about 8.6% higher on average than the I concentration for the investigated paste samples with different types of binders. Therefore, the time series Cl concentration profiles of different mixtures can be estimated based on the measured I concentration profiles by TXM. This

means that these concentration profiles can be useful to estimate the Cl penetration depth to initiate corrosion of embedded reinforcing steel.

Figure 5.12 shows the estimated Cl concentration profiles for different mixtures after 5 d of ponding. An assumed Cl threshold value of 0.21% by weight of paste (≈ 0.05% weight of concrete) is shown in the figure. Comparisons will be made between samples by identifying the depth within the sample when this Cl value is estimated to compare the penetrability of Cl ions. This provides a useful tool to make a comparison between the different binders. To simplify the analysis a constant critical Cl threshold value was used. Other studies have shown that CSA cements showed a lower chloride threshold in comparison to OPC due to their low pore solution pH [42]. Whereas, CAC cements showed a higher Cl threshold value because of their high capacity of buffering and high level of Cl binding [22]. This is an area of ongoing research and future publications will provide additional insights.

Based on **Fig. 5.12**, the Cl concentration in the entire scanned depth (≈ 15 mm) of CSA2 is above the assumed threshold value after 5 d ponding; while CSA2B has only 3 mm above the threshold value. At this same time period the corrosion initiation depth is about 6 mm for the OPC sample. While the CSA2B performed well early in the ponding experiment, the ion intrusion increased over time and penetrated the entire scan depth after 28 d of ponding.

The AA1 sample also shows a high corrosion initiation depth (≈ 14 mm) at 5 d. Both CAC3 and CAC2 which show limited corrosion initiation depths of 2 mm and 4.5 mm, respectively. While both CAC3 and CAC2 show good performance, it should be noted that the conversion process is expected to cause an increase in porosity of the microstructure [3,43-44]. This may change the performance of this type cements against ion penetration. Additional work is underway to further investigate this.

While these observations are made with limited materials and sample sizes, these early age results are consistent with long term trends (e.g. 180 d ponding) from previous studies [13,20,22-23]. This suggests that TXM is a useful and powerful technique to investigate the ion diffusivity of materials at early ages and consequently provide insights into the corrosion resistance of the materials.

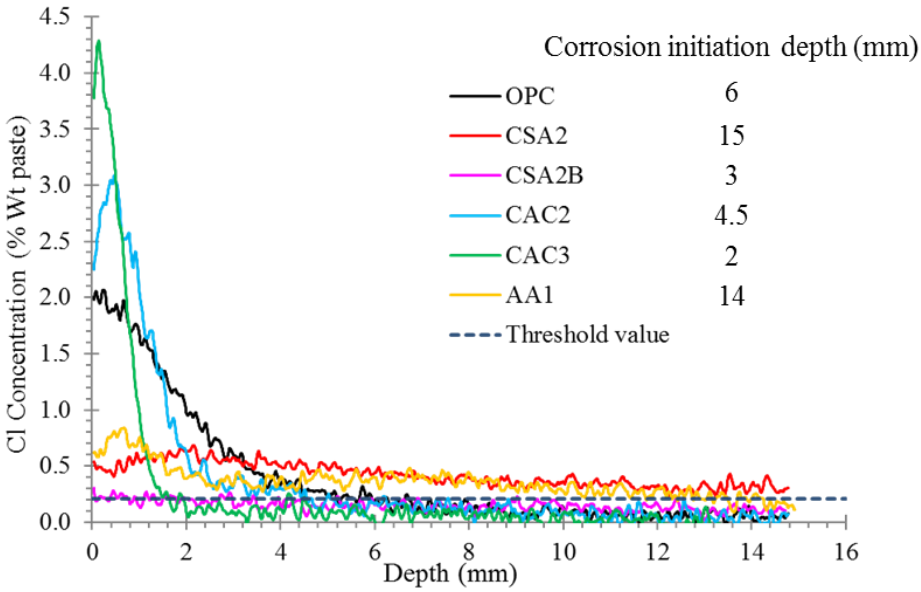

Fig. 5.12 Estimated Cl concentration profiles of different paste mixtures from I concentration profiles after 5 d of ponding.

5.3.5 Time-dependent I Surface Concentration and Diffusion Coefficient

The calculated time-dependent surface I concentration and diffusion coefficient for paste samples with different types of binders are plotted in **Figs 5.13** and **5.14**, respectively. Based on **Fig. 5.13**, the I concentration at the surface of the CAC2 and CAC3 paste samples increases with a higher rate when compared to OPC and other ACM samples. Also, the surface I content immediately reaches 2 and 3.9 weight % of the paste respectively for CAC2 and CAC3 samples after 5 d of ponding. As explained earlier, this can be due to higher level of I binding in these cements. On the contrary, the CSA2, CSA2B, and AA1 samples show lower rate of I build up at the surface of

the sample when compared to OPC. According to previous studies, the major hydration products of CSA type cements, ettringite and aluminum hydroxide, are not expected to chemically bind anions [4]. This can explain the lower rate of I build up at surface of CSA2 and CSA2B samples. The I diffusion rate increases over the ponding time for different mixtures and the I surface concentration becomes almost constant after 20 d in all samples except CAC2.

Based on **Fig. 5.14**, the CSA2 and CSA2B samples show the highest apparent diffusion coefficient when compared to OPC and other ACM samples. The calculated diffusion coefficient of these ACMs is about 10x OPC diffusion coefficient at 28 d of ponding. This result is in agreement with previous studies [20,23]. As mentioned earlier, this high diffusivity in CSA pastes can be attributed to interconnected pores created among the ettringite crystals and also the expansion of ettringite crystals during the curing time [21,23]. However, the decreasing rate of diffusion coefficient with time in CSA2 and CSA2B samples is higher than OPC sample. Therefore, the ratio of $D_{c,(CSA2,\ CSA2B)}$ to $D_{c,(OPC)}$ may decrease at later ages. The AA1 sample also presents higher diffusivity when compared to OPC sample ($D_{c,(AA1)} / D_{c,(OPC)} = 4.5$ at 28 d of ponding). This can be a consequence of the early age porous microstructure of the AA1 paste [13].

In addition, the CAC3 sample results in the lowest apparent diffusion coefficient between the investigated binders. The CAC3 lowers the diffusion coefficient by 96% when compared to OPC at 28 d of ponding. The CAC2 also shows an improved performance against I diffusion as compared to OPC. The superior performance of CAC3 may be due to the dense microstructure of hydration products and also the higher level of iodide binding in this type of cements [3,6,22]. The reader should be reminded that these properties may decline with conversion.

In addition, a diffusion decay coefficient was calculated for different mixtures by using the following equation [45] and results are summarized in **Table 5.6**.

$$D_t = D_{ref}\left(\frac{t_{ref}}{t}\right)^m \qquad (5.3)$$

where D_t is diffusion coefficient at time t; D_{ref} is diffusion coefficient at reference time t_{ref}; and m is the diffusion decay coefficient, which depends on mixture proportions. The diffusion coefficient at 1 d from ponding was used as a reference diffusion coefficient in this study. A regression was not possible in order to predict the early age diffusion coefficient of CSA2, CSA2B and AA1 samples. In these samples, a reference time of 10 d was used to estimate the m value.

Based on results, all the ACMs show higher diffusion decay coefficient than OPC. In addition, AA1 shows the highest diffusion decay coefficient which can be attributed to rapid change of microstructure in this type of binder at early ages. It is worth mentioning that obtaining the early age diffusion coefficients by TXM would improve the accuracy of the predicted diffusion decay coefficient and accordingly the estimated service life of structures. These results also show that testing of the properties of these ACMs at 28 d may not be appropriate to determine their long term performance. This highlights how testing practices typically used for OPC may need to be modified to investigate ACMs.

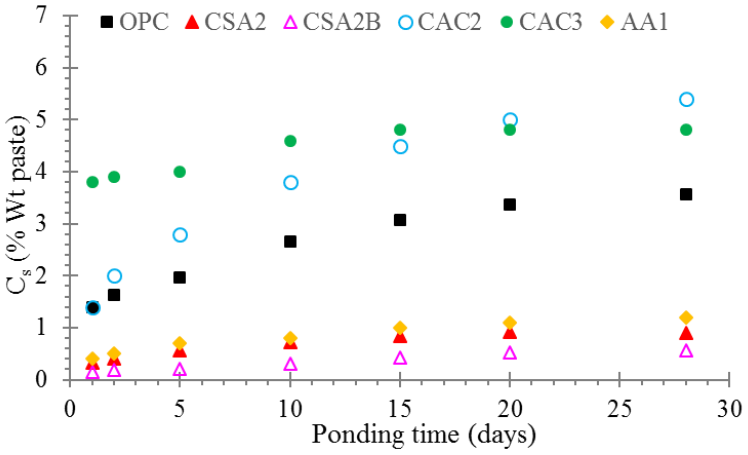

Fig. 5.13 Time-dependent surface I concentration by TXM.

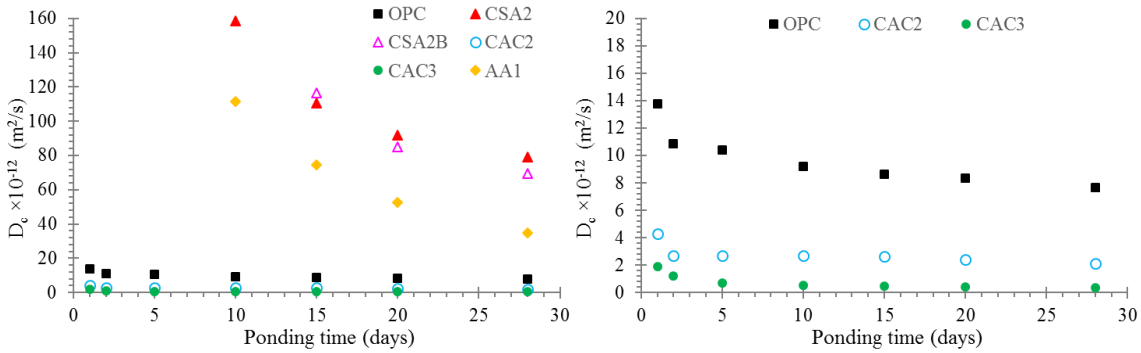

Fig. 5.14 Time-dependent I diffusion coefficients by TXM: (left) comparison between all binders (right) comparison between OPC, CAC2, and CAC3. Note: A regression was not possible in order to predict the early age diffusion coefficient of CSA2, CSA2B and AA1 samples.

Table 5.6 Diffusion decay coefficient of different mixtures

Sample	m	R^2
OPC	0.178	0.93
CSA2	0.752	0.98
CSA2B	0.899	0.97
CAC2	0.219	0.61
CAC3	0.566	0.99
AA1	1.08	0.99

5.3.6 Practical Implications

Before ACMs can be widely used the long term durability of these materials must be better understood. This work used several novel experimental methods to understand and quantify the ion transport into five commercially available ACMs in comparison to OPC. The results highlight that after 14 d of curing and 28 d of ponding that the microstructure of many of these ACMs are still evolving. This is an important insight that suggests that the properties within the first 40 d are not representative of the long term performance of these materials. For some materials they appear to be continuing to improve (AA and CSA) while others are anticipated to degrade (CAC). This work highlights the need to establish curing methods that can be used in the

lab that will be representative of the long term performance of these materials in the field. This will allow long term field performance to be predicted.

These experiments were completed with comparable mixtures that are representative of the mortar and paste fraction of concrete mixtures of equivalent setting and workability. These findings can be used to make quantitative comparisons of the service life of these materials and quantify the sustainability of these materials. Furthermore, this work allowed critical insights into the rate of refinement of the microstructure of ACMs.

While it is a goal to create equivalent systems of ACMs and OPCs, users of these material should be aware that these materials have fundamentally different chemistries and therefore produce concretes with vastly different microstructure and properties. This can lead to both an opportunity and challenge with using these materials. All of these materials have some property improvement over OPC (sustainability, strength gain, dimensional stability, and chloride binding). Finding applications for where these needs are the most important provides an excellent opportunity for the usage of these materials. While some of the ACMs investigated show lower performance than OPC, pairing of these ACMs with other technologies such as sealers, polymer additives, and reinforcing with higher resistance to Cl provides an opportunity for their usage and is an area of future research. The work in this paper provides some important baseline comparisons for these materials that will continue to be refined in future publications.

5.4 Conclusions

The presented work uses TXM to image in-situ and time resolved I diffusion into cement paste and mortar samples of five commercially available ACMs and an OPC paste and mortar. In addition, a time-dependent surface iodide concentration and diffusion coefficient of paste samples of different binders were studied. The following conclusions can be drawn from the examination of these samples between 14 and 42 d of age:

- The CAC cements showed superior resistance to I and Cl penetration compared to the other binders investigated. These cements lower the effective diffusion coefficient by 96% (CAC3) and 73% (CAC2) when compared to OPC at 28 d after ponding. Additional work is underway to further investigate the long-term performance of this cement after the expected conversion.

- The apparent I diffusion coefficient of the AA and CSA cements investigated are about 5x and 10x higher than OPC in the testing, respectively. However, these cements show lower rate of I build up at surface of the sample when compared to other cements.

- The estimated diffusion decay coefficient for the investigated ACMs is higher than OPC. These changes were the most significant with CSA and AA binders.

- A non-uniform I penetration was observed for AA paste samples at after 14 d of curing and 5 d of ponding. The non-uniform penetration is attributed to the continued development of the microstructure.

- The polymer additive used in the CSA cement reduced the ion penetration at early ages. However, these improvements in the performance were not substantially improved over time.

- When comparing I and Cl diffusion with μXRF the average difference in diffusion coefficients is about 13.6% and the Cl concentration is 8.6% higher on average than the I concentration.

- μXRF and TXM techniques showed a good correlation and statistically comparable results. The concentration values from TXM was on average 5.4% lower than the μXRF measurement at comparable time periods.

The use of TXM offers advantages over conventional methods to investigate the resistance of cement-based materials with different chemistry against ion intrusion. Since TXM allows non-destructive and time-dependent diffusion profiles to be measured with little sample preparation and analysis this makes it a powerful method to measure the developing microstructure of ACMs and ultimately better understand the evolution of the ion diffusion of these materials.

Acknowledgments

The authors acknowledge the financial support from the Federal Highway Association (FHWA) Exploratory Advanced Research (EAR) Program (Project No. CMMI 1030972), and the United State National Science Foundation CMMI 1635878 and CMMI 1150404 CAREER Award. The authors would like to thank Ms. Katelyn Oquin for her assistance with casting the samples. The authors would also like to recognize their collaborators Dr. Kimberly Kurtis, Dr. Lisa Burris, and Prasanth Alapati of Georgia Tech, Dr. Neal Berke of Tourney Consulting and Dr. Robert Moser of the US Army Corps of Engineers for their assistance and discussion on this work.

References

[1] J.S. Damtoft, J. Lukasik, D. Herfort, D. Sorrentino, E.M. Gartner, Sustainable development and climate change initiatives, Cem. Concr. Res. 38 (2008) 115–127. doi:10.1016/j.cemconres.2007.09.008.

[2] E. Gartner, Industrially interesting approaches to "'low-CO2'" cements, Cem. Concr. Res. 34 (2004) 1489–1498. doi:10.1016/j.cemconres.2004.01.021.

[3] M.C.G. Juenger, F. Winnefeld, J.L. Provis, J.H. Ideker, Advances in alternative cementitious binders, Cem. Concr. Res. 41 (2011) 1232–1243. doi:10.1016/j.cemconres.2010.11.012.

[4] G. Paul, E. Boccaleri, L. Buzzi, F. Canonico, D. Gastaldi, Friedel's salt formation in sulfoaluminate cements: A combined XRD and Al MAS NMR study, Cem. Concr. Res. 67 (2015) 93–102. doi:10.1016/j.cemconres.2014.08.004.

[5] L.E. Burris, L. P. Alapati, R.D. Moser, M.T. Ley, N. Berke, K.E. Kurtis, Alternative Cementitious Materials: Challenges and Opportunities. ACI SP 305-27, (2015) 1-10.

[6] K.L. Scrivener, J. Cabiron, R. Letourneux, High-performance concretes from calcium aluminate cements, Cem. Concr. Res. 29 (1999) 1215–1223.

[7] A. Klein, Calcium aluminosulfate and expansive cements containing same, US Patent No. 3, 155, 526, 1963, 4 pp.

[8] J.P. Sharp, C.D. Lawrence, R. Yang, Calcium sulfoaluminate cements — low-energy cements, special cements or what? Adv. Cem. Res. 11 (1) (1999) 3–13.

[9] A.O. Purdon, The action of alkalis on blast-furnace slag, J. Soc. Chem. Ind. Trans. Commun. 59 (1940) 191–202.

[10] P. Duxson, J.L. Provis, G.C. Lukey, J.S. van Deventer, The role of inorganic polymer technology in the development of 'green concrete', Cem. Concr. Res. 37 (2007) 1590–1597.

[11] P. Duxson, J.L. Provis, Designing precursors for geopolymer cements, J. Am. Ceram. Soc. 91 (12) (2008) 3864–3869.

[12] J.L. Provis, Activating solution chemistry for geopolymers, in: J.L. Provis, J.S.J. van Deventer (Eds.), Geopolymers: Structures, Processing, Properties and Industrial Applications, Woodhead, Cambridge, UK, 2009, pp. 50–71.

[13] I. Ismail, S.A. Bernal, J.L. Provis, R. San, D.G. Brice, A.R. Kilcullen, S. Hamdan, J.S.J. Van Deventer, Influence of fly ash on the water and chloride permeability of alkali-activated slag mortars and concretes, Constr. Build. Mater. 48 (2013) 1187–1201. doi:10.1016/j.conbuildmat.2013.07.106.

[14] G.H. Koch, M.P. Brongers, N.G. Thompson, Y.P. Virmani, J.H. Payer, Corrosion costs and preventive strategies in the United States, Report by CC Technologies Laboratories, Inc. to Federal Highway Administration (FHWA)-RD-01-151, September 2001.

[15] P.K. Mehta, Durability of Concrete- Fifty Years of Progress?, ACI SP 126-1, (1991) 1-31.

[16] M. Khanzadeh Moradllo, M.H. Meshkini, E. Eslamdoost, S. Sadati, M. Shekarchi, Effect of Wet Curing Duration on Long-Term Performance of Concrete in Tidal Zone of Marine Environment, Int. J. Concr. Struct. Mater. (2015). doi:10.1007/s40069-015-0118-3.

[17] K. Basham, J. Meredith, Measuring water penetration: A simple, inexpensive tube test can yield valuable, quantitative information, Mag. Mason. Constr. 8 (1995) 539-543.

[18] S. Lu, E.N. Landis, D.T. Keane, X-ray microtomographic studies of pore structure and permeability in Portland cement concrete, Mater. Struct. 39 (2007) 611–620. doi:10.1617/s11527-006-9099-7.

[19] G. Sant, W.J. Weiss, Using X-Ray Absorption to Assess Moisture Movement in Cement-Based Materials, J. ASTM Int. 6 (2009) 15. doi:10.1520/JAI102234.

[20] K. Quillin, Performance of belite – sulfoaluminate cements, Cem. Concr. Res. 31 (2001) 1341–1349.

[21] J. Zhao, G. Cai, D. Gao, S. Zhao, Influences of freeze – thaw cycle and curing time on chloride ion penetration resistance of Sulphoaluminate cement concrete, Constr. Build. Mater. 53 (2014) 305–311. doi:10.1016/j.conbuildmat.2013.11.110.

[22] S.H. Jin, H.J. Yang, J.P. Hwang, K.Y. Ann, Corrosion behaviour of steel in CAC-mixed concrete containing different concentrations of chloride, Constr. Build. Mater. 110 (2016) 227–234. doi:10.1016/j.conbuildmat.2016.02.032.

[23] E.G. Moffatt, M.D.A. Thomas, Durability of rapid-strength concrete production with ettringite-based binders, in: C.H. Fentiman, R.J. Manganhai, K.L. Scrivener (Eds.), Calcium Aluminate: Proceedings of the International Conference, Avignon, France, 2014, pp. 488–497.

[24] P. Chindaprasirt, W. Chalee, Effect of sodium hydroxide concentration on chloride penetration and steel corrosion of fly ash-based geopolymer concrete under marine site, Constr. Build. Mater. 63 (2014) 303–310. doi:10.1016/j.conbuildmat.2014.04.010.

[25] S. Berger, G. Aouad, C.C. Dit, P. Le Bescop, D. Damidot, Leaching of calcium sulfoaluminate cement pastes by water at regulated pH and temperature: Experimental investigation and modeling, Cem. Concr. Res. 53 (2013) 211–220. doi:10.1016/j.cemconres.2013.06.014.

[26] E.N. Landis, D.T. Keane, X-ray microtomography, Mater. Charact. 61 (2010) 1305–1316. doi:10.1016/j.matchar.2010.09.012.

[27] Q. Hu, M.T. Ley, J. Davis, J.C. Hanan, R. Frazier, Y. Zhang, 3D chemical segmentation of fly ash particles with X-ray computed tomography and electron probe microanalysis, Fuel. 116 (2014) 229–236. doi:10.1016/j.fuel.2013.07.037.

[28] V.C. Tidwell, L.C. Meigs, T. Christian-Frear, C.M. Boney, Effects of spatially heterogeneous porosity on matrix diffusion as investigated by X-ray absorption imaging, J. Contam. Hydrol. 42 (2000) 285–302. doi:10.1016/S0169-7722(99)00087-X.

[29] L. Cavé, T. Al, Y. Xiang, P. Vilks, A technique for estimating one-dimensional diffusion coefficients in low-permeability sedimentary rock using X-ray radiography: Comparison with through-diffusion measurements, J. Contam. Hydrol. 103 (2009) 1–12. doi:10.1016/j.jconhyd.2008.08.001.

[30] B. Sudbrink, M. Khanzadeh Moradllo, Q. Hu, M.T. Ley, J.M. Davis, N. Materer, A. Apblett, Imaging the presence of silane coatings in concrete with micro X-ray fluorescence. Cem.Concr. Res. (2016); accepted for publication. doi:10.1016/j.cemconres.2016.11.019.

[31] M. Khanzadeh Moradllo, B. Sudbrink, Q. Hu, M. Aboustait, B. Tabb, M.T. Ley, J.M. Davis, Using micro X-ray fluorescence to image chloride profiles in concrete. Cem.Concr. Res. (2016), in press. doi:10.1016/j.cemconres.2016.11.014.

[32] A.A. Adam, Strength and durability properties of alkali activated slag and fly ash-based geopolymer concrete, Ph.D. Thesis, RMIT University, Melbourne, Australia, 2009.

[33] M. Khanzadeh Moradllo, Q. Hu, M.T. Ley, Using X-ray imaging to investigate in-situ ion diffusion in cementitious materials. Constr. Build. Mater. (2016); Submitted for publication.

[34] K.H.A. Janssens, F. Adams, A. Rindby, Microscopic X-ray fluorescence analysis, John Wiley & Sons Inc, New York, 2000.

[35] D. Bright, Lispix: An image processing and analysis tool for the PC, 2011. http://www.nist.gov/lispix/doc/contents.htm, (last accessed on July 2016).

[36] J. Crank, The mathematics of diffusion, second ed., Oxford Science Publication, London, 1975.

[37] P.K. Mehta, Mechanism of expansion associated with ettringite formation, Cem. Concr. Res. 3 (1973) 1-6.

[38] Y. Bu, Service life prediction of concrete: Considerations of specimen conditioning and testing methods on the measurement of porosity and diffusion coefficient of chloride, Ph.D. Thesis, Purdue University, West Lafayette, 2014.

[39] T.U. Mohammed, H. Hamada, Relationship between free chloride and total chloride contents in concrete, Cem. Concr. Res. 33 (2003) 1487–1490. doi:10.1016/S0008-8846(03)00065-6.

[40] R.R. Lloyd, J.L. Provis, K.J. Smeaton, J.S.J. Van Deventer, Spatial distribution of pores in fly ash-based inorganic polymer gels visualized by Wood's metal intrusion, Microporous Mesoporous Mater. 126 (2009) 32–39. doi:10.1016/j.micromeso.2009.05.016.

[41] J.L. Provis, R.J. Myers, C.E. White, V. Rose, J.S.J. Van Deventer, X-ray microtomography shows pore structure and tortuosity in alkali-activated binders, Cem. Concr. Res. 42 (2012) 855–864. doi:10.1016/j.cemconres.2012.03.004.

[42] I. Janotka, L. Krajci, A. Ray, S.C. Mojumdar, The hydration phase and pore structure formation in the blends of sulfoaluminate-belite cement with Portland cement, Cem. Concr. Res. 33 (2007) 489–497.

[43] Calcium aluminate cements in construction: a re-assessment, Concrete Society Technical Report TR 46, 1997.

[44] K.L. Scrivener, Historical and present day applications of calcium aluminate cements, Proceedings of the International Conference on Calcium Aluminate Cements (CAC), Heriot-Watt University, Edinburgh, Scotland, UK, IOM Communications, 2001, pp. 3–23.

[45] P.S. Mangat, B.T. Molloy, Prediction of long term chloride concentration in concrete, Mater. Struct. 27 (1994) 338–346.

Supplementary Section

I and Cl Calibration Curves

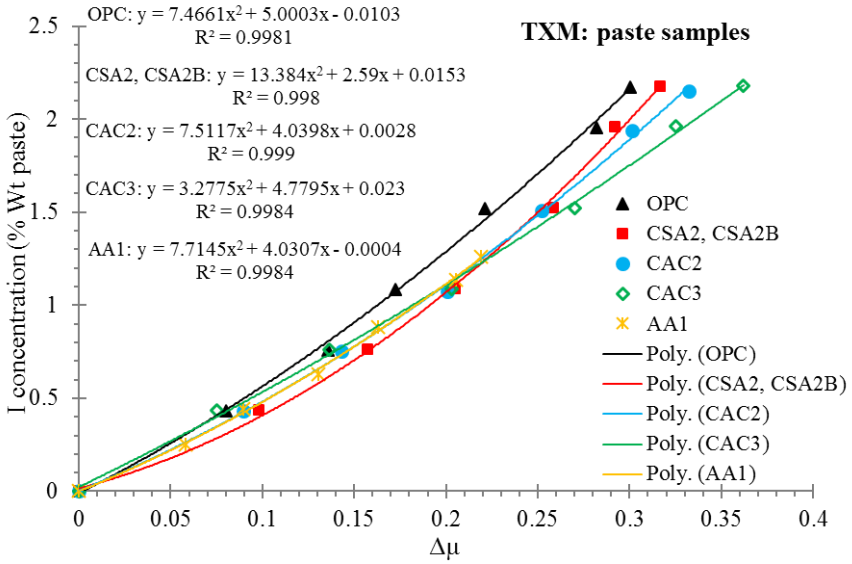

Fig. 5.S1 I calibration curve used to change from attenuation to weight percentage in the TXM analysis – paste samples.

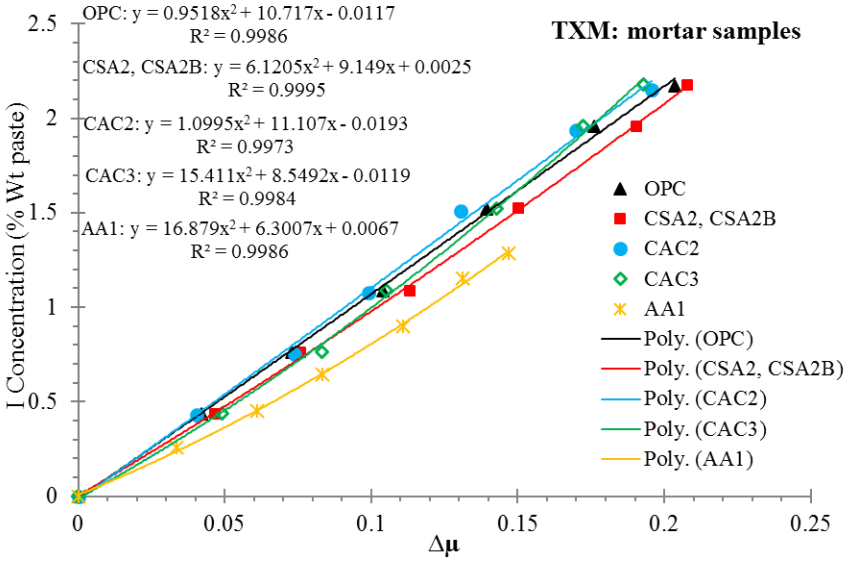

Fig. 5.S2 I calibration curve used to change from attenuation to weight percentage in the TXM analysis – mortar samples.

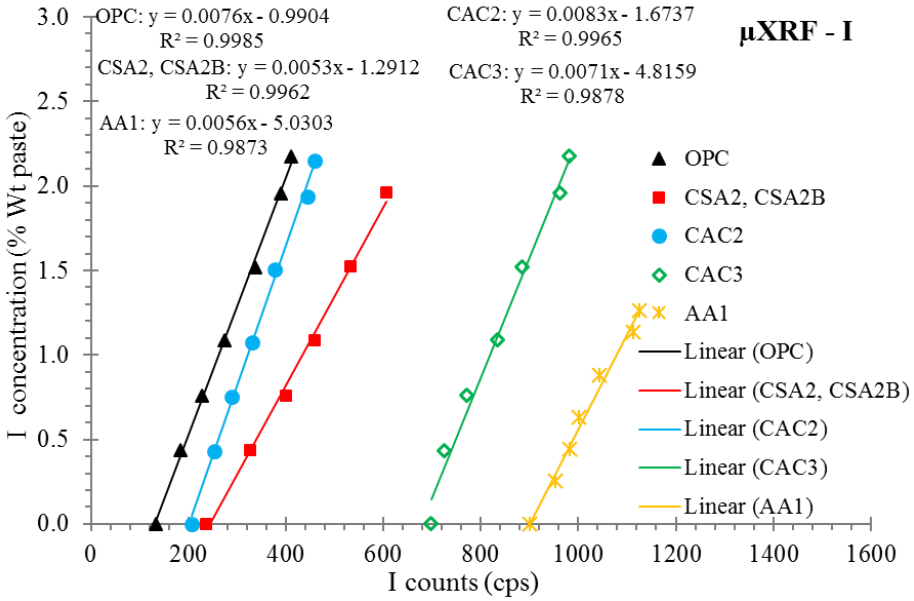

Fig. 5.S3 I calibration curve used to change from counts to weight percentage in the µXRF analysis of the paste samples.

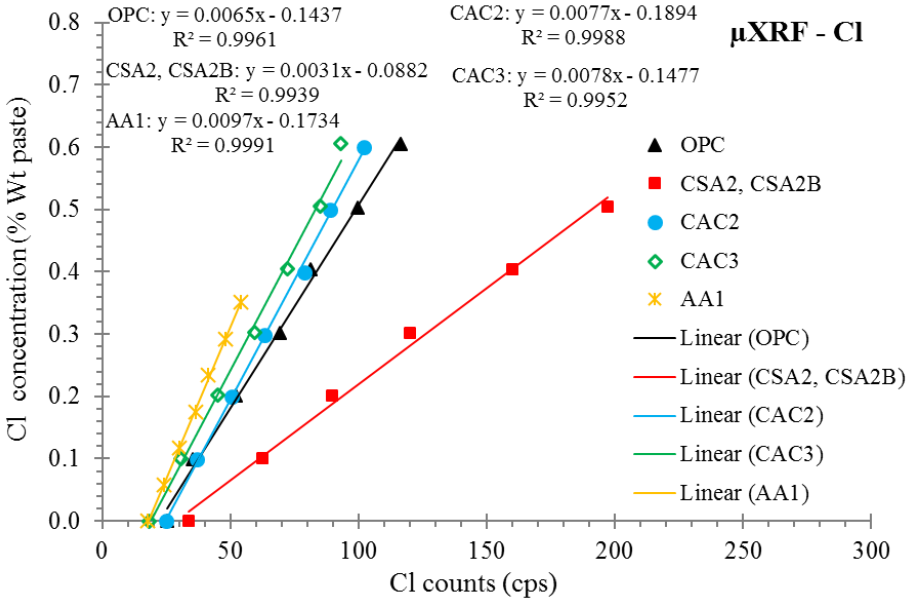

Fig. 5.S4 Cl calibration curve used to change from counts to weight percentage in the µXRF analysis of the paste samples.

CHAPTER VI

APPLICATION OF MICRO X-RAY FLUORESCENCE TO STUDY THE SILANE RESISTANCE TO PENETRATION OF CHLORIDE IONS

Abstract

The most prevalent and costly durability problem with structural concrete is the corrosion of internal reinforcing steel from chloride ions. One cost effective method to extend the service life of concrete is to use hydrophobic sealers that decrease the penetration of fluids. Silane is a commonly used surface treatment to reduce fluid entry into the concrete matrix. This chapter uses micro X-ray fluorescence (μXRF) to compare the Cl penetration resistance of the new two-part silane-epoxy system with a widely used type of silane in Oklahoma. Based on results, the two part silane-epoxy system showed better performance over the first 90 days but then similar performance to conventional silane at 180 days. However, both of silane systems have significantly reduced Cl penetration into concrete samples after 6 months of ponding.

Keywords: Service life; Durability; Chloride; Corrosion; Silane.

6.1 Introduction

Concrete structures face a multitude of problems that threaten the serviceability of the structure, one of the largest being chloride ingress [1-3]. Chlorides permeate through the concrete matrix causing corrosion of the steel reinforcement. According to a study conducted by the Federal Highway Administration (FHWA), the total direct cost of corrosion from 26 analyzed sectors was determined to be $279 billion per year in the United States. Of this total, it was estimated that $8.3 billion in damages occurred specifically to highway bridges [4].

One cost effective method to prevent chloride ingress is the use of protective coatings. These coatings reduce chloride ingress by either clogging the pores of the matrix thus reducing the material that permeates into the concrete, or by lining the concrete pores with a water repellent coating [5-8]. An example of the latter is organosilane or silane. Silane is used by the state of Oklahoma and many others to prolong the service life of bridge decks. These coatings are advantageous because they line pores and make them hydrophobic providing a barrier to ingress of water but allowing vapor in or out of the concrete. As vapor is allowed to leave the concrete, the internal moisture of the concrete is thought to decrease over time. A wide range of silane sealers are currently available for protection of concrete. However, the availability of various silanes makes the right selection difficult since they can provide different levels of protection. This chapter uses micro X-ray fluorescence (μXRF) to compare the Cl penetration resistance of the new two-part silane-epoxy system with a widely used type of silane in Oklahoma. μXRF is a non-destructive chemical imaging technique which measures Cl profile with less human effort and provides important insights not possible with the typical profile grinding analysis [9-13].

6.2 Experiments

6.2.1 Materials

A concrete mixture with a water-to-cementitious ratio (w/cm) of 0.45 was investigated in this chapter. An ASTM C 618 Class C fly ash is used as 20% of the mass of the binder. The cement is an ASTM C 150; Type I. The chemical composition of cementitious materials is in **Table 6.1** and was obtained by bulk XRF. The coarse aggregate is a dolomitic limestone and the fine aggregate is a locally available natural sand. Two different sealers, an Alkyltrialkoxysilane (silane) and two-part silane-epoxy system (sinale-epoxy) are used to seal and waterproof concrete surfaces. The properties of applied silanes are given in **Table 6.2**.

Table 6.1 Chemical composition with bulk XRF

Binder	cement	fly ash
SiO_2 (%)	20.40	38.71
Al_2O_3 (%)	5.03	18.82
Fe_2O_3 (%)	2.95	5.88
CaO (%)	62.89	23.12
MgO (%)	2.08	5.55
Na_2O (%)	0.35	1.78
K_2O (%)	0.35	0.58
TiO_2 (%)	0.28	1.35
MnO_2 (%)	0.10	0.02
P_2O_5 (%)	0.16	1.46
SrO (%)	0.16	0.39
BaO (%)	0.12	0.72
SO_3 (%)	3.05	1.27
L.O.I (%)	2.09	0.35
Moisture (%)	0.16	0.11

Table 6.2 Properties of applied silanes

Type	chemical type	solid content (by weight)	density (kg/m^3)	application rate (m^2/L)
Silane	Alkyl trialkoxy silane	> 40%	810	3.0 - 6.1
Silane-epoxy	Alkyl trialkoxy silane	100%	920	2.45

6.2.2 Mixture Proportion and Sample Preparation

The concrete mixture was prepared according to ASTM C 192. All of the aggregate, both coarse and fine, were brought into the temperature controlled mixing facility at least a day before and their batch weights were corrected based on their moisture content. The aggregates were charged into the mixer along with approximately two-thirds of the mixing water. The combination was mixed for 3 min. Next, the walls of the mixer were scraped to remove material that stuck to the walls. Then the cement and fly ash was loaded into the mixer, followed by the remaining mixing water. The mixer was turned on for 3 min. Once this mixing period was complete, the mixture was left to ‘‘rest’’ for 2 min while buildup of material along the walls was removed. Next the mixer was run for 3 min. After mixing, the slump, unit weight, and the air content were measured according to ASTM C 143, ASTM C 138, and ASTM C 231, respectively. The concrete mixture proportion is given in **Table 6.3**.

The concrete was placed in 10 x 10 x 8 cm plastic molds. The samples were sealed cured for seven days at 23°C. Three samples were used for each sealer type and three samples as a control without any sealer. Next, all the samples were dried in an environmental chamber with a temperature of 23°C and 40% relative humidity for 70 days. Then the sample surface was cleaned to remove any residue before application of sealers.

Table 6.3 Concrete mixture proportion

Material	cement (kg/m^3)	fly ash (kg/m^3)	coarse agg. (kg/m^3)	fine agg. (kg/m^3)	water (kg/m^3)	w/cm
Content	290	72.5	1088.6	709	163	0.45

6.2.3 Silane Application

After drying period, all edges of the samples were sealed with wax. Then three samples were ponded with an silane with 40% solid content (conventional silane) and three others with silane with 100% solid content (silane-epoxy) for 1 h. Through successive iteration, it was found that after 1 h of ponding the 0.45 w/c concrete had a depth of conventional silane penetration of 3.2 mm.

Next, the surface of samples with the silane-epoxy was dried for 30 minutes at 23°C and 40% relative humidity before applying the epoxy sealer at the surface. The manufacturer instructions were followed for mixing and applying the epoxy with a brush. A fine aggregate was then broadcast on the sample surface to follow the field application procedure. Weights of samples are measured before and after ponding with silane and epoxy to determine the amount of penetrated silane and the application rate of epoxy polymer. Then all samples were dried in an environmental chamber at 23°C and 40% relative humidity for 21 days after silane application.

6.2.4 Ponding in Sodium Chloride Solution

After drying, the area between the concrete and the container was sealed with wax and the specimen was then stored in saturated lime solution for three days. This was done to fill the surface pores with lime water. The weight before and after saturation was measured to determine a mass change after ponding. Next, the specimen was ponded with 165 g/L aqueous sodium chloride solution according to ASTM C1556 for either 45, 90, or 180 days at 23°C. After the ponding period, the Cl solution was removed and the samples were stored for 24 hours in

laboratory conditions. Then, samples were cut and the exposed cross section was polished on a sanding belt for 5 minutes with 120 grit sandpaper to create a flat surface. Ethanol was then used to remove dirt and residue from the polished surface. This flat surface allowed for easier interpretation of the μXRF and optical microscopy results.

6.2.5 μXRF Test Procedure

The μXRF analysis was conducted using the Orbis by EDAX. The instrument uses an 80 mm^2 Silicon Drift Detector Energy Dispersive Spectrometer (SDD-EDS) and a capillary optic that produces a 50 μm diameter beam. Images are created by moving the sample under the stationary X-ray beam. The X-ray beam causes characteristic fluorescence X-rays to be emitted at each spot, the intensity of these characteristic X-rays are measured by the SDD-EDS and stored in a database for later processing and analysis. **Table 6.4** summarizes the settings used by the μXRF in this work. More details can be found in other publications [9-11].

Table 6.4 Summary of μXRF settings used

counts per second	minimum of 20,000
current	1 mA
dead time	maximum of 20%
dwell time	400 ms/pixel
Filter	25 μm Al
vacuum	1.0 Torr
voltage	40 keV

Next, a set of reference standards were used to develop a calibration curve to change the count data to Cl concentration. This was done by making concrete samples with known amounts of NaCl. The samples were then cured for seven days, polished, and then cleaned as described previously.

6.2.6 Determining Silane Depth of Penetration

After cutting the samples, a cross section was exposed by polishing with 120 grit sandpaper for 5 minutes. Then the sample is ponded in water for 60 s to determine hydrophobic region. Next, the depth of the silane was measured at six different points by using a caliper and an optical microscope and an average was reported for each sample.

6.2.7 μXRF Data Analysis

After each sample is scanned with μXRF, the compositional maps were analyzed with an image processing software package called Lispix [14]. This program groups areas of similar composition, which are referred to as clusters. This analysis is helpful as one can combine individual compositional maps into a single map that simultaneously provides unique compositions and location. This separation of unique regions is useful in data display and analysis. For example, the cement paste was defined and separated by different elemental concentration levels (i.e., different levels of Cl). These regions were separated by selecting threshold values for different elemental concentration levels (i.e., observed low, medium and high counts of a given element). These ranges were chosen by the user to show that there are distinct differences in concentration within the sample. This single map of paste provides a complete separation of the different Cl levels in the paste and is useful for displaying the data and not for data analysis.

Finally, an image analysis code in Matlab was developed to analyze the spatial and compositional data. A border detection algorithm is used to find the top surface of the sample. The sample is then separated into 0.50 mm layers of equal thickness from the surface of the sample through the entire depth. The average Cl counts in each layer can then be plotted for different depths. Next, developed calibration curves are used to convert Cl counts to concentrations. Additional details can be found in previous publications [9-11].

6.3 Results and Discussion

6.3.1 Silane Application Rate and Penetration Depth

The penetration depth and amount of material based on mass change are given in **Table 6.5**. In addition, **Figure 6.1** illustrates the silane penetration depth for samples with different sealer types. Based on weight change after applying the epoxy polymer on treated samples, the application rate of epoxy polymer is 3.8 kg. per sq. m. The epoxy-silane had 20% more penetration than conventional silane. This may provide a longer effective life if deterioration from high alkaline pore solution. This greater penetration could be due to differences in the formulations of silane-epoxy (100% solid content) and silane (40% solid content) or the reduction in evaporation caused by the epoxy coating used with the silane-epoxy. More work on this topic is needed to draw further conclusions.

Table 6.5 Silane application rate and penetration depth

Sealer type	silane	Silane-epoxy
Ave. silane uptake (% Wt sample)	0.21±0.02	0.31±0.02
Ave. silane penetration depth (mm)	3.6±0.2	4.3±0.2

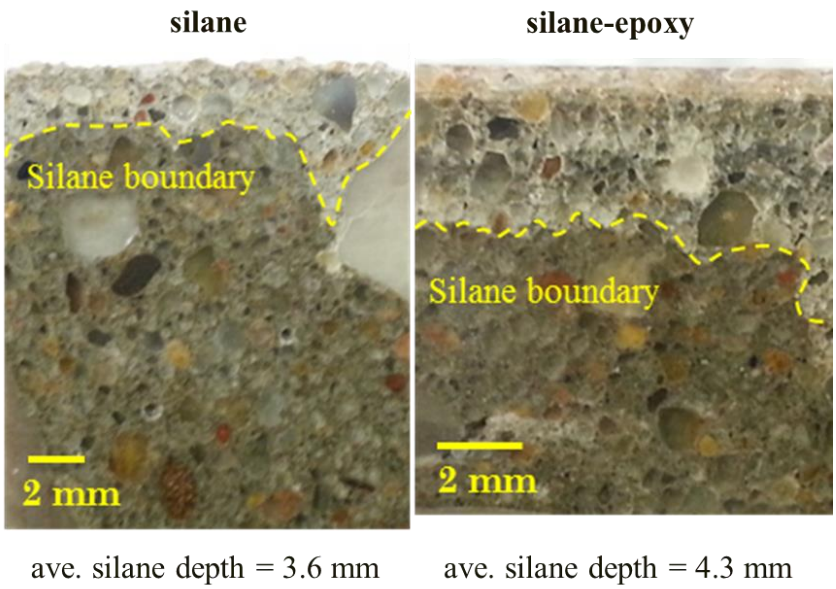

Fig. 6.1 Silane penetration depth: (left) concrete sample with conventional silane (right) concrete sample with silane-epoxy.

6.3.2 Mass Change after Ponding in Lime Water

The average mass change of specimens is compared in **Fig. 6.2**. Results show that applying either sealer systems reduced water uptake by about seven times when compared to the control samples. The samples with silane-epoxy showed a little higher water uptake than samples with silane. This could be due to the water absorption by the sand placed on the surface of the samples with silane-epoxy.

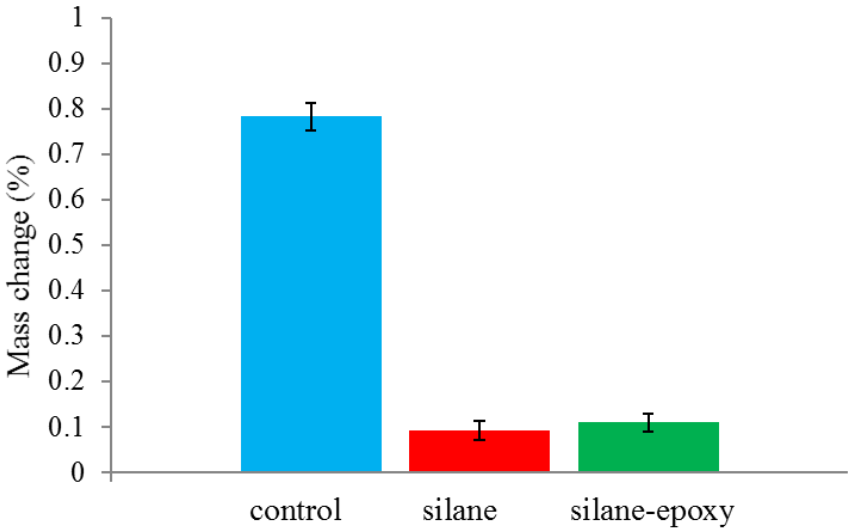

Fig. 6.2 Mass change of different samples after ponding in lime water.

6.3.3 Compositional Maps and Cl Concentration Profiles from µXRF

Figures 6.3 to 6.**5** compare a segmented paste map and concentration profiles of the different samples after 45, 90 and 180 d of ponding with the NaCl solution. In addition, a comparison between treatments performance against Cl uptake over time is shown in **Fig. 6.6**. Based on segmented paste maps in **Figs 6.3** to **6.5**, both of the sealers showed significant reduction in the Cl penetration into the concrete samples over time. The Cl profiles confirm the results of the segmented maps and provide a quantitative measurement. In the control sample, Cl penetrated up to 13.5 mm, while Cl penetration depth is limited to 2 mm in the silane sample and almost immeasurable amounts of penetration for silane-epoxy sample after 45 d of ponding. This suggests the silane-epoxy system seems to show superior abilities to resist Cl penetration at early ages. In addition, the silane and silane-epoxy reduced total Cl uptake about 85% and 99% when compared to the control sample at 45 d of ponding, respectively. The conventional silane still shows limited depth of Cl penetration (8 mm) compared to control sample (20 mm) after 180 d ponding and the silane-epoxy reduced Cl penetration by nine times when compared to the control sample after 180 d ponding. Based on **Fig. 6.6**, it seems that the two part silane-epoxy system

showed better performance over the first 90 days but then similar performance to conventional silane system at 180 days. This is likely caused by deterioration of the epoxy sealer over ponding time.

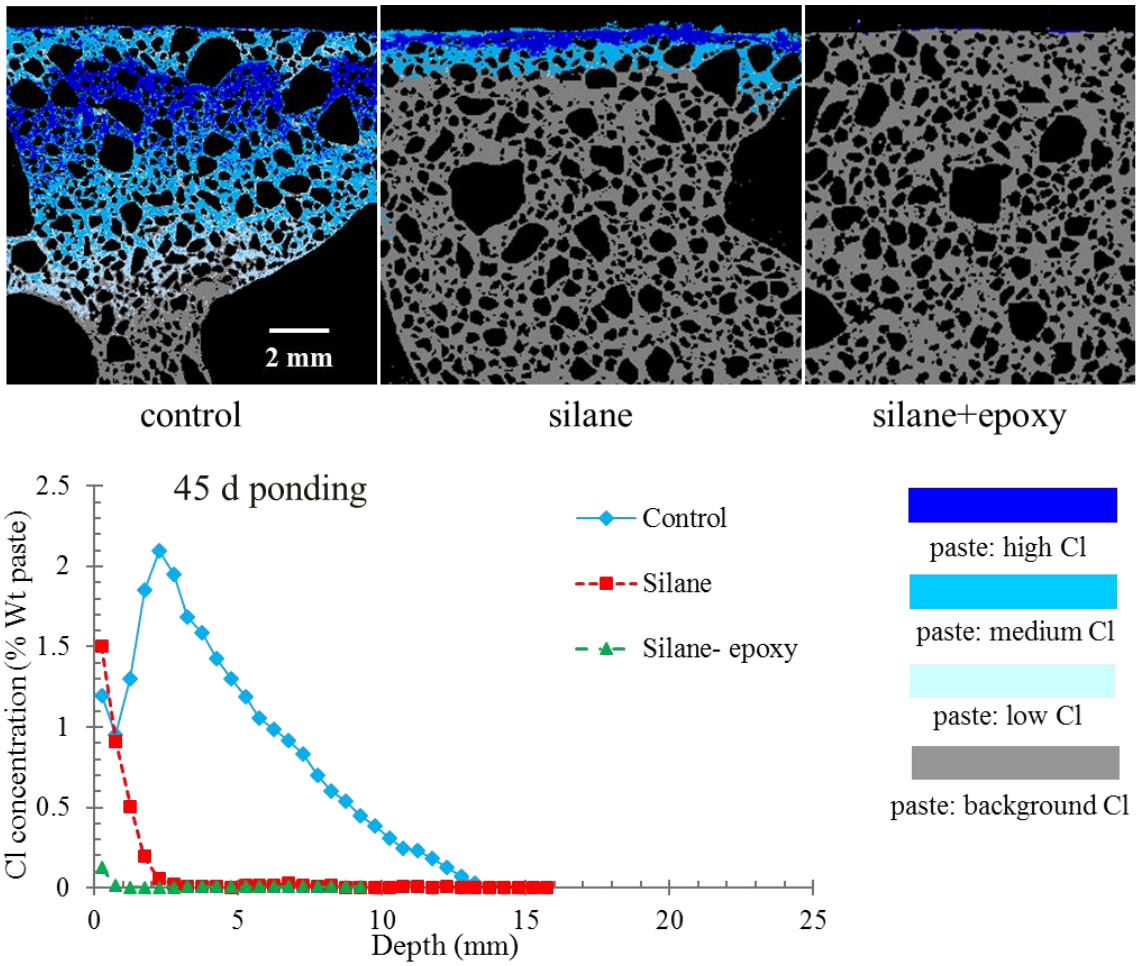

Fig. 6.3 Paste compositional maps and Cl concentration profiles of different samples after 45 d of ponding - µXRF.

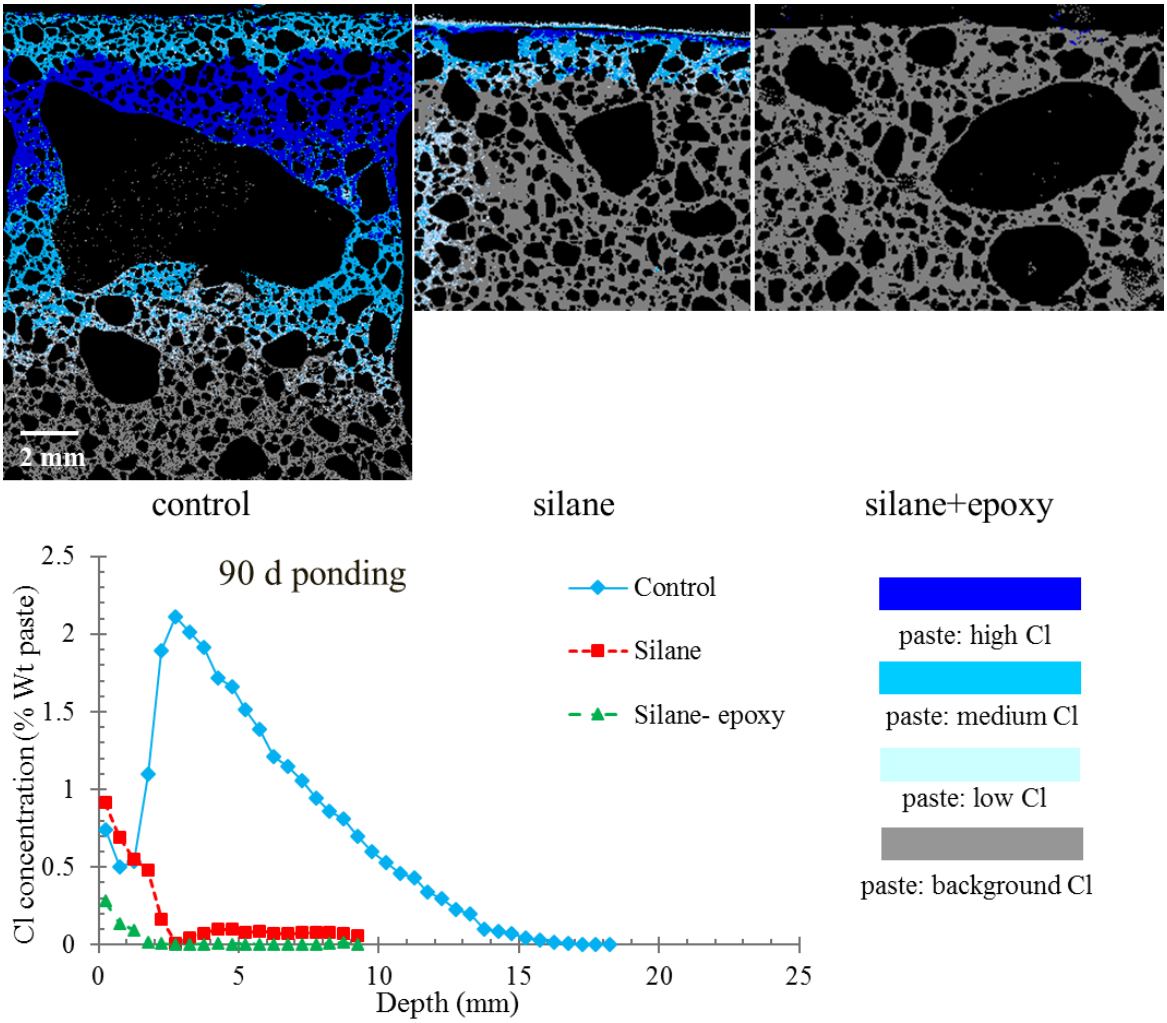

Fig. 6.4 Paste compositional maps and Cl concentration profiles of different samples after 90 d of ponding - µXRF.

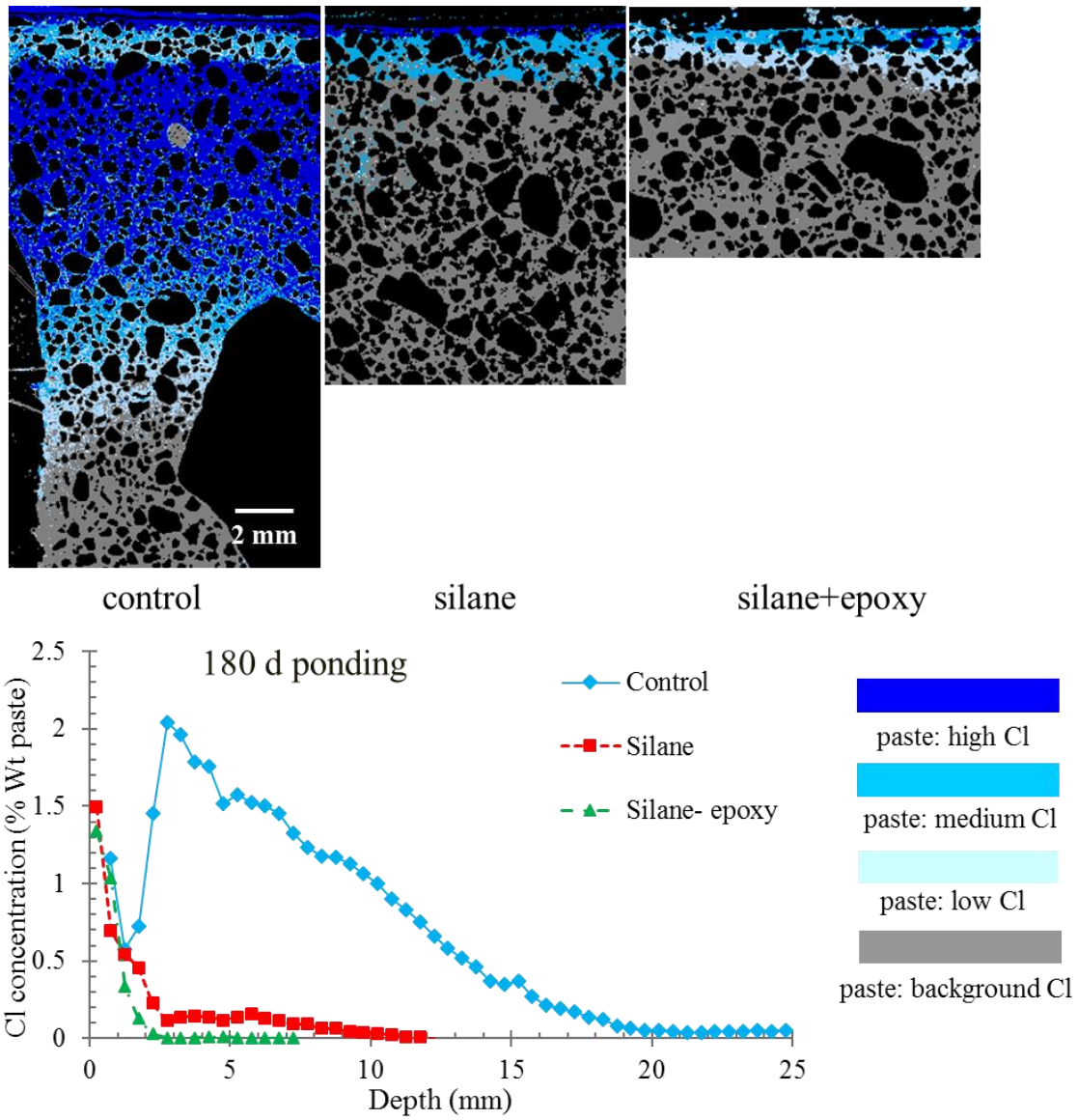

Fig. 6.5 Paste compositional maps and Cl concentration profiles of different samples after 180 d of ponding - µXRF.

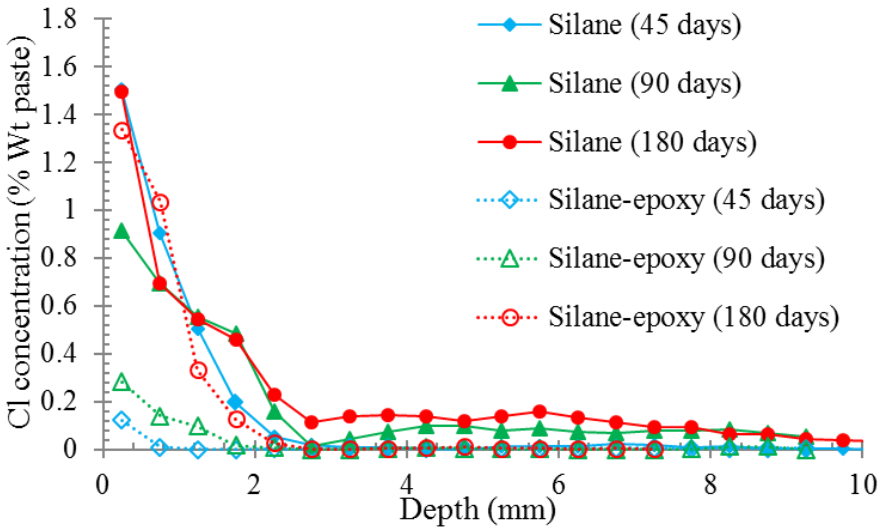

Fig. 6.6 Comparison of treatments performance against Cl uptake over time.

6.4 Conclusions

In this chapter, a micro X-ray fluorescence (μXRF) is used to compare the Cl penetration resistance of two sealer systems in comparison to concrete without the sealer. The following observations were made:

- The two-part silane-epoxy sealer system shows 20% greater penetration when compare to a silane commonly used in Oklahoma when they were applied in the same manner on the same concrete.
- Both of silane systems have significantly reduced Cl penetration into concrete samples after 180 d ponding.
- The two part silane-epoxy system showed better performance over the first 90 days but then similar performance to commonly used silane system at 180 days. This is likely caused by deterioration of the epoxy sealer.

This work shows the utility of using μXRF to efficiently and rapidly evaluate Cl profiles in concrete samples and compare the effectiveness of different sealers.

References

[1] P.K. Mehta, Durability of Concrete- Fifty Years of Progress?, ACI SP 126-1, (1991) 1-31.

[2] M. Khanzadeh Moradllo, B. Sudbrink, M.T. Ley, Determining the effective service life of silane treatments in concrete bridge decks, Constr. Build. Mater. 116 (2016) 121–127. doi:10.1016/j.conbuildmat.2016.04.132.

[3] M. Khanzadeh-Moradllo, Mehdi; Meshkini, Mohammad H; Eslamdoost, Ehsan ; Sadati, Seyedhamed; Shekarchi, Effect of Wet Curing Duration on Long-Term Performance of Concrete in Tidal Zone of Marine Environment, Int. J. Concr. Struct. Mater. 9 (2015) 487–498. doi:10.1007/s40069-015-0118-3.

[4] G.H. Koch, M.P. Brongers, N.G. Thompson, Y.P. Virmani, J.H. Payer, Corrosion costs and preventive strategies in the United States, Report by CC Technologies Laboratories, Inc. to Federal Highway Administration (FHWA)-RD-01-151, September 2001.

[5] A. Bentur, S. Diamond, N. Berke, Steel Corrosion in Concrete: Fundamentals and civil engineering practice, E & FN Spon, London, 1997, 123-189.

[6] A.A. Kamel, T.D. Bush, A.P. Hagen, Silane performance: Testing procedures and effect on concrete mix design, Transp. Res. Rec. 13 (1993) 32-37.

[7] L. Schueremans, D. Van Gemert, Service life prediction model for reinforced concrete constructions, treated with water-repellent compounds, In: Proceeding of Conchem. Dusseldorf, 1997, pp. 103-113.

[8] M. Khanzadeh Moradllo, M. Shekarchi, M. Hoseini, Time-dependent performance of concrete surface coatings in tidal zone of marine environment, Constr. Build. Mater. 30 (2012) 198–205. doi:10.1016/j.conbuildmat.2011.11.044.

[9] M.T. Ley, B. Sudbrink, H. Kotha, N. Materer, A. Apblett, Expected life of silane water repellant treatments on bridge decks, Research & Development Division Oklahoma Department of Transportation. No. FHWA/ODOT-2229, December 2012.

[10] B. Sudbrink, M. Khanzadeh Moradllo, Q. Hu, M.T. Ley, J.M. Davis, N. Materer, A. Apblett, Imaging the presence of silane coatings in concrete with micro X-ray fluorescence. Cem.Concr. Res. (2016); accepted for publication. doi:10.1016/j.cemconres.2016.11.019.

[11] M. Khanzadeh Moradllo, B. Sudbrink, Q. Hu, M. Aboustait, B. Tabb, M.T. Ley, J.M. Davis, Using micro X-ray fluorescence to image chloride profiles in concrete. Cem.Concr. Res. (2016), in press. doi:10.1016/j.cemconres.2016.11.014.

[12] J.M. Davis, D.E. Newbury, A. Fahey, N.W.M. Ritchie, E. Vicenzi, D. Bentz, Bridging the micro-to-macro gap: a new application for micro X-ray fluorescence., Microsc. Microanal. 17 (2011) 410–417. doi:10.1017/S1431927611000183.

[13] J.M. Davis, D.E. Newbury, P.R. Rangaraju, S. Soundrapanian, C. Giebson, Milli X-ray fluorescence X-ray spectrum imaging for measuring potassium ion intrusion into concrete samples, Cem. Concr. Compos. 31 (2009) 171–175. doi:10.1016/j.cemconcomp.2008.12.005.

[14] D. Bright, Lispix: An image processing and analysis tool for the PC, 2011. http://www.nist.gov/lispix/doc/contents.htm, (last accessed on August 2016).

CHAPTER VII

DETERMINING THE EFFECTIVE SERVICE LIFE OF SILANE TREATMENTS IN CONCRETE BRIDGE DECKS

Abstract

Silane is a commonly used surface treatment to reduce water entry into concrete. Only limited work has been done to show the effective lifespan of silane treatments. This work uses 360 cores taken from 60 bridge decks treated with silane that have been in-service between 6 and 20 years. Optical staining techniques showed that the average silane thickness started decreasing after 12 years of service. The deterioration primarily occurs from the bulk of the concrete towards the surface. This suggests that deterioration from the alkali pore solution of the concrete may be important.

Keywords: Hydrophobic treatment; Mass transport; Corrosion; Durability; Chloride.

7.1 Introduction

When external liquids penetrate into concrete then corrosion, alkali silica reaction, sulfate attack, bulk freezing and thawing damage, and scaling can occur [1-2]. One cost effective method to extend the service life of concrete is to use protective coatings that decrease the penetration of these fluids. This is done by either lining the concrete pores with a hydrophobic surface, filling the pores, or a combination of these [3-6].

Organosilanes or silanes are monomeric silicon-containing chemicals that contain at least one carbon-silicon bond. The organic groups of the silane are bound to the silicon atoms by hydrolytically-stable carbon-silicon bonds and they coat the surface of the pores with a non-polar, low surface energy, and hydrophobic lining [7-10]. This coating inhibits water intrusion, but allows vapor in or out of the concrete [11]. Silanes are usually dissolved in a carrier, such as water or alcohol, to ensure deeper and more equal distribution into the concrete. The performance of silanes is a balance between the amount of active ingredients and the ability of the carrier to penetrate into the concrete [8, 11, 12-14].

Although silanes have been proven to be effective at reducing the ingress of brine solutions [15-17], little work has been done to show the effective lifespan of these pore lining materials and their long-term performance [18]. The effectiveness of silanes has been suggested to decrease from ultraviolet light, physical abrasion, weathering, and alkaline attack of the hydrophobic molecules [19-22]. The latter deterioration mechanism could be caused by a breakdown of silicon bonding by the alkalinity of pore solution [22-23]. Tosun et al. [23] have observed the loss of Si-O and Si-O-Si bonds of silane hydrophobic layer in high alkaline environments by using Fourier transform infrared spectroscopy (FT-IR) analysis on concrete samples.

One method for evaluating the long-term performance of silanes is to conduct a field assessment of in-service structures [12]. Currently, there is little guidance in the literature about the expected

lifespan of silanes from field structures. According to Christodoulou et al. [18], silane treatments on eight bridges in the United Kingdom maintained a hydrophobic lining after 20 years of service. Schueremans et al. [24] showed that a silane treated sea wall maintained a reduced rate of chloride penetration after 12 years of exposure in an aggressive marine environment in Belgium. According to Weyers et al. [25], the estimated service life of silane is 9 to 10 years based on the estimated rate of abrasion for two highly traveled bridges in the United States. This limited number of studies shows that only a small collection of information exists for the field performance of silane treatments.

The objective of this study was to evaluate the performance of silane treatments for 60 bridges that were in-service between 6 and 20 years in the state of Oklahoma, in the United States. The bridges were in a hot and humid climate with moderate deicer usage during the winters. The samples were investigated with techniques that stain non-hydrophobic portions of the concrete [26-27]. These findings will be helpful to practitioners to determine the long-term performance of silane treatments.

7.2 Experimental Methods

7.2.1 Sample Acquisition

Cores that were approximately 18 mm in diameter by 25 mm in height were taken from the driving lane and shoulder of 60 bridge decks. Six cores were taken from each bridge for a total of 360 cores. Three cores were taken from the shoulder and three from the travel lane. These cores were taken at parallel locations so that the amount surface wear could be compared. Cores were taken from areas that were clear of debris, cracks, oil, and salt scaling damage. These cores were also inspected to be sure that they did not contain a large aggregate near their surface as this would interfere with the measurement of the silane penetration. If this occurred then another core was taken. These cores were collected with a cordless drill without using water to cool the

bit. This technique allowed two researchers to sample each bridge in about 1 h. This minimized the requirement for traffic control and allowed more samples to be collected in a day. Since the cores were small, this minimized damage and patching to the bridges. These bridges had an age range of 6 to 20 years. Details about the sampled bridges can be found in another publication [28]. The investigated bridges had an average annual daily traffic (AADT) between 3,800-18,000 [29]. Typical weather conditions in Oklahoma are shown in **Fig. 7.1**.

Although the concrete mixture designs and silanes varied, all of them were constructed to known specifications [30]. The concrete mixture had a maximum water to binder ratio of 0.42, a minimum cement content of 335 kg/m^3 and class C fly ash was allowed to be used at 20% replacement. All approved silanes are alcohol based with a recommended coverage rate of 3.7-6.1 m^2/L and used between 40% and 50% active ingredient and were treated within a year of construction. The specified depth of silane was 3.2 mm (1/8") or greater and was verified by using a dye and visual inspection with an optical microscope from extracted cores at the time of construction by the Oklahoma Department of Transportation.

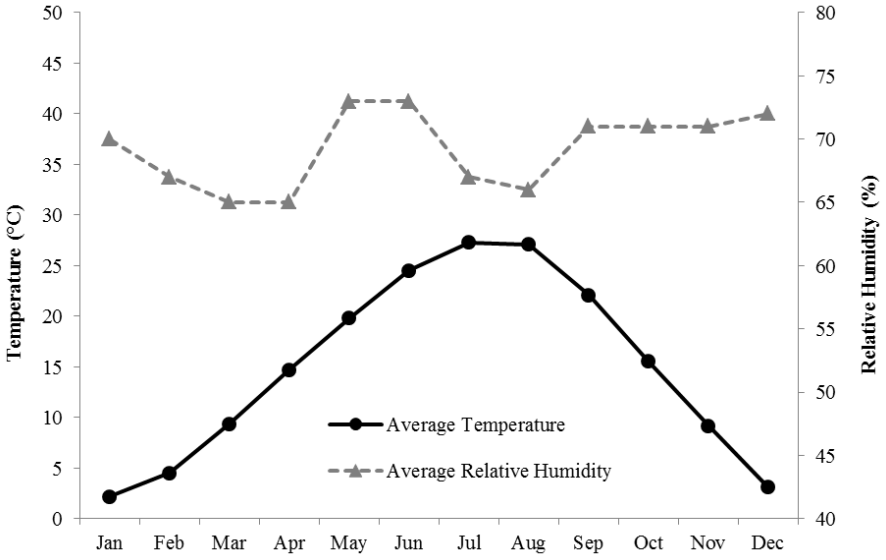

Fig. 7.1 Variations in mean ambient temperature and relative humidity of Stillwater, Oklahoma [31].

7.2.2 Sample Preparation and Testing

A cross section of each core was exposed by polishing with 120 grit sandpaper for 5 minutes. Next, the polished surface was cleaned with ethanol to remove any dirt and residue. A new piece of sand paper was used for each sample. Each sample was inspected with two techniques to determine the presence of the silane.

First, the core is ponded in blue clothes dye for 30 minutes. The dye stains the concrete that is not treated with the silane. An example can be seen in **Fig. 7.2b**. Past publications used X-ray fluorescent microscopy to image silane sealed concrete before and after treatment with the dye to verify the accuracy [26-27]. Next, the depth of the silane was measured at six different points by using a caliper and an optical microscope and an average was reported for each core.

Next, the core was polished to remove the dye from the exposed surface and then ponded in mineral based cutting oil for 60 seconds. The oil will wet the surface of the concrete that does not contain the silane. The depth is then measured as described previously with the optical microscope and calipers. Typical results are shown in **Fig. 7.2c**. Both methods had good agreement with one another and allowed a verification of the measurement. While it common practice to use water to highlight the silane layer, this method was not successful with any of the samples that had been in the field for more than six years.

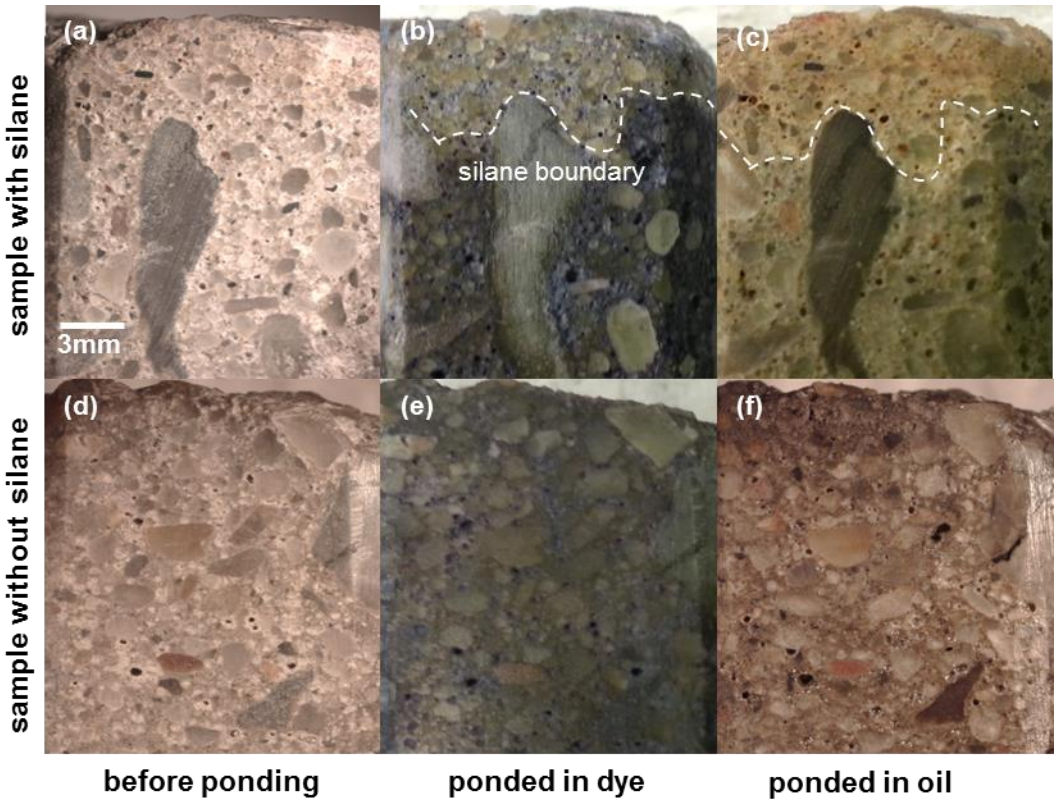

Fig. 7.2 Example of cores before and after being ponded in the blue dye and oil. (a) core containing silane before ponding (7 years old sample) (b) core containing silane after ponding in dye (c) core containing silane after ponding in oil (d) core without silane before ponding (17 years old sample) (e) core without silane after ponding in dye (f) core without silane after ponding in oil.

7.2.3 Statistical Analysis Methods

The results were statistically analyzed with an analysis of variance (ANOVA) together with a Duncan's multiple range pairwise comparison. ANOVA is an appropriate procedure for testing the equality of several means. Duncan's multiple range pairwise comparison is useful for pairwise comparison of group means. This is useful to establish the population means of two groups are statistically different from one another [32-34]. In the ANOVA, the dependent variable was the mean of the silane depth, and the independent variable was the age of bridge decks. The statistical analysis was undertaken to compare the average silane depths from different bridges with various

ages and to evaluate the significance of difference between the averages. In addition, two-way ANOVA was used to determine the significance of difference between results of travel lane and shoulder.

7.3 Results and Discussion

7.3.1 Silane Penetration Depth

Figures 7.3 and **7.4** show the average and standard deviation of the silane depth from the three cores in the travel lane and shoulder for each bridge. A horizontal line at 3.2 mm is shown in the graphs, as this is the minimum value required by specification and verified at construction. Based on results, all of the bridges that are less than 12 years old showed a silane depth higher than 3.2 mm. After 15 years of service, 67% of the bridges (8/12) had a silane depth greater than 3.2 mm. For bridges that had 17 to 20 years of service, 16% (3/19) of the bridges had a silane depth greater than 3.2 mm.

Based on Duncan's multiple range pairwise comparison, no significant difference was found between the means of silane depth of bridges with age of 6 to 12 years. The difference between means of silane depth of bridges with 17 to 20 years of age was also not significant. Therefore, the investigated bridges were grouped into three age intervals to further discuss their performance: 6 to 12 years old, 15 years old and 17 to 20 years old.

Table 7.1 shows the average and standard deviation of the silane treatments and the percentage of bridges that had silane treatments greater than or less than 3.2 mm. Comparing the silane thickness to 3.2 mm is useful because all of the silane treatments should have been greater than this at construction. If the thickness is less than 3.2 mm then it suggests that the material may be deteriorating. This is discussed in more detail in the mechanism section.

Table 7.1 shows that the average depth of silane is decreasing with time for the cores from the main lane and the shoulder. After 15 years of service the average silane layer thickness reduced by 25% compared to the bridges that were less than 12 years of age. For bridges with 17 to 20 years of service, the average layer thickness reduced by 75% compared to the bridges that were less than 12 years of age. Previous studies based on various experimental methods also showed that silane treatments can successfully perform in different environmental conditions for 9-15 years [18, 20, 24-25].

Based on the ANOVA analysis, there is a probability of less than 0.01% that the silane depth of bridge decks from 6-12 years of service and 17-20 years are the same. This means there is a significant difference between the mean silane depth of the two groups. In addition, the probability that the 15 year old and 17 to 20 year old bridges have an equal average silane depth is less than 1%.

One hypothesized reduction in silane effectiveness is removal by abrasion. The travel lanes on a bridge should receive significantly more traffic than the shoulders. By comparing the difference in between cores from these two locations then this will allow the impact of abrasion on silane thickness to be quantified. As described in the experimental methods, all comparisons between the traffic lane and shoulder are made at parallel locations and so this should be an appropriate comparison.

Figure 7.5 shows the difference between these two regions for each bridge and **Table 7.1** shows the average and standard deviation of the difference between the two locations. The means and standard deviations for these measurements were similar. Based on the two-way ANOVA analysis, there is a probability of less than 10% that the mean silane depth of travel lane and shoulder is not the same. This suggests that the differences between these regions are small and

that removal of the silane by abrasion was minimal over the first 20 years of service for the investigated bridges.

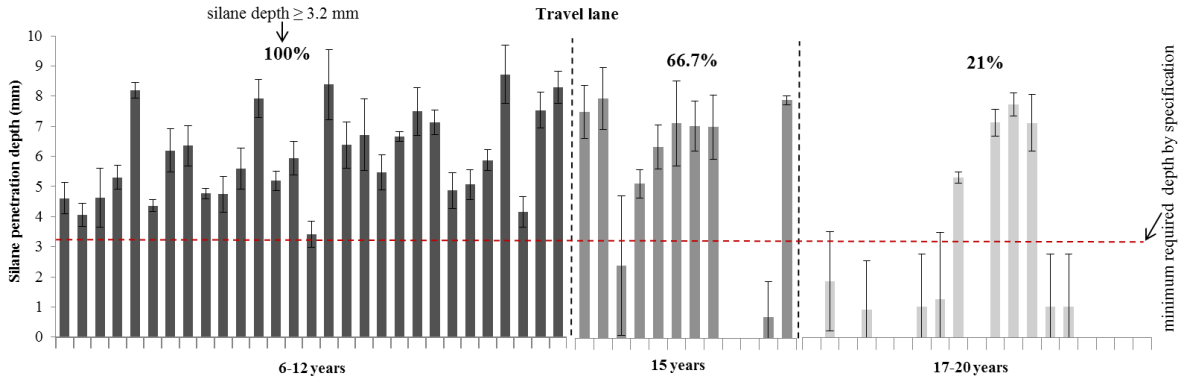

Fig. 7.3 Average silane visual detection depth of samples from bridge decks in travel lane.

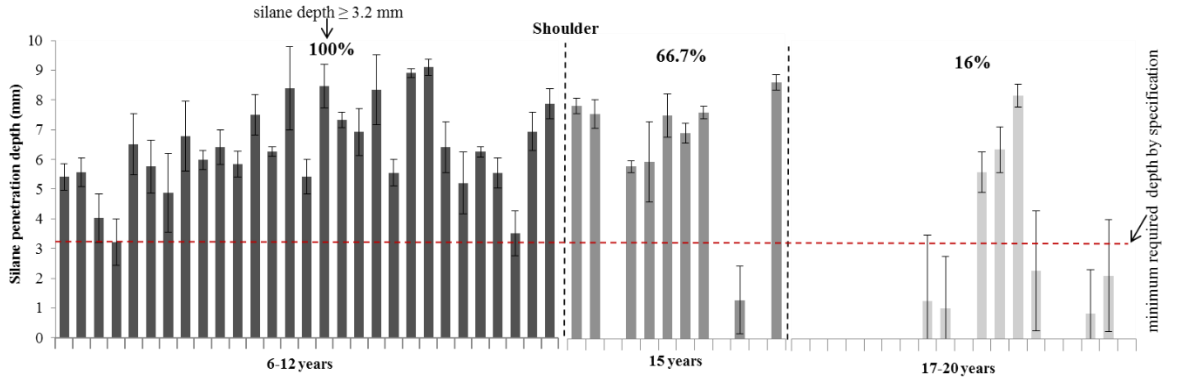

Fig. 7.4 Average silane visual detection depth of samples from bridge decks in shoulder.

Table 7.1 Summary of the number and the percentage of concrete bridge decks that still have an effective silane layer after a given service life.

Years of service		6-12 years	15 years	17-20 years
Total No. of bridges		29	12	19
Travel lane	silane depth ≥ 3.2 mm	29 (100%)	8 (66.7%)	4 (21%)
	silane depth < 3.2 mm	0 (0%)	4 (33.3%)	15 (79%)
Shoulder	silane depth ≥ 3.2 mm	29 (100%)	8 (66.7%)	3 (16%)
	silane depth < 3.2 mm	0 (0%)	4 (33.3%)	16 (84%)
Travel lane	average silane depth ±std (mm)	6.00±1.48	4.86±3.16	1.81±2.74
Shoulder	average silane depth ±std (mm)	6.36±1.51	4.79±3.40	1.45±2.48
average difference in silane depth in shoulder and travel lane ±std (mm)		1.19±0.83	0.64±0.63	0.91±1.08

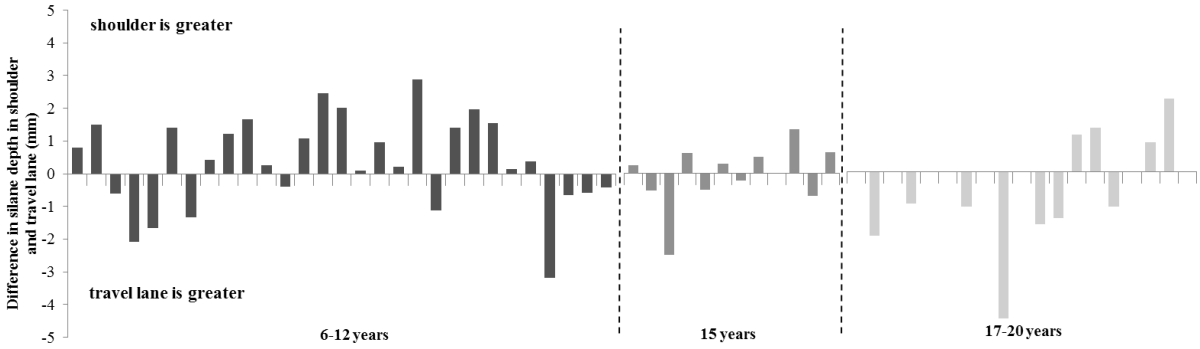

Fig. 7.5 Difference between silane penetration depth of travel lane and shoulder.

7.3.2 Mechanisms of Silane Deterioration

The work in this paper shows that the average silane layer starts to decrease after 12 years of service. Several mechanisms for silane deterioration have been proposed including: ultraviolet light, physical abrasion, deterioration from external moisture, and deterioration by the alkaline pore solution [19-22]. If the silane was deteriorating from ultraviolet light or from external moisture then we would expect there to be an area at the surface that lost silane and is no longer hydrophobic. An example of this is shown in **Fig. 7.6** from bridges that are 8 and 17 years old. However, this surface deterioration was observed in less than 5% of the samples investigated. This suggests that deterioration from ultraviolet light and external moisture is not a significant

deterioration mechanism for the materials, locations, and environmental exposure investigated. Moreover since there was very little difference in the silane depth between the driving lane and the shoulder, this suggests that abrasion is also not a major contributor to the silane deterioration.

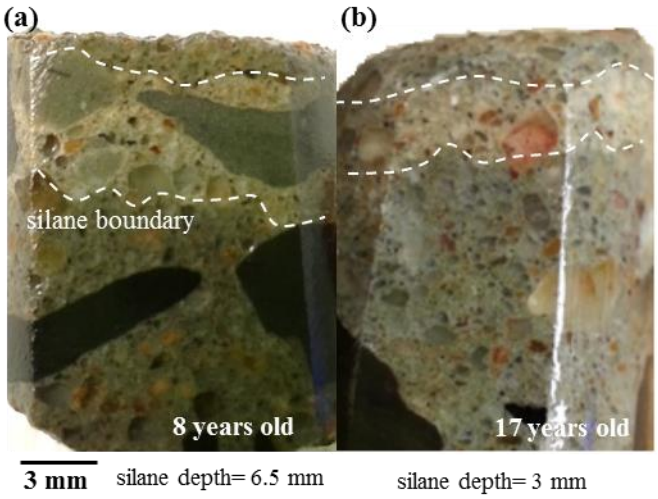

Fig. 7.6 Example of cores with surface silane deterioration. (a) 8 years old sample with average silane depth of 6.5 mm (b) 17 years old sample with average silane depth of 3 mm. This occurred in less than 5% of the bridges investigated.

Based on **Fig. 7.7**, the silane deterioration seems to move from the bulk of the concrete towards the surface. One possible cause for the deterioration of the hydrophobic could be the alkaline pore solution. As explained earlier, this could be caused by a breakdown of silicon bonding by the alkalinity of pore solution [22-23]. Tosun et al. [23] have observed the loss of Si-O and Si-O-Si bonds of silane hydrophobic layer in high alkaline environments by using Fourier transform infrared spectroscopy (FT-IR) analysis on concrete samples. The deterioration likely initiates in the bulk of the concrete because the pore solution would be more alkaline in the non-hydrophobic region.

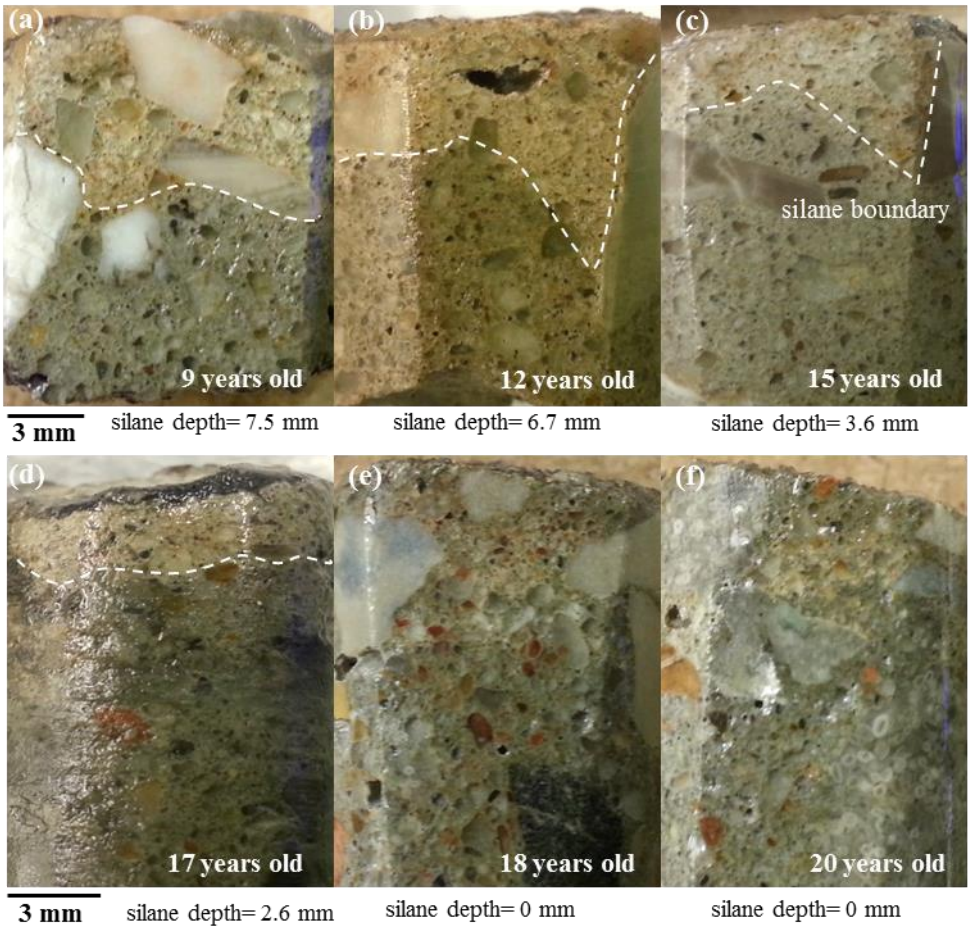

Fig. 7.7 Example of cores with different ages being ponded in the oil. (a) 9 years old sample with average silane depth of 7.5 mm (b) 12 years old sample with average silane depth of 6.7 mm (c) 15 years old sample with average silane depth of 3.6 mm (d) 17 years old sample with average silane depth of 2.6 mm (e) 18 years old sample without silane (f) 20 years old sample without silane.

7.3.3. Practical Recommendations

This work shows that silane treatments provide a hydrophobic surface on the concrete for about 12 years and then the thickness starts decreasing for the bridge decks investigated. Since the deterioration of the silane appears to be related to the alkaline pore solution, then one would expect similar performance in other locations and environments but at different rates depending on the average temperature and possibly humidity. However, mixtures that use higher dosages of

supplementary cementitious materials (SCMs), such as fly ash, slag, and silica fume, may see an even larger lifespan, as these materials are known to produce lower amounts of calcium hydroxide from dilution of portland cement and consume calcium hydroxide during their reaction. By decreasing the calcium hydroxide then this should decrease the alkalinity of the pore solution and possibly delay the attack on the silane treatment, and possibly prolong the life of the material. This is an area of future study. Another way to prolong the life of the material may be to use a thicker silane coating. This thicker coating should take longer to deteriorate from the attack of the concrete pore solution.

Other literature has suggested that silane should be reapplied at intervals of 10–20 years to stay effective [35-37]. Unfortunately, there is very little data about the effectiveness of reapplying silane or the expected lifespan of this new coating. This reapplication would be a function of the cleanness of concrete surface, exposure conditions, level of chloride ion contamination at the time of treatment, and the concrete quality. More research is needed to investigate these recommendations in field conditions.

7.4 Conclusion

This work used 360 cores from 60 concrete bridge decks with ages between 6 and 20 years that were treated with silane in order to determine the effective service life of silane treatments. Two different optical staining techniques were used on these cores to determine the average penetration of the silane with visual contrast.

The following observations were made:

- After 12 years of service, 100% of the bridge decks in the driving lane and the shoulders were found to have a silane layer greater than the minimum specified value of 3.2 mm.

- After 15 years of service, only 68% and after 17 to 20 years only 16% of the bridges showed evidence of a silane layer greater than 3.2 mm in thickness.

- The average depth of silane starts to decrease after about 12 years of service in both the main lane and the shoulder. For bridges with 15 and 17 to 20 years of service, the average silane layer thickness reduced by 25% and 75% respectively compared to the bridges that were less than 12 years of age.

- The silane thickness was similar for the samples from the travel lane and shoulder for all bridges. This suggests that abrasion was not a significant deterioration mechanism of the silane treatment for these structures.

- Less than 5% of the field samples showed deterioration of the silane treatment at the surface of the concrete. This suggests that damage from ultra violet light and external moisture was not significant, and the deterioration by the alkaline pore solution appears to be a more important silane deterioration mechanism for these materials and exposure level.

Although these findings are limited to the materials, environment, and construction practices used on these 60 bridges, this work suggests that silane treatments are a useful tool to help extend the service life of structural concrete. This work has shown that these materials have a limited lifespan and the results suggest that the deterioration is likely caused from the alkaline pore solution. More work is needed to understand how these findings translate to different environments and concretes.

Acknowledgements

The authors gratefully acknowledge the financial support from the Oklahoma Department of Transportation (ODOT). The authors would like to thank Mr. Jake Leflore, Mr. Colin Fleishacker, Mr. Chad Stevenson, and Mr. Jeffery Terronez for their assistance with conducting of the field experiments.

References

[1] P.K. Mehta, Durability of Concrete- Fifty Years of Progress?, ACI SP 126-1(1991) 1-31.

[2] M. Shekarchi, M. Khanzadeh Moradllo, S.R. Taheri, Corrosion Assessment in the Off-Shore Cooling Water Outlet Channel RC Structure of Thermal Power Plant Placed in Caspian Sea: A Case Study, International Conference on Durability of Building Materials and Components, Porto, Portugal, April 2011, pp:1-8.

[3] A. Bentur, S. Diamond, N. Berke, Steel Corrosion in Concrete: Fundamentals and civil engineering practice, London, E & FN Spon, 1997, 123-89.

[4] A.A. Kamel, T.D. Bush, A.P. Hagen, Silane performance: Testing procedures and effect on concrete mix design, Transp. Res. Rec. 13 (1993) 32-37.

[5] L. Schueremans, D. Van Gemert, Service life prediction model for reinforced concrete constructions, treated with water-repellent compounds, In: Proceedings of Conchem. Dusseldorf (Germany), 1997. p. 103-13.

[6] M. Khanzadeh Moradllo, M. Shekarchi, M. Hoseini, Time-dependent performance of concrete surface coatings in tidal zone of marine environment, Constr. Build. Mater. 30 (2012) 198–205. doi:10.1016/j.conbuildmat.2011.11.044.

[7] R. Anderson, B. Arkles, G.L. Larson, Silicon compounds register and review, Petrarch Product Catalog. Bristol, 1987.

[8] U. Attanayaka, S.Y.C. Ng, H. Aktan, Criteria and benefits of penetrating sealants for concrete bridge decks, Michigan Department of Transportation, 2002.

[9] Dow Corning . A guide to silane solutions from Dow Corning. Dow Corning: Chemical Manufacturing Solutions. 2005.

[10] E. Petrie, Handbook of adhesives, New York, McGraw Hill, 2007, 288-297, 554-559.

[11] P.D. Carter, Evaluation of dampproofing performance and effective penetration depth of silane sealers in concrete, ACI SP 151-5 (1994) 95-117.

[12] T.D. Bush Jr, A.A. Kamel, P.A. Kalluri, Influence of field variables on laboratory performance of silane treated concrete, ACI Mater J 94 (1997) 193-201.

[13] B. Kerkhoff, Effects of substances on concrete and guide to protective treatments. Skokie, Portland Cement Association, 2007.

[14] L.A. Stark, B. Narula, R.S. Woodward, New water-borne systems for the water repellent market. In: Proceeding of 19th Water-borne, Higher-solids and Powder Coatings Symposium. New Orleans (USA). 1994, 334-54.

[15] D.W. Pfeifer, M.J. Scali, Concrete sealers for protection of bridge structures, Department of Transportation, NCHRP 244, Washington (DC), 1981.

[16] M. Medeiros, P. Helene, Efficacy of surface hydrophobic agents in reducing water and chloride ion penetration in concrete, Mater. Struct. 41 (2007) 59–71. doi:10.1617/s11527-006-9218-5.

[17] M.H.F. Medeiros, P. Helene, Surface treatment of reinforced concrete in marine environment: Influence on chloride diffusion coefficient and capillary water absorption, Constr. Build. Mater. 23 (2009) 1476–1484. doi:10.1016/j.conbuildmat.2008.06.013.

[18] C. Christodoulou, C.I. Goodier, S.A. Austin, J. Webb, G.K. Glass, Long-term performance of surface impregnation of reinforced concrete structures with silane, Constr. Build. Mater. 48 (2013) 708–716. doi:10.1016/j.conbuildmat.2013.07.038.

[19] R.B. Polder, H. de Vries, Prevention of reinforcement corrosion by hydrophobic treatment of concrete, Heron 46 (2001) 227–238.

[20] A. Selander, Hydrophobic impregnation of concrete structures: Effects on concrete properties, Ph.D. thesis, Royal Institute of Technology, Stockholm, Sweden, 2010.

[21] J.G. Dai, Y. Akira, F.H. Wittmann, H. Yokota, P. Zhang, Water repellent surface impregnation for extension of service life of reinforced concrete structures in marine environments: the role of cracks, Cem. Concr. Compos. 32 (2010) 101-109.

[22] C. Murray, Durability of silane sealer in a highly alkaline environment, MSc thesis, University of Arkansas, 2014.

[23] K. Tosun, B. Felekoglu, B. Baradan, Effectiveness of alkyl alkoxy silane treatment in mitigating alkali-silica reaction, ACI Mater J. 105 (2008) 20–27.

[24] L. Schueremans, D. Van Gemert, S. Giessler, Chloride penetration in RC-structures in marine environment - Long term assessment of a preventive hydrophobic treatment, Constr. Build. Mater. 21 (2007) 1238–1249. doi:10.1016/j.conbuildmat.2006.05.006.

[25] R.E. Weyers, J. Zemajtis, R.O. Drumm. Service lives of concrete sealers. Transportation Res. Record 1490 (1995) 54-59.

[26] B. Sudbrink, M. Khanzadeh Moradllo, Q. Hu, M.T. Ley, J.M. Davis, N. Materer, A. Apblett, Imaging the presence of silane coatings in concrete with micro X-ray fluorescence. Cem.Concr. Res. (2016); accepted for publication. doi:10.1016/j.cemconres.2016.11.019.

[27] M.T. Ley, B. Sudbrink, H. Kotha, N. Materer, A. Apblett, Expected life of silane water repellant treatments on bridge decks, Research & Development Division Oklahoma Department of Transportation, No. FHWA/ODOT-2229, December 2012.

[28] M.T. Ley, M. Khanzadeh Moradllo, Expected life of silane water repellant treatments on bridge decks, Research & Development Division Oklahoma Department of Transportation, No. FHWA/ODOT-2229, October 2015.

[29] Oklahoma Department of Transportation, Planning & Research Division, Engineering Services Branch/Data Analysis Section, Annual Average Daily Traffic Maps 2011. http://www.okladot.state.ok.us/Maps/aadt/index.htm, (last accessed on August 2015)

[30] Oklahoma Department of Transportation. Standard Specifications Book 2009. http://www.okladot.state.ok.us/cnstrctengr.htm, (last accessed on August 2015).

[31] The Oklahoma Climatological Survey. Temperature and relative humidity averages: 1971-2003. <http://climate.ok.gov/index.php/climate/category/oklahoma_climate> (last accessed on August 2015).

[32] D.B. Duncan, Multiple range and multiple F tests, Biometrics 11 (1955) 1-42.

[33] W.G. Hunter, J.S. Hunter, Statistics for experimenters: an introduction to design, data analysis, and model building, New York: Wiley, 1978.

[34] A. Hajibabaee, M. Khanzadeh Moradllo, M.T. Ley, Comparison of curing compounds to reduce volume change from differential drying in concrete pavement, Int. J. Pavement Eng. c (2016) 1–10. doi:10.1080/10298436.2016.1210442.

[35] S.A. Freitag, S.M. Bruce, The influence of surface treatments on the service lives of concrete bridges, NZ Transport Agency research report 403, 2010, 91pp. ISBN 978-0-478-36420-0.

[36] P. Sandeford, G. Bendell, A. Mansoor, Corrosion management strategy for reinforced concrete wharf infrastructure located at the mouth of the Brisbane River, Corr. Mater. 34 (2009) 32–37.

[37] P.A.M. Basheer, L. Basheer, D.J. Cleland, A.E. Long, Surface treatments for concrete: assessment methods and reported performance, Constr. Build. Mater. 11 (1997) 413–429. doi:10.1016/S0950-0618(97)00019-6.

CHAPTER VIII

CONCLUSION

Fluid transport properties of cement-based materials are becoming increasingly more important because fluid transport is the primary factor influencing the durability of cement-based materials and determining the accurate fluid transport properties of cement-based materials is essential in predicting the service life of concrete structures. The research presented in this dissertation develops two novel analytical techniques to use μXRF and TXM to study a complex transport phenomenon and observe the influence of local abnormalities on fluid transport in cement-based materials in 2D and 3D. These methods have been used to investigate fluid transport in alternative cementitious materials and study effectiveness of silane surface treatments in deleterious environment.

The main conclusions of the dissertation are:

8.1 Using Micro X-Ray Fluorescence to Image Cl Profiles in Concrete

- μXRF is a powerful, non-destructive X-ray imaging technique used to find Cl profiles in concrete with minimal sample preparation.
- The average Cl penetration at comparable depths is similar between profile grinding and μXRF.
- μXRF was able to image the presence of cracks > 100 μm in concrete and their impact on local Cl penetration.

- μXRF identified Cl rich aggregate in a sample and allowed it to be removed in order to find the Cl concentrations.
- A high local concentration of aggregates caused an underestimation of the apparent diffusion coefficient. μXRF can be used to resolve this issue by solely investigating Cl profiles based on the paste.

8.2 Using X-Ray Imaging to Investigate In-Situ Ion Diffusion in Cementitious Materials

- TXM and μCT are powerful, non-destructive, and fast imaging techniques to investigate in-situ iodide diffusion in cementitious materials.
- Iodide and chloride diffusivity is shown to be comparable for paste samples with w/s of 0.40.
- There is a good agreement between μXRF and TXM for investigated samples and conditions.
- Features such as large air voids and aggregates are shown to influence the fluid flow within cement paste.
- Air voids with diameter of less than 200 μm were observed to fill with solution at high degrees of saturation.
- TXM and μCT techniques can be quite useful to study different durability mechanisms.

8.3 Quantitative Measurement of the Influence of Degree of Saturation on Ion Penetration by Using X-Ray Imaging

- The saturated samples showed about 75% reduction in I penetration depth compared to samples conditioned at 0% and 35% RHs even at 1 h of ponding.
- The P_c of the 35% and 70% RH samples is about 40x and 10x higher than the saturated sample at 2 d of ponding, respectively. This ratio decreases over time. However, this

calculated P_c combines the effect of capillary absorption and diffusion in partially-saturated samples.

- Previously suggested equations to estimate the depth of ion transport based on gravimetric analysis is unconservative by ≈ 23% for the materials and conditions investigated and can cause an overestimation of the predicted service life.
- A power model was successfully used to estimate the P_c of partially-saturated paste samples based on the P_c of fully saturated samples.
- Iodide shows a similar absorption and penetration performance to Cl in paste samples with different DoS.

8.4 Comparing In-Situ Ion Diffusion in Alternative Cementitious Materials by Using X-Ray Imaging

- The use of TXM offers advantages over conventional methods to investigate the resistance of cement-based materials with different chemistry against ion intrusion.
- Since TXM allows non-destructive and time-dependent diffusion profiles to be measured with little sample preparation and analysis this makes it a powerful method to measure the developing microstructure of ACMs and ultimately better understand the evolution of the ion diffusion of these materials.
- The calcium aluminate cements showed improved resistance to ion penetration and increased level of ion binding during the time period investigated (42 d).
- Both the calcium sulfoaluminate cement and alkali-activated binders showed a higher rate of ion penetration than portland cement and the calcium aluminate cements.
- The effective diffusion coefficient decreased rapidly between 14 d and 42 d for both calcium sulfoaluminate and alkali activated binders.

- Iodide and chloride diffusivity is shown to be comparable for paste samples in all of the binders investigated.

8.5 Application of Micro X-Ray Fluorescence to Study the Silane Resistance to Penetration of Cl Ions

- The two-part silane-epoxy sealer system shows 20% greater penetration when compare to a silane commonly used in Oklahoma when they were applied in the same manner on the same concrete.
- Both of silane systems have significantly reduced Cl penetration into concrete samples after 180 d ponding.
- The two part silane-epoxy system showed better performance over the first 90 days but then similar performance to commonly used silane system at 180 days. This is likely caused by deterioration of the epoxy sealer.
- This work shows the utility of using μXRF to efficiently and rapidly evaluate Cl profiles in concrete samples and compare the effectiveness of different sealers.

8.6 Determining the Effective Service Life of Silane Treatments in Concrete Bridge Decks

- The effectiveness of silane is investigated in 60 bridge decks with service life of 6 y to 20 y.
- The silane layer starts to decrease after 12 years of service.
- The average silane thickness is reduced by 75% in 17 to 20-year-old bridges.
- Only 16% of the bridges had an effective silane layer after 17 to 20 years of service.
- Abrasion was not a significant silane deterioration mechanism in investigated structures.
- Silane deterioration starts in the bulk of the concrete and progresses towards the surface.

8.7 Future Work

The developed non-destructive techniques from this study open up many future research opportunities to study different durability mechanisms such as freeze thaw attack, alkali silica reaction, physical salt attack, salt scaling, sulfate attack, and impact of temperature changes. In addition, the produced data sets can be used in computational modeling efforts. The following is a list of proposed future work:

- The effective diffusion coefficient of concrete samples could be obtained by using the same methodologies outlined in Chapter III but using a X-ray machine used in the medical field to investigate the skeletal structure of humans or animals. Since X-ray machines are so widely available they could be used to economically gather the data.
- The developed power model in Chapter IV can be extended to other relative humidities and materials, then the developed model can be used in computational modeling efforts to predict the service life of concrete structures in harsh environments.
- The developed methods can be used to investigate the effect of cracks with various geometries, aggregates, and air void system on fluid penetration into cement-based materials.

VITA

Mehdi Khanzadeh Moradllo

Candidate for the Degree of

Doctor of Philosophy

Thesis: USE OF NON-DESTRUCTIVE X-RAY MICROSCOPIC TECHNIQUES TO STUDY FLUID TRANSPORT IN CEMENT-BASED MATERIALS

Major Field: Civil Engineering

Biographical: Mehdi Khanzadeh Moradllo was born in Meshkinshahr, Ardabil, Iran on October 23, 1984.

Education:

Completed the requirements for the Doctor of Philosophy in Civil Engineering at Oklahoma State University, Stillwater, Oklahoma in December, 2016.

Completed the requirements for the Master of Science in Civil Engineering at University of Tehran, Tehran, Iran in January, 2010.

Completed the requirements for the Bachelor of Science in Civil Engineering at University of Mohaghegh Ardabili, Ardabil, Iran in June, 2007.

Experience:

Graduate Research Assistant, Oklahoma State University, Stillwater, OK, 2013-2016.

QC Manager, ARSA International Construction Company, Tehran, Iran, 2012-2013.

Project Manager, Construction Materials Institute, University of Tehran, Tehran, Iran, 2010-2012.

Graduate Research Assistant, University of Tehran, Tehran, Iran, 2007-2010.

Professional Memberships:

American Concrete Institute (ACI), since 2009.
American Society of Civil Engineering (ASCE), since 2013.
American Society for Testing and Materials (ASTM), since 2015.
NACE International, since 2010.
Precast/Prestressed Concrete Institute (PCI), since 2015.